STATE OF CALIFORNIA • DEPARTMENT OF TRANSPORTATION

TECHNICAL REPORT DOCUMENTATION PAGE

DRISI-2011 (REV 10/1998)

1. REPORT NUMBER CA17-2561	2. GOVERNMENT ASSOCIATION NUMBER	3. RECIPIENT'S CATALOG NUMBER
4. TITLE AND SUBTITLE Cut-and-Cover Shake Table Test Program		5. REPORT DATE December 2017 6. PERFORMING ORGANIZATION CODE UCSD
7. AUTHOR Kyungtae Kim and Ahmed Elgamal		8. PERFORMING ORGANIZATION REPORT NO. UCSD / SSRP-17-09
9. PERFORMING ORGANIZATION NAME AND ADDRESS Department of Structural Engineering School of Engineering University of California, San Diego La Jolla, California 92093-0085		10. WORK UNIT NUMBER 11. CONTRACT OR GRANT NUMBER 65A0563
12. SPONSORING AGENCY AND ADDRESS California Department of Transportation Engineering Service Center 1801 30th Street, MS 9-2/5i Sacramento, California 95816 California Department of Transportation Division of Research and Innovation, MS-8 1227 O Street Sacramento CA 95814		13. TYPE OF REPORT AND PERIOD COVERED Final Report 6/1/2015 – 10/31/2017 14. SPONSORING AGENCY CODE 913

15. SUPPLEMENTARY NOTES

Prepared in cooperation with the State of California Department of Transportation.

16. ABSTRACT

A series of shake table tests of a 1/9 scale shallow tunnel was performed to assess: i) overall peak dynamic response of the soil-structure system associated with different backfill conditions and thickness of overburden soil, and ii) seismic demands in terms of resultant lateral earth pressure force. The test model response was interpreted in full-scale dimensions representative of the idealized cross section of the Doyle Drive Battery Tunnel in San Francisco, CA. In the cases studied, seismic demand in terms of racking and wall bending moment increased as thickness of overburden soil increased. This trend was influenced as well by the relative stiffness between the tunnel and the surrounding soil. Overall, the tunnel lateral deformation was an outcome of the relative difference between the resultant force and its point of action on both sides of the tunnel. Finally, the test results in both model and prototype scale were compared to those estimated using a practice-oriented FHWA step-by-step procedure. In general, the FHWA procedure produced reasonable estimates for relatively lower levels of soil shear strain (i.e., cases of Peak Ground Acceleration (PGA) of up to about 0.6g). For higher levels of shaking, conservatism in the FHWA estimate was noted, particularly for cases with shallow overburden soil.

17. KEYWORDS Cut-and-Cover Tunnel, Shake Table Test, Soil-Structure-Interaction, Laminar Soil Container, FHWA	18. DISTRIBUTION STATEMENT Unlimited	
19. SECURITY CLASSIFICATION (*of this report*) Unclassified	20. NUMBER OF PAGES 241	21. COST OF REPORT CHARGED

DISCLAIMER

This document is disseminated in the interest of information exchange. The contents of this report reflect the views of the authors who are responsible for the facts and accuracy of the data presented herein. The contents do not necessarily reflect the official views or policies of the State of California or the Federal Highway Administration. This publication does not constitute a standard, specification or regulation. This report does not constitute an endorsement by the California Department of Transportation of any product described herein.

For individuals with sensory disabilities, this document is available in Braille, large print, audiocassette, or compact disk. To obtain a copy of this document in one of these alternate formats, please contact: the Division of Research and Innovation, MS-83, California Department of Transportation, P.O. Box 942873, Sacramento, CA 94273-0001

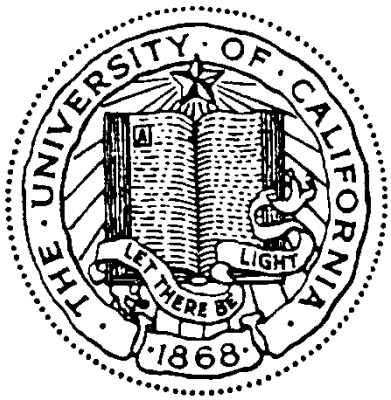

STRUCTURAL SYSTEMS

RESEARCH PROJECT

Report No.
SSRP-17-09

CUT-AND-COVER TUNNEL SHAKE TABLE TEST PROGRAM

by

KYUNGTAE KIM

AHMED ELGAMAL

Final Report Submitted to the California Department of Transportation (Caltrans) under Contract No. 65A0563

December 2017

Department of Structural Engineering
University of California, San Diego
La Jolla, California 92093-0085

University of California, San Diego
Department of Structural Engineering
Structural Systems Research Project

Report No. SSRP-17-09

Cut-and-Cover Tunnel Shake Table Test Program

by

Kyungtae Kim
Postdoctoral Scholar, UC San Diego

Ahmed Elgamal
Professor of Structural Engineering, UC San Diego

Final Report Submitted to the California Department of Transportation under Contract No. 65A0563

Department of Structural Engineering
University of California, San Diego
La Jolla, California 92093-0085

December 2017

ACKNOWLEDGMENTS

Funding for the investigations presented in this report was provided by the California Department of Transportation (Caltrans) under Contract No. 65A0563. This support is most appreciated. Dr. Charles Sikorsky of Caltrans, the project manager, provided continuous support and guidance throughout the project. In addition, the authors are most grateful to Caltrans engineers for their continuous technical input and advice. The authors also express sincere appreciation to Dr. Jinchi Lu at the University of California, San Diego for his thoughtful review and helpful comments on this report.

ABSTRACT

A series of shake table tests of a 1/9 scale shallow tunnel was performed to assess: i) overall peak dynamic response of the soil-structure system associated with different backfill conditions and thickness of overburden soil, and ii) seismic demands in terms of resultant lateral earth pressure force. The test model response was interpreted in full-scale dimensions representative of the idealized cross section of the Doyle Drive Battery Tunnel in San Francisco, CA. In the cases studied, seismic demand in terms of racking and wall bending moment increased as thickness of overburden soil increased. This trend was influenced as well by the relative stiffness between the tunnel and the surrounding soil. Overall, the tunnel lateral deformation was an outcome of the relative difference between the resultant force and its point of action on both sides of the tunnel. Finally, the test results in both model and prototype scale were compared to those estimated using a practice-oriented FHWA step-by-step procedure. In general, the FHWA procedure produced reasonable estimates for relatively lower levels of soil shear strain (i.e., cases of Peak Ground Acceleration (PGA) of up to about 0.6g). For higher levels of shaking, conservatism in the FHWA estimate was noted, particularly for cases with shallow overburden soil. For such scenarios, a site specific analysis with possible numerical simulation might be of value.

TABLE OF CONTENTS

LIST OF TABLES

LIST OF FIGURES

1. Introduction

1.1. Background

Seismic response of an underground structure is governed by deformation and inertial response of surrounding soil in view of (Wang 1993): (1) low stiffness of the surrounding soil due to the relatively small overburden pressure, and (2) site amplification effects. Moreover, soil backfill may consist of compacted materials with properties that are different from those of the in-situ soil, resulting in some added complexities in the overall system response (Wang 1993). As such, understanding the seismic loading demands imposed by ground shaking and deformation is needed in design practice (Hashash et al. 2001). In addition, soil-structure interaction (SSI) effects that modify the free-field ground deformation need to be considered in the design of underground structures (Wang 1993).

Wang (1993) provided a simple and practical procedure to account for dynamic SSI effects. This procedure was adopted in the Technical Manual for Design and Construction of Road Tunnels – Civil Elements (FHWA 2009). In evaluating the SSI effects, a number of factors are considered such as relative stiffness between the surrounding soil and the tunnel, structure geometry, earthquake input motion, and variation of the tunnel embedment depth (Wang 1993). Among those, the most important factor is the relative stiffness of soil in pure shear relative to the structure, defined as the flexibility ratio (F_{rec}) in the following expression (Wang 1993):

$$F_{rec} = \frac{G_m}{K_s}\frac{W}{H} \tag{1.1}$$

where G_m is the average strain-compatible shear modulus of the surround grounding, W is the width of the structure, H is the height of the structure, and K_s is the racking stiffness of the tunnel. As such, the tunnel stiffness plays an important role in evaluating the SSI effects.

In the Phase 1 report titled “racking response of reinforced concrete cut-and-cover tunnel” (Kim et al. 2015), the 1/3 scale reinforced concrete (RC) tunnel model segment was tested under quasi-static cyclic lateral loading at the University of California, San Diego (UCSD). This RC tunnel model was based on an idealized cross-section of the Doyle Drive Battery tunnel (Caltrans 2012). The test was performed to evaluate the tunnel lateral stiffness and large deformation response characteristics. In addition to the RC tunnel test, an additional model at 1/9 scale was

tested incorporating ground representative of realistic backfill conditions using a laminar soil container in a transverse shear loading pattern (Kim et al. 2015). Thereafter, as a continuation of this study, using a similar soil-structure model configuration, a series of shake table tests were performed at UCSD to further evaluate the involved SSI effects.

In this report, details of the performed shake table testing phase are presented. The recorded response of the test models is discussed mainly in model scale. Afterwards, the associated response in the full-scale model configuration is presented. Finally, a FHWA step-by-step procedure is used to estimate the racking and bending moment of the tested tunnel in both model and prototype scales. The FHWA estimates were compared to the test results and further discussion of the FWHA procedure outcomes are presented.

1.2. Research Scope

The objectives of this research are:

1. To evaluate seismic response of a shallow tunnel under different backfill conditions and thickness of overburden soil (associated with burial depth) in the 1/9 model scale configuration and on this basis, at the actual full-scale dimensions.
2. To provide recommendations regarding current seismic design criteria for shallow tunnels. For this purpose, a comparison study is conducted between the shake table test results, and tunnel deformation estimated using a simplified step-by-step procedure presented in FHWA (2009).

1.3. Report Outline

This report is composed of six chapters. A summary of each chapter is provided below:

- Chapter 2 describes details of the shake table test program. Three test model configurations including the tunnel structure, soil properties, and earthquake input motions are discussed.
- Chapter 3 presents the shake table test results in model scale. Peak dynamic response of the tunnel structure and the backfill is summarized.
- Chapter 4 discusses the observed lateral earth pressure (including the static response) along the tunnel walls at peak racking in model scale. The earth pressure is expressed as a resultant lateral earth pressure force and associated point of action.
- Chapter 5 presents the shake table test results in prototype scale. In the end, the total bending moment including the static value is discussed.

- Chapter 6 shows comparison of the shake table results with the estimates using the FHWA step-by-step procedure in both model and prototype scale.
- Chapter 7 provides a summary of this study as well as major observations and conclusions. Recommendations for the FHWA step-by-step procedure are provided as well.
- Appendix A presents photographs taken during the shake table test model construction.
- Appendix B displays the instrumentation layout for the shake table test models.
- Appendix C shows the recorded response time histories of the shake table tests in model scale.
- Appendix D provides further details about the scaling laws associated with the shake table test models.
- Appendix E presents main recorded response time histories in prototype scale.
- Appendix F presents finite element analyses of the 1st test model configuration in both model and prototype scales. The prototype scale numerical model was further used to study the influence of possible pinned connection at the interface between wall and roof on both sides of the tunnel.
- Appendix G includes a summary of the 1/3 RC tunnel test presented in the Phase I report.

2. Shake Table Test Program

2.1. Test Configuration

A tunnel-soil model was tested using the large-scale outdoor shake table at UCSD (Figure 2–1). A relatively large laminar soil container (15 ft high, 22 ft long, and 9.6 ft wide) was employed in order to reduce the boundary effect during earthquake excitation. Figure 2–2 shows photographs of the tunnel model employed in the shake table tests.

Three test model configurations were employed with different backfill conditions for the surrounding soil and thickness of overburden soil. Two levels of compaction were considered in terms of the relative density (D_r; about 99% and 85%). The tunnel was placed on 9.3 ft deep compacted ground at about 99% D_r (Figure 2–3). The three test model configurations are as follows:

1) Model 1 (1st test model configuration) backfilled at D_r of 99% overlain by 2ft overburden soil (Figure 2–3)
2) Model 2 (2nd test model configuration) backfilled at D_r of 85% without overburden (Figure 2–4)
3) Model 3 (3rd test model configuration) backfilled at D_r of 85% overlain by 1ft overburden soil (Figure 2–5)

During the replacement of backfill next to the tunnel, the soil below the structure base remained unchanged. Appendix A provides photographs taken during model construction.

2.2. Tunnel Model

Figure 2–6 shows the tested tunnel model (3.3 ft high and 6 ft wide). Length of the tunnel (9.25 ft) perpendicular to its cross-section was essentially equal to that of the container width (i.e., resulting in a plane strain-type model configuration). This model was designed to represent a possible 1/9 scale model in terms of the geometric dimensions and lateral stiffness. In prototype scale, the equivalent dimensions for height, width, and length are 30 ft, 53 ft, and 83 ft, respectively. The corresponding scaling laws are presented in Appendix D.

The prototype structure was adopted based on an idealized 1/3rd scale cross-section of the Doyle Drive Tunnel presented in the previous Phase I study titled “Racking response of reinforced concrete cut-and-cover tunnel” by Kim et al. (2015). This 1/9 scale tunnel model was also based on the 1/3rd scale reinforced concrete (RC) tunnel segment (Kim et al. 2015; see Appendix G for

a summary of this RC tunnel model.). This RC tunnel was fabricated and tested with fixed connections near the tunnel roof on both sides of the tunnel as shown in the as-built drawings. As such, this pinned connection was not taken into consideration in the steel tunnel model for the shake table tests. Upon completion of the shake table test, the pinned connection was studied in a finite element model to further evaluate its effect on the tunnel deformation. This preliminary numerical study and its outcomes is presented in Appendix F.

Due to model detail challenges in construction of an RC specimen at 1/9 scale, the tunnel was built out of steel (Figure 2–6). An added advantage of using steel is that this model remains in the linear range during the testing phase without any permanent deformation during the tests. The wall was 27.25 inches in height, measured from the top face of the 6 in high hollow structural steel (HSS) base (Figure 2–6a). To obtain high flexural (*EI*) and axial (*EA*) rigidities against lateral loads in the roof and slab sections, 12 HSS columns were deployed in the roof and slab at a center-to-center spacing of 1 ft (Figure 2–6a). As such, the laterally induced deformation was completely dictated by the walls. To produce the actual curved roof geometry of the prototype, a wooden frame was mounted above the top of the tunnel model.

2.2.1. Lateral stiffness testing

Figure 2–7 shows the test setup to measure lateral stiffness of the 1/9 scale tunnel model (without the wooden frame affixed to the roof) under a fixed base condition. Figure 2–8 shows the measured displacement upon application of a point loads at top of the wall. Elastic response was observed up to the lateral displacement of 0.21 in (at the loading of 25.7 kip) corresponding to a 0.8% drift ratio with an effective height of 27.25 in. The measured lateral stiffness was 123 kip/in. Table 2–1 summarizes the test results in both model and prototype scales. In prototype scale, lateral displacement was 5.67 in (scale factor of 27, $\lambda^{1.5}$ where $\lambda = 9$) and drift ratio was 2.4% based on the scale factor of 3 (= $\lambda^{0.5}$, where $\lambda = 9$). The corresponding lateral stiffness was 3,321 kip/in (39.9 kip/in per unit length of 1 ft) by using a scale factor of 27 (= $\lambda^{1.5}$ where $\lambda = 9$).

Based on a simple frame analytical approach (e.g., one bay/story frame with rigid beam along the roof), associated lateral stiffness of the tunnel is expressed as:

$$k = \sum_{colums} \frac{12EI}{h^3} = \frac{24EI}{h^3} \tag{2.1}$$

where h is height of the wall (h = 27.25 in and k = 123 k/in in this study). Using the Eq. (2.1), EI of the wall (both sides) were computed as 98.2 x 10^3 kip·in^2 in model scale. It is noted that the EI measured from the test was very similar to that resulting from the moment of inertia (I) using the wall thickness of 0.75 inch and elastic modulus (E) of 29,000 ksi for steel.

2.3. Soil Material Properties

2.3.1. Soil gradation

Sieve analysis was performed to characterize the particle size distribution of the employed backfill materials. Figure 2–9 shows the resulting particle gradation curve with a coefficient of uniformity (C_u) of 6.2 and a coefficient of curvature (C_c) of 0.8. The soil was classified as poorly graded sand (SP) according to the Unified Soil Classification System (USCS).

2.3.2. Triaxial test

A series of consolidated-drained (CD) triaxial tests were performed on a dry sample of the sand (used for the backfill) to measure the shear strength and volume change. The triaxial tests were performed at confining stresses of 1 psi, 3 psi, 5 psi, 7 psi, and 12 psi, which encompassed the stress range to be expected in the shake table tests.

The specimens were compacted within the latex membrane held by a split-wall compaction mold at nearly 100% D_r and dry unit weight of 122 pcf. After compaction, vacuum was applied to the soil specimen, and the split-wall mold was removed. The sand specimens had a diameter of 3 in (71.1 mm) and height of 5.6 in (142.2 mm). Similar to the free-field condition used in the shake table tests, the soil specimens had 7% water content. The confining pressure was applied prior to shearing. The shear force was applied using a constant strain rate of 1%, and the volume change reading was taken during shearing.

Figure 2–10 shows the stress-strain and volume change response under different confining stresses. The peak shear strength for each test was used to define the Mohr-Coulomb failure envelope. Figure 2–11 shows the Mohr circles and the best-fit failure envelope for the specimens with a zero cohesion and a friction angle (ϕ) of 53.2° (Figure 2–11a). In addition, the modified Mohr Circle diagram (also known as the MIT p-q diagram) was established using the mean stress (p) and the deviator stress (q) to determine any cohesion (c) in the soil sample (Figure 2–11b). For this modified diagram, the resulting ϕ and c were calculated to be 51.9^o and 2.0 psi, respectively.

It is noted that any post-construction evaporation of water from the soil model might change the properties measured during the triaxial test (Wilson 2009).

2.3.3. Sand cone test

Sand cone tests were performed to measure the D_r of the backfill at five elevations during construction. Table 2–2 summarizes the sand cone test results.

2.4. Earthquake Input Motions

2.4.1. Northridge earthquake (USC, Fire station 108 record)

A shake table motion taken from the 1994 Northridge earthquake was employed (recorded at Fire Station 108, 12520 Mulholland Dr., USC station 5314, Component 35, http://strongmotioncenter.org/vdc/scripts/plot.plx?stn=424&evt=21). Figure 2–12 shows the measured shake table response from Model 1.

2.4.2. Kobe earthquake (Takatori record)

With a large velocity pulse (representative of a near source motion), the Takatori record (from the 1995 Kobe earthquake) was used as an input (Takatori station in Japan, Component 0, http://strongmotioncenter.org/vdc/scripts/event.plx?evt=1098#4053). Figure 2–12 shows the measured shake table response from Model 1.

2.4.3. Scaled earthquake motions

According to the model scale (1/9) and the resulting model dynamic frequency, the time duration of the above Northridge and Takatori earthquake motions were scaled by a factor of 1.0/5.2. To further investigate the seismic response under different ground motions, additional scale factors were taken into consideration in terms of time duration (using a factor of 1.0/2.5) and acceleration amplitude (a factor of 2 for the Northridge earthquake record) as summarized in Table 2–3. This table also includes the measured peak acceleration, velocity, and displacement of the shake table from Model 1.

Table 2–4 summarizes the sequence of shaking events. The recoded acceleration time histories are shown in Figure 2–13 through Figure 2–15 from Models 1-3, respectively. Figure 2–16 shows the pseudo-acceleration response spectra for the records of Model 1.

2.5. Instrumentation Plan

Table 2–5 summarizes the employed types and numbers of instruments used in the tests. Detailed instrumentation drawings can be found in Appendix B.

2.6. Archived Test Data

The test data was provided via the following cloud address:
https://drive.google.com/open?id=0B6LnvH3L0K7IbW1KQ2dqcEUtb3M
Figure 2–17 shows the names of the test data files listed according to the loading sequence (Table 2–4). In the directory of each shaking event, a total of six data files were stored. Test data of each file were collected from the channels listed in Table 2–6. For example, Figure 2–18 shows the "Data2_acceleration.dat" file measured from a shaking event using the Nor100PT0 motion for the 1st test model. As shown in this file, the records were saved with 8-decimal scientific format and delimited by tab characters (Microsoft Excel can be used to open this file).

Table 2–1: Lateral stiffness test results of the steel tunnel specimen in model and prototype scales

Quantity	1/9 Scale	Scaling factors	Prototype scale
Target lateral displacement (in)	0.21	27 (= 9^3)	5.67
Lateral stiffness (kip/in)	123	9 (= 9^1)	3,321 (40 kip/in per unit length of 1ft)

Table 2–2: Summary of sand cone test measurement for Model 1 (2ft overburden soil)

Test No.	Depth (inch)	Field moisture (%)	Dry density (pcf)	Maximum dry density (pcf)	Relative compaction (%)	Remarks
1	36	7.2	120.6	122	99	
2	36	7.6	120.3	122	98	
3	72	6.5	122.3	122	100	
4	72	6.4	120.8	122	99	
5	111	8.3	123.1	122	100	At tunnel base
6	111	7.1	121.2	122	99	At tunnel base
7	149	7.3	119.4	122	98	
8	149	7.9	119.6	122	98	
9	178	6.7	120.3	122	99	
10	178	6.3	121.1	122	99	

Table 2–3: Ground motions used in the shake table tests

No.	Input motion	Earthquake	Amplitude scale factor	Time scale factor	PGA† (g)	PGV† (in/s)	PGD† (in)
1	Nor100PT0	Northridge	1	1	0.51	11.3	2.6
2	Nor100PT1		1	1.0/2.5	0.40	4.2	0.3
3	Nor100PT2		1	1.0/5.2	0.38	1.8	0.7
4	Nor200PT1		2	1.0/2.5	0.93	8.8	0.7
5	Tak100PT0	Takatori	1	1	0.68	53.0	13.8
6	Tak100PT1		1	1.0/2.5	0.72	20.6	2.4
7	Tak100PT2		1	1.0/5.2	0.55	8.4	1.1

†Measured from Model 1 (2ft overburden soil)

Table 2–4: Sequence of the shaking events

No.	Model 1 (2ft overburden soil)	Models 2 -3 (0 to 1 ft overburden soil)
1	Nor100PT1	Nor100PT2
2	Nor200PT1	Nor100PT1
3	Nor100PT0	Nor100PT0
4	Tak100PT1	Tak100PT2
5	Tak100PT0	Nor200PT1
6	Nor100PT2	Tak100PT1
7	Tak100PT2	Tak100PT0

Table 2–5: Type and number of sensors

Sensor Type	Location	Description	No. of Sensors
Accelerometer	Shake table	3 DOF accelerations at top center of shake table platen	3
	Soil box	Soil box acceleration along the height	24
	Soil, free-field	Soil (free-field) acceleration response	31
	Tunnel	tunnel acceleration response at the top and bottom of the walls	16
String Potentiometer	Soil box	Soil box lateral displacement along the height	15
	Tunnel and soil box	Lateral translations of the tunnel relative to the soil box	8
Linear Potentiometer	Tunnel	Racking	8
	Soil surface	Vertical soil displacement	7
Inclinometer	Tunnel	Rotation of the tunnel base	2
Strain gauge	Tunnel	Bending strain along the wall height	56
Pressure sensor	Tunnel	Lateral earth pressure along the wall height	35
Total no. of sensors			205

Table 2–6: Channel information about data directory

Data	Response	Channel label	No. of channels
Data 1	Shake table	Acc./ Vel./ Disp.	3
Data 2	Acceleration	A01-A71	71
Data 3	Displacement (SP)	SP01-SP23	23
Data 4	Displacement (LP)	LP01-LP07 / LP11-LP18	15
Data 5	Bending strain	S01-S56	56
Data 6	Pressure	TS01-TS31	31

Figure 2–1: Pictures of shake table test model; (a) North view and (b) East view

Figure 2–2: Pictures of the tunnel specimen

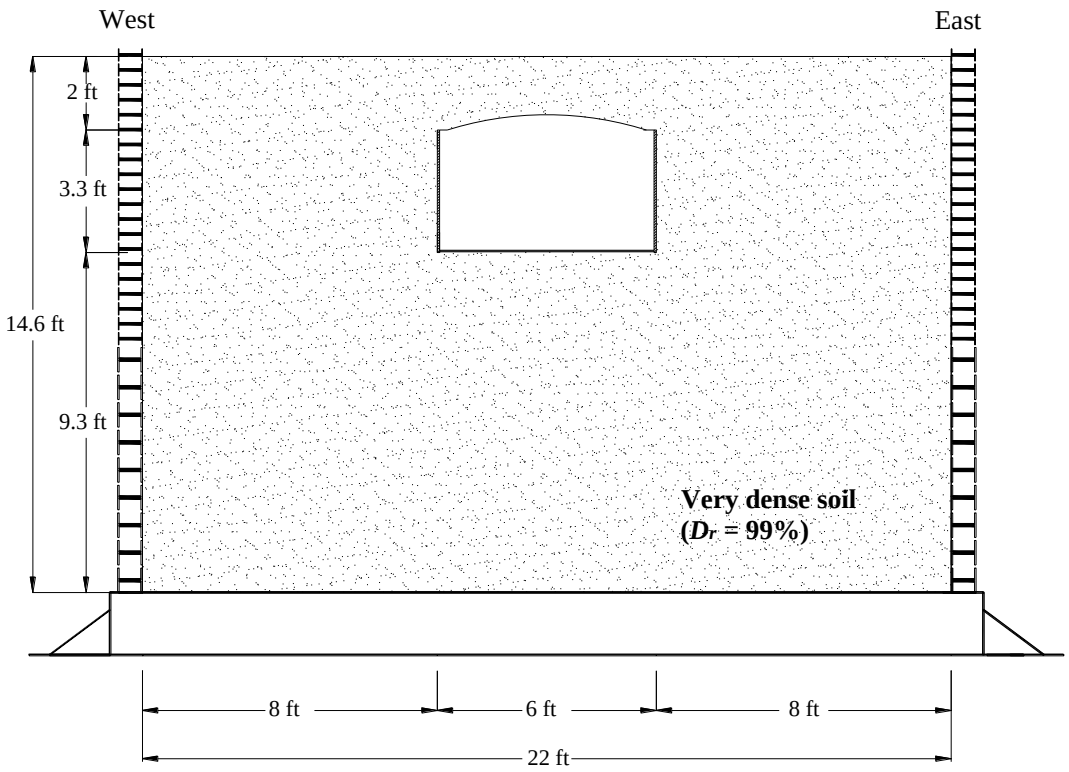

Figure 2–3: 1st Test model configuration (Model 1)

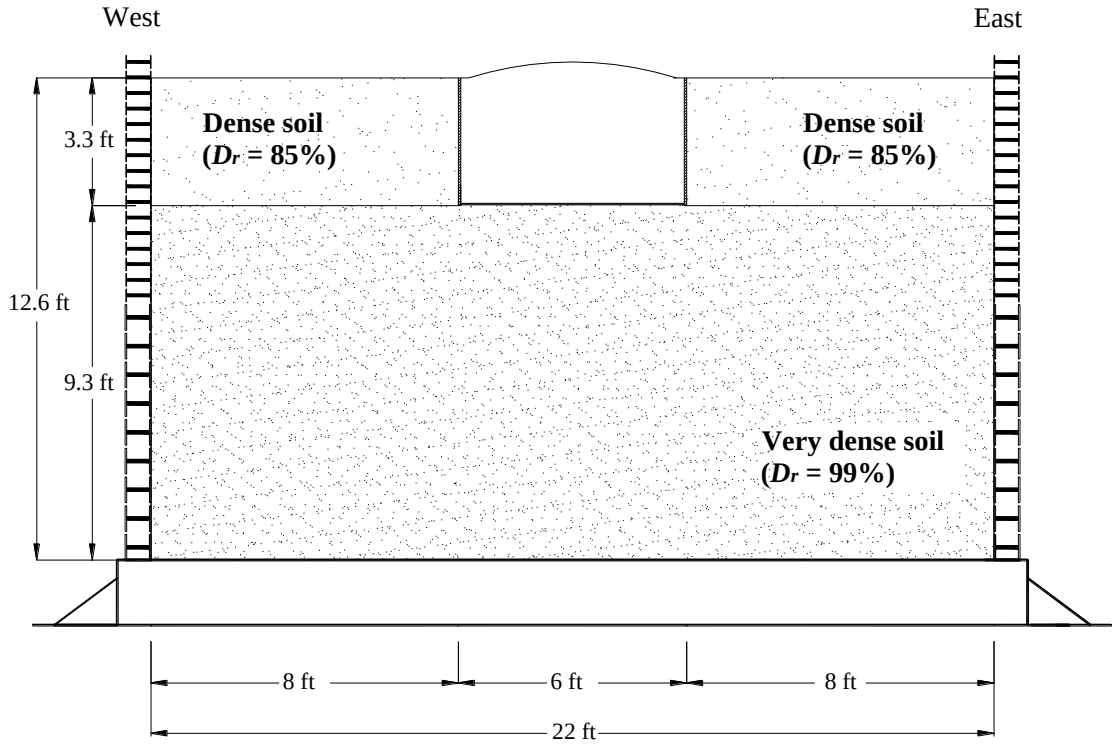

Figure 2–4: 2nd Test model configuration (Model 2)

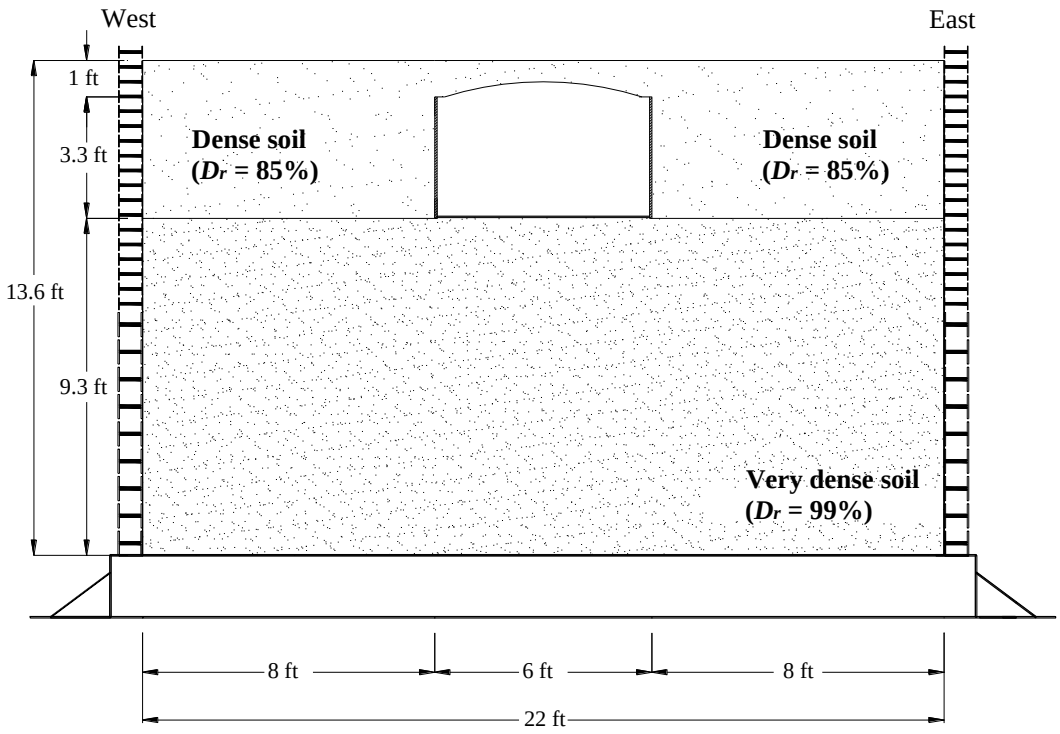

Figure 2–5: 3rd Test model configuration (Model 3)

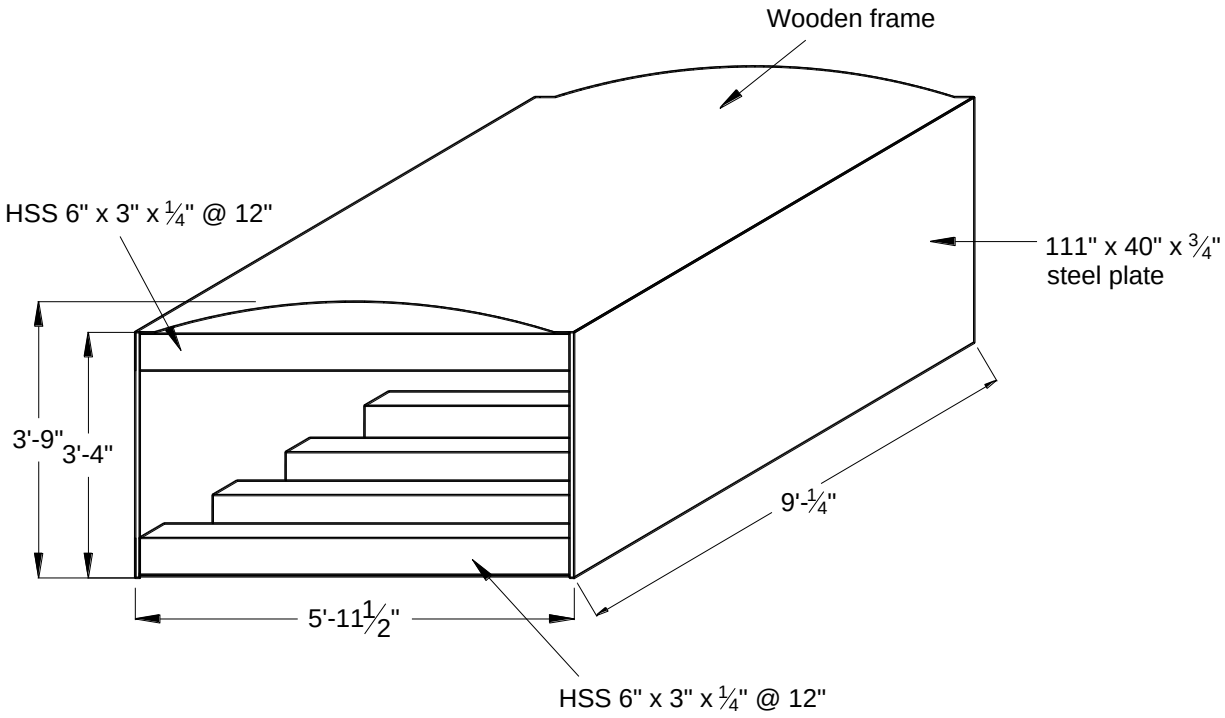

(a) Overall drawing of the 1/9 scale tunnel specimen

(b) Photograph of the 1/9th scale tunnel specimen (cross-sectional view)

Figure 2–6: 1/9th scale tunnel specimen used for the shake table tests

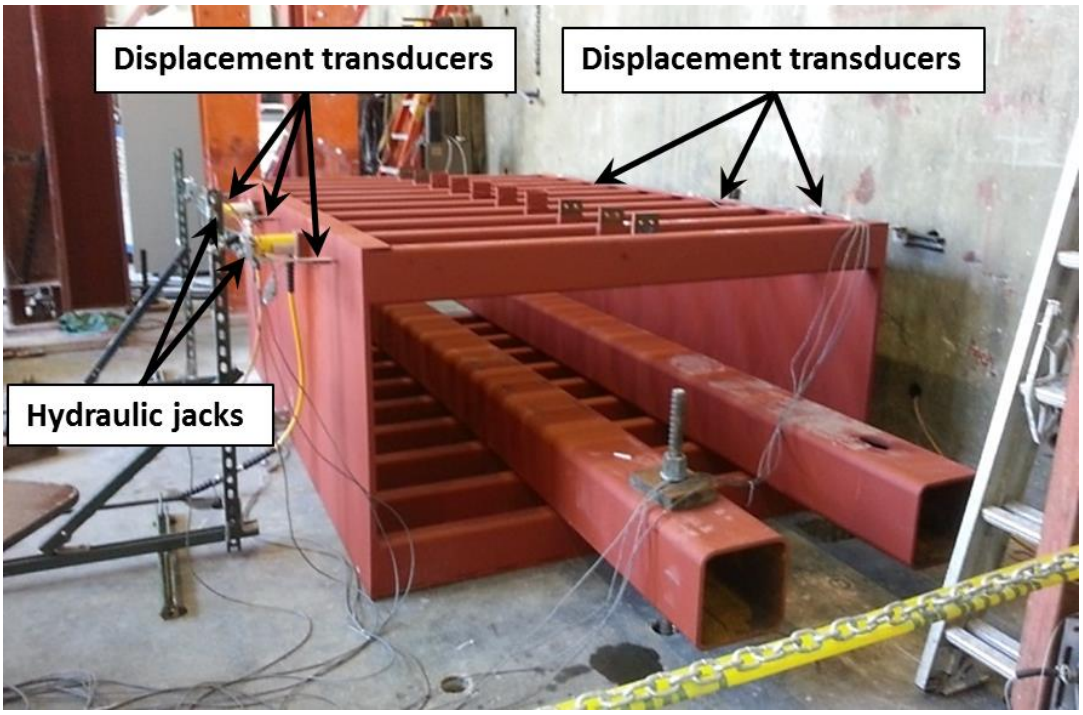

Figure 2–7: Photographs of test setup to measure lateral stiffness of the 1/9 scale steel tunnel specimen

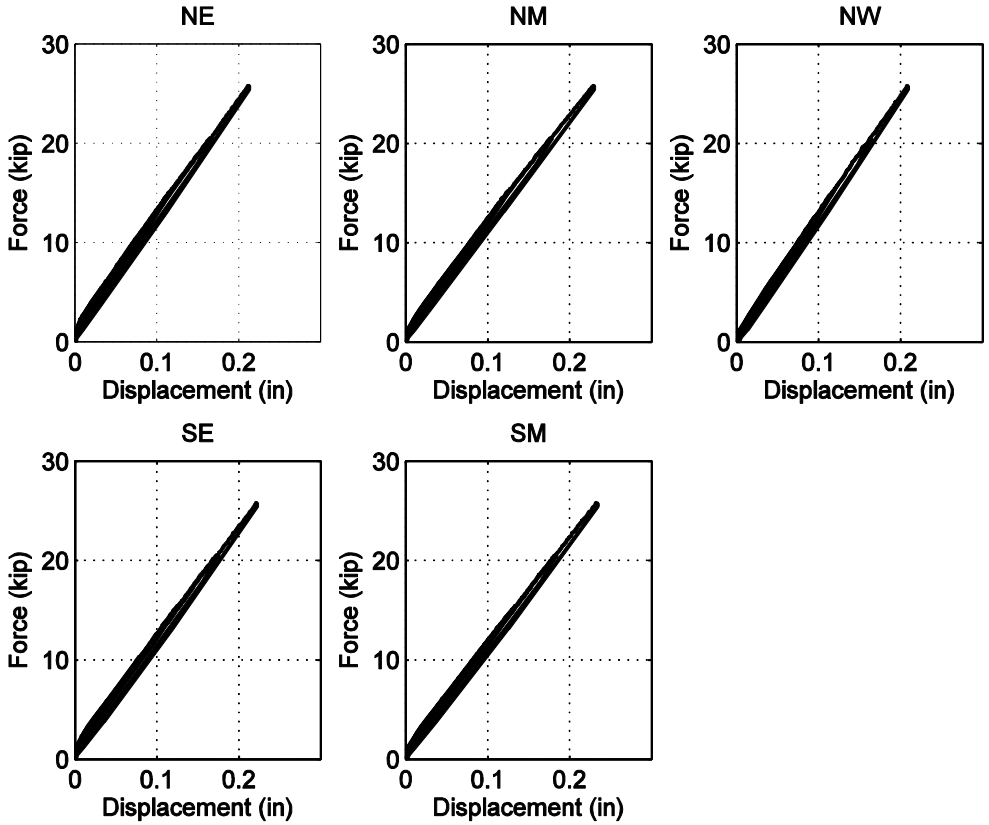

Figure 2–8: Lateral load vs. displacement measured from the physical test

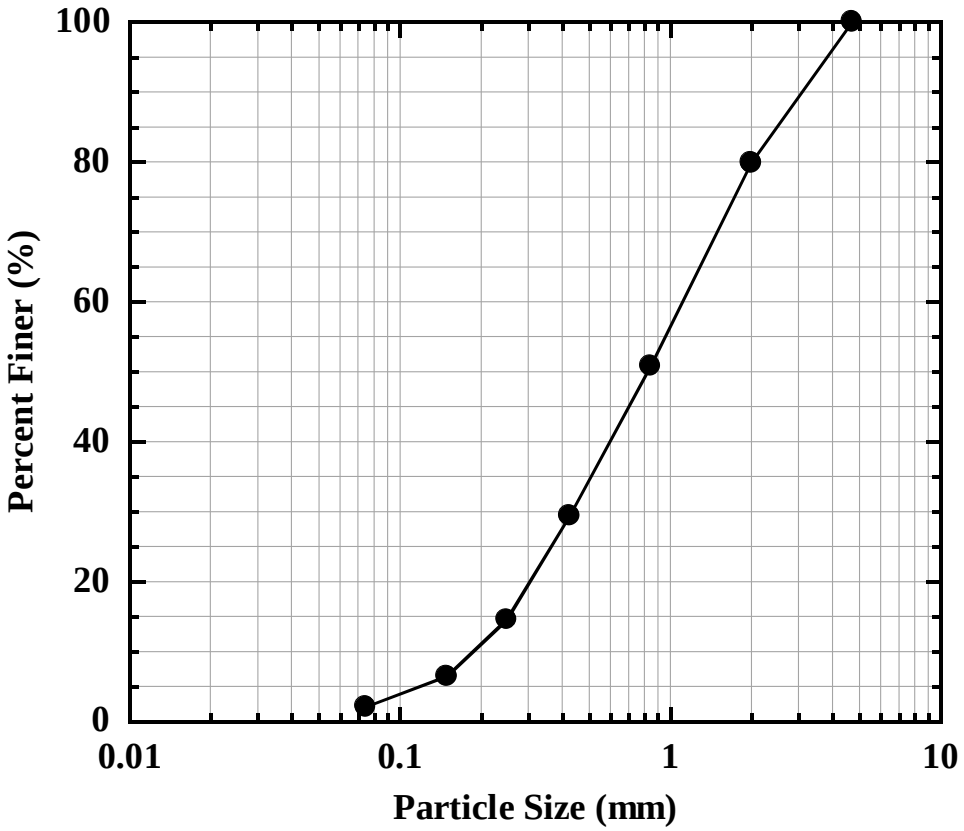

Figure 2–9: Particle gradation curve of the soil backfill materials used in the shake table tests

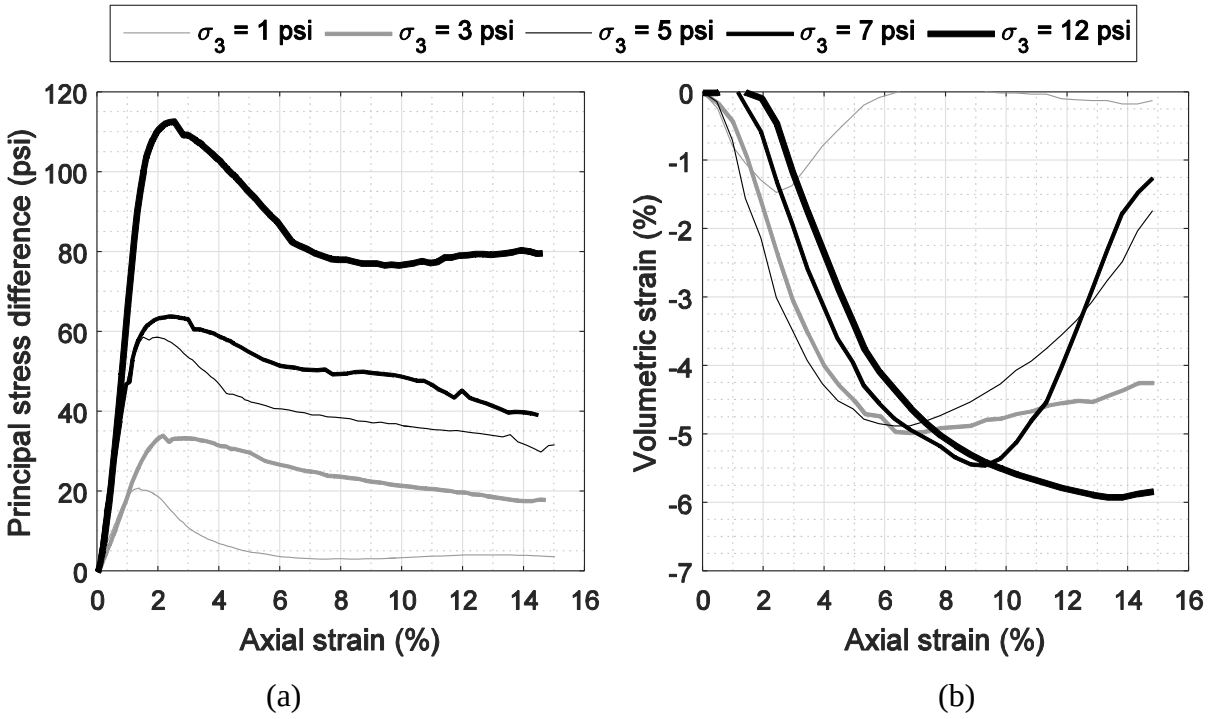

(a) (b)

Figure 2–10: Triaxial test results: (a) deviator stress vs. axial strain; (b) volumetric strain vs. axial strain.

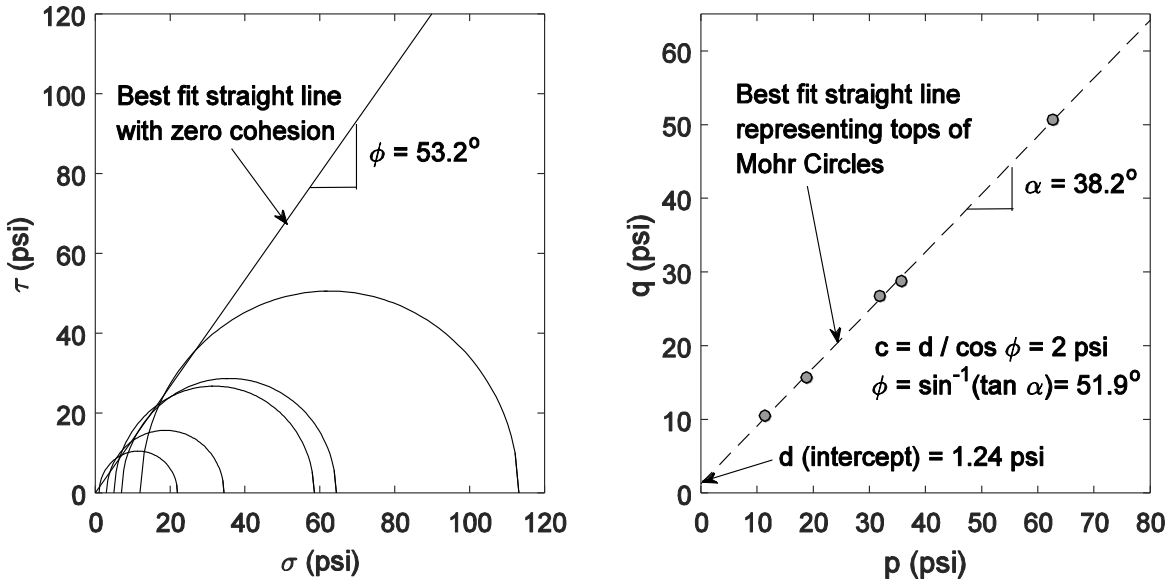

Figure 2–11: (a) Mohr circles and failure envelope for zero cohesion and (b) modified Mohr-Coulomb diagram (MIT p-q diagram)

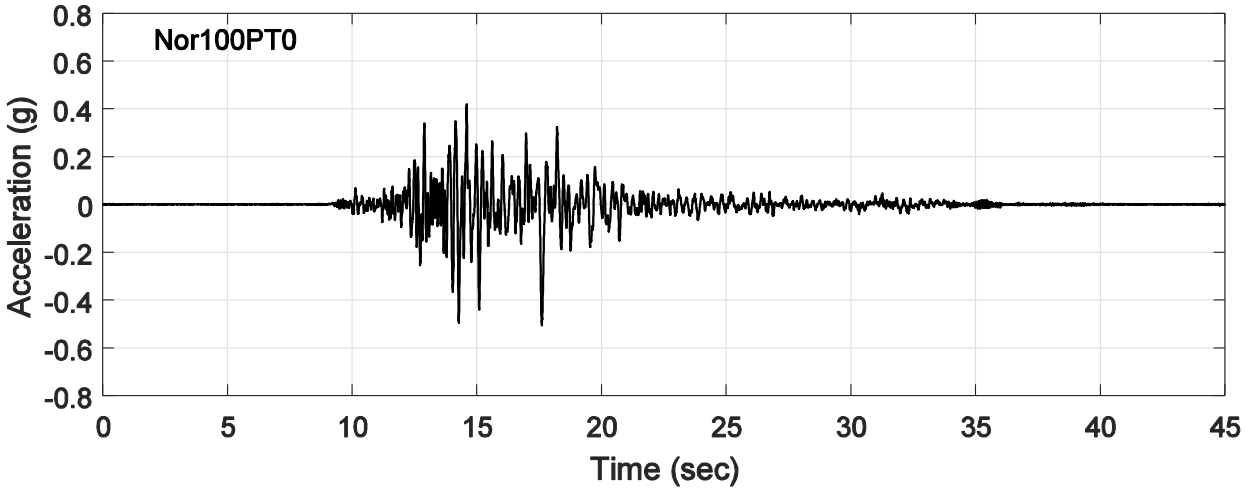

(a)

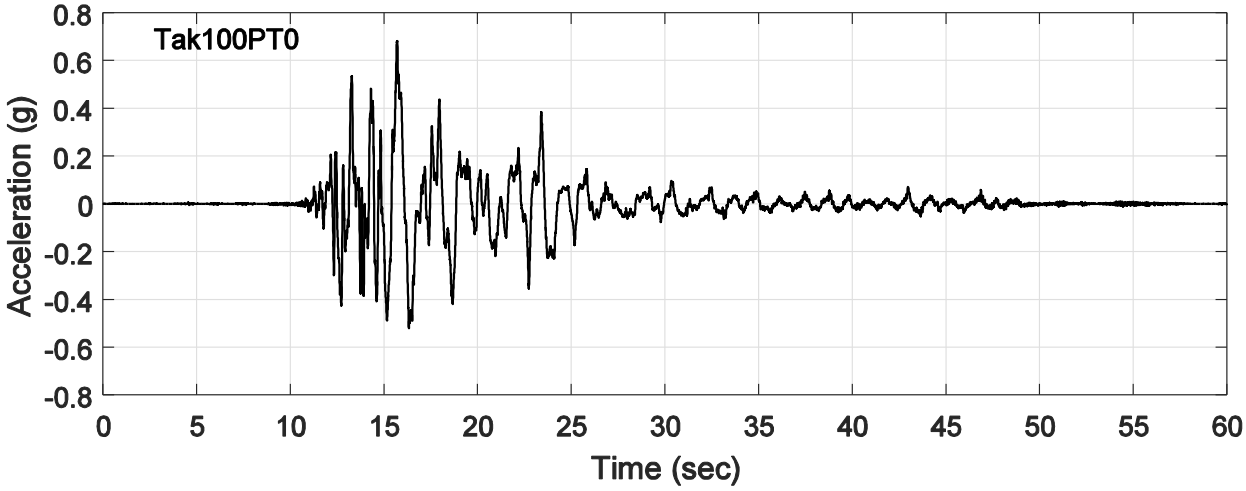

(b)

Figure 2–12: Acceleration time histories recorded at the model base using (a) Northridge 100% original time duration (Nor100PT0) and (b) Takatori 100% original time duration (Tak100PT0)

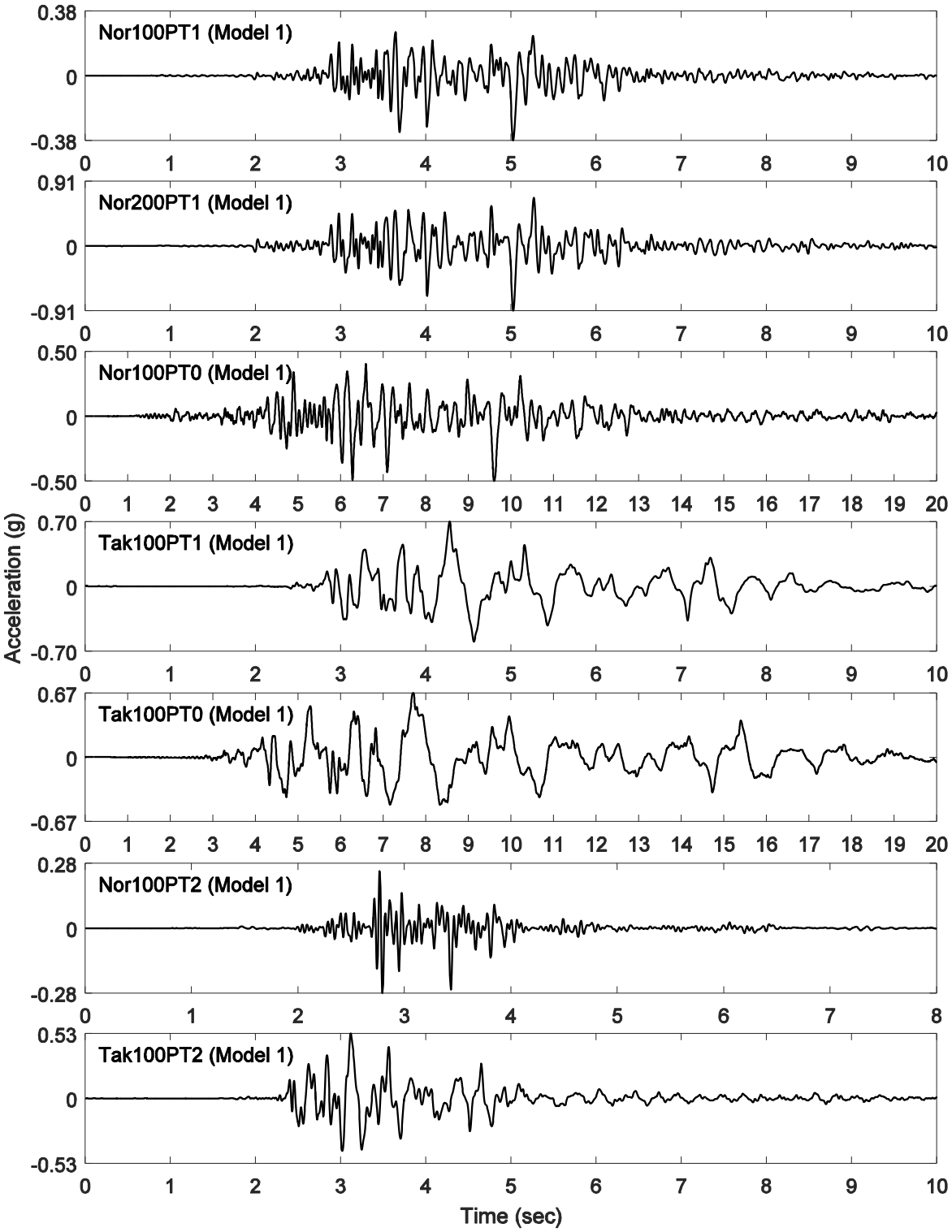

Figure 2–13: Earthquake input motions measured at the shake table for Model 1

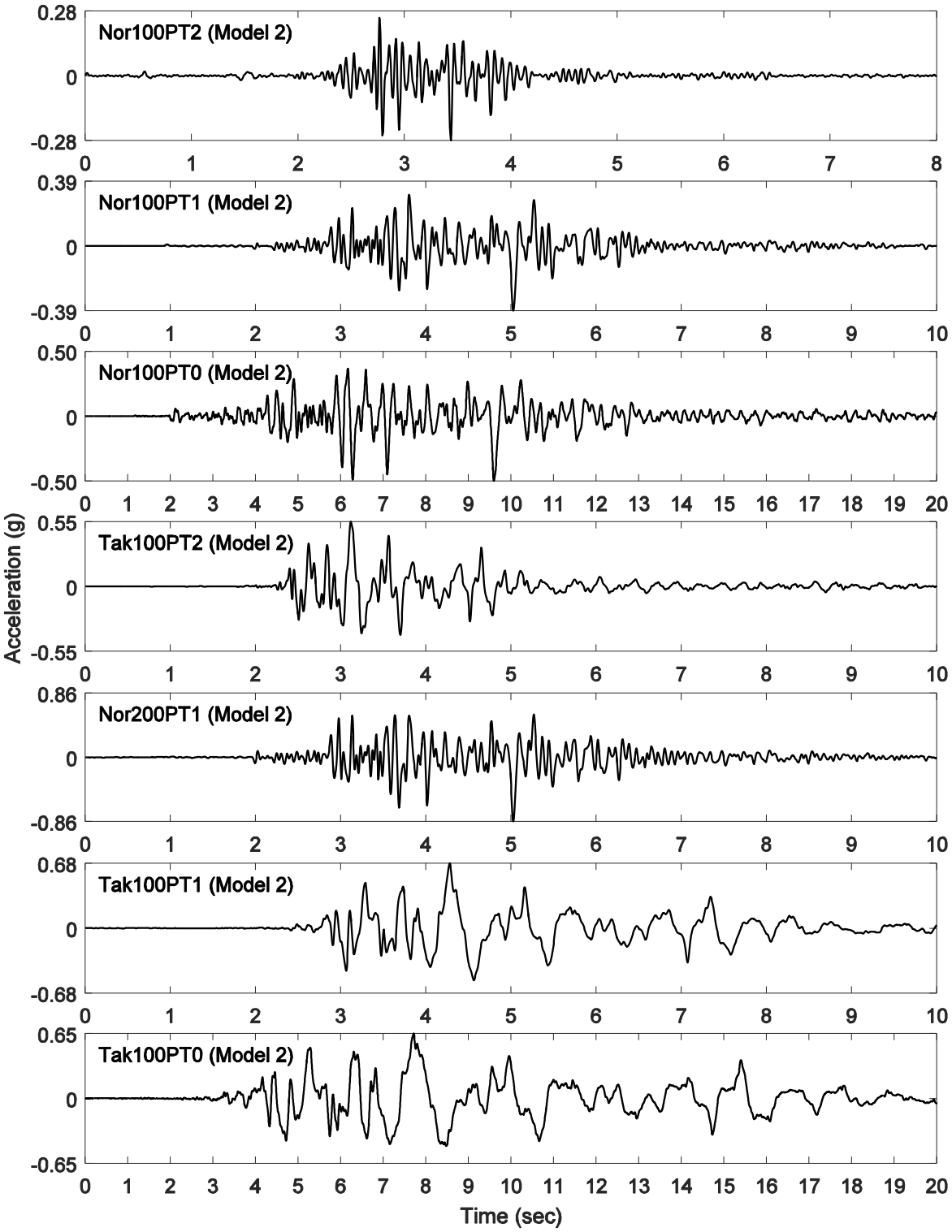

Figure 2–14: Earthquake input motions measured at the shake table for Model 2

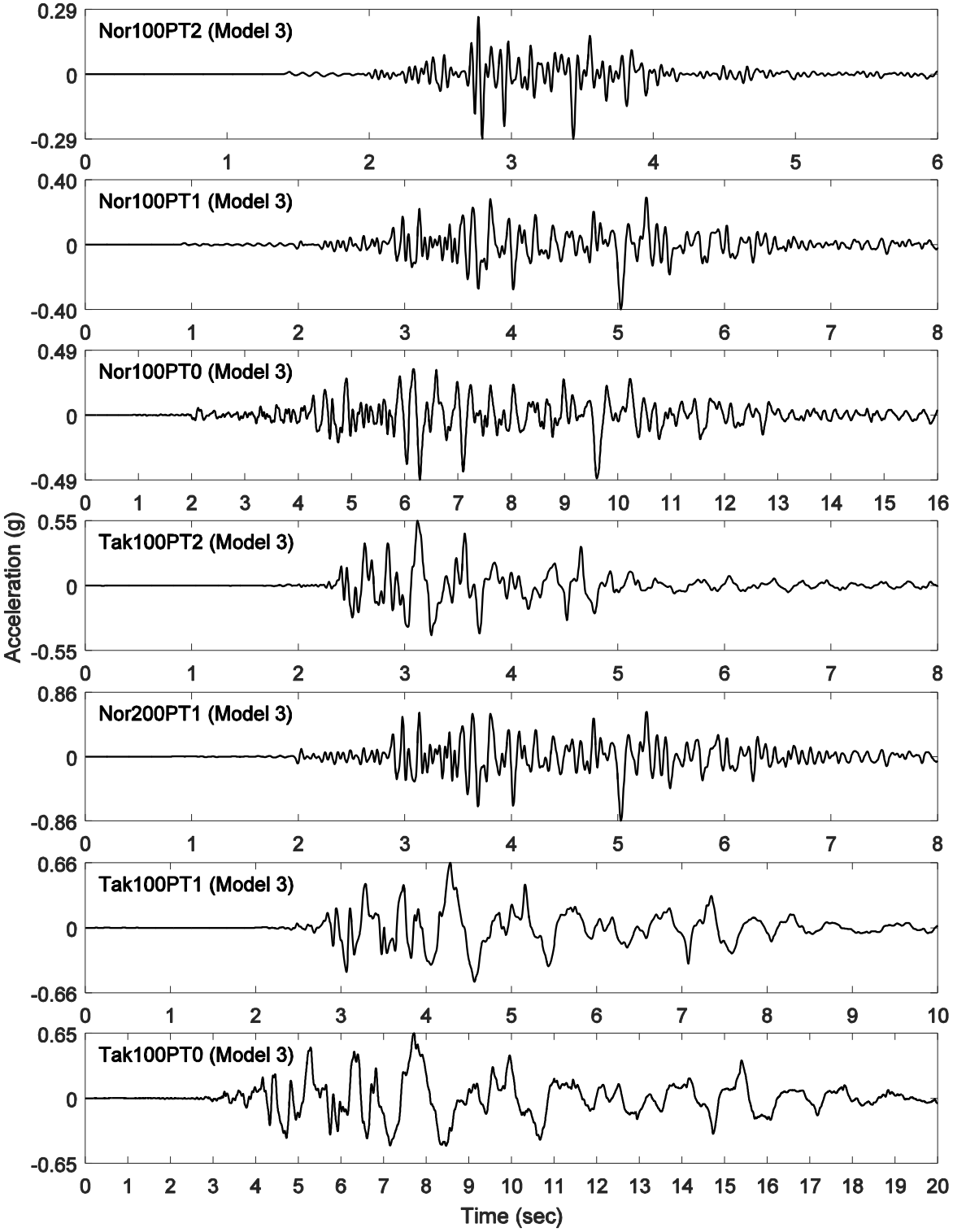

Figure 2–15: Earthquake input motions measured at the shake table for Model 3

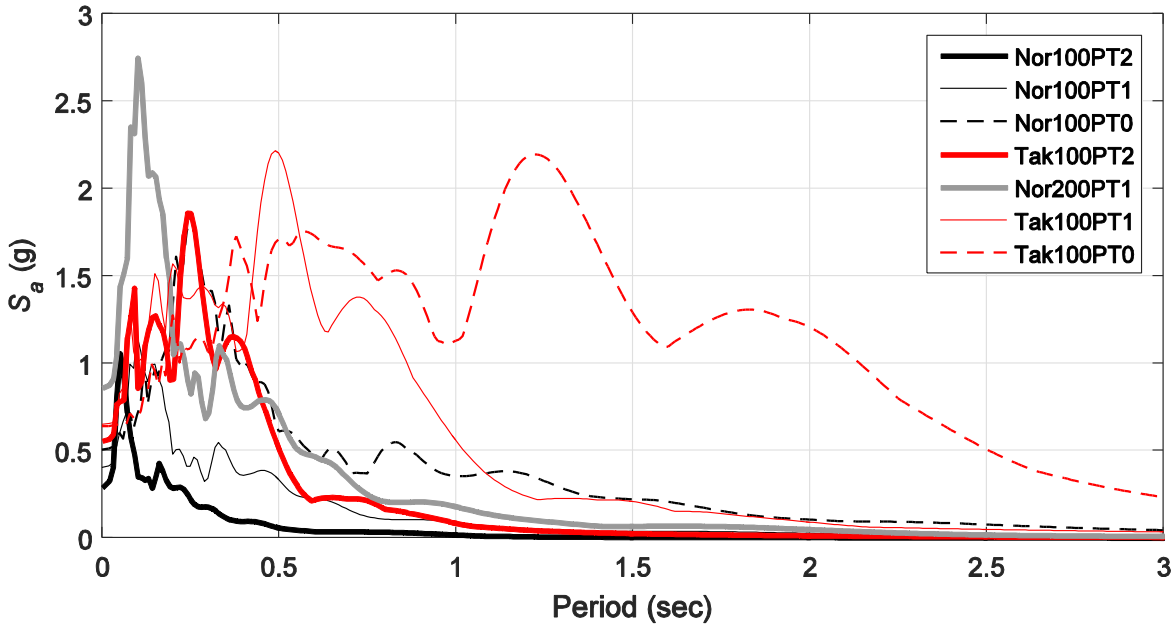

Figure 2–16: Pseudo-acceleration response spectra of shake table acceleration records for Model 1

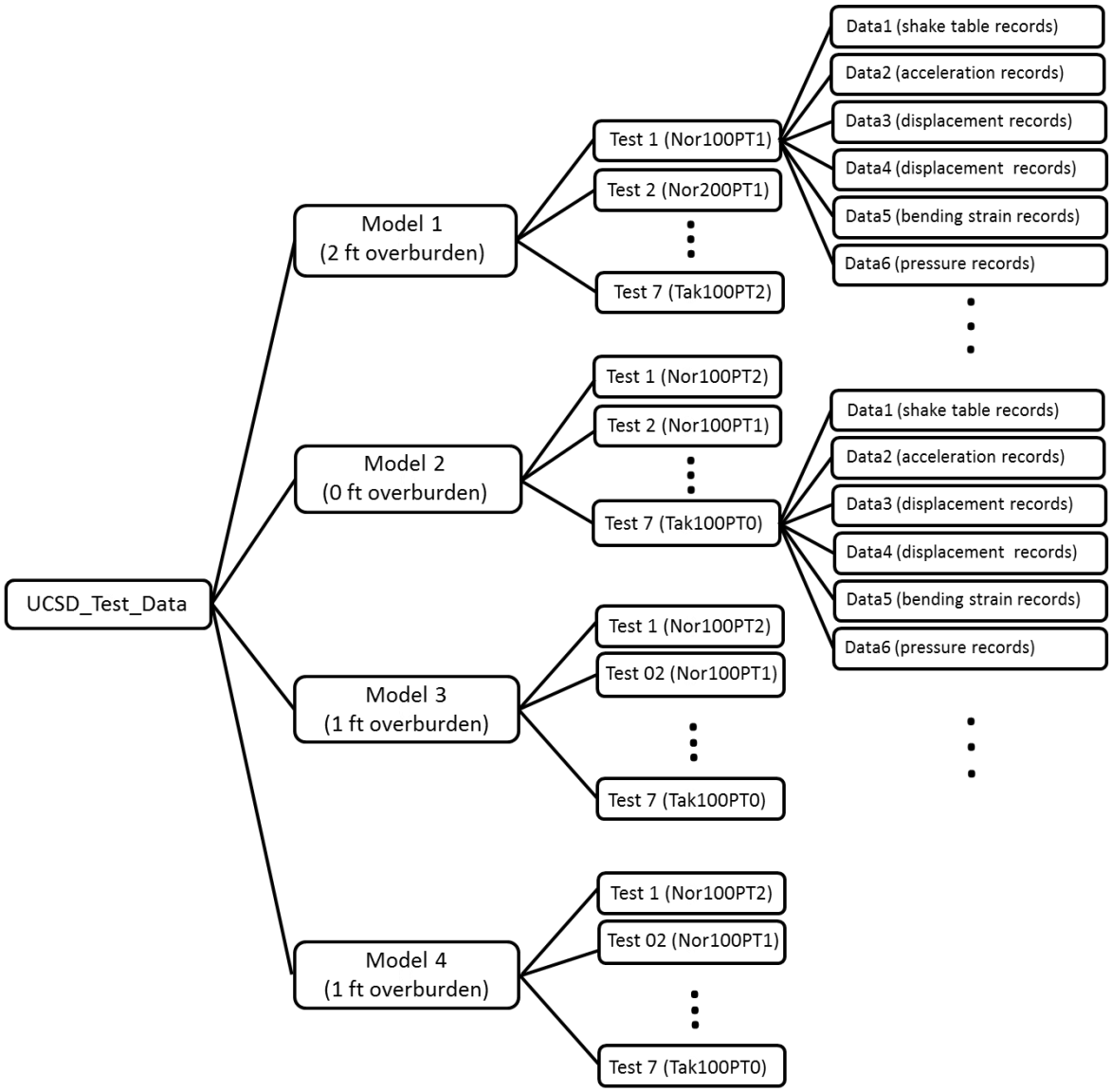

Figure 2–17: Flow charts of the shared test data

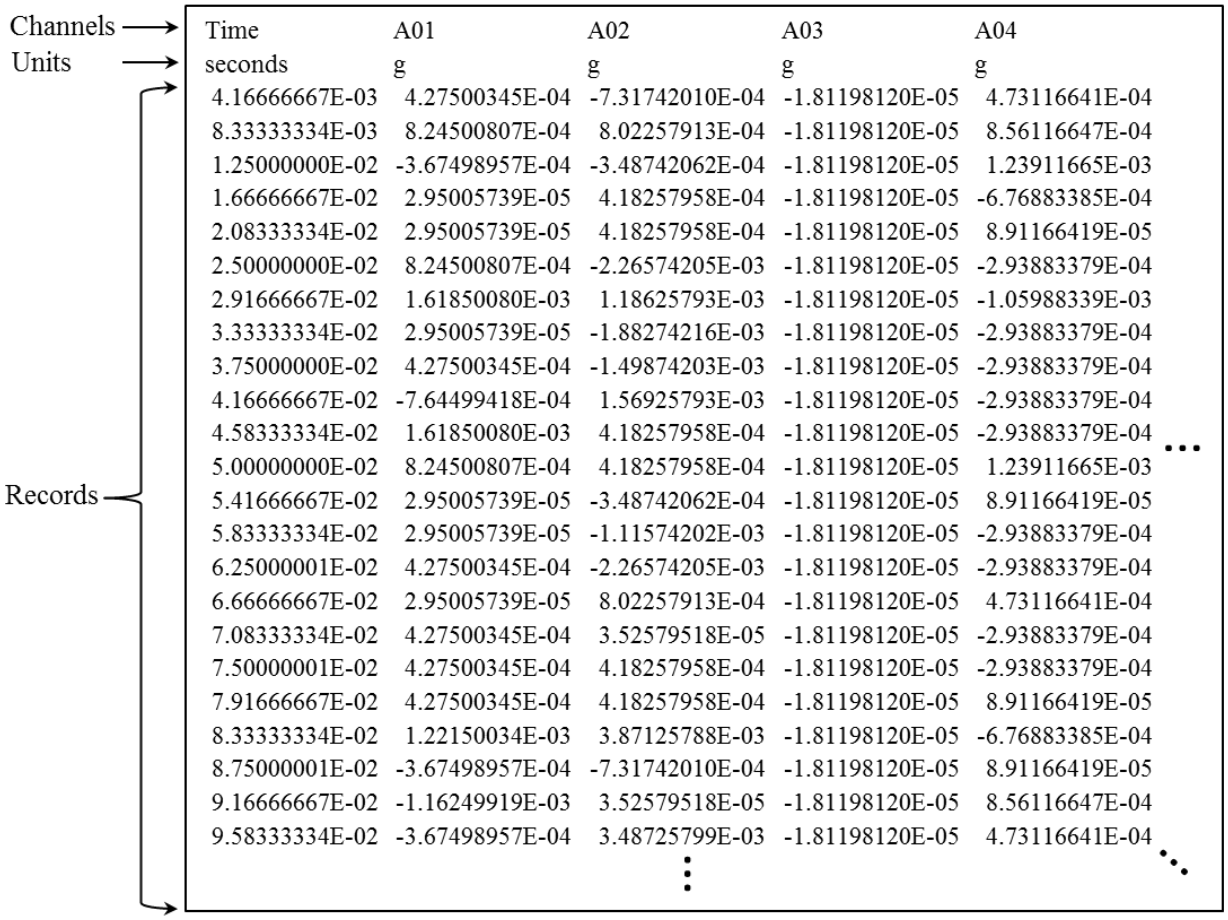

Time	A01	A02	A03	A04
seconds	g	g	g	g
4.16666667E-03	4.27500345E-04	-7.31742010E-04	-1.81198120E-05	4.73116641E-04
8.33333334E-03	8.24500807E-04	8.02257913E-04	-1.81198120E-05	8.56116647E-04
1.25000000E-02	-3.67498957E-04	-3.48742062E-04	-1.81198120E-05	1.23911665E-03
1.66666667E-02	2.95005739E-05	4.18257958E-04	-1.81198120E-05	-6.76883385E-04
2.08333334E-02	2.95005739E-05	4.18257958E-04	-1.81198120E-05	8.91166419E-05
2.50000000E-02	8.24500807E-04	-2.26574205E-03	-1.81198120E-05	-2.93883379E-04
2.91666667E-02	1.61850080E-03	1.18625793E-03	-1.81198120E-05	-1.05988339E-03
3.33333334E-02	2.95005739E-05	-1.88274216E-03	-1.81198120E-05	-2.93883379E-04
3.75000000E-02	4.27500345E-04	-1.49874203E-03	-1.81198120E-05	-2.93883379E-04
4.16666667E-02	-7.64499418E-04	1.56925793E-03	-1.81198120E-05	-2.93883379E-04
4.58333334E-02	1.61850080E-03	4.18257958E-04	-1.81198120E-05	-2.93883379E-04
5.00000000E-02	8.24500807E-04	4.18257958E-04	-1.81198120E-05	1.23911665E-03
5.41666667E-02	2.95005739E-05	-3.48742062E-04	-1.81198120E-05	8.91166419E-05
5.83333334E-02	2.95005739E-05	-1.11574202E-03	-1.81198120E-05	-2.93883379E-04
6.25000001E-02	4.27500345E-04	-2.26574205E-03	-1.81198120E-05	-2.93883379E-04
6.66666667E-02	2.95005739E-05	8.02257913E-04	-1.81198120E-05	4.73116641E-04
7.08333334E-02	4.27500345E-04	3.52579518E-05	-1.81198120E-05	-2.93883379E-04
7.50000001E-02	4.27500345E-04	4.18257958E-04	-1.81198120E-05	-2.93883379E-04
7.91666667E-02	4.27500345E-04	4.18257958E-04	-1.81198120E-05	8.91166419E-05
8.33333334E-02	1.22150034E-03	3.87125788E-03	-1.81198120E-05	-6.76883385E-04
8.75000001E-02	-3.67498957E-04	-7.31742010E-04	-1.81198120E-05	8.91166419E-05
9.16666667E-02	-1.16249919E-03	3.52579518E-05	-1.81198120E-05	8.56116647E-04
9.58333334E-02	-3.67498957E-04	3.48725799E-03	-1.81198120E-05	4.73116641E-04

Figure 2–18: Format of test data file (TEST1_1_Nor100PT1\Data2_Acceleration.dat)

3. Shake Table Test Result in Model Scale: Part 1-Peak Model Response

3.1. Introduction

The shake table tests were performed using a total of seven earthquake input motions for three test model configurations (Models 1-3). This chapter first presents time histories of the recorded dynamic response (excluding the static part) from the three models in terms of ground acceleration, racking (lateral tunnel deformation), and wall bending moment. Afterwards, the recorded response for Nor100PT2 and Tak100PT2 (related to the scaling law for 1/9 model scale) from Models 1-3 and the related observations are presented. From all the shaking events, the corresponding peak response is summarized. In the end, correlation between the ground and tunnel response is addressed. All quantities presented in this chapter are in model scale.

3.2. Recorded Response Sign Conventions

As presented in the figures of this report, the following conventions are adopted:

1) Acceleration/Velocity/Displacement: a positive value indicates the test model moves toward the East
2) Lateral earth pressure is positive in compression.
3) Bending moment: a positive value is associated with wall motion towards East (both sides of the tunnel). For the bending moment, the recorded strain gauge data from outside and inside the wall (see Figure B-8 in Appendix B) were used to compute associated bending strain and curvature (κ; the bending strain divided by half of the wall thickness). Afterwards, EI of the wall (see Section 2.2.1) was employed to express the bending moment (= $EI\kappa$).

3.3. Dynamic Response Time Histories

Response time histories of Models 1-3 from all the shaking events (in the order of the test sequence) are shown in Figure 3–1 through Figure 3–3, respectively, in terms of:

1) Ground surface acceleration
2) Tunnel racking (dynamic component)
3) Wall bending moment (dynamic component) at the base

As shown in these figures, racking was generally associated with the amplitude of ground acceleration. The wall bending moment also corresponded to the level of racking.

Model 1 recorded response time histories for Nor100PT2 and Tak100PT2 (among the seven earthquake events) are shown in Figure 3–4 and Figure 3–5, respectively, in the following order (from top to bottom):

1) Ground surface acceleration along with the shake table acceleration for comparison.
2) Ground surface velocity obtained by integrating the acceleration (Item 1 above), along with the shake table velocity for comparison.
3) Ground distortion (lateral deformation) between the tunnel top and base (i.e., as shear deformation) computed from double integration of the ground acceleration at corresponding levels.
4) Tunnel racking (lateral deformation) measured from the displacement sensor (linear potentiometer) that was placed inside the tunnel.
5) Lateral tunnel base translation measured from the displacement sensor (string potentiometer) connected between the laminar soil container and the structure base.
6) Bending moment at top and base of the tunnel walls (per unit wall length of 1 ft

Recorded response from Models 2-3 are presented in Figure 3–6 through Figure 3–9. Table 3–1 also summarizes the above peak response values as well as acceleration of the tunnel at the top and bottom from all shaking events. Appendix C presents the recorded response from all shaking events.

3.3.1. Test results from Model 1 Nor100PT2

During Nor100PT2 input excitation (Figure 3–4), the following observations were drawn:

- Peak ground acceleration (PGA) was about 0.42g.
- Peak racking was about 0.022 inch (0.05% drift if divided by the tunnel height of 40 inches) as the test model moved towards East (at 3.5 sec.)
- Peak racking coincided with other peak response such as PGA, ground distortion, and wall bending moment.
- Ground distortion (shear deformation herein) was about 0.061 inch (about 0.15% shear strain, divided by the tunnel height). Compared to the peak racking, this distortion was as much as about three times, indicating that the ground surrounding the tunnel was relatively softer than the tunnel. Ratio of the racking to the ground distortion, also known as the racking coefficient (or racking ratio; Wang 1993; FHWA 2009) was about 0.36.

- Similar peak bending moment (about 200 lb·ft/ft; dynamic component) occurred near the top and bottom of both tunnel walls.

3.3.2. Test results from Model 1 Tak100PT2

During Nor100PT2 input excitation (Figure 3–5), the following observations were drawn:

- Peak ground acceleration (PGA) was about 0.75g.
- Peak racking was about 0.15 inch (0.37% drift divided by the tunnel height of 40 inches) as the test model moved towards East (at 3.4 sec.)
- Peak racking generally coincided with other peak response such as PGA, ground distortion, and wall bending moment.
- Ground distortion was about 0.3 inch (about 0.75% shear strain). Compared to the peak racking, this distortion was nearly as much as twice, indicating that the ground surrounding the tunnel was relatively softer than the tunnel (corresponding racking ratio of about 0.5).
- Peak bending moment of about 620 lb·ft/ft (positive moment) occurred near the base of the West wall. On the East wall, larger bending moment of 660 lb·ft/ft (negative moment) was observed near the base.

3.3.3. Test results from Models 2-3 during Nor100P2 and Tak100PT2

Similarly, Model 2 response time histories during Nor100PT2 and Tak100PT2 input excitation are shown in Figure 3–6 and Figure 3–7, respectively. For Model 3, the response time histories are shown in Figure 3–8 and Figure 3–9. Table 3–1 summarizes main peak response values from the Models 2-3 from all the shaking events (corresponding response time histories are presented in Appendix C)

3.4. Summary of Peak Dynamic Response from Models 1-3

From each test model, peak racking generally coincided with the PGA (based on the time history plots shown in Figure 3–4 through Figure 3–9). The level of the peak racking was also proportional to the PGA and PGV in general but somewhat scattered beyond PGA of about 0.8g (Figure 3–10). The maximum racking (dynamic component) throughout the entire study was about 0.2 inch (0.48% drift ratio), which occurred in Model 1 for motion Tak100PT1 (Table 3–1). In this case (Model 1 Tak100PT1), the West wall suffered the highest bending at the base (about 850 lb·ft per unit wall length of 1ft).

Under the identical input excitation for different test models, PGA and PGV tended to slightly decrease as the overburden soil pressure increased (e.g., during Nor100PT2, 0.64g in Model 2, 0.52g in Model 3, 0.42g in Model 1). Despite this trend, the level of peak racking tended to increase along with higher overburden soil pressure (Figure 3–10).

For the tunnel located at shallow depth (experiencing the highest PGA), the ground deformation between the tunnel top and base was highest (resulting in more strain softening as shown in Figure 3–12). Consequently, the tunnel became relatively stiffer than the surrounding soil (i.e., corresponding flexibility ratio decreased), leading to less deformation than the ground (i.e., R_r, < 1.0). Figure 3–13 shows the R_r associated with the PGA and the soil distortion between top and bottom of the tunnel. This figure shows a clear tendency for the racking ratio decreasing with increasing PGA as well as the soil distortion (shear strain). Particularly, from Model 2, the R_r was likely to be constant ($R_r \approx 0.05$) regardless of the level of the soil deformation, implying that the tested tunnel model was considerably stiffer than the surrounding soil.

Table 3–1: Peak dynamic response of ground and tunnel in model scale

Model	Shaking	EQ[1]	At surface		At level of tunnel top			At level of tunnel base			Soil distortion (%)	Racking (%)	Bending moment (kip-ft)				Base translation (%)
													West wall		East wall		
			PGA (g)	PGV (in/s)	Acc. (g)	Vel. (in/s)	Tunnel (g)	Acc. (g)	Vel. (in/s)	Tunnel (g)			Top	Base	Top	Base	
1	1	Nor100PT1	0.60	8.1	0.52	7.2	0.45	0.33	3.9	0.33	0.29	0.17	0.27	0.33	-0.32	-0.26	0.01
	2	Nor200PT1	1.06	18.7	0.82	16.3	0.71	0.79	10.2	0.68	1.04	0.33	0.62	0.54	-0.52	-0.60	0.10
	3	Nor100PT0	0.90	22.1	0.80	21.3	0.72	0.55	15.3	0.58	1.33	0.40	0.59	0.69	-0.66	-0.62	0.13
	4	Tak100PT1	0.88	35.7	0.86	34.9	0.78	0.74	28.0	0.76	1.56	0.48	0.73	0.85	-0.79	-0.79	0.12
	5	Tak100PT0	0.79	35.4	0.77	35.6	0.74	0.70	31.9	0.71	1.18	0.38	0.68	0.73	-0.66	-0.78	0.07
	6	Nor100PT2	0.42	3.7	0.38	3.8	0.29	0.26	2.6	0.24	0.15	0.05	0.17	0.20	-0.19	-0.17	0.00
	7	Tak100PT2	0.75	13.8	0.73	13.6	0.60	0.49	7.0	0.49	0.76	0.37	0.61	0.62	-0.58	-0.66	0.07
2	1	Nor100PT2	0.64	4.9	0.64	4.9	0.39	0.36	2.3	0.32	0.24	0.01	0.06	0.10	-0.08	-0.08	0.01
	2	Nor100PT1	0.96	8.2	0.96	8.2	0.49	0.44	4.9	0.41	0.61	0.03	0.11	0.15	-0.12	-0.13	0.06
	3	Nor100PT0	1.19	23.4	1.19	23.4	0.85	0.76	15.1	0.85	2.84	0.11	0.20	0.27	-0.21	-0.24	0.26
	4	Tak100PT2	0.90	17.7	0.90	17.7	0.74	0.65	9.5	0.77	1.65	0.10	0.18	0.26	-0.19	-0.23	0.20
	5	Nor200PT1	1.27	22.1	1.27	22.1	0.83	0.81	13.3	0.77	2.19	0.09	0.17	0.20	-0.15	-0.22	0.20
	6	Tak100PT1	0.82	40.4	0.82	40.4	0.76	0.75	26.0	0.77	2.69	0.08	0.20	0.23	-0.17	-0.24	0.19
	7	Tak100PT0	0.92	35.8	0.92	35.8	0.81	0.64	31.5	0.78	1.96	0.08	0.15	0.25	-0.15	-0.24	0.18
3	1	Nor100PT2	0.52	4.7	0.39	3.8	0.37	0.33	2.1	0.28	0.21	0.05	0.15	0.18	-0.16	-0.16	0.01
	2	Nor100PT1	0.78	8.1	0.50	6.3	0.48	0.39	4.1	0.34	0.44	0.10	0.25	0.24	-0.23	-0.26	0.04
	3	Nor100PT0	1.04	24.2	0.87	21.3	0.87	0.70	14.6	0.81	1.78	0.23	0.40	0.43	-0.37	-0.44	0.16
	4	Tak100PT2	0.80	14.6	0.76	13.5	0.74	0.58	8.6	0.65	1.14	0.23	0.39	0.43	-0.38	-0.43	0.15
	5	Nor200PT1	1.11	21.6	0.83	17.2	0.79	0.77	11.9	0.75	1.77	0.19	0.33	0.36	-0.31	-0.37	0.14
	6	Tak100PT1	0.95	37.4	0.91	37.0	0.82	0.74	26.1	0.79	3.00	0.26	0.43	0.46	-0.42	-0.50	0.24
	7	Tak100PT0	0.80	37.6	0.81	36.2	0.77	0.63	31.6	0.74	2.17	0.22	0.39	0.41	-0.38	-0.47	0.20

[1]For Model 1, earthquake input motions were not in the same order applied for Models 2-3

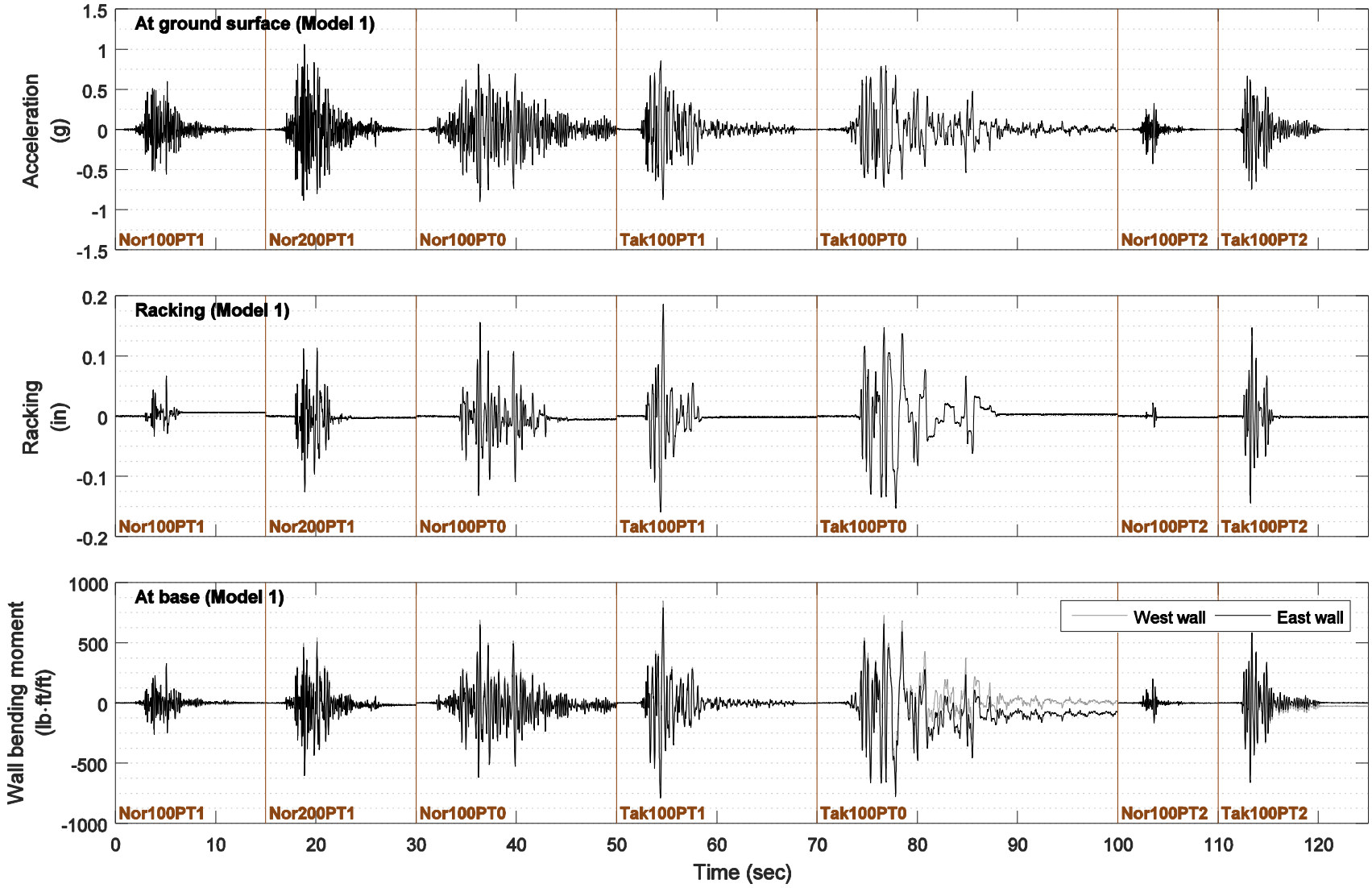

Figure 3–1: Model 1 response time histories of the surface ground acceleration (top), tunnel racking (middle), and bending moment at the wall base for all the shaking events (in the order of the test sequence) in model scale

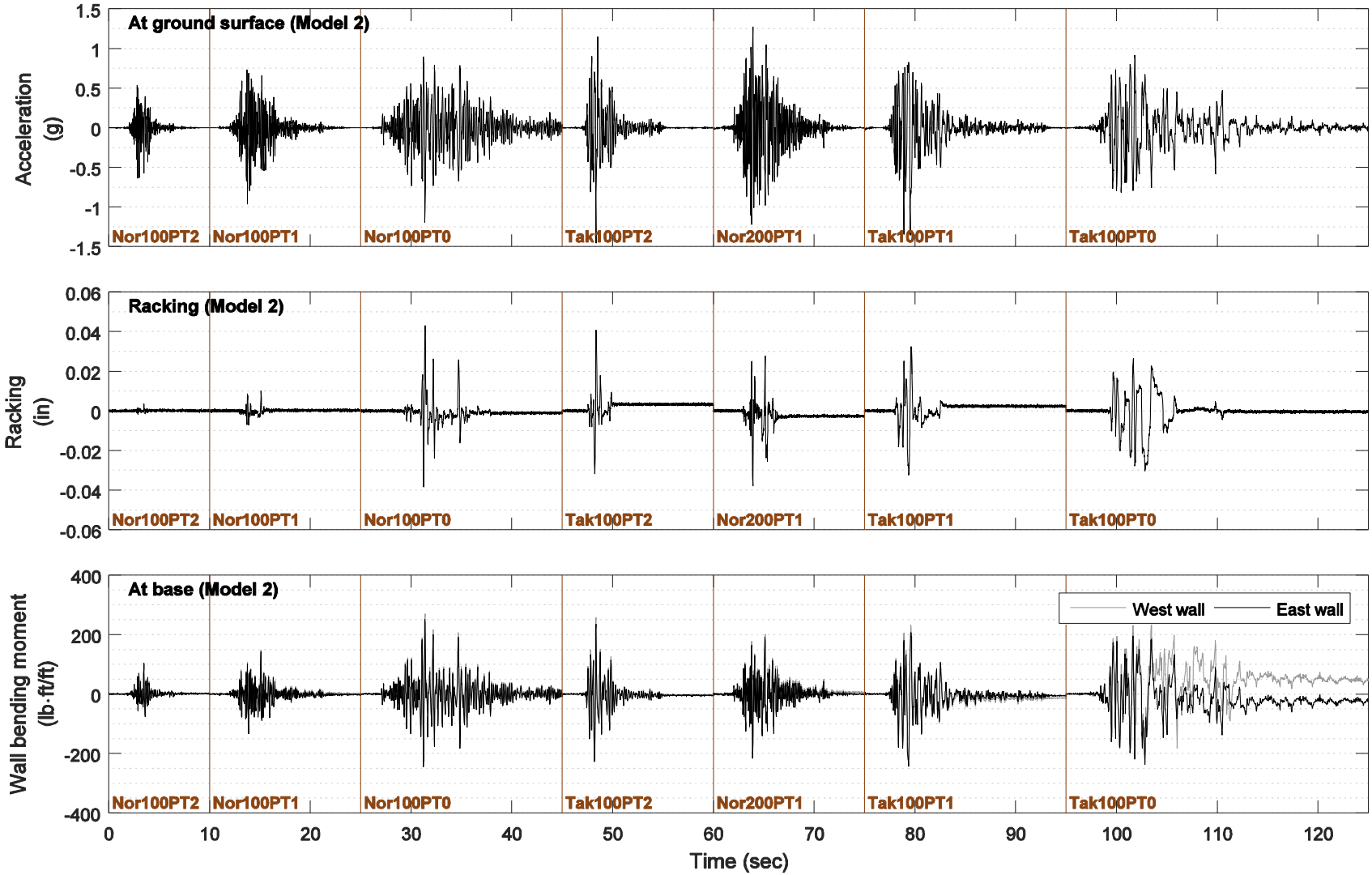

Figure 3–2: Model 2 response time histories of the surface ground acceleration (top), tunnel racking (dynamic component; middle), and bending moment (dynamic component; bottom) at the wall base for all the shaking events (in the order of the test sequence) in model scale

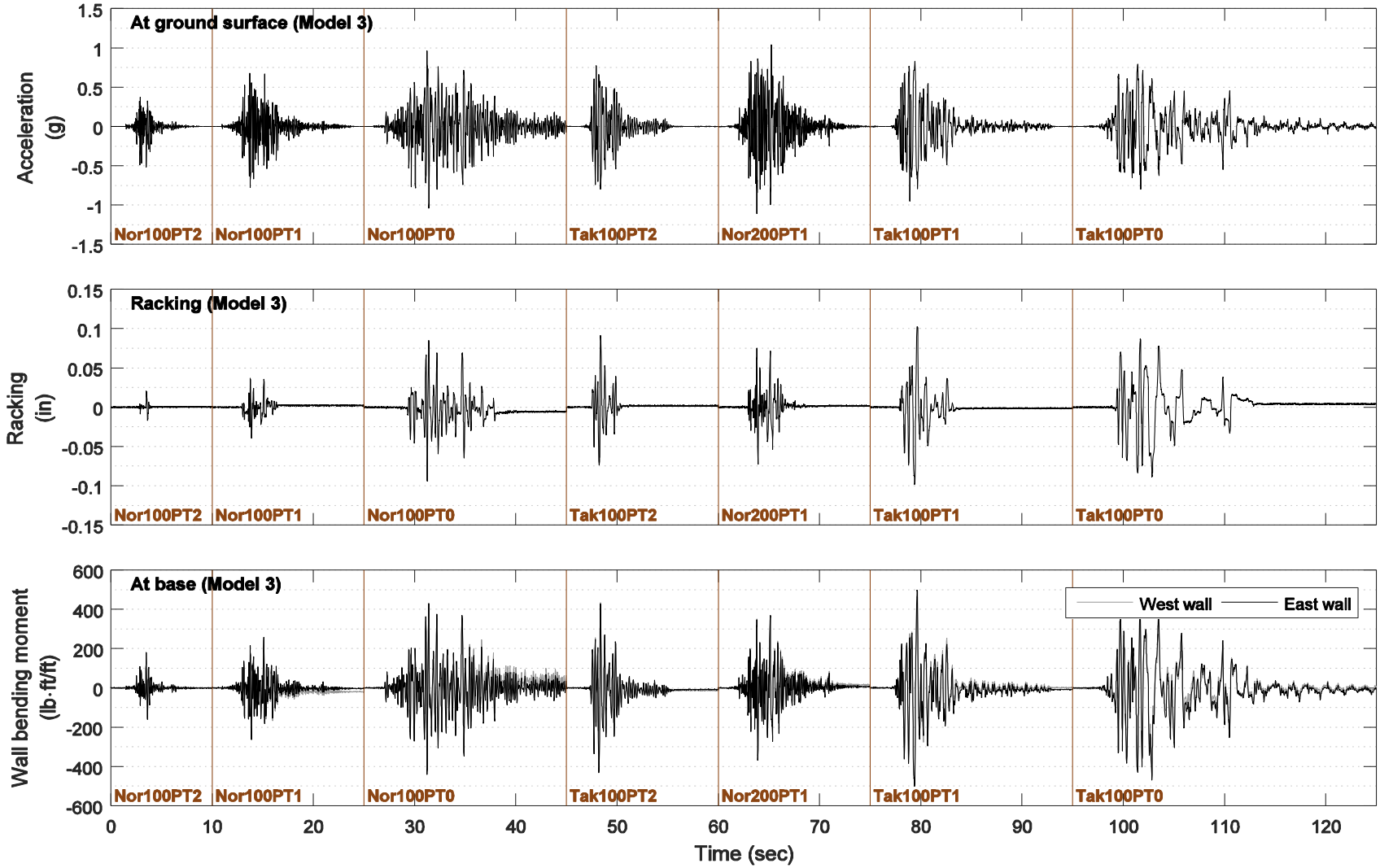

Figure 3–3: Model 3 response time histories of the surface ground acceleration (top), tunnel racking (dynamic component; middle), and bending moment (dynamic component; bottom) at the wall base for all the shaking events (in the order of the test sequence) in model scale

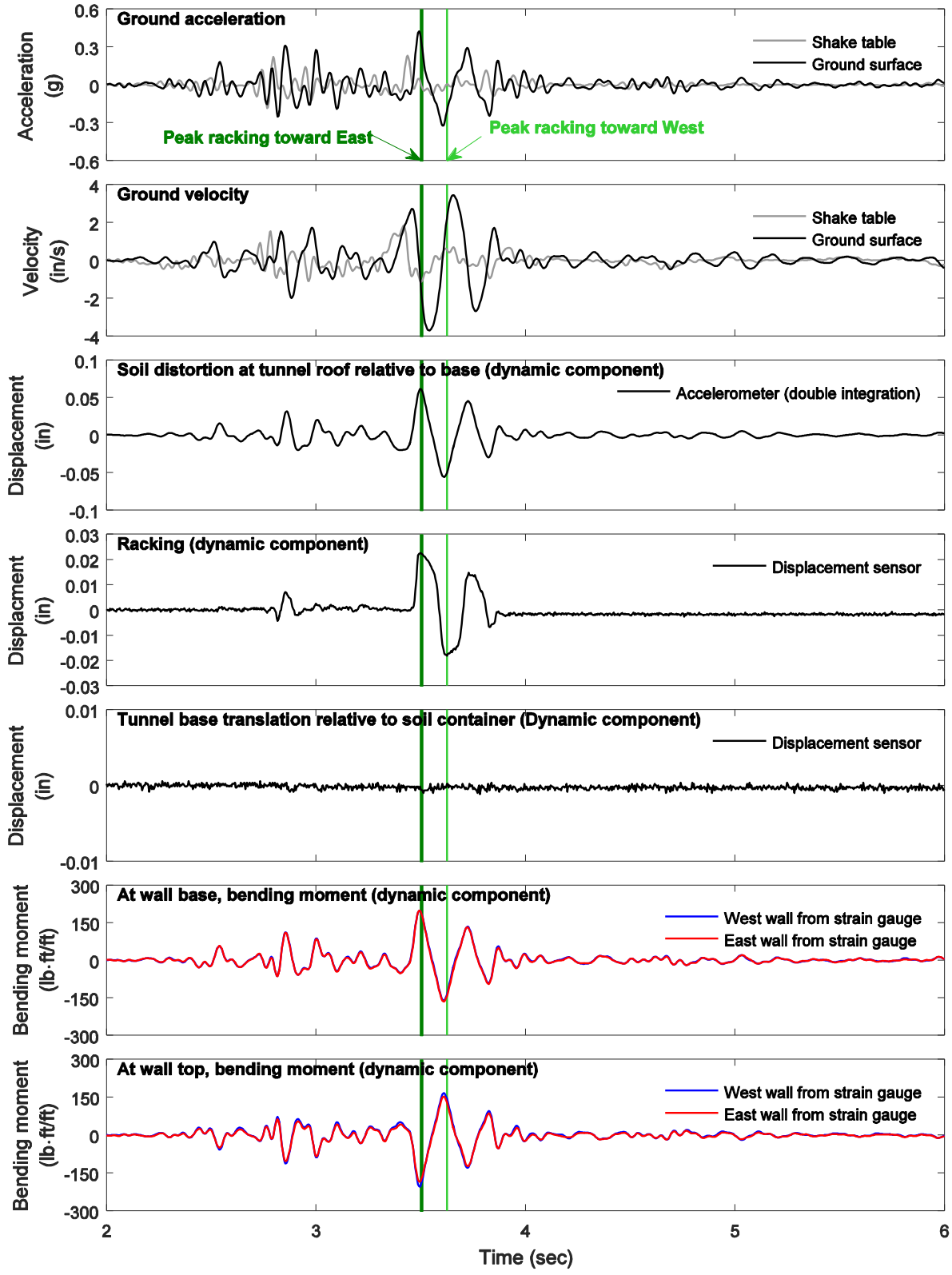

Figure 3–4: Model 1 response time histories for Nor100PT2 in model scale (2 ft overburden soil)

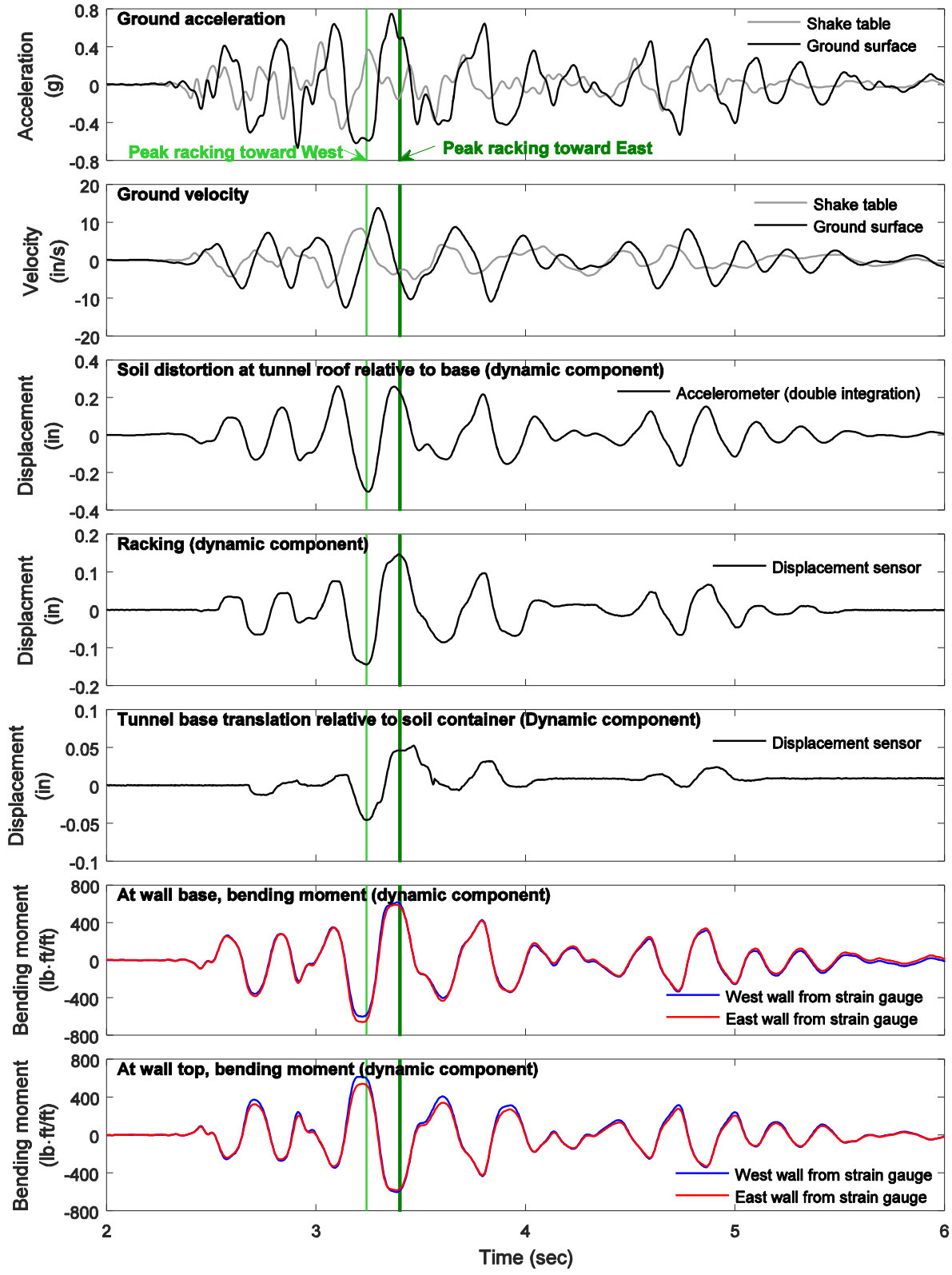

Figure 3–5: Model 1 response time histories for Tak100PT2 in model scale (2 ft overburden soil)

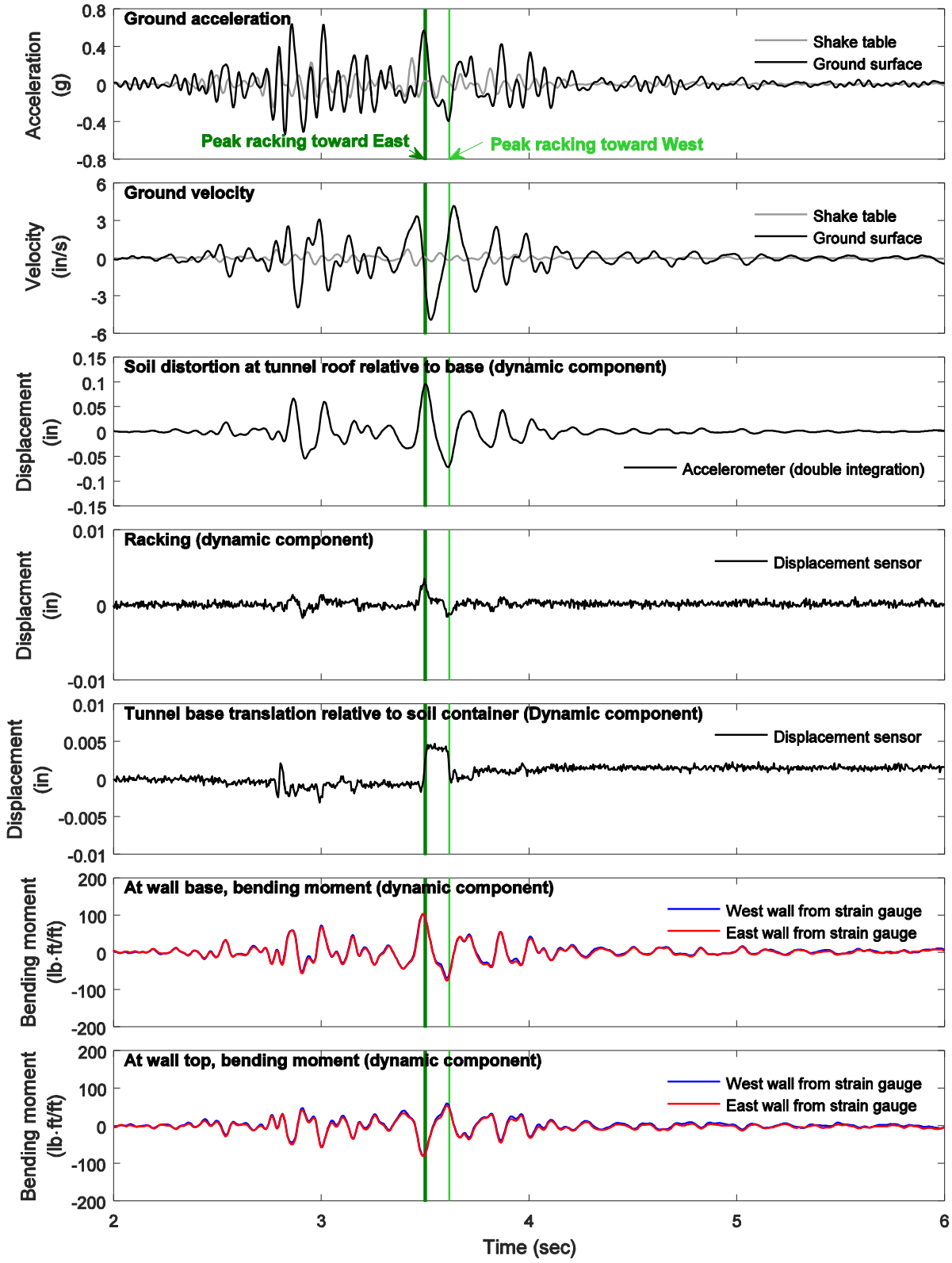

Figure 3–6: Model 2 response time histories for Nor100PT2 in model scale (without overburden soil)

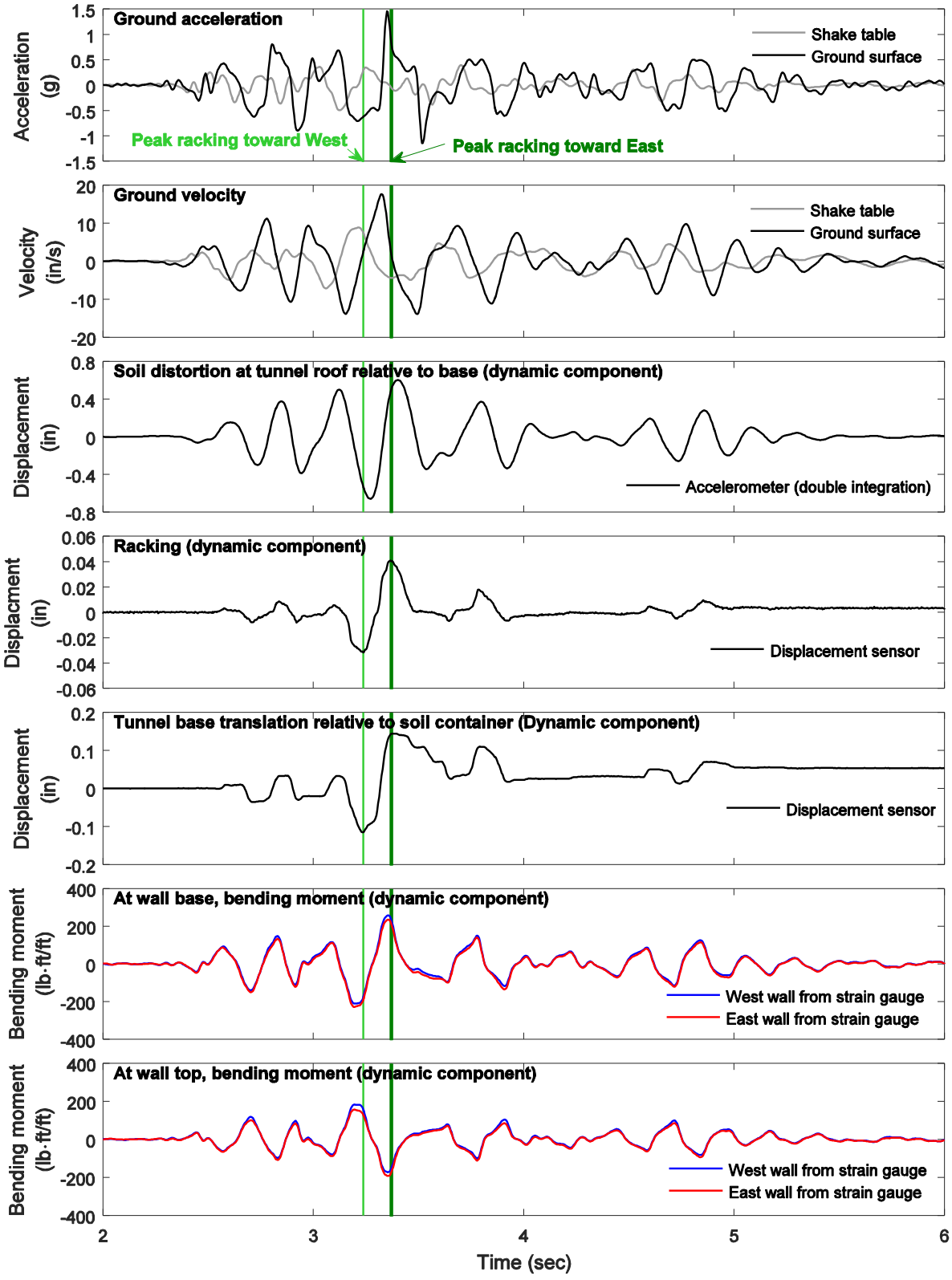

Figure 3–7: Model 2 response time histories for Tak100PT2 in model scale (without overburden soil)

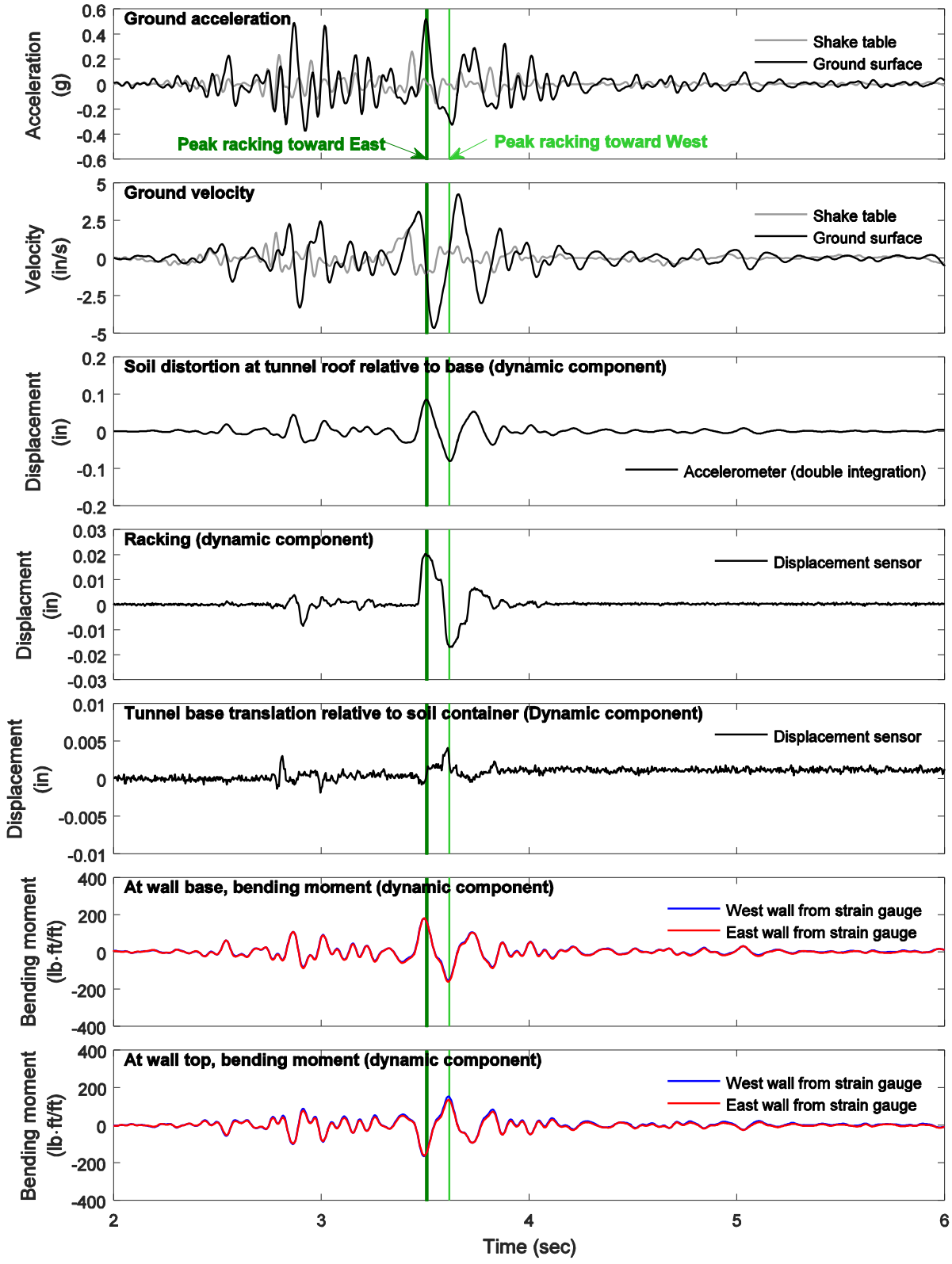

Figure 3–8: Model 3 response time histories for Nor100PT2 in model scale (1 ft overburden soil)

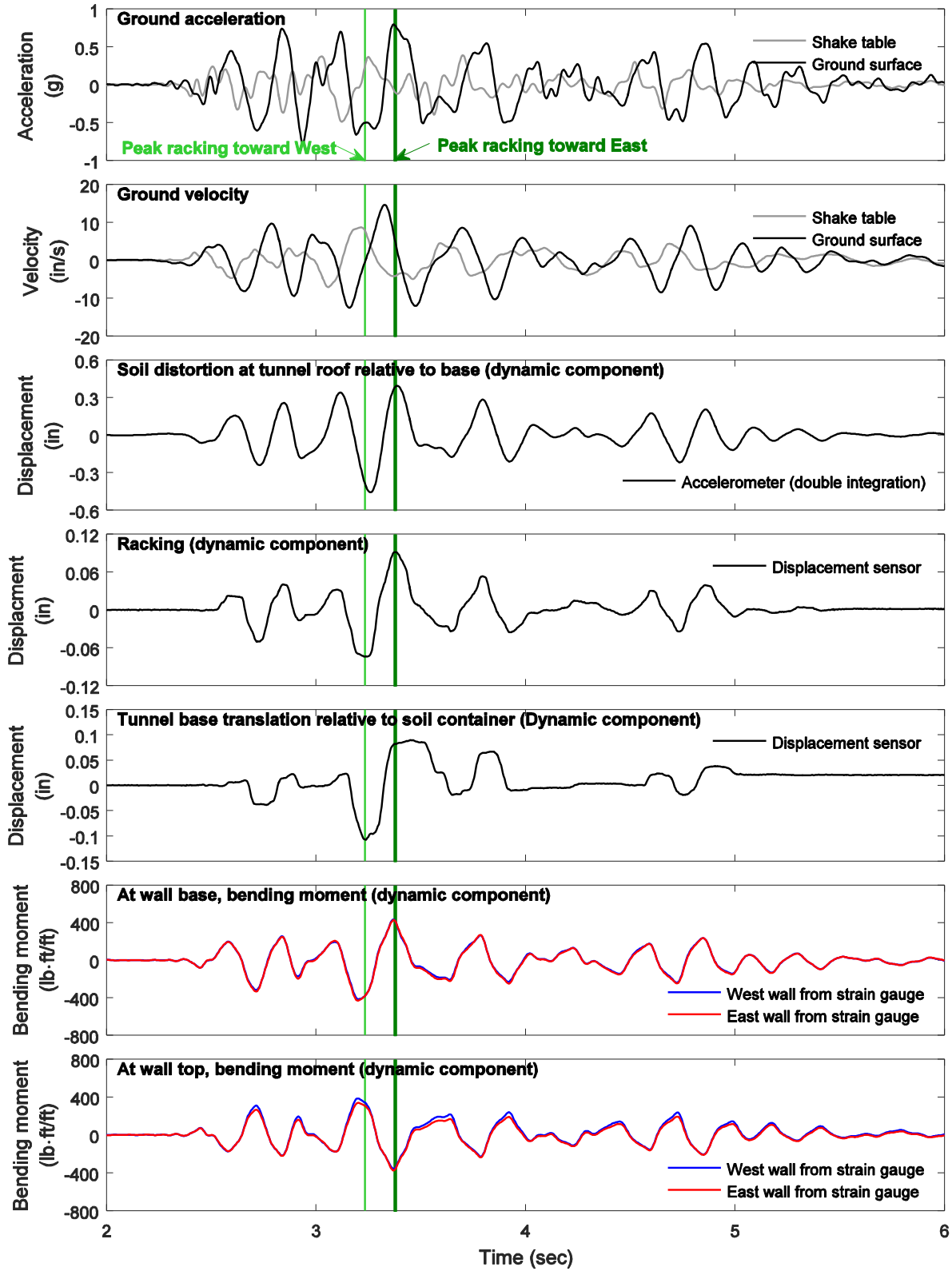

Figure 3–9: Model 3 response time histories for Tak100PT2 in model scale (1 ft overburden soil)

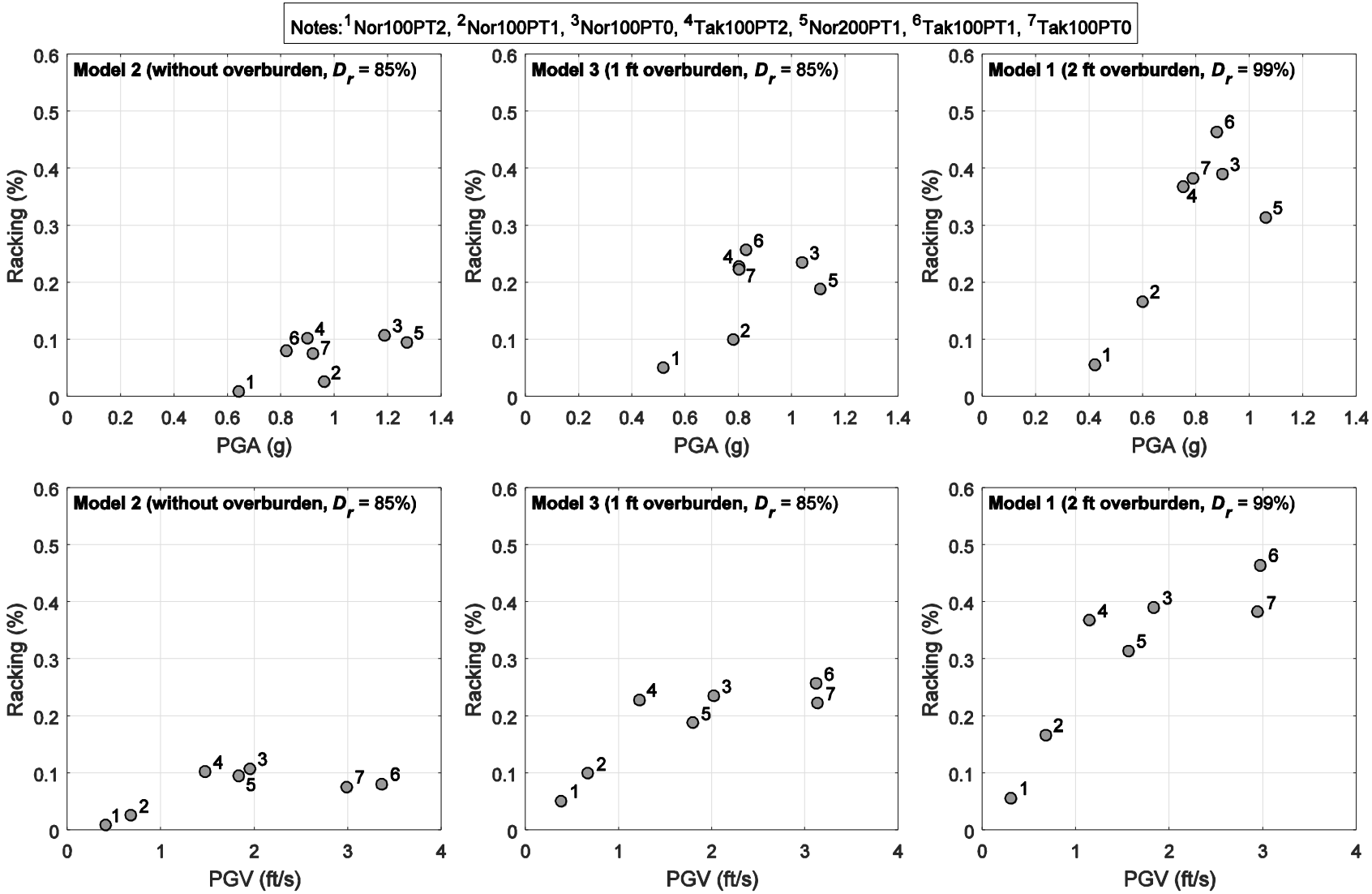

Figure 3–10: Correlation of peak racking with peak ground acceleration (top) and peak ground velocity (bottom)

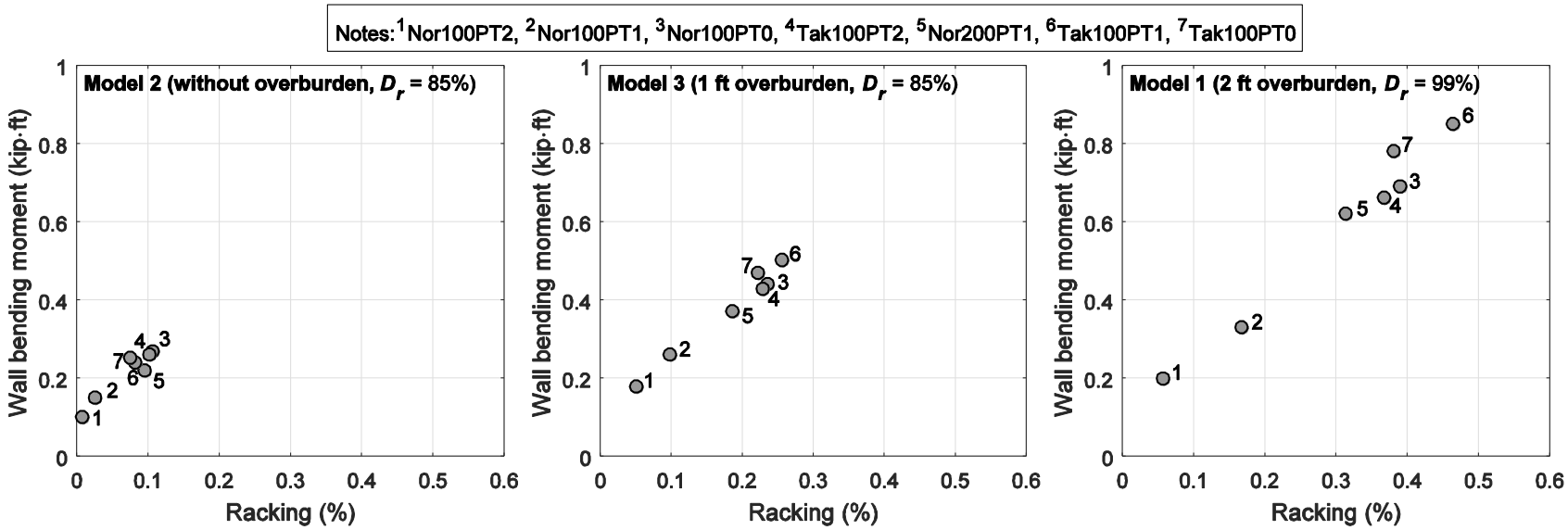

Figure 3–11: Relationship between the peak racking and the peak wall bending moment

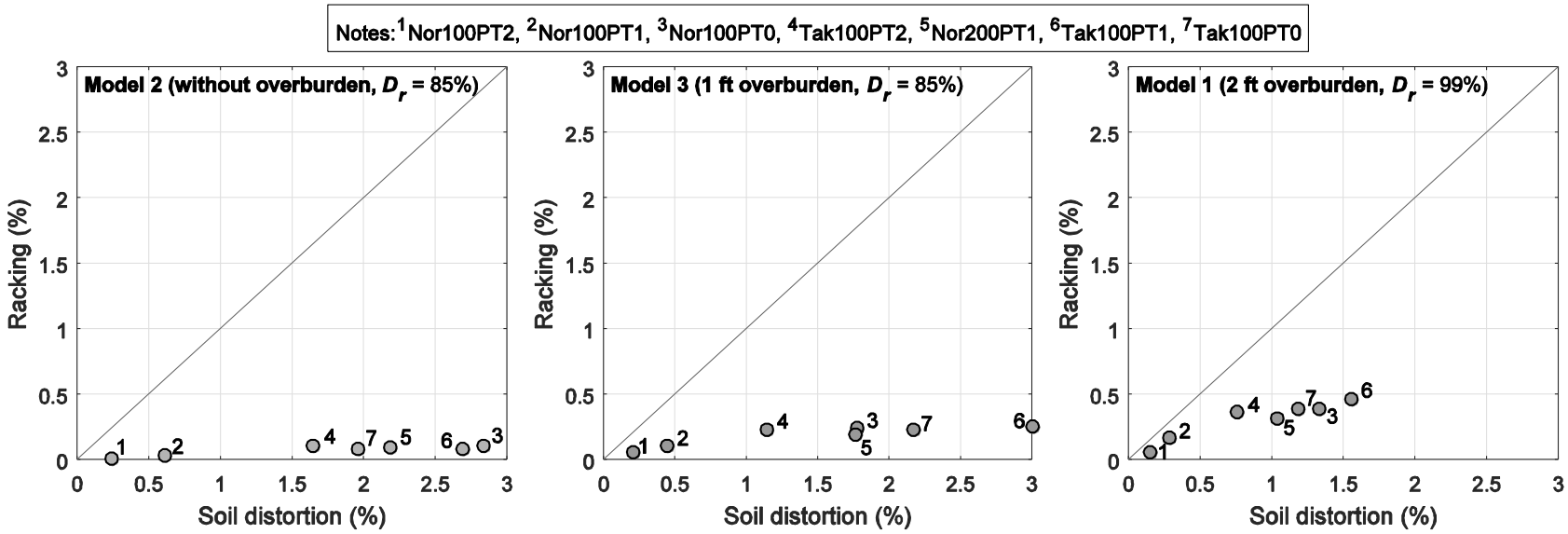

Figure 3–12: Relationship of the peak racking and the ground distortion between top and bottom of the tunnel

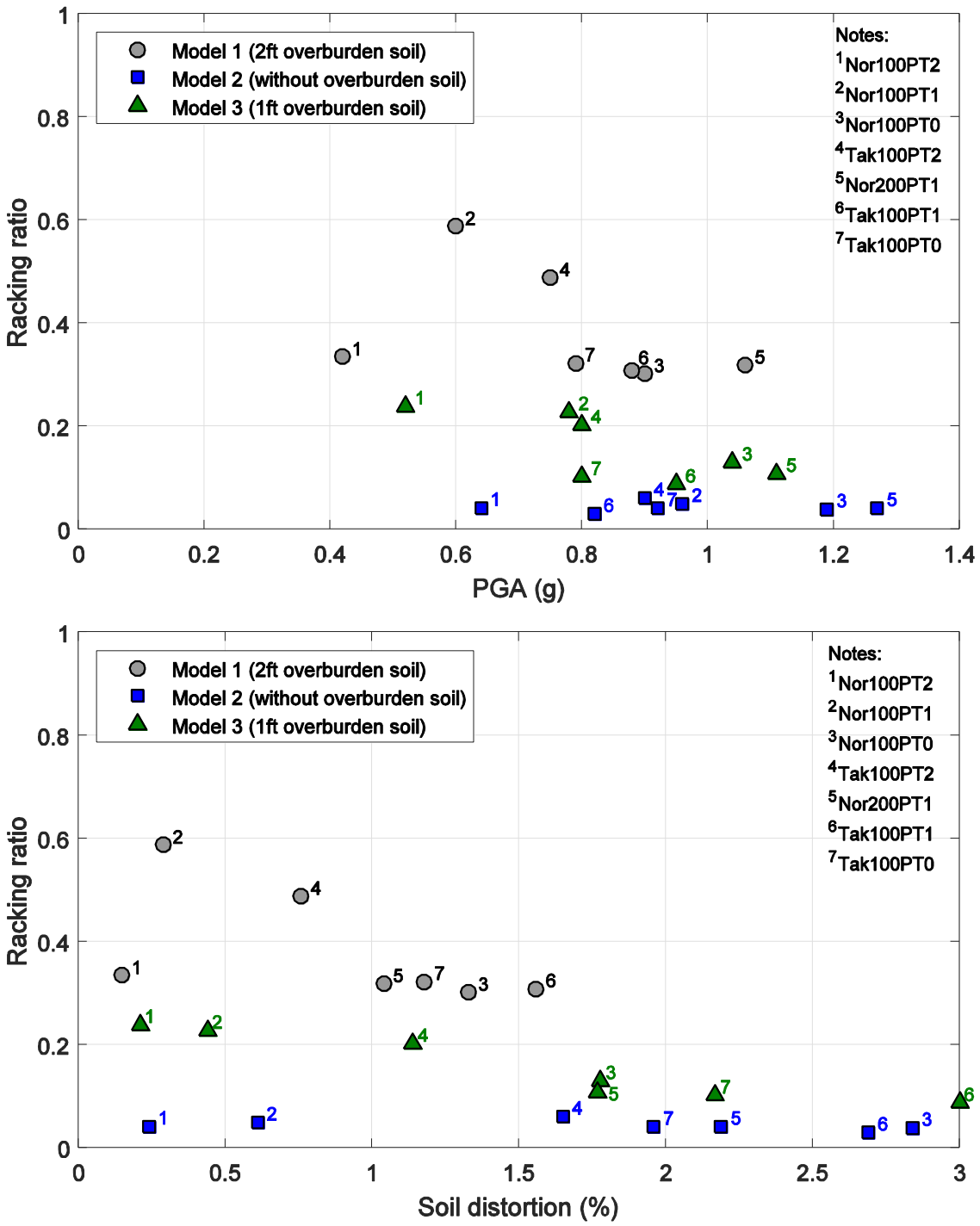

Figure 3–13: Relationship of racking ratio with peak ground acceleration (top) and soil distortion between top and bottom of tunnel (bottom)

4. Shake Table Test Result in Model Scale: Part 2-Lateral Earth Pressure

4.1. Introduction

This chapter presents the lateral earth pressure measured from the Tactilus pressure sensors along the tunnel walls (Figure 4–1). The data from Model 1 during Nor100PT2 and Tak100PT2 and Model 2 (the entire shakings) were excluded because the Tactilus sensor malfunctioned during the test. At peak racking, the pressure time histories and profiles along the wall are presented. Afterward, the earth pressure was expressed in terms of force (i.e. pressure multiplied by the corresponding sensing area). The lateral earth force was summed up to obtain the resultant lateral earth pressure force for each wall. Finally, this resultant force is correlated with racking and bending moment.

4.2. Lateral Earth Pressure along the Wall

4.2.1. Model 1 (2 ft overburden soil)

Model 1 (backfill compacted at D_r of 99%) earth pressure time histories along the wall height (7 locations; see Figure 4–1) are shown in Figure 4–2 for Nor100PT1 (1st shaking event after model construction). This figure also includes the corresponding vertical stress (σ_v) at the sensor locations (i.e. $\sigma_v = \gamma z$ where γ is the unit weight of 120 pcf and z is depth of a pressure sensor measured from the surface). As shown in Figure 4–2, the static lateral pressure was generally higher than the vertical stress due to the manner of employed compaction. This higher static lateral pressure dropped considerably at the beginning of the shaking phase (about 2.5 sec), particularly during Nor100PT1 (Figure 4–1). At the peak racking towards East (at about 5 sec), the corresponding lateral pressure was still lower than the static values. Afterwards, as the test continued (also the level of the shaking increased), the lateral pressure at peak racking tended to be higher than the static values (Appendix D presents the earth pressure time histories for all the shaking events where the pressure sensors functioned).

During the entire studied cases, peak racking generally occurred as the tunnel moved towards East. At peak racking, it can be seen that the lateral pressure increased near the roof (as the soil pushed the tunnel) but decreased near the base (as the tunnel base moved away from the soil) on the West wall, and vice versa on the East wall (Figure 4–3). Consequently, the total lateral pressure exerted on the West wall was in a shape of inverted-triangular distribution, with a triangular distribution on the East wall (Figure 4–3). This figure also presents the relative lateral

pressure on the West wall with respect to the East wall (as net pressure). In general, the net pressure was in a shape of the inverted-triangular distribution in the upper part. The negative net pressure did not contribute to the wall deformation, implying the resulting force was located above one half of the wall height.

4.2.2. Model 3 (1ft overburden soil)

Model 3 (backfill compacted at about 85% D_r) earth pressure time histories along the wall height (7 locations) are shown in Figure 4–4 for Nor100PT2 (1st shaking event after model construction). Associated with the employed compaction effort and thickness of the overburden soil, the lateral pressure was somewhat lower or higher than the vertical stress. As peak racking towards East, lateral pressure was higher than the static values on the West side of the tunnel in most cases. Similar to Model 1, lateral pressure tended to increase near the roof but decreased near the base on the West wall, and vice versa on the East wall.

As the test continued (the shaking intensity became relatively stronger), the net pressure distribution tended to be in the shape of an inverted-triangle (Figure 4–5) as shown in Model 1 (Figure 4–3). The resulting pressure also increased as the test continued, and its location was likely to be located at the middle of the wall.

4.3. Resultant Lateral Earth Pressure Force and Point of Action

Figure 4–6 shows a schematic view of the resultant force and the associated point of action. It is noted that the pressure sensors near the base (e.g. TS 01 and TS 11 as shown in Figure 4-1) were excluded in computing the resultant force because the pressure measured from these sensors are irrelevant to wall deformation. For quantifying this contribution to the tunnel deformation, the difference of the product of the resultant force and the point of action on the East wall with respect to the West wall was taken into consideration (designated as resultant moment in this study).

4.3.1. Reference resultant force

For comparison, a reference resultant force (P_{ref}) was introduced. For P_{ref}, it was assumed that the horizontal pressure (σ_h) was equal to the vertical pressure (σ_v, i.e. $\sigma_h = \sigma_v$ or the coefficient of earth pressure at rest, $K = 1.0$). Figure 4–7 illustrates P_{ref} acting on the wall excluding the base part. The corresponding P_{ref} for Models 1 and 3 are as follows:

1. Model 1: 1,137 lb/ft per unit wall length of 1 ft (where γ is the unit weight of the backfill, 120 pcf).
2. Model 3: 696 lb/ft per unit wall length of 1 ft (where γ = 104 pcf)

4.3.2. Model 1 (2ft overburden soil)

The time histories of the resultant force and the associated point of action are shown in Figure 4–8 through Figure 4–12 (in the order of the shaking sequence). These plots also included the main recorded response such as ground surface acceleration and racking, as shown earlier in Section 3.

As discussed earlier in Section 4.2, the static force was relatively higher than the vertical force (compared to P_{ref} of 1137 lb/ft for Model 1). This higher static force significantly dropped at the beginning of shaking. Afterwards, the resultant force tended to become lower than the static value even at the peak racking towards East. At this racking, the West resultant force was relatively higher than that on the East side. Meanwhile, the point of action on the West side was likely to be lower than that on the East side. As such, the upward (West wall) and downward (East) resultant forces contributed to the observed peak racking, rather than higher lateral force on the West wall.

The resultant moment time histories showed a good agreement with the measured ground surface acceleration in terms of response phase. It can be seen that the peak resultant moment coincided with the racking.

4.3.3. Model 3 (1ft overburden soil)

Time histories of the resultant force and the associated point of action are shown in Figure 4–13 through Figure 4–19 (in the order of the shaking sequence). Associated with the relatively lower compaction effort and shallow overburden soil, the static force was more or less similar to P_{ref} (696 lb/ft assuming K = 1.0). At peak racking towards East, both resultant force and point of action on the West wall were higher than those on the East wall. As observed in Model 1, the resultant moment time histories showed good agreement with the ground surface acceleration in terms of response phase as well as occurrence of peak values.

4.4. Discussion of resultant force and point of action

In this entire study, racking and wall bending moment were quantitatively obtained from the employed displacement sensors and strain gauges. Along with these data sets, the resultant

force measured from the Tactilus pressure sensors still provided valuable insights in understanding the deformation mechanism of the tunnel. As such, this section includes further discussion of the resultant force and the point of action, associated with the tunnel deformation.

4.4.1. Analytical solution for tunnel deformation

The resultant force and the associated point of action on both sides of the tunnel simultaneously contributed to the tunnel racking and the bending moment (Figure 4–20). For the rigid base and roof in the test model (see Section 2.2), the tunnel racking and bending moment at the wall base can be computed in an analytical approach as illustrated in Figure 4–20.

4.4.2. Tunnel deformation estimated from resultant force and point of action

Associated with the tunnel geometry (curved roof), it might be expected that the overburden soil shearing along the roof surface would induce more deformation. Racking (dynamic component) estimated from the resultant force (and the point of action) was generally less than that measured directly from the displacement sensor. At peak racking towards East, the West soil pushed the wall and, simultaneously, the East soil tended to move away from the wall. In this situation, as discussed earlier, the earth pressure in the upper part of the East wall was reduced with respect to the static value. However, the pressure record did not possibly capture that the overburden soil dragged the tunnel roof towards East. This additional behavior contributed to more deformation than that due to the lateral resultant force exerted on both sides of the tunnel. Unfortunately, the Tactilus pressure data from the test model without overburden soil (Model 2) were not available to validate this contribution. As an alternative, a numerical model validated from the test result shall shed light on this contribution.

In this study, the measured resultant force and the associated point of action served as the lower bound for wall deformation as shown in Figure 4–8 through Figure 4–19. Particularly under relatively strong shaking (e.g., during Nor200PT1, Tak100PT1, and Tak100PT0 input excitations), the total bending moment estimated from the resultant force and point of action showed good agreement with that from the strain gauges (but the static value was still obtained from the Tactilus pressure sensors).

4.5. Summary

Based on the lateral earth pressure measured from the Tactilus pressure sensors, the following observations are made:

1. At peak racking towards East, difference of the lateral earth pressure on the West wall with respect to the East side (net pressure) was in a shape an inverted triangular distribution.
2. Peak racking is caused by the relative difference between resultant forces and associated point of action on both sides of the tunnel. For instance, generally at peak racking eastwards, the following mechanisms were involved:

   For 1ft overburden soil (D_r of 85%):

   - The resultant force and point of action on the West wall were high, and
   - The resultant force and point of action on the East wall were low,
   - Reduction of the resultant force on the East wall was a main reason for the observed peak racking (rather than the increase of the resultant force on the West wall).

   For 2 ft overburden soil (D_r of 99%):

   - The resultant force on the West wall was low but associated point of action was high, and
   - The resultant force on the East wall was high but associated point of action was low,
   - Upward and downward shift of the resultant forces on the West and the East wall, respectively, was a main reason for the observed peak racking (rather than the increase of the resultant force on the West wall).

   3. Wall bending moment estimated from the resultant forces and associated point of action showed reasonable agreement with that from the strain gauge data under relatively strong shaking.

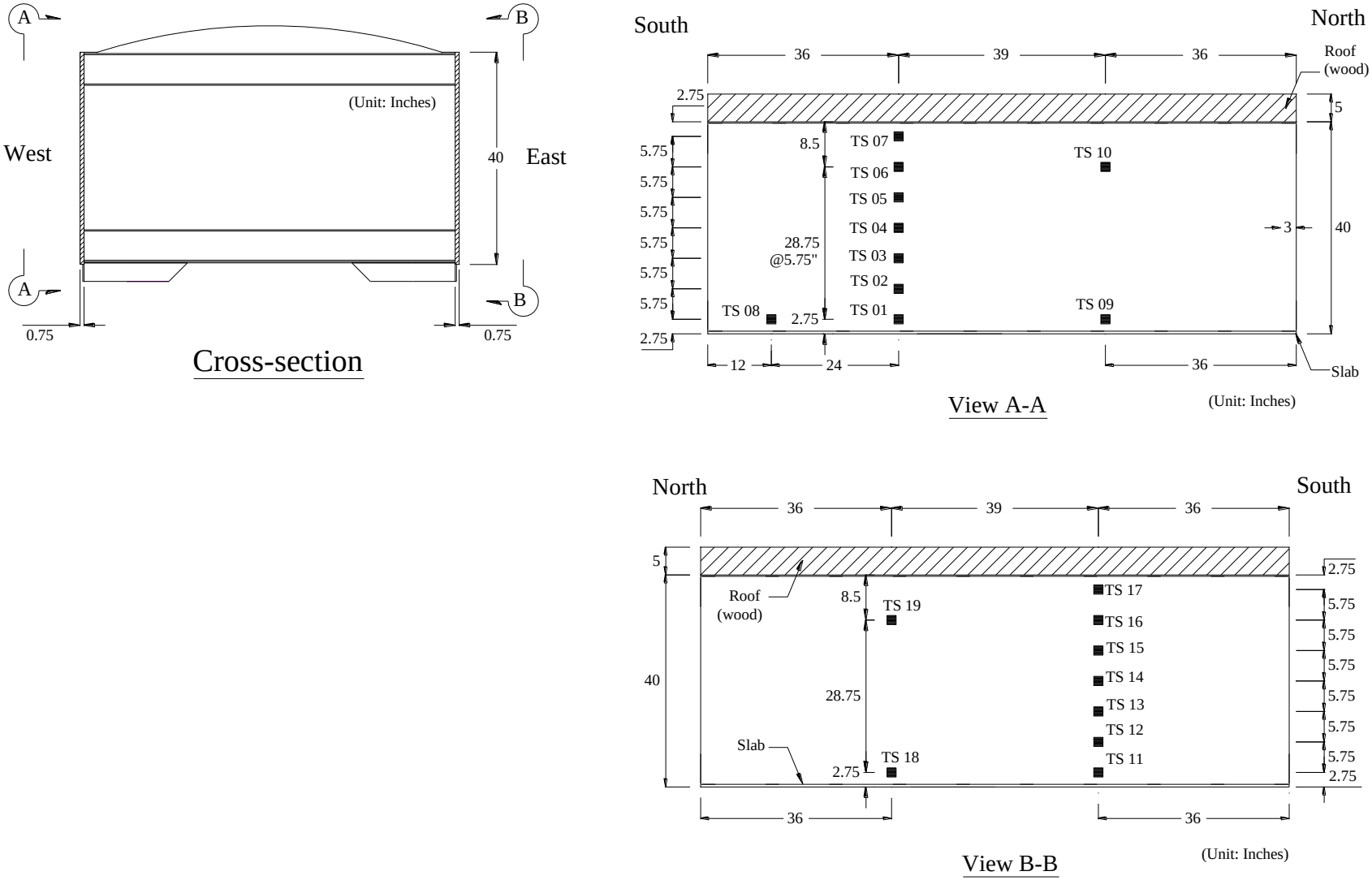

Figure 4–1: Tactilus pressure sensor (TS) layout along the tunnel walls

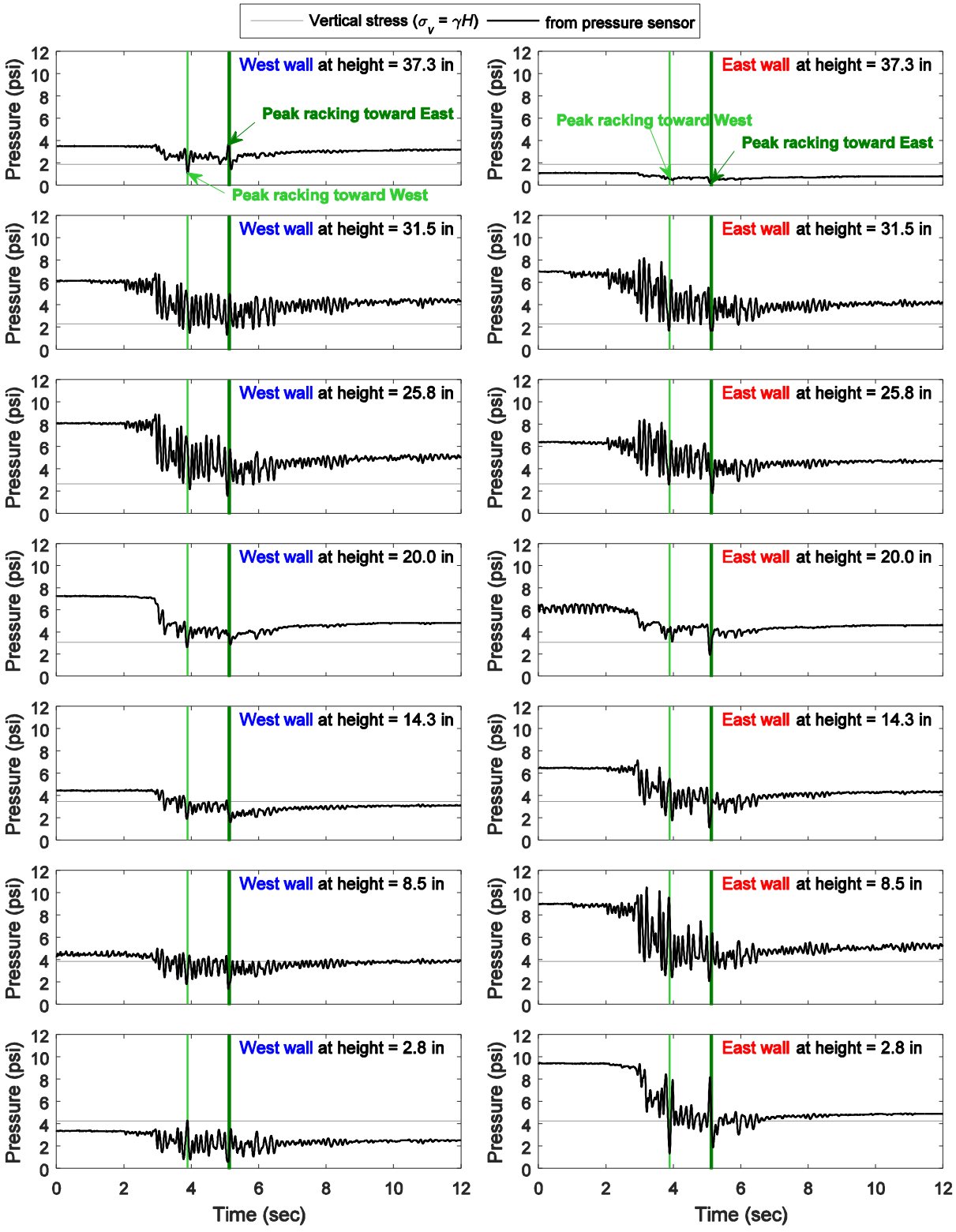

Figure 4–2: Model 1 earth pressure time histories along the wall height for Nor100PT1 (2 ft overburden soil)

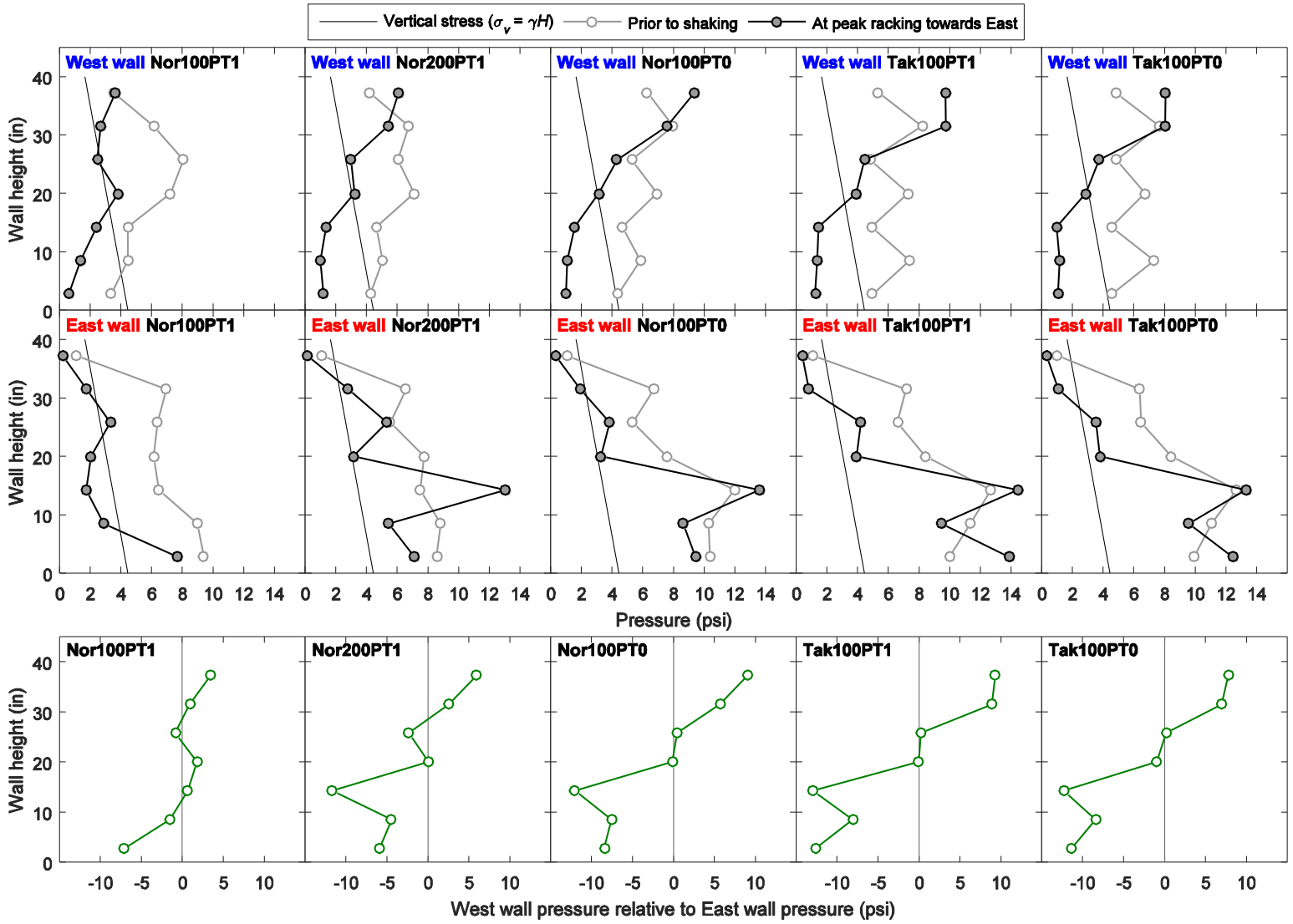

Figure 4–3: Model 1 earth pressure distribution along the wall height at peak racking towards East; West wall (top); East wall (middle); West wall pressure relative to East wall pressure (bottom)

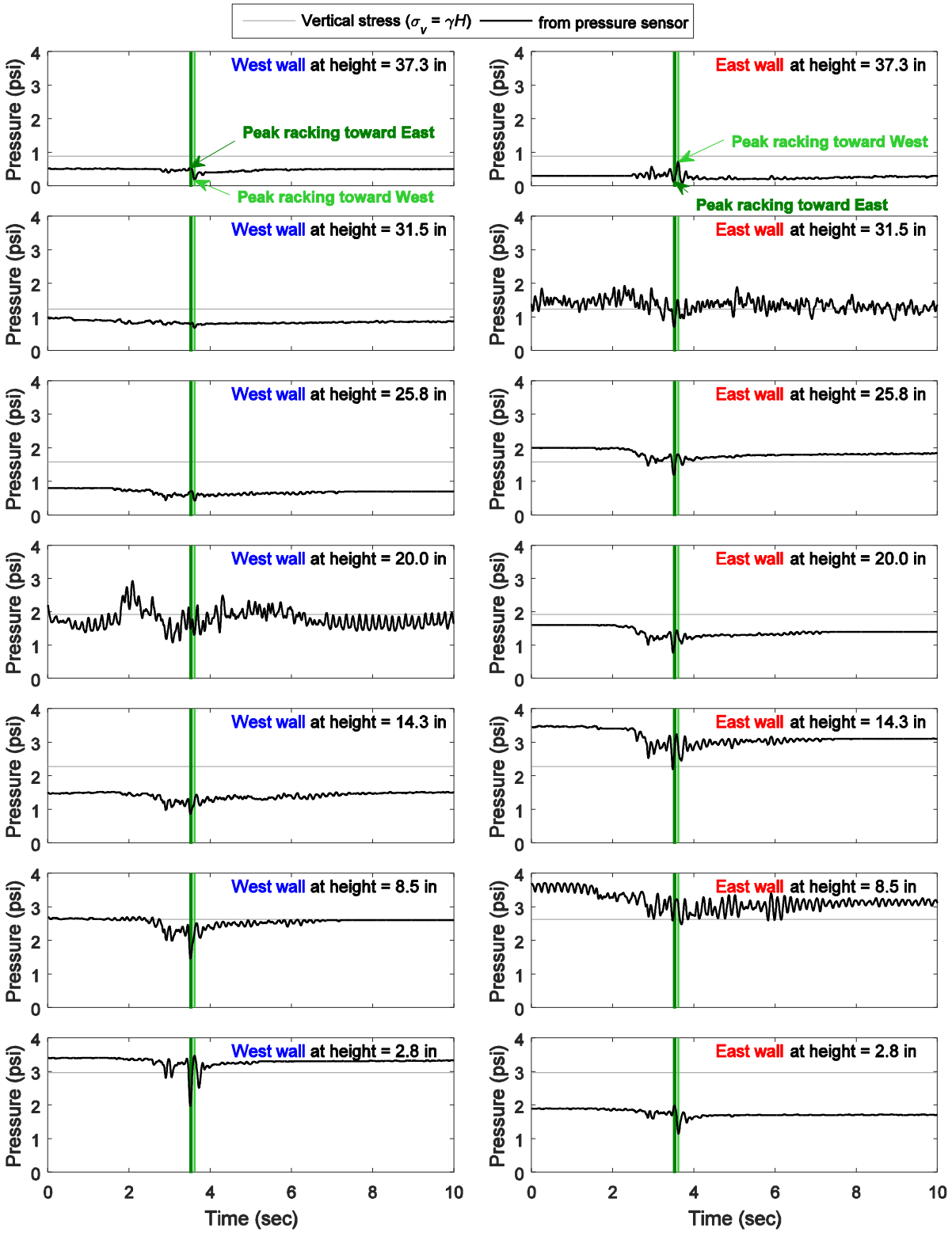

Figure 4–4: Model 3 earth pressure time histories along the wall height for Nor100PT2 (1 ft overburden soil)

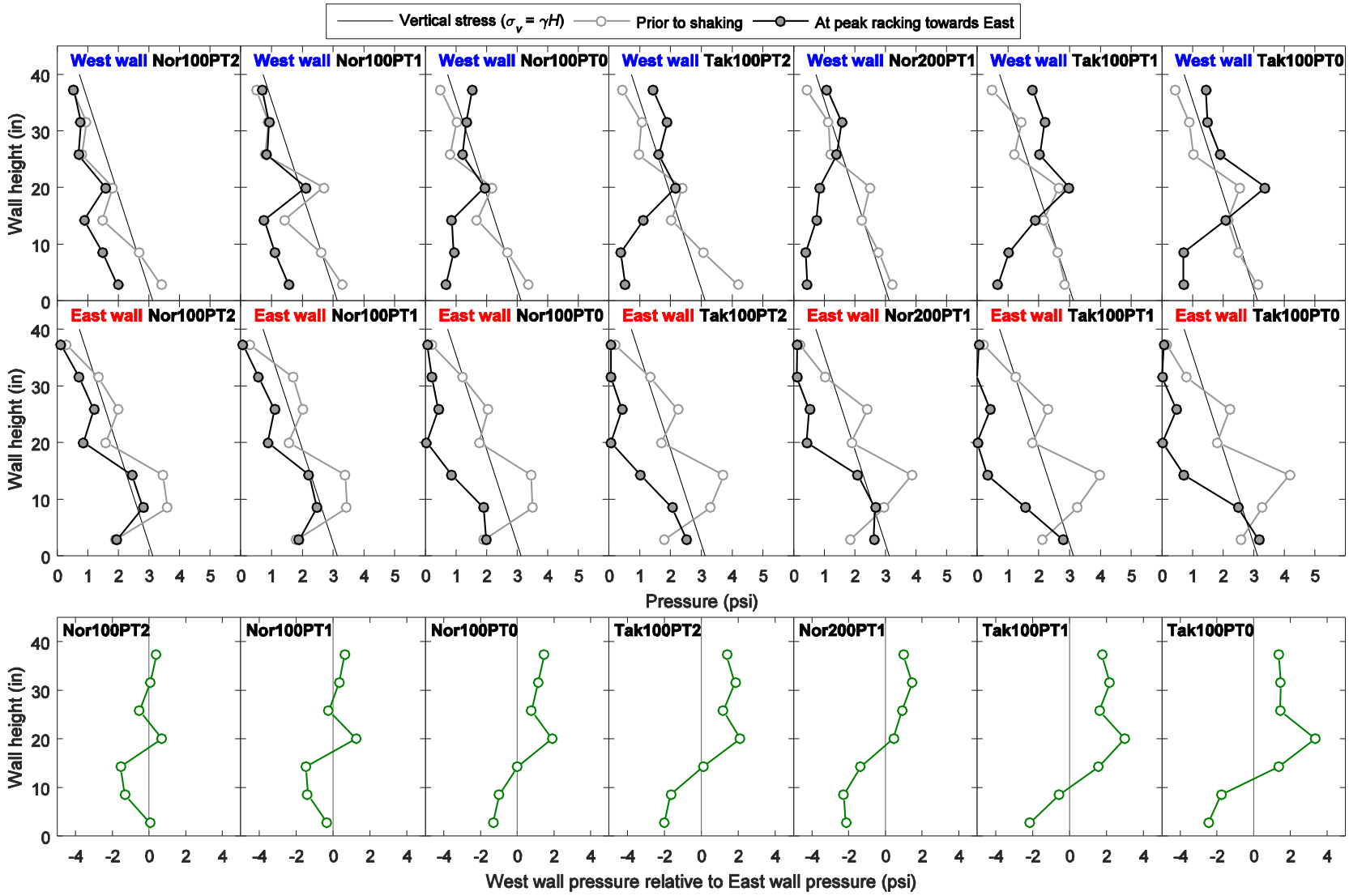

Figure 4–5: Model 3 earth pressure distribution along the wall height at peak racking towards East; West wall (top); East wall (middle); West wall pressure relative to East wall pressure (bottom)

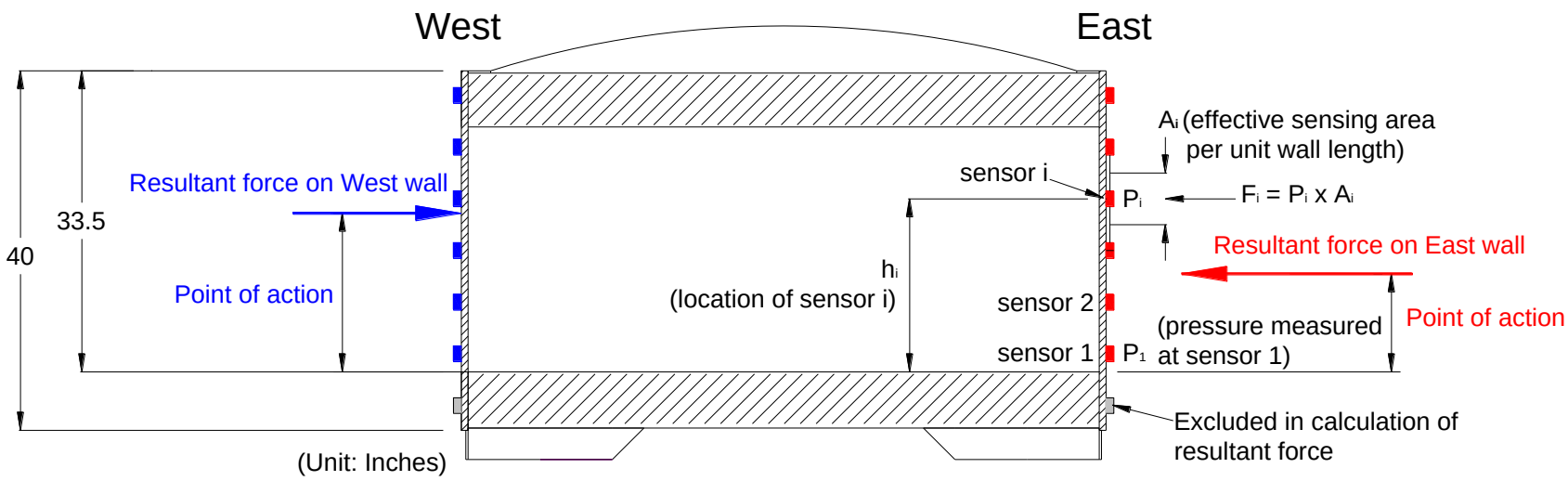

$$\text{Resultant force} = \sum F_i = \sum P_i \times A_i$$

$$\text{Point of action} = \frac{\sum (F_i \times h_i)}{\sum F_i}$$

Figure 4–6: Schematic view of the resultant force and point of action

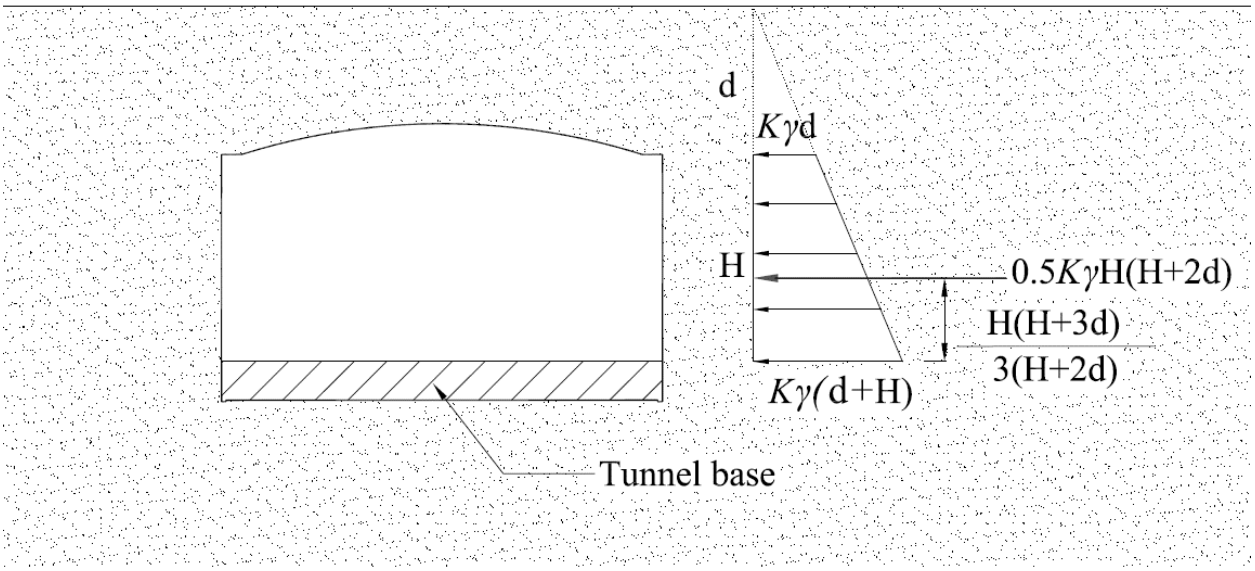

Figure 4–7: Schematic view of the reference lateral earth pressure force at rest (K = 1.0 as the reference pressure)

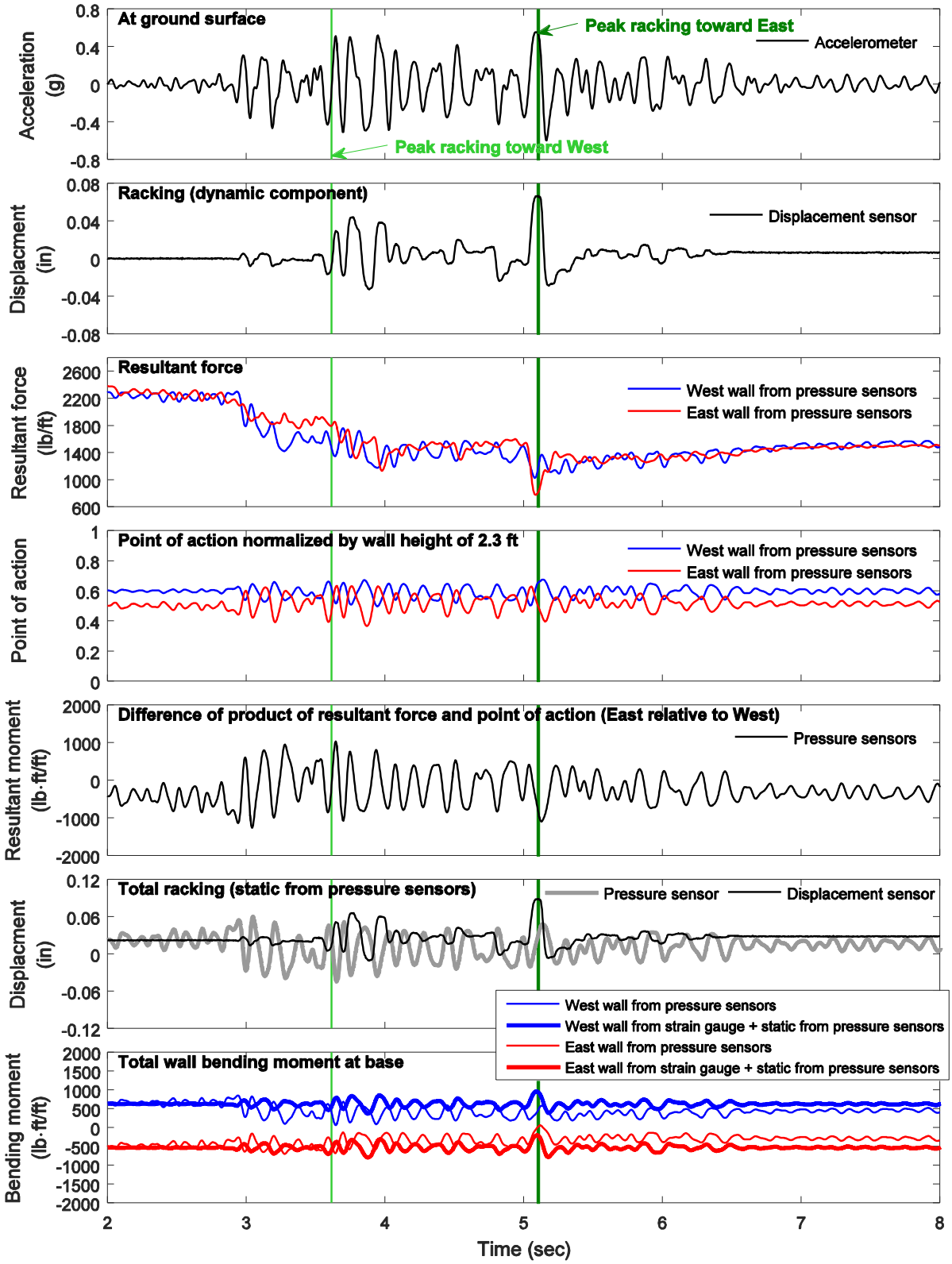

Figure 4–8: Model 1 resultant earth pressure force, point of action, and total wall bending moment at wall base for Nor100PT1 in model scale (2 ft overburden soil)

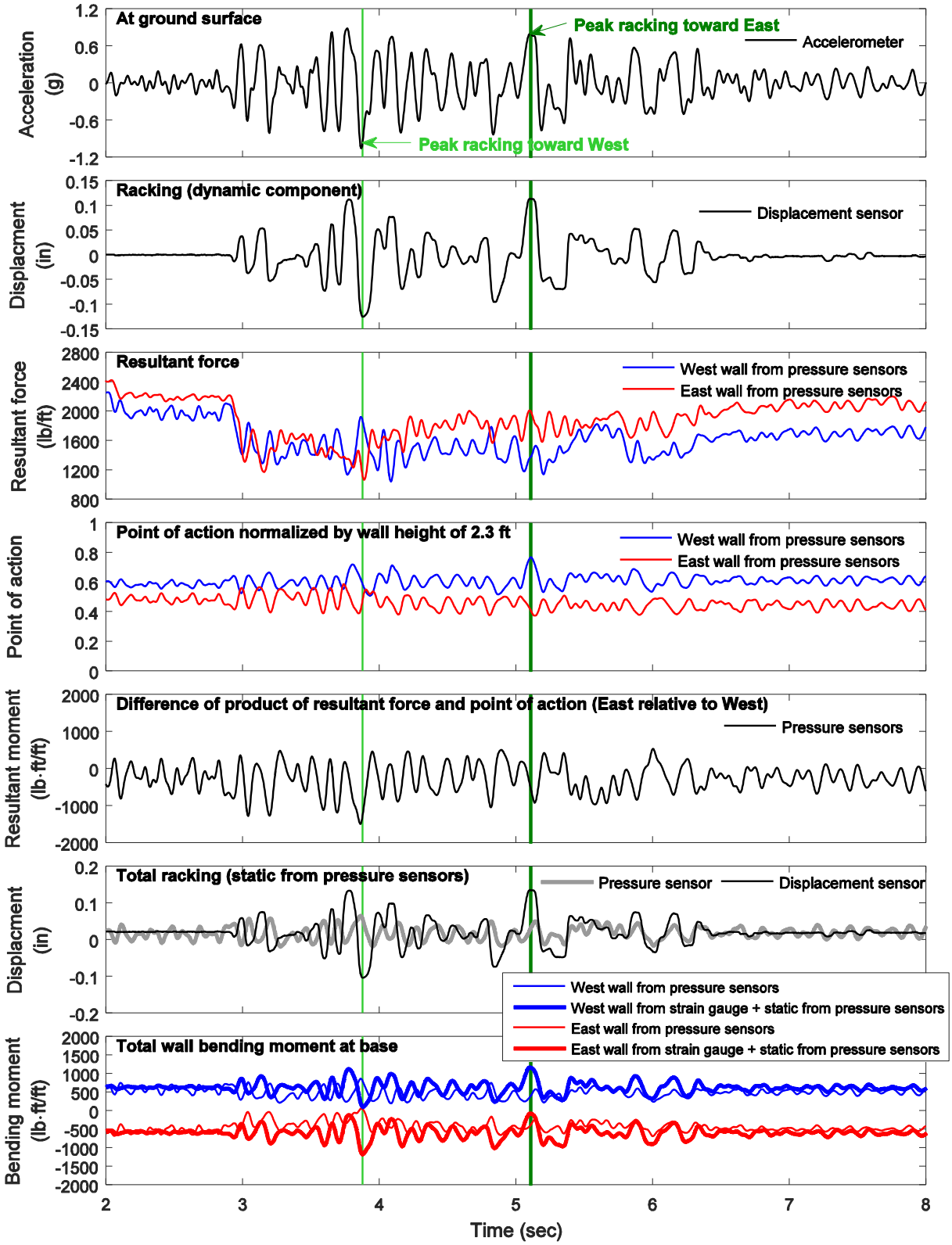

Figure 4–9: Model 1 resultant earth pressure force, point of action, and total wall bending moment at wall base for Nor200PT1 in model scale (2 ft overburden soil)

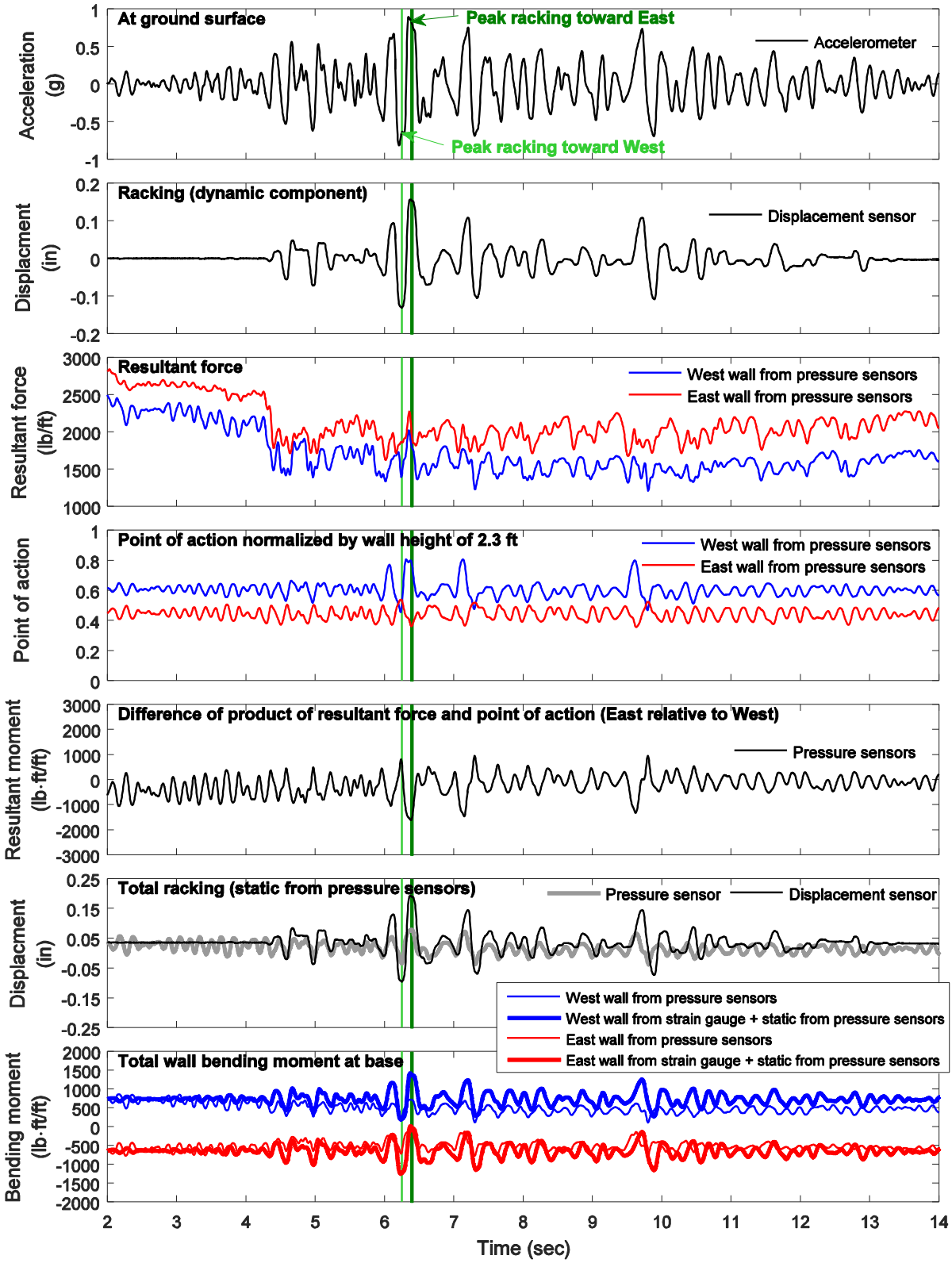

Figure 4–10: Model 1 resultant earth pressure force, point of action, and total wall bending moment at wall base for Nor100PT0 in model scale (2 ft overburden soil)

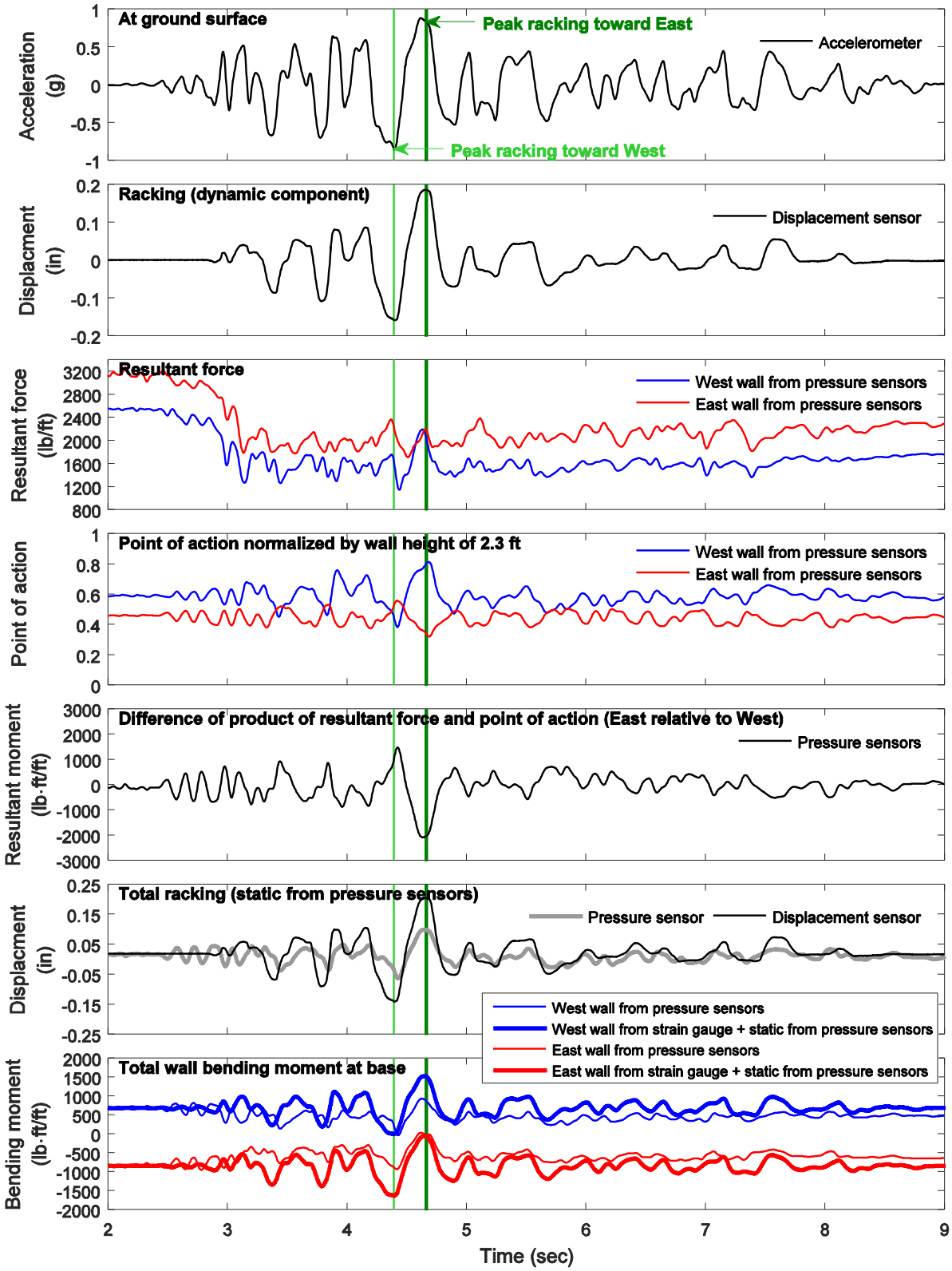

Figure 4–11: Model 1 resultant earth pressure force, point of action, and total wall bending moment at wall base for Tak100PT1 in model scale (2 ft overburden soil)

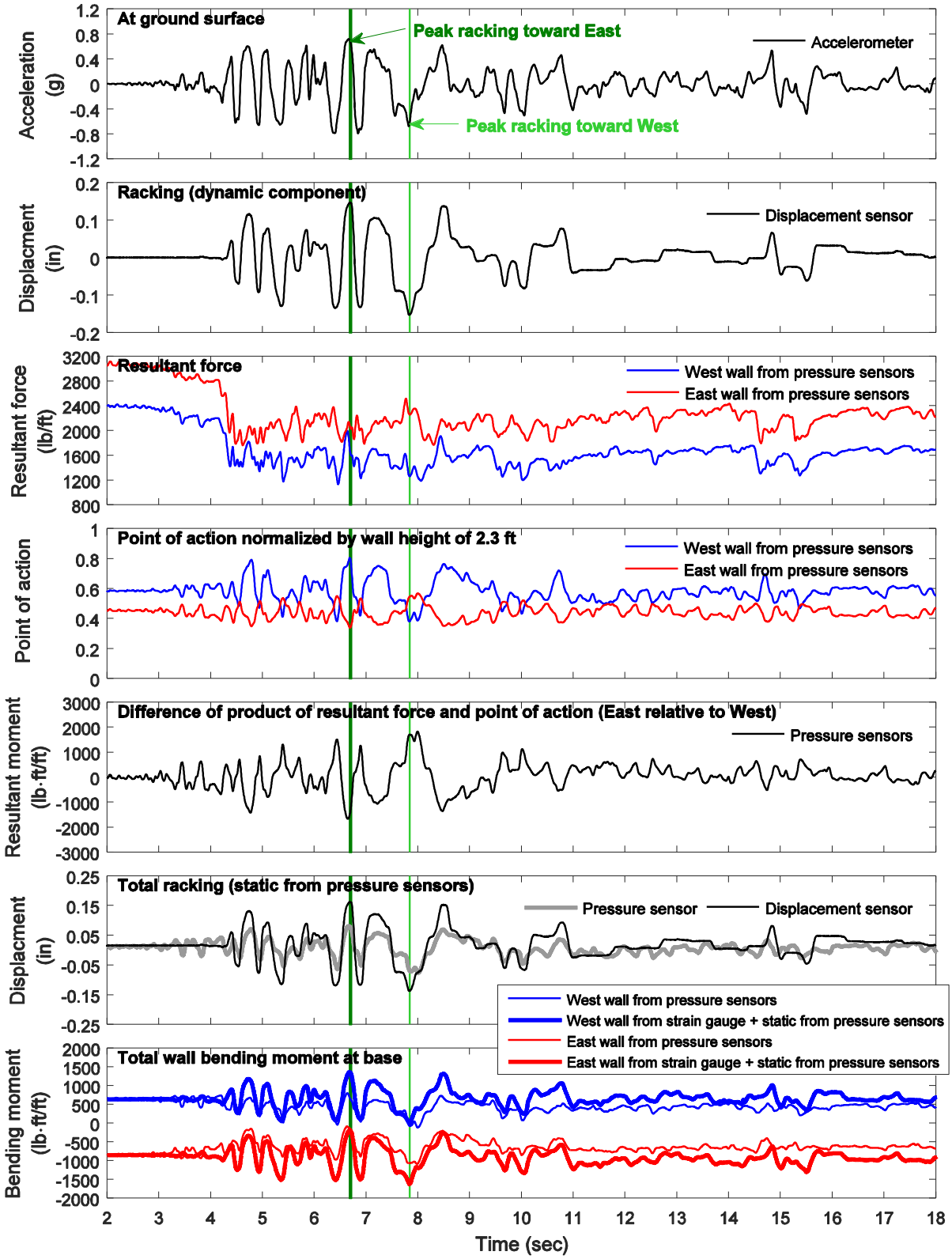

Figure 4–12: Model 1 resultant earth pressure force, point of action, and total wall bending moment at wall base for Tak100PT0 in model scale (2 ft overburden soil)

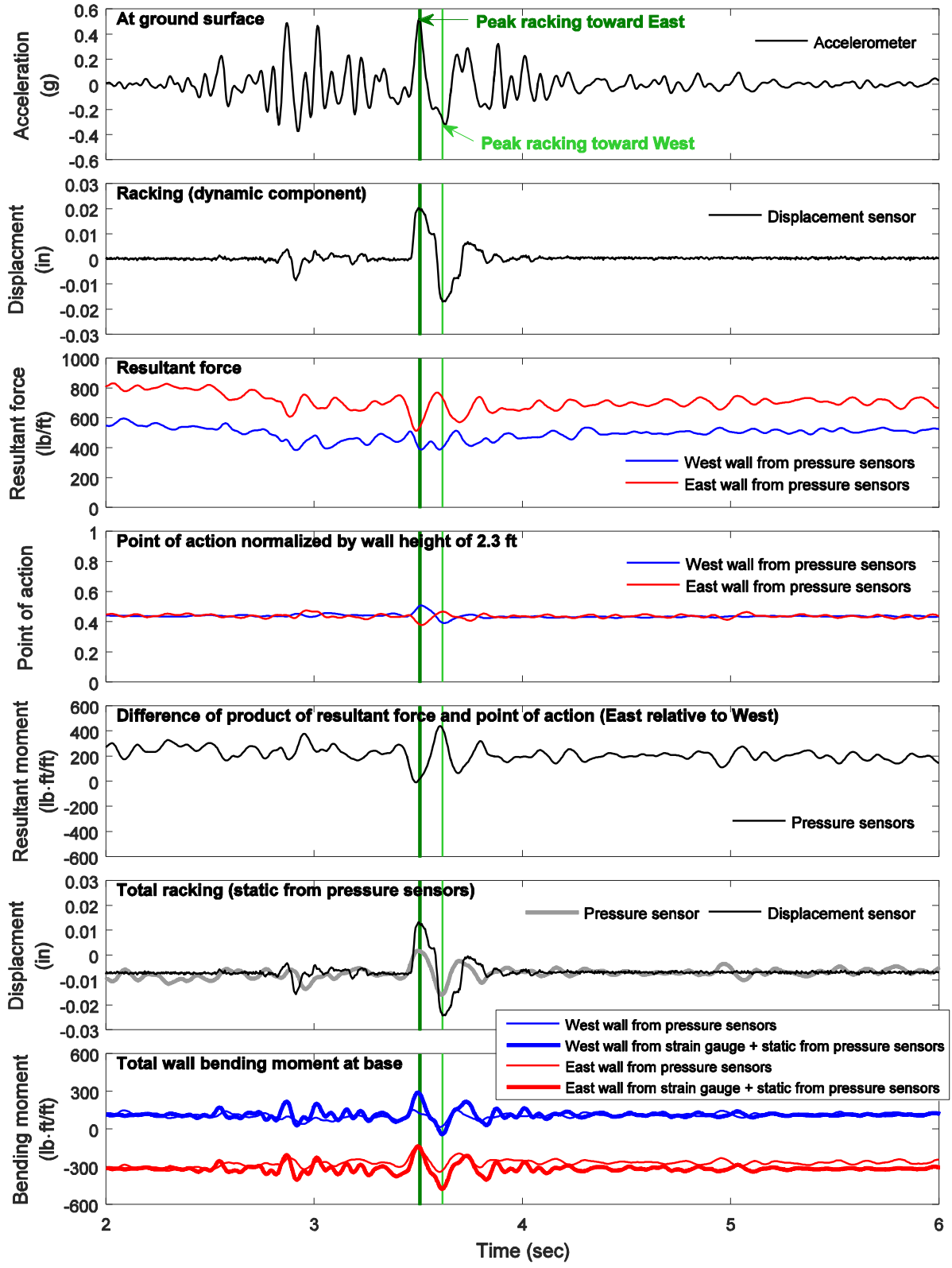

Figure 4–13: Model 3 resultant earth pressure force, point of action, and total wall bending moment at wall base for Nor100PT2 in model scale (1ft overburden soil)

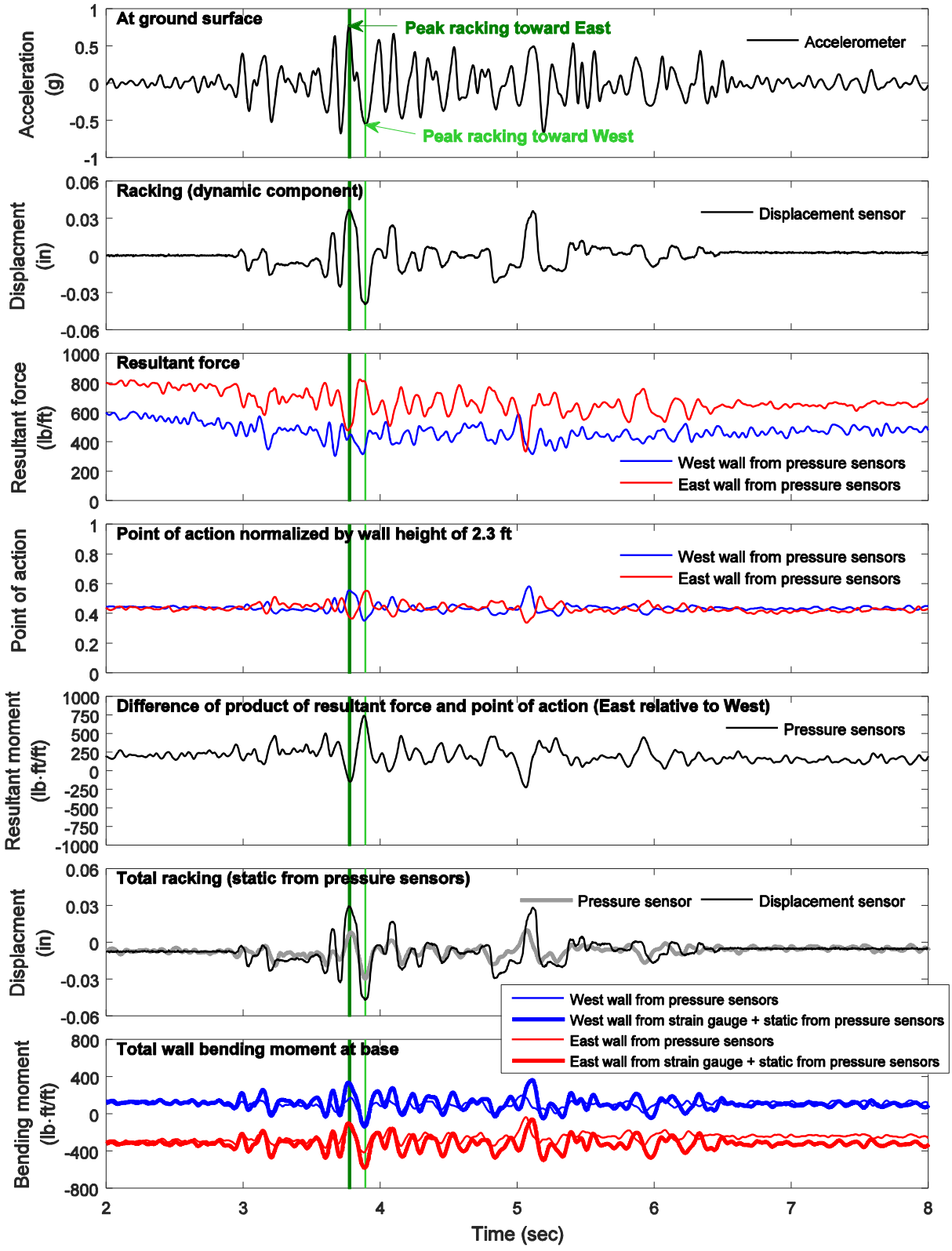

Figure 4–14: Model 3 resultant earth pressure force, point of action, and total wall bending moment at wall base for Nor100PT1 in model scale (1ft overburden soil)

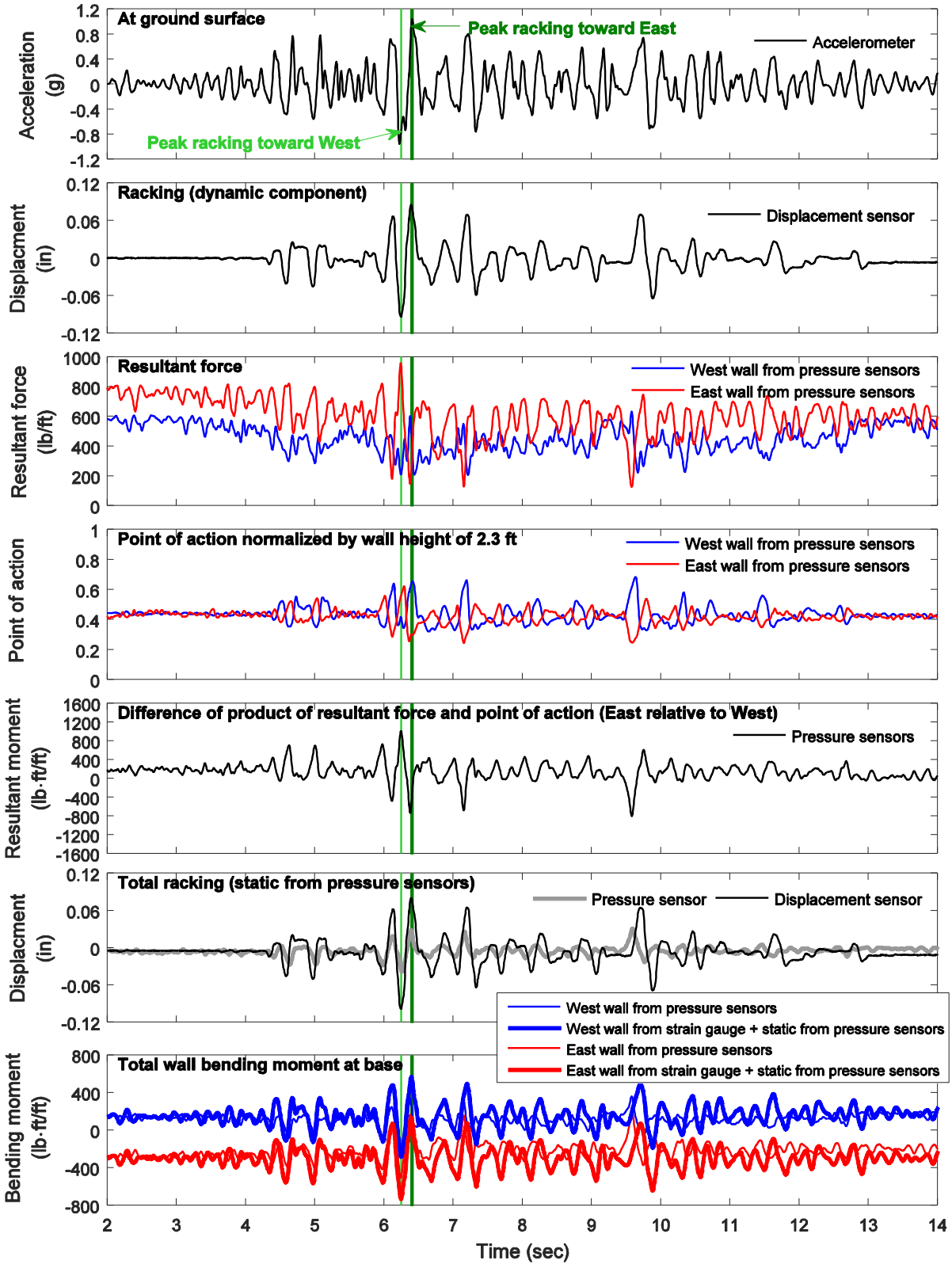

Figure 4–15: Model 3 resultant earth pressure force, point of action, and total wall bending moment at wall base for Nor100PT0 in model scale (1ft overburden soil)

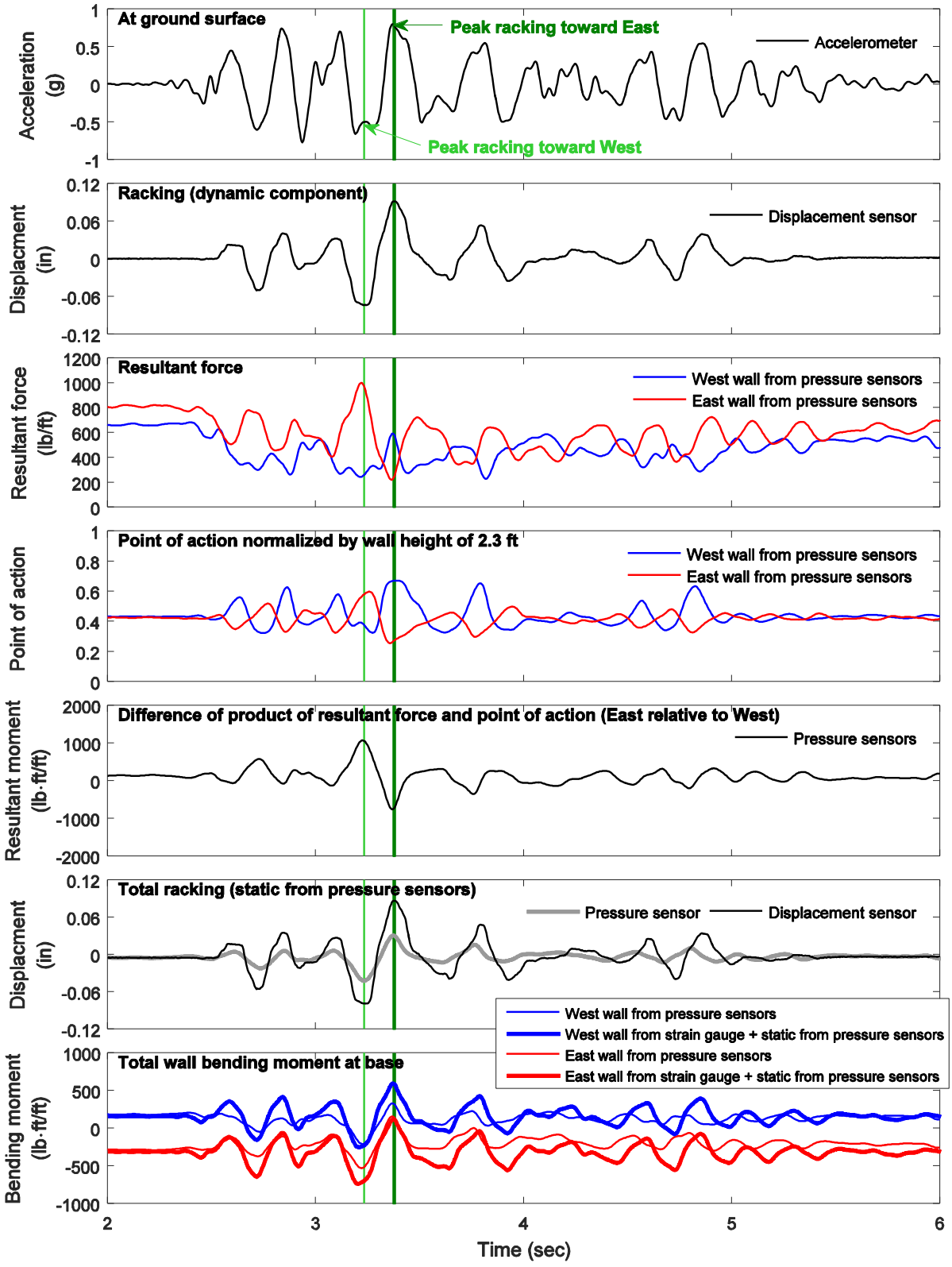

Figure 4–16: Model 3 resultant earth pressure force, point of action, and total wall bending moment at wall base for Tak100PT2 in model scale (1ft overburden soil)

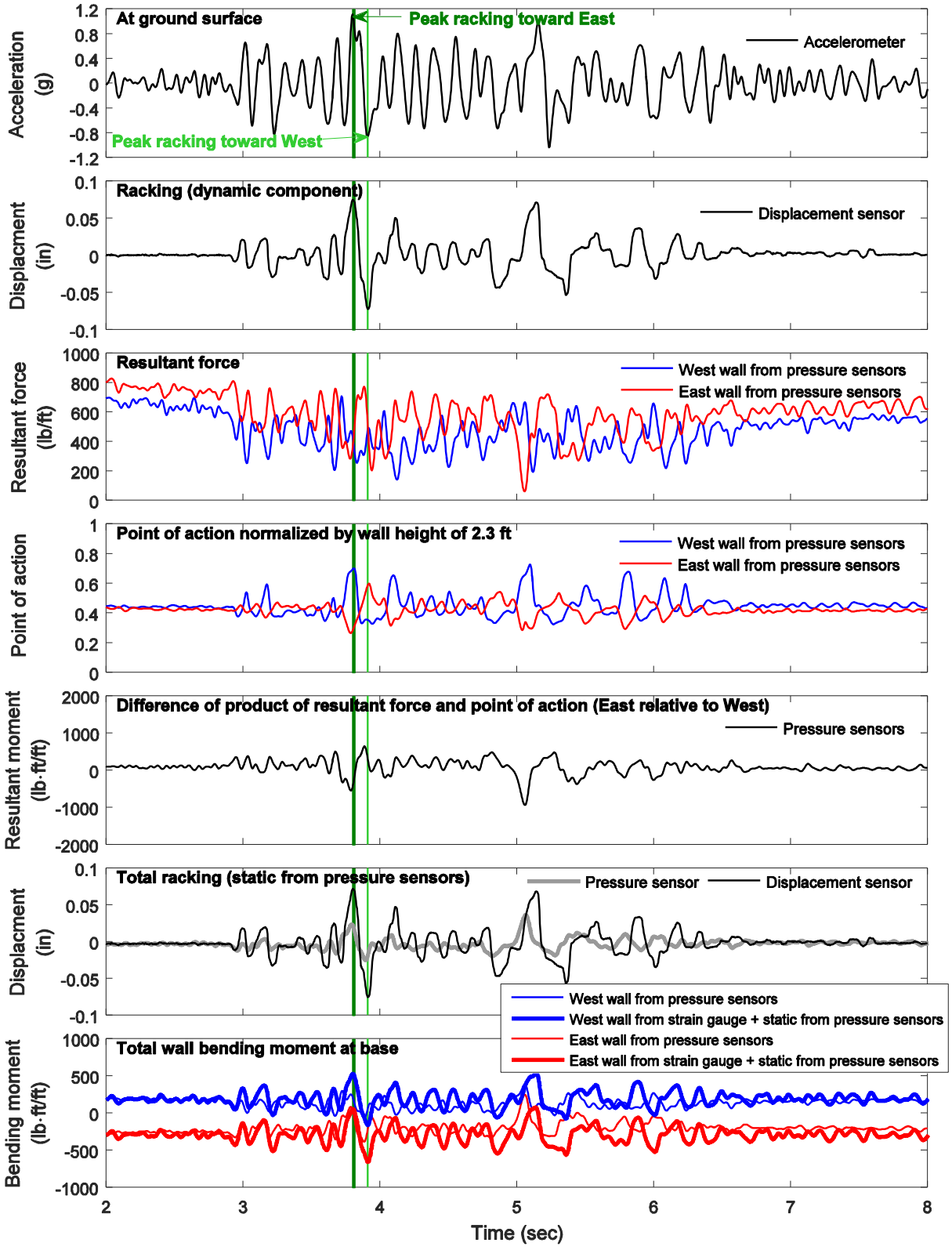

Figure 4–17: Model 3 resultant earth pressure force, point of action, and total wall bending moment at wall base for Nor200PT1 in model scale (1ft overburden soil)

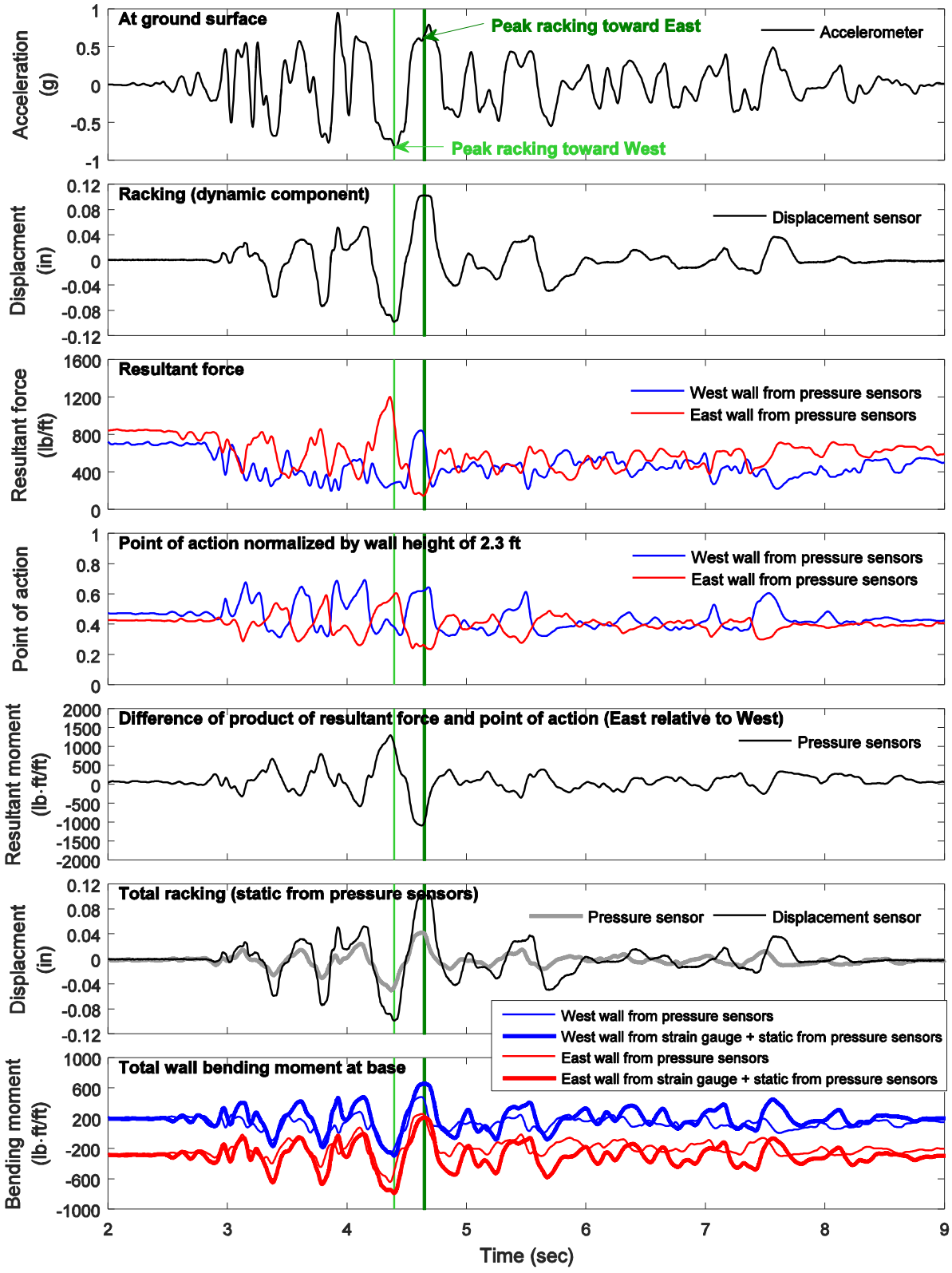

Figure 4–18: Model 3 resultant earth pressure force, point of action, and total wall bending moment at wall base for Tak100PT1 in model scale (1ft overburden soil)

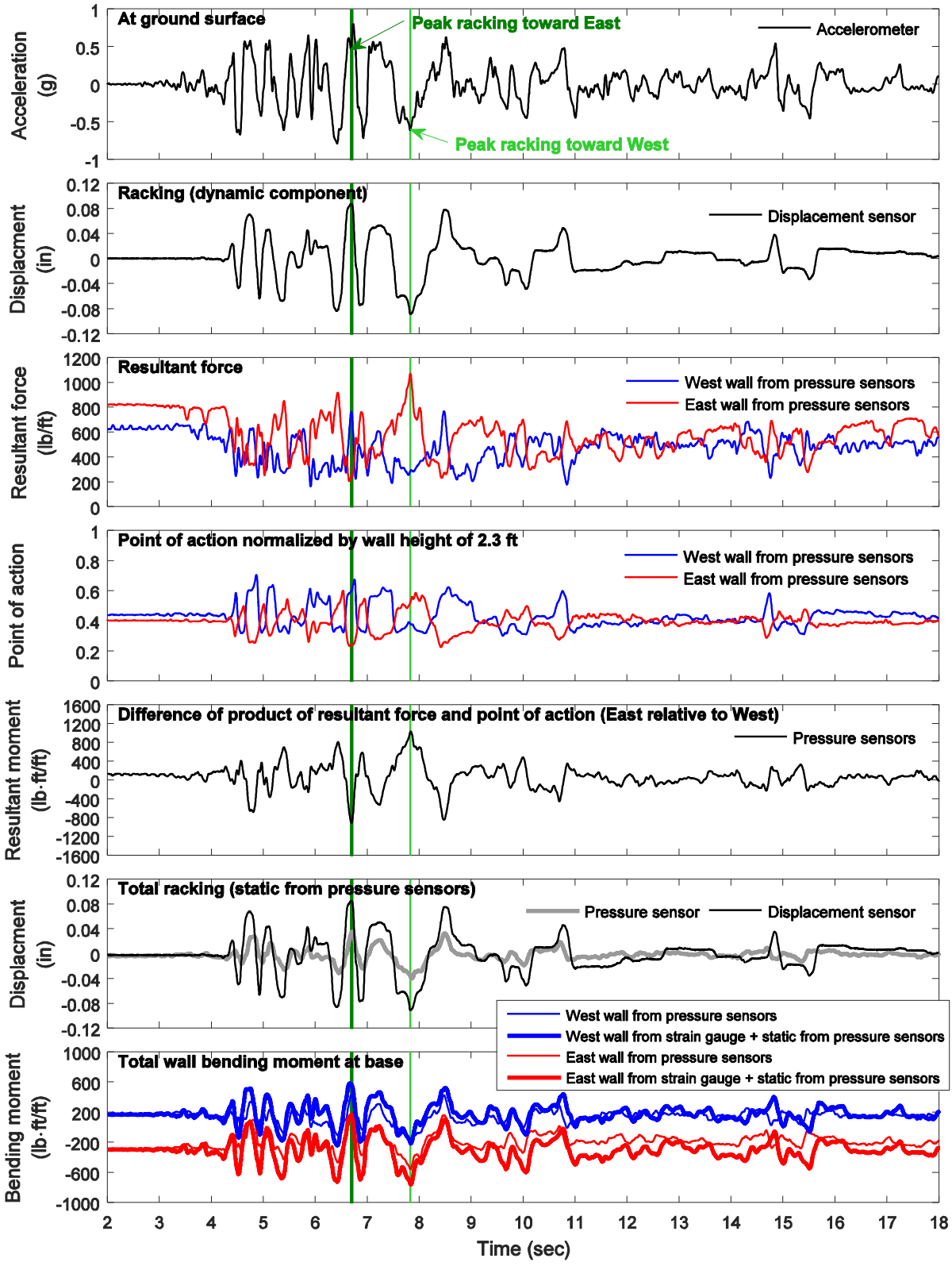

Figure 4–19: Model 3 resultant earth pressure force, point of action, and total wall bending moment at wall base for Tak100PT0 in model scale (1ft overburden soil)

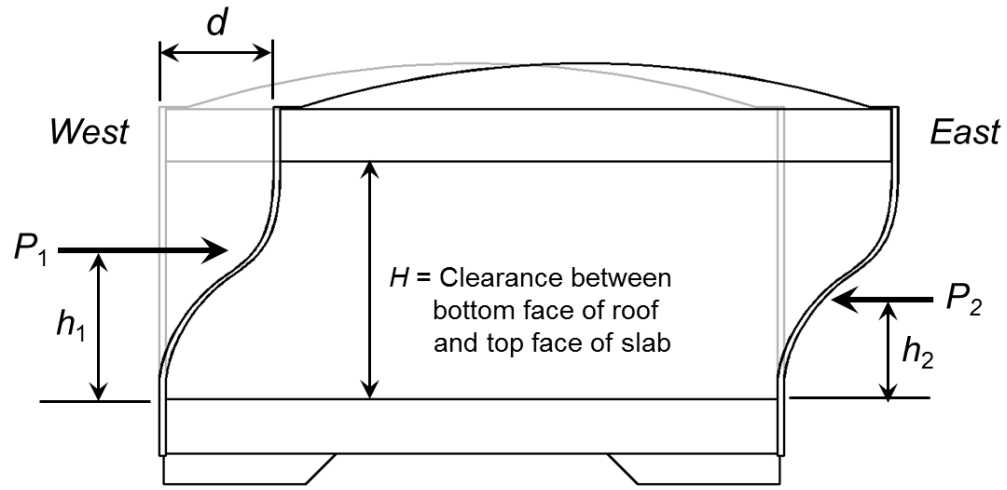

Notes:

- Positive displacement indicates the model moves toward the East
- Resultant earth pressure force is positive in compression

(a)

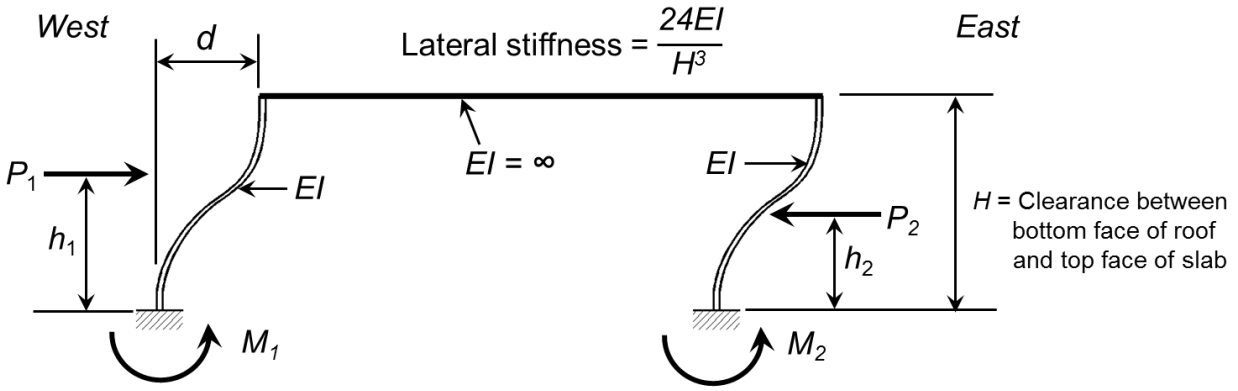

$$d = \frac{P_1 h_1^2(3H-2h_1) - P_2 h_2^2(3H-2h_2)}{24EI}$$

$$M_1 = \frac{P_1 h_1^2(3H-2h_1)}{4H^2} + \frac{P_1 h_1(H-h_1)^2}{H^2} - \frac{P_2 h_2^2(3H-2h_2)}{4H^2}$$

$$M_2 = \frac{P_1 h_1^2(3H-2h_1)}{4H^2} - \frac{P_2 h_2^2(3H-2h_2)^2}{4H^2} - \frac{P_2 h_2(H-h_2)^2}{H^2}$$

Note: Moment sign convention

Positive moment indicates tension on the West side of wall

(b)

Figure 4–20: Schematic view of seismic demand for tunnel: (a) tunnel deformation resulting from lateral earth pressure resultant forces and (b) racking and wall bending moment at base

5. Shake Table Test Result in Prototype Scale

5.1. Introduction

The tested model was designed to represent a 1/9 scale model in terms of the geometric dimensions and lateral stiffness of the employed steel tunnel walls. The associated scaling laws were applied to the recorded test results to interpret the full-scale model response (in prototype scale). Among the seven earthquake motions, the time duration of Nor100PT2 and Tak100PT2 were appropriately compressed by a factor of 5.2, associated with the model frequency. As such, these two shaking events are mainly discussed. In addition, the shaking cases such as Nor100PT0, Tak100PT1, and Tak100PT00 where the PGV exceeds 10 ft/s (the associated scale factor of 5.2) were excluded because this level of shaking is hardly manifested in actual situations. All quantities presented in this chapter are in prototype scale unless otherwise noted.

5.2. Scaling Law

Table 5–1 summarizes the main scaling factors derived by Iai (1989). The scaling factors for the tunnel are specified per unit length in two dimensions (2D). In particular, the scale factor for the displacement was 27 ($= 9^{1.5}$), compared to the dimensional factor of 9. As such, the tunnel racking in terms of drift was three times larger than that in model scale. Further details of the scaling laws and related derivation are presented in Appendix D.

5.3. Peak Dynamic Response

As shown earlier in Section 3.3 (in model scale), the recorded (but scaled) time histories of the main response of Models 1-3 for Nor100PT2 and Tak100PT2 are presented in Figure 5–1 through Figure 5–6. Table 5–2 summarizes the main peak response values from all the test models in the order of the shaking sequence in terms of:

1) Peak ground acceleration and velocity (PGA and PGV)
2) Ground acceleration and velocity at levels of the tunnel roof and base
3) Tunnel acceleration at the roof and the base
4) Ground distortion between top and bottom of the tunnel wall obtained from double integration of the ground acceleration (above Item 2)
5) Tunnel racking
6) Wall bending moment at the base and top

7) Tunnel base translation relative to the laminar container

5.3.1. Model 1 Nor100PT2

For Nor100PT2 (Figure 5–1), the following observations are drawn:

- Peak ground acceleration (PGA) was about 0.42g.
- Peak racking was about 0.59 inch (0.17% drift divided by the tunnel height of 30 ft) as the test model moved towards East (at 18.2 sec.)
- Peak racking coincided with other peak responses such as PGA, ground distortion, and wall bending moment.
- Ground distortion (shear deformation herein) was about 1.66 inch (about 0.46%, also divided by the tunnel height). Compared to the peak racking, this distortion was as much as about three times, indicating that the ground surrounding the tunnel was relatively softer than the tunnel. The ratio of the racking to the ground distortion, also known as the racking coefficient (Wang 1993; FHWA 2009) was about 0.36.
- Similar peak bending moment (about 140 kip·ft/ft; dynamic component) occurred near the top and bottom of both tunnel walls.

5.3.2. Model 1 Tak100PT2

For Nor100PT2 (Figure 5–2), the following observations are drawn:

- Peak ground acceleration (PGA) was about 0.75g.
- Peak racking was about 3.97 inch (1.1% drift divided by the tunnel height of 30 ft) as the test model moved towards East (at 17.7 sec.)
- Peak racking generally coincided with other peak responses such as PGA, ground distortion, and wall bending moment.
- Ground distortion (shear deformation herein) was about 8.2 inch (about 2.3%, also divided by the tunnel height). Compared to peak racking, this distortion was as much as about twice, indicating that the ground surrounding the tunnel was relatively softer than the tunnel (the corresponding racking ratio of about 0.5).
- Peak bending moment of about 450 kip·ft/ft (positive moment) occurred near the base of the West wall. On the East wall, larger bending moment of 480 lb·ft/ft (negative moment) was observed near the base.

5.3.3. Summary of Peak Dynamic Response from All Shaking Events

From each test model, peak racking generally coincided with PGA (based on the time history plots as shown in Figure 5–1 through Figure 5–6). The level of peak racking was also proportional to the PGA and PGV (Figure 5–7). Among all the shake table tests, the maximum racking (dynamic component) was about 4 inches (1.1% drift ratio) which occurred in Model 1 during Tak100PT2 input excitation. In this case, the East wall suffered the highest bending moment at the base (about 480 kip·ft per unit wall length of 1ft; Figure 5–8). The level of the wall bending moment was essentially dictated by peak racking (Figure 5–9).

Under identical earthquake input excitation for different test models, the PGA and PGV tended to slightly decrease as the thickness of overburden soil increased (e.g. during Nor100PT2, 0.64g in Model 2, 0.52g in Model 3, 0.42g in Model 1). Despite this trend, the level of peak racking tended to increase along with higher overburden soil pressure (Figure 5–7). As discussed earlier in Section 3.4, this trend was associated with the lower degree of strain softening of the surrounding soil and corresponding higher flexibility and racking ratios (Figure 5–10). For the given soil displacement demand, the higher the flexibility ratio, the larger the tunnel deformation (Wang 1993).

5.4. Resultant Lateral Earth Pressure Force

As presented earlier in Section 4.3 (in model scale), the resultant force and the associated point of action were interpreted in prototype scale. The time histories of these quantities are shown in Figure 5–11 from Model 3 for Nor100PT2 as well as the following response:

1) Ground surface acceleration
2) Tunnel racking
3) Resultant moment as the difference of the product of the resultant force and the point of action on the East wall with respect to the West wall
4) Total wall bending moment including the static value estimated from the resultant force and point of action, compared to that from strain gauges (from which only the dynamic component was added to the same static value).

Similar plots from Model 3 during Nor100PT1, Tak100PT2, and Nor200PT1 are shown in Figure 5–12 through Figure 5–16. Model 1 resulting time histories are shown in Figure 5–15 and Figure 5–16 for Nor100PT1 and Nor200PT1, respectively.

5.4.1. Total wall bending moment

As discussed earlier in Section 4.4, Figure 5–17 shows the peak total bending moment for which the dynamic component from the strain gauge and the static value from the resultant force and point of action. In the entire studied cases, maximum total bending moment was about 920 kip-ft per unit wall length of 1ft from Model 1 during Nor200PT1 (the corresponding dynamic moment about 450 kip-ft). This total bending moment exceeds the bending moment capacity of about 300 kip-ft of the 1/3 reinforced concrete (RC) test model (Kim et al. 2015). As such, the required ductility may be necessary to reach a value of 3 in view of inelastic response. It is noted that the dynamic bending moment for Tak100PT2 (Model 1) was relatively higher than that for Nor200PT1 (Figure 5–17) but the static value was not available in this case. The dynamic bending moment for Tak100PT2 (Models 1 and 3) and Nor200PT1 (Model 1) was also higher than the capacity (1/3 RC test model in prototype scale).

Table 5–1: Main scaling factors for 1g model tests (Iai 1989)

Quantity	Scaling factor (prototype to 1/9 scale)		
	Generalized scaling factors	**$\lambda_\varepsilon = \lambda^{0.5}$, $\lambda_\rho = 1$**	**CASE of $\lambda = 9$**
Length	λ	λ	9
Density	λ_ρ	1	1
Time	$(\lambda\lambda_\varepsilon)^{0.5}$	$\lambda^{0.75}$	5.2
Acceleration	1	1	1
Velocity	$(\lambda\lambda_\varepsilon)^{0.5}$	$\lambda^{0.75}$	5.2
Displacement	$\lambda\lambda_\varepsilon$	$\lambda^{1.5}$	27
Stress	$\lambda\lambda_\rho$	λ	9
Strain	λ_ε	$\lambda^{0.5}$	3
Stiffness	$\lambda\lambda_\rho/\lambda_\varepsilon$	$\lambda^{0.5}$	3
EI*	$\lambda^4\lambda_\rho/\lambda_\varepsilon$	$\lambda^{3.5}$	2187
EA*	$\lambda^2\lambda_\rho/\lambda_\varepsilon$	$\lambda^{1.5}$	27
Moment*	$\lambda^3\lambda_\rho$	λ^3	729
Shear*	$\lambda^2\lambda_\rho$	λ^2	81
Axial Force*	$\lambda^2\lambda_\rho$	λ^2	81

*specified per unit breadth of the tunnel along its longitudinal axis (based on 2D Plane Strain)

Table 5–2: Peak dynamic response of ground and tunnel in prototype scale

Model	Shaking	EQ	At surface		At level of tunnel top			At level of tunnel base			Soil distortion (%)	Racking (%)	Bending moment (kip-ft)				Base translation (%)
													West wall		East wall		
			PGA (g)	PGV (in/s)	Acc. (g)	Vel. (in/s)	Tunnel (g)	Acc. (g)	Vel. (in/s)	Tunnel (g)			Top	Base	Top	Base	
1	1	Nor100PT1	0.60	3.5	0.52	3.1	0.45	0.33	1.7	0.33	0.87	0.50	198	239	-230	-191	0.03
	2	Nor200PT1	1.06	8.1	0.82	7.1	0.71	0.79	4.4	0.68	3.12	0.94	451	395	-382	-440	0.29
	3	Nor100PT0	0.90	9.6	0.80	9.2	0.72	0.55	6.6	0.58	4.00	1.17	430	501	-483	-451	0.38
	4	Tak100PT1	0.88	15.5	0.86	15.1	0.78	0.74	12.1	0.76	4.69	1.39	533	618	-573	-576	0.35
	5	Tak100PT0	0.79	15.3	0.77	15.4	0.74	0.70	13.8	0.71	3.55	1.14	499	530	-479	-568	0.20
	6	Nor100PT2	0.42	1.6	0.38	1.6	0.29	0.26	1.1	0.24	0.46	0.17	120	144	-135	-121	0.01
	7	Tak100PT2	0.75	6.0	0.73	5.9	0.60	0.49	3.0	0.49	2.27	1.10	448	449	-425	-480	0.22
2	1	Nor100PT2	0.64	2.1	0.64	2.1	0.39	0.36	1.0	0.32	0.72	0.03	43	74	-59	-56	0.02
	2	Nor100PT1	0.96	3.5	0.96	3.5	0.49	0.44	2.1	0.41	1.83	0.08	77	108	-84	-97	0.17
	3	Nor100PT0	1.19	10.1	1.19	10.1	0.85	0.76	6.5	0.85	8.51	0.32	144	197	-150	-178	0.78
	4	Tak100PT2	1.45	7.7	1.45	7.7	0.74	0.65	4.1	0.77	4.94	0.31	133	187	-140	-166	0.61
	5	Nor200PT1	1.27	9.6	1.27	9.6	0.83	0.81	5.8	0.77	6.56	0.28	127	146	-109	-158	0.59
	6	Tak100PT1	1.36	17.5	1.36	17.5	0.76	0.75	11.3	0.77	8.08	0.24	143	169	-124	-178	0.58
	7	Tak100PT0	0.92	15.5	0.92	15.5	0.81	0.64	13.7	0.78	5.88	0.23	112	185	-109	-173	0.54
3	1	Nor100PT2	0.52	2.0	0.39	1.6	0.37	0.33	0.9	0.28	0.63	0.15	112	131	-118	-117	0.02
	2	Nor100PT1	0.78	3.5	0.50	2.7	0.48	0.39	1.8	0.34	1.31	0.30	183	177	-164	-192	0.13
	3	Nor100PT0	1.04	10.5	0.87	9.2	0.87	0.70	6.3	0.81	5.35	0.70	292	311	-273	-320	0.49
	4	Tak100PT2	0.80	6.3	0.76	5.8	0.74	0.58	3.7	0.65	3.43	0.69	281	317	-274	-315	0.45
	5	Nor200PT1	1.11	9.4	0.83	7.4	0.79	0.77	5.1	0.75	5.31	0.56	241	263	-228	-269	0.42
	6	Tak100PT1	0.95	16.2	0.91	16.0	0.82	0.74	11.3	0.79	8.99	0.77	311	338	-307	-366	0.72
	7	Tak100PT0	0.80	16.3	0.81	15.7	0.77	0.63	13.7	0.74	6.50	0.67	286	299	-276	-342	0.59

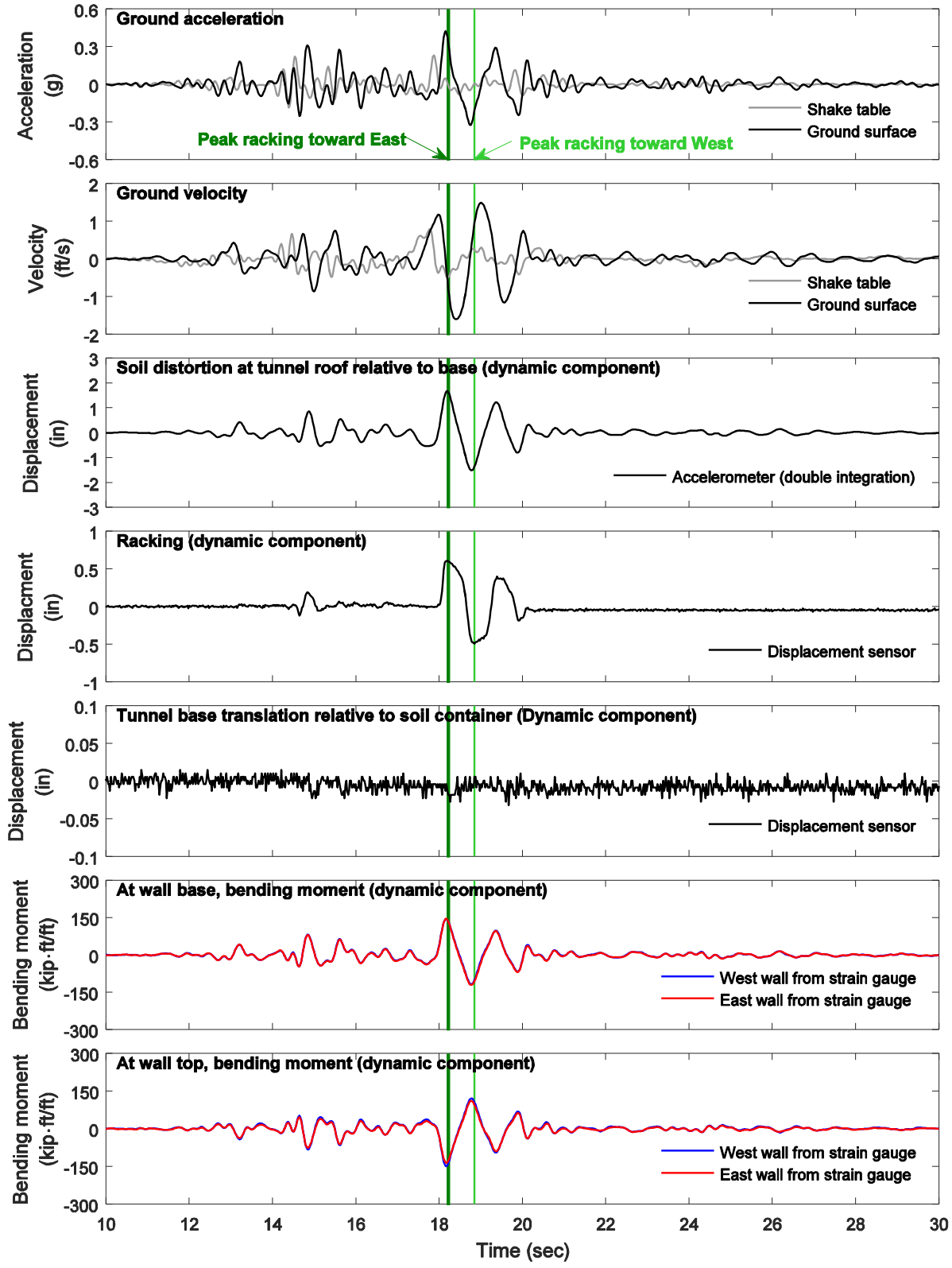

Figure 5–1: Model 1 response time histories for Nor100PT2 in prototype scale (18 ft overburden soil)

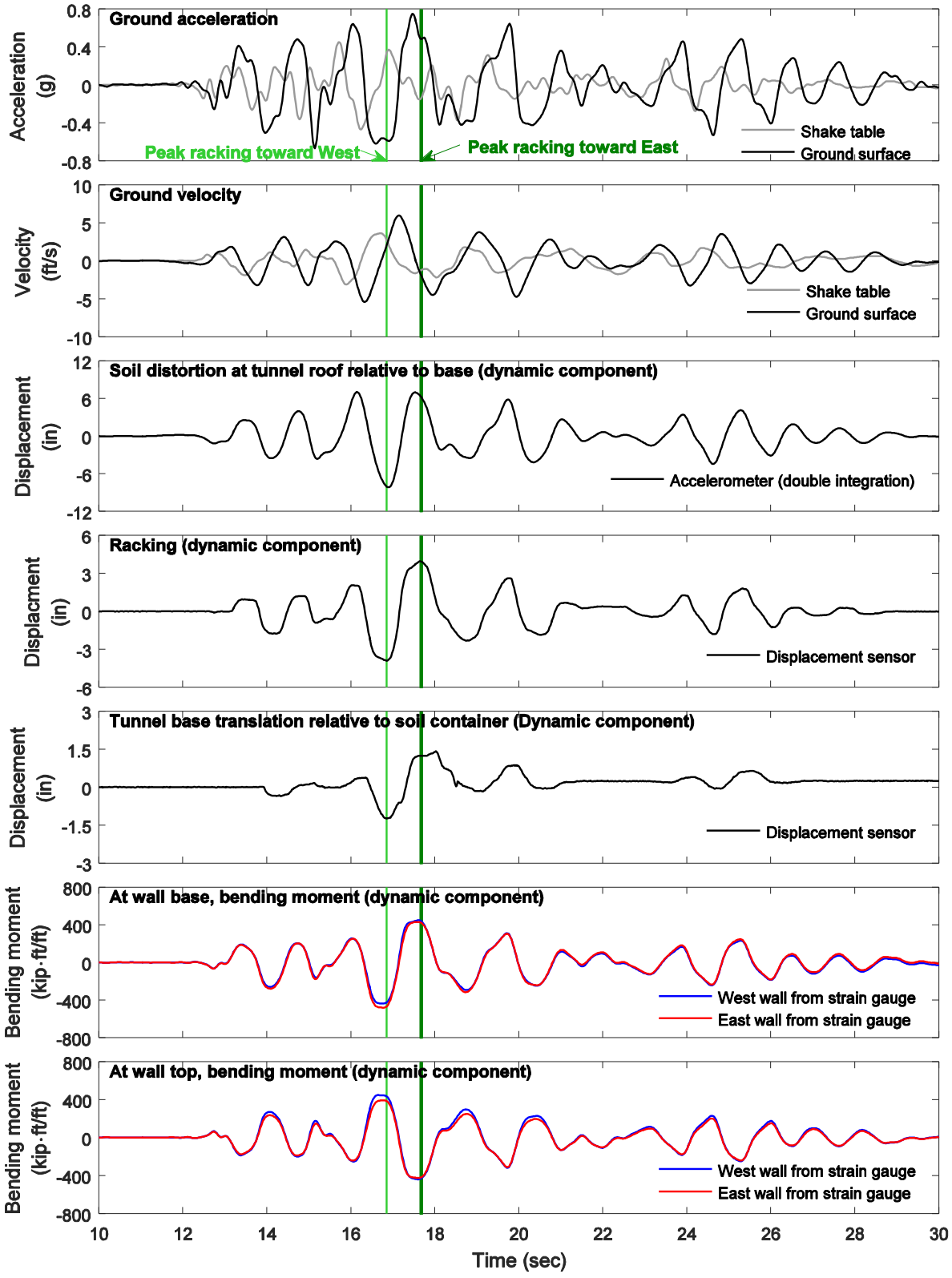

Figure 5–2: Model 1 response time histories for Tak100PT2 in prototype scale (18 ft overburden soil)

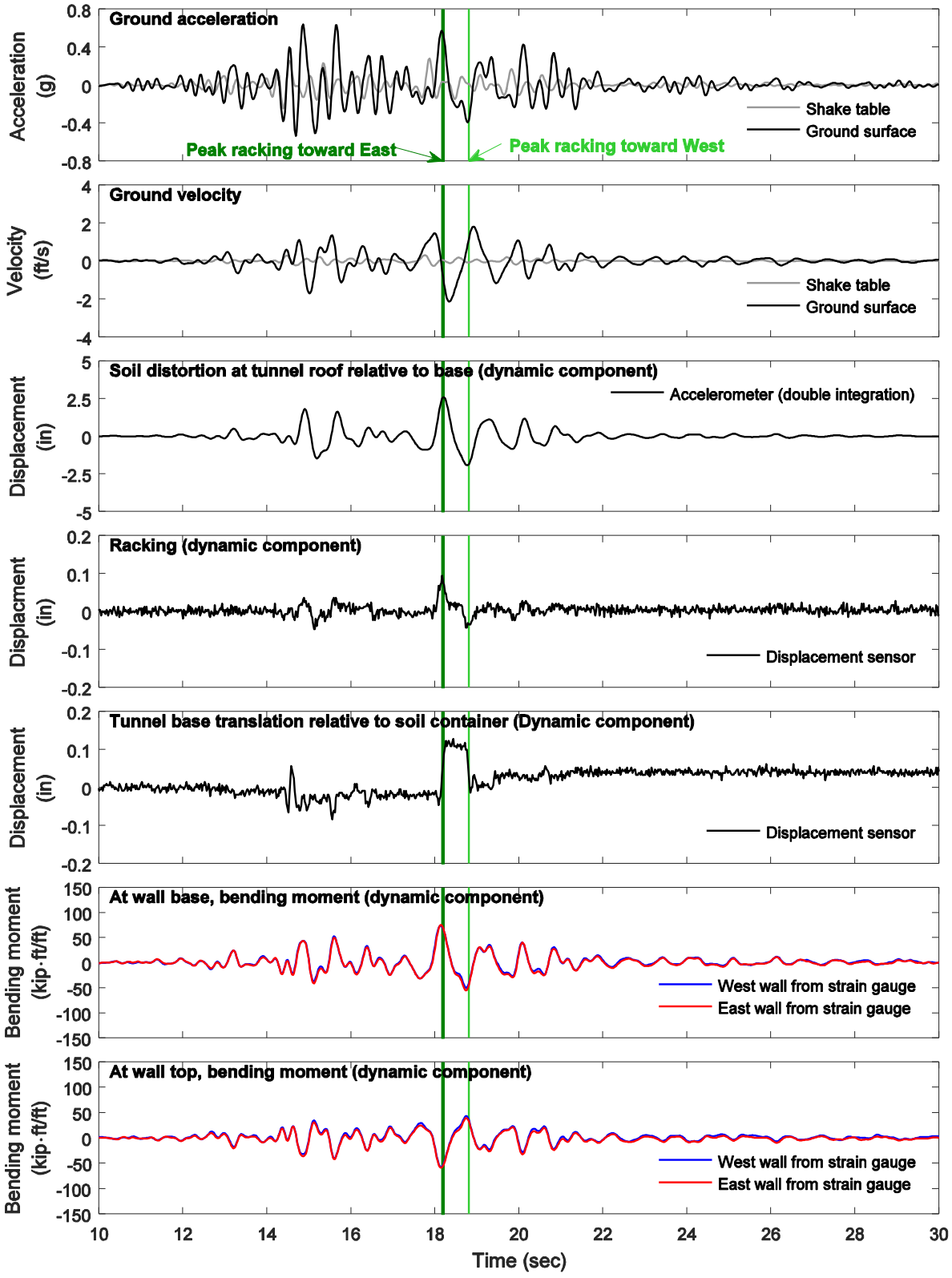

Figure 5–3: Model 2 response time histories for Nor100PT2 in prototype scale (without overburden soil)

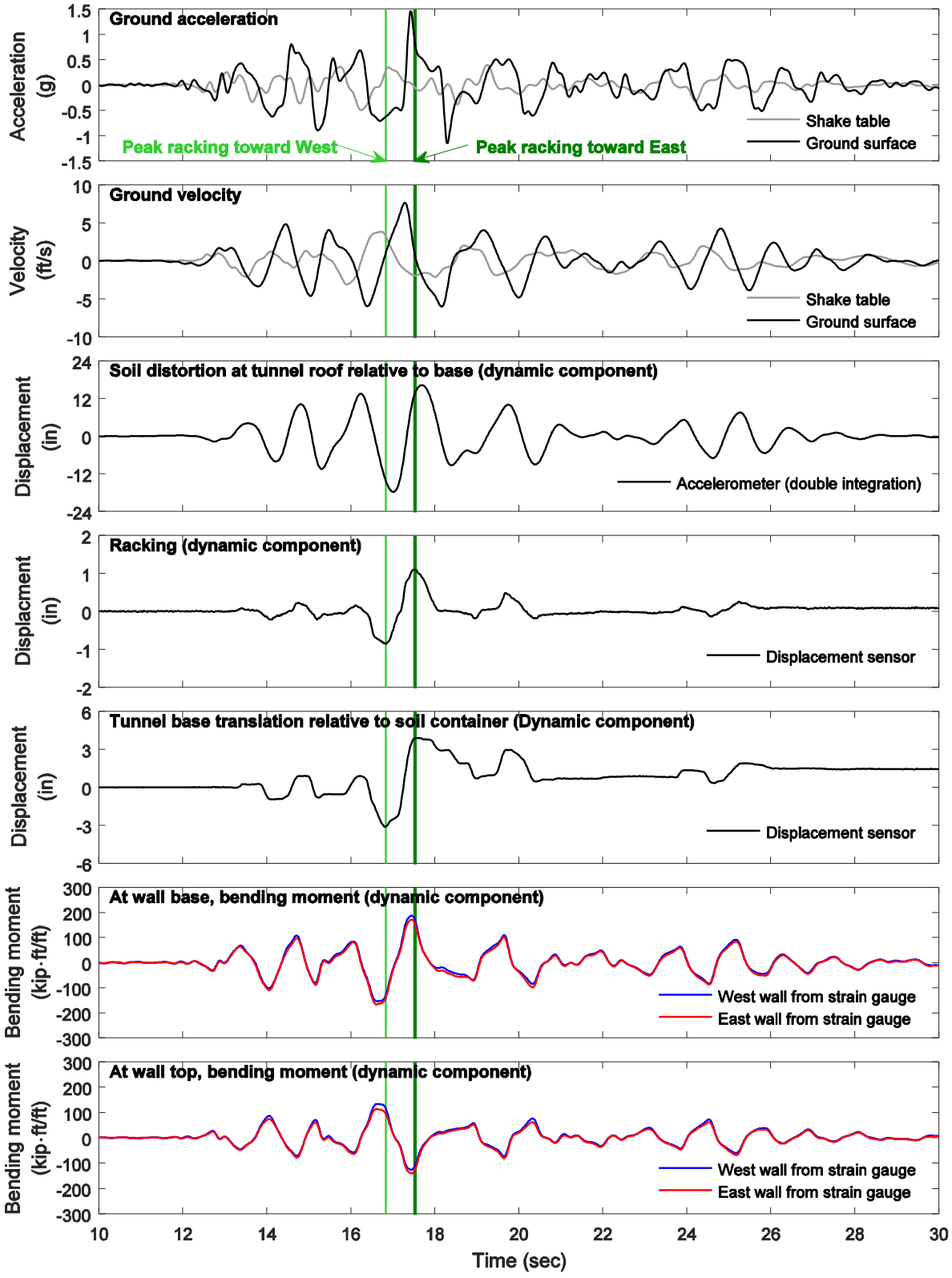

Figure 5–4: Model 2 response time histories for Tak100PT2 in prototype scale (without overburden soil)

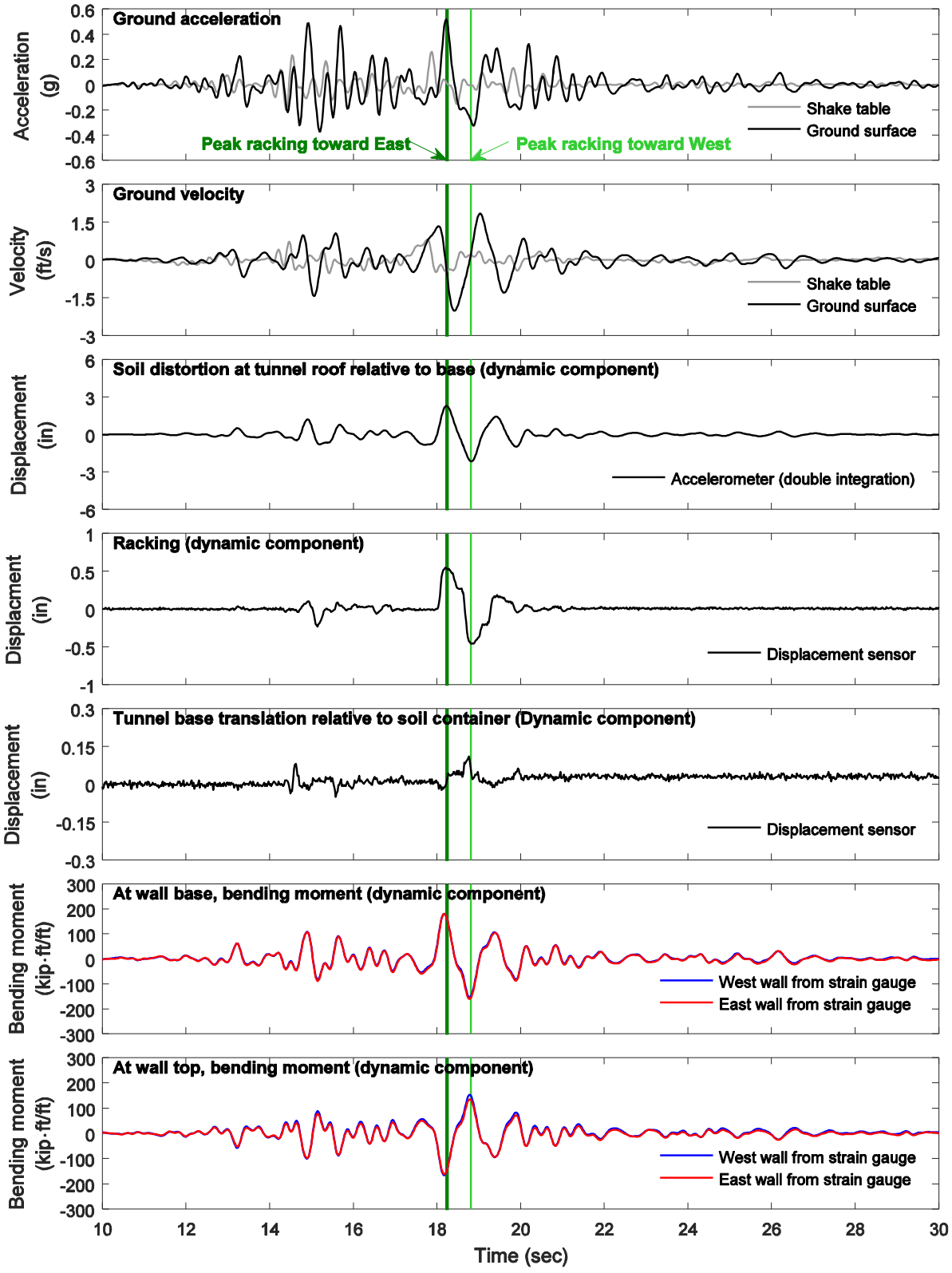

Figure 5–5: Model 3 response time histories for Nor100PT2 in prototype scale (9 ft overburden soil)

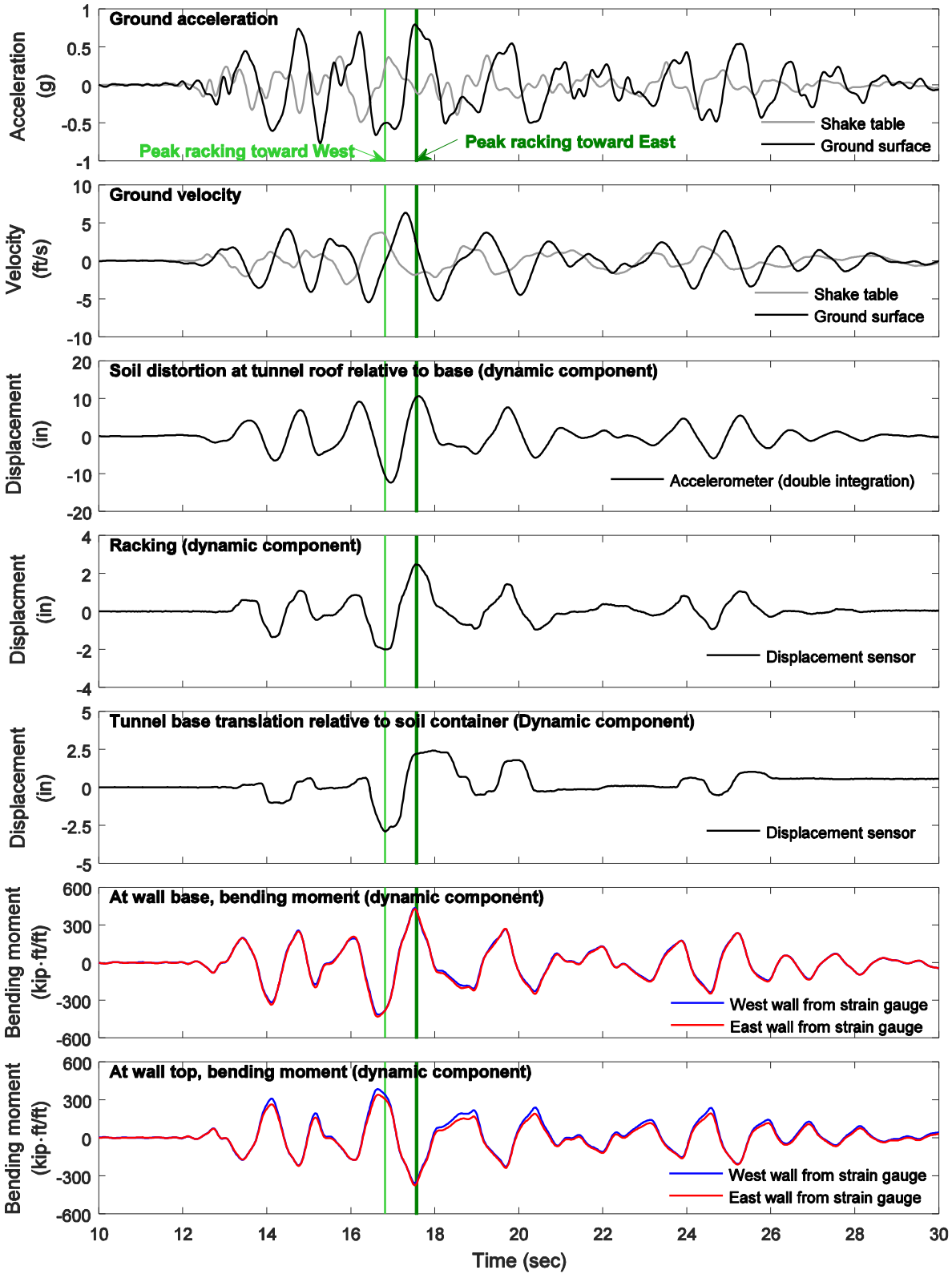

Figure 5–6: Model 3 response time histories for Tak100PT2 in prototype scale (9 ft overburden soil)

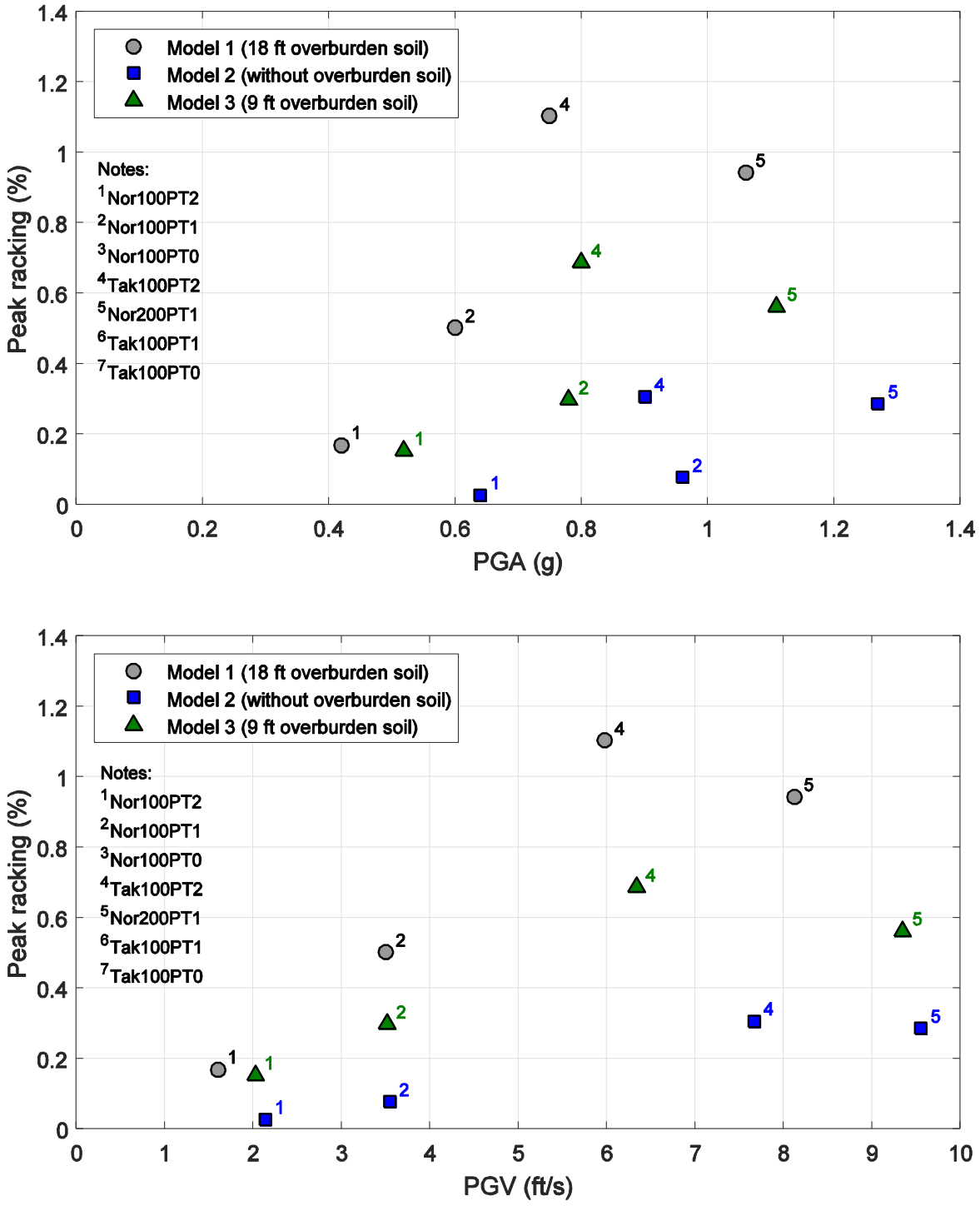

Figure 5–7: Relationship of peak racking with peak ground acceleration (top) and peak ground velocity (bottom) in prototype scale

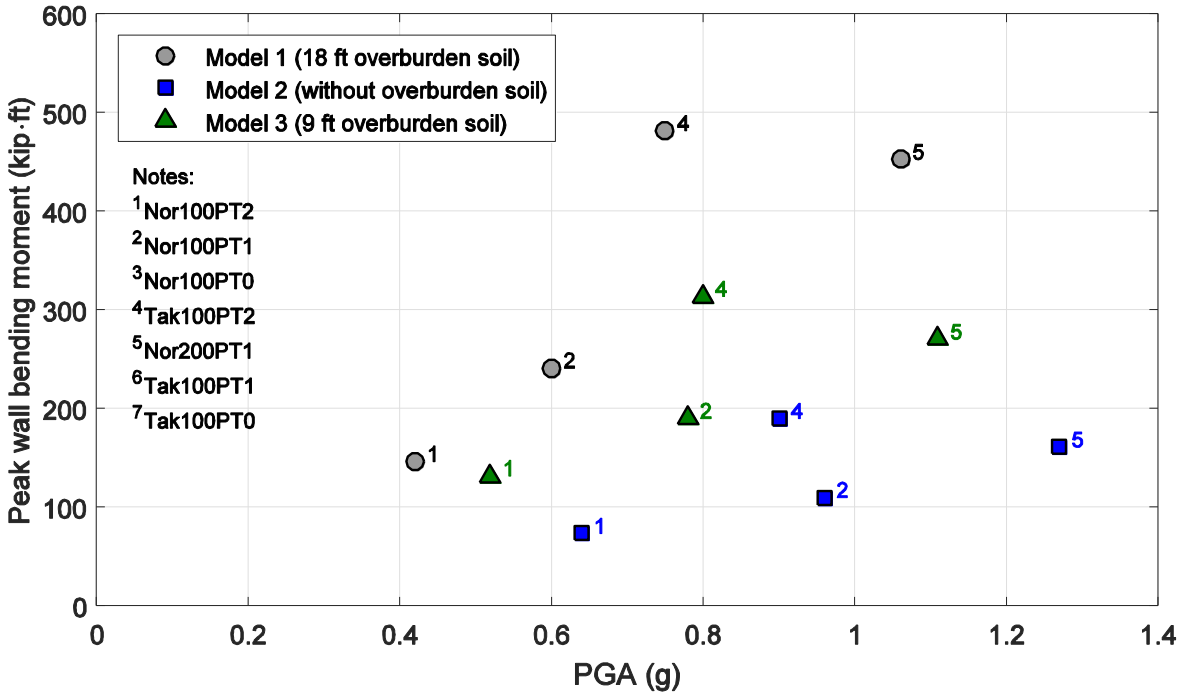

Figure 5–8: Relationship of peak dynamic wall bending moment with peak ground acceleration in prototype scale

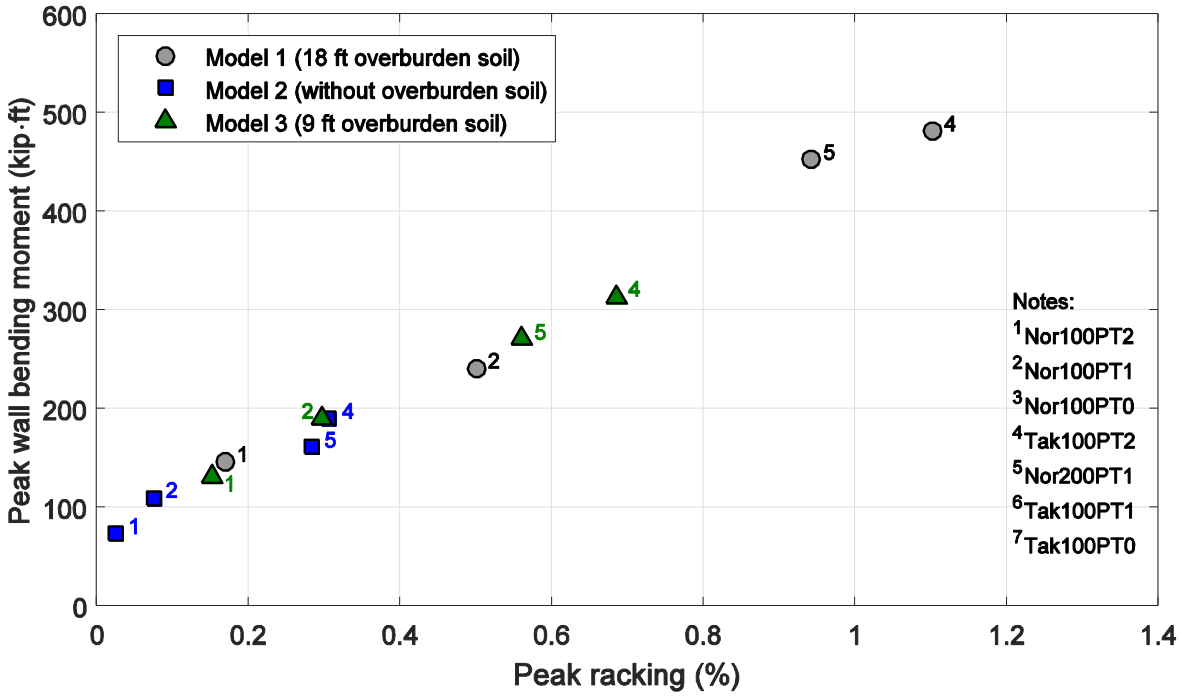

Figure 5–9: Relationship between the peak racking and the peak wall bending moment in prototype scale

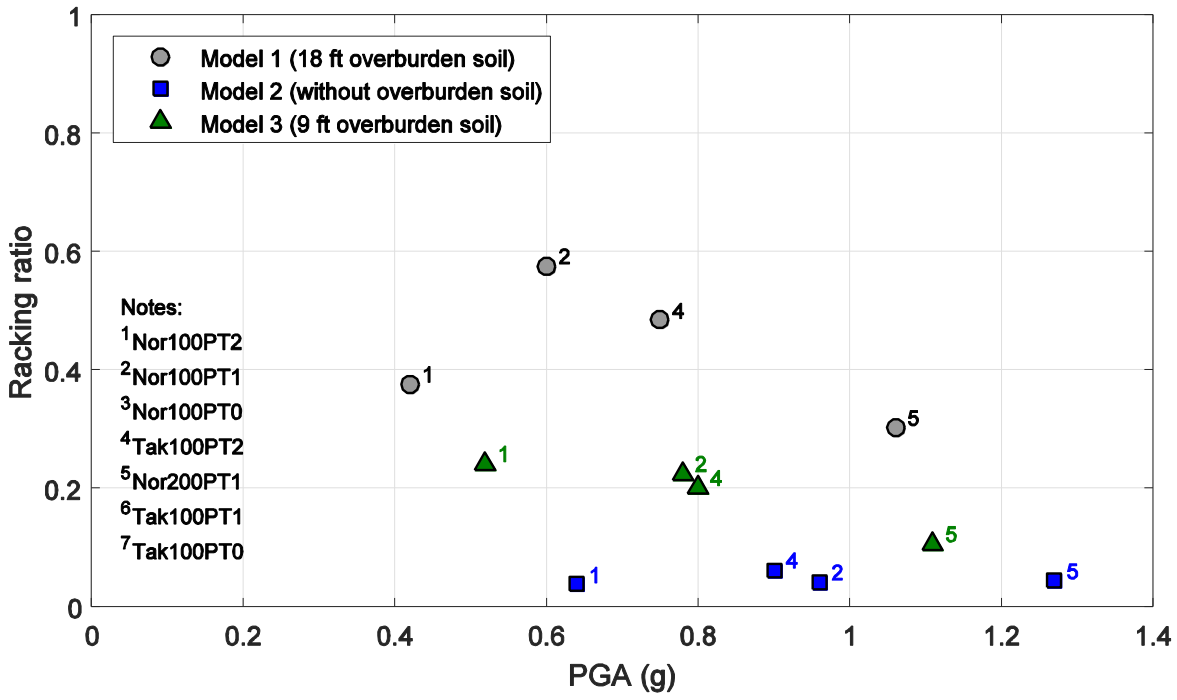

Figure 5–10: Relationship of racking ratio with peak ground in prototype scale

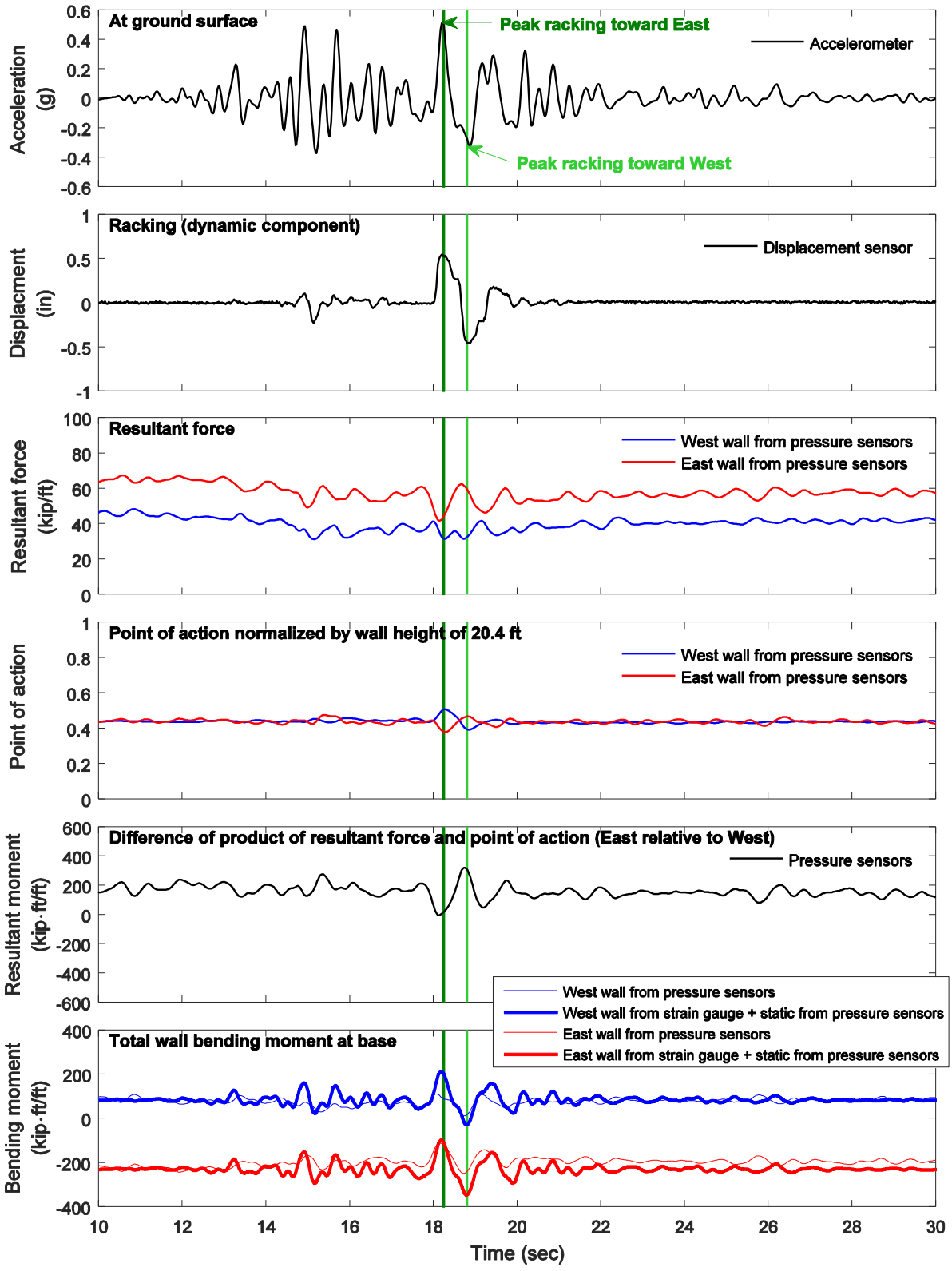

Figure 5–11: Model 3 resultant earth pressure force, point of action, and total wall bending moment at wall base for Nor100PT2 in prototype scale (9 ft overburden soil)

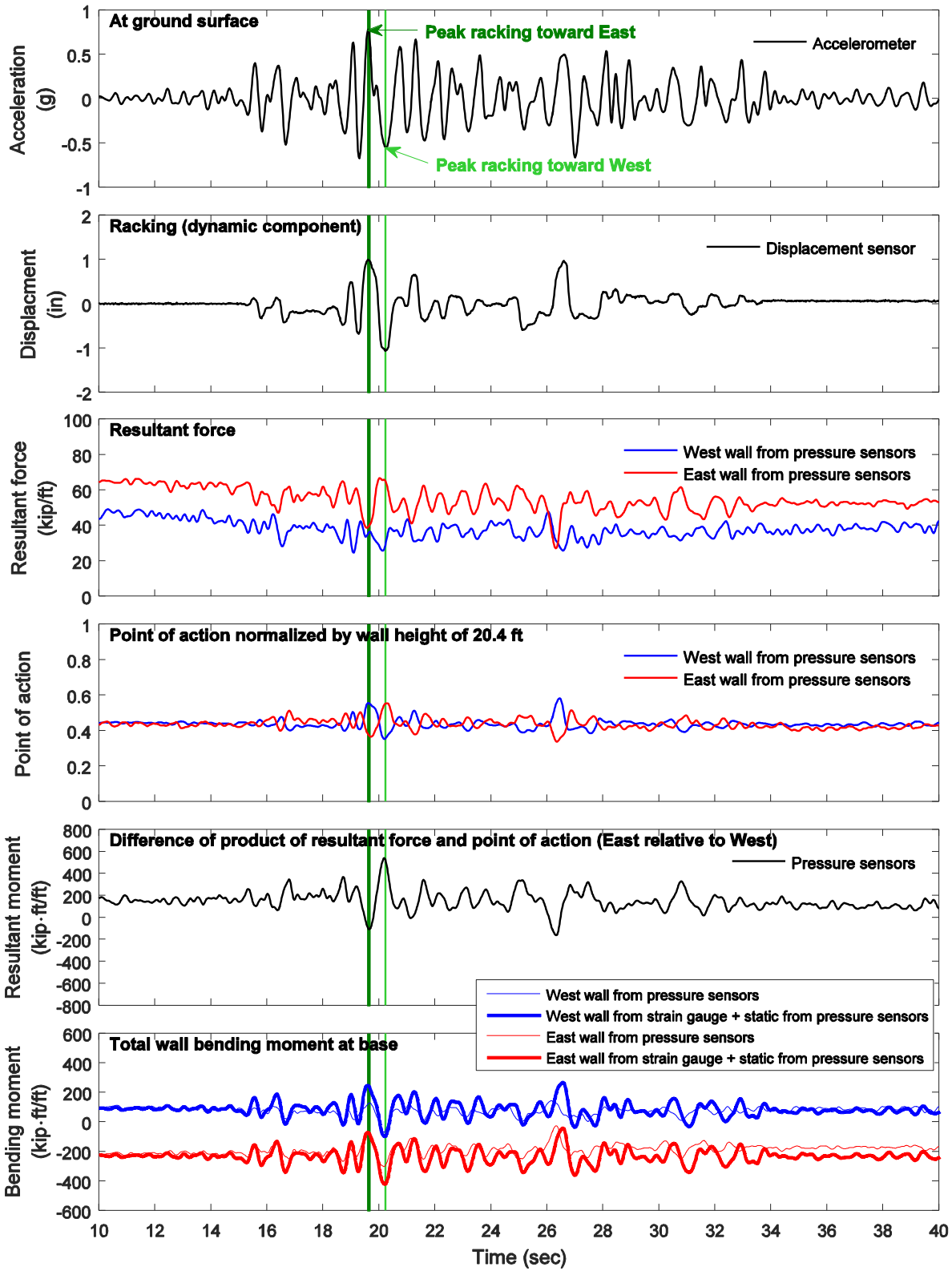

Figure 5–12: Model 3 resultant earth pressure force, point of action, and total wall bending moment at wall base for Nor100PT1 in prototype scale (9 ft overburden soil)

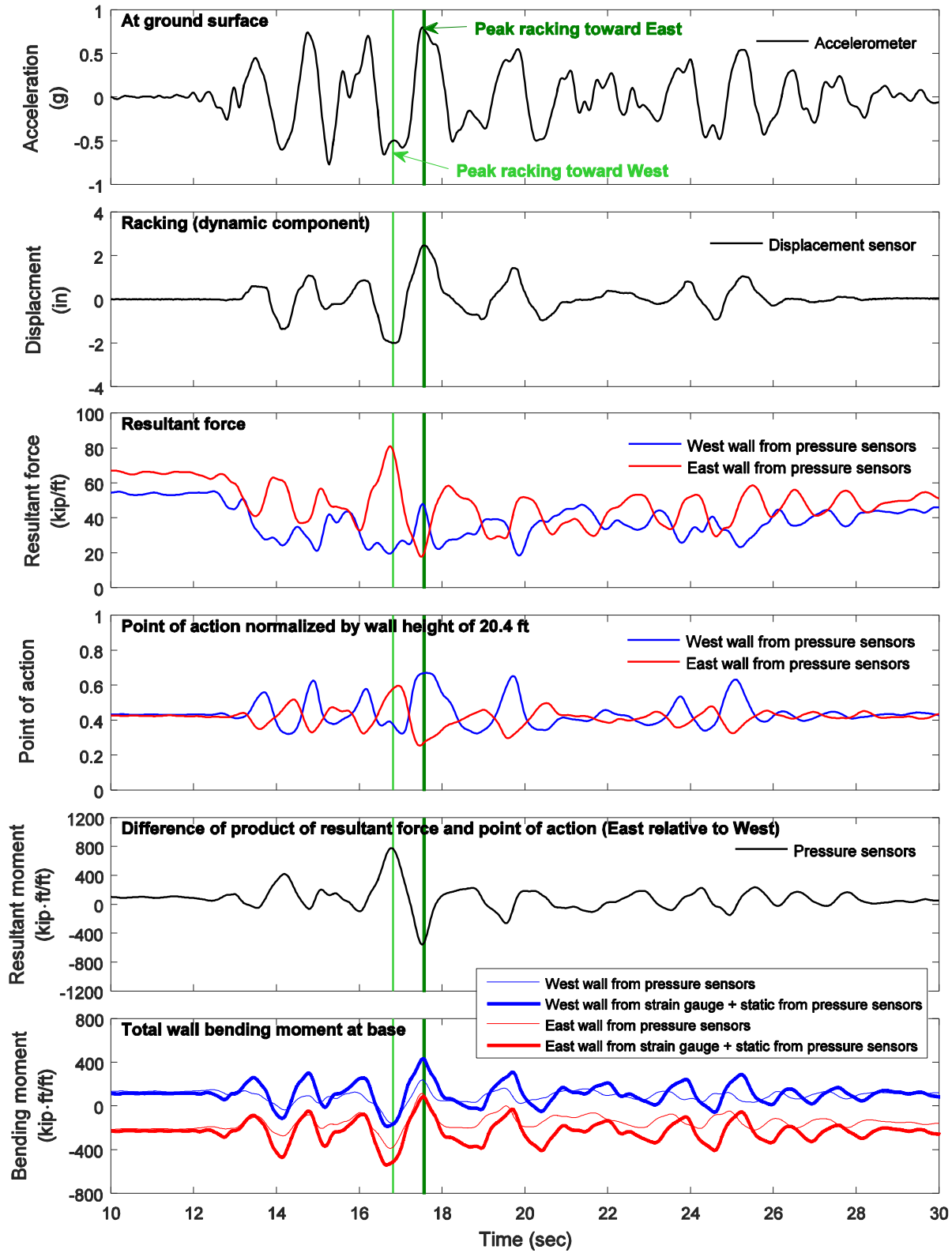

Figure 5–13: Model 3 resultant earth pressure force, point of action, and total wall bending moment at wall base for Tak100PT2 in prototype scale (9 ft overburden soil)

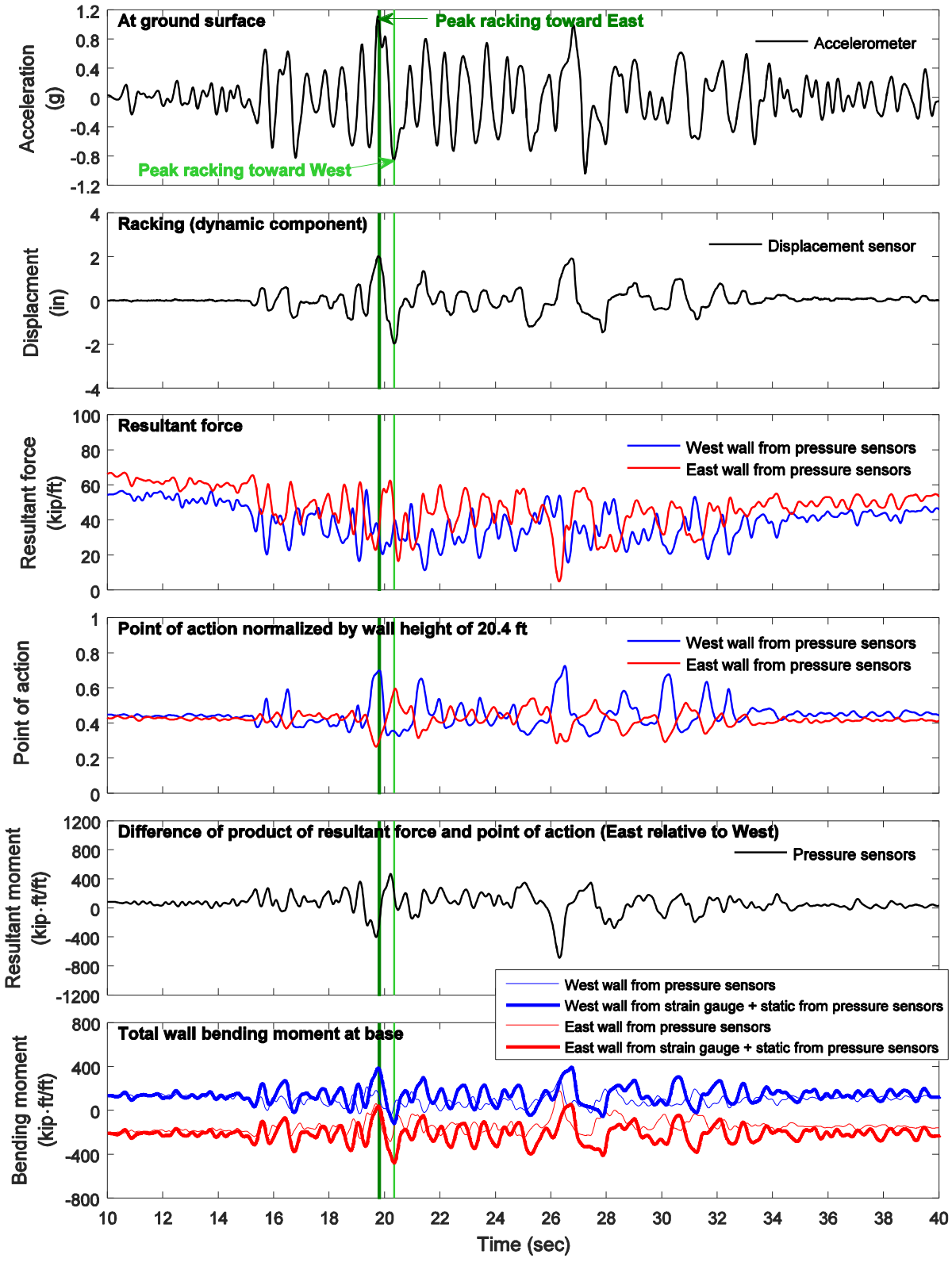

Figure 5–14: Model 3 resultant earth pressure force, point of action, and total wall bending moment at wall base for Nor200PT1 in prototype scale (9 ft overburden soil)

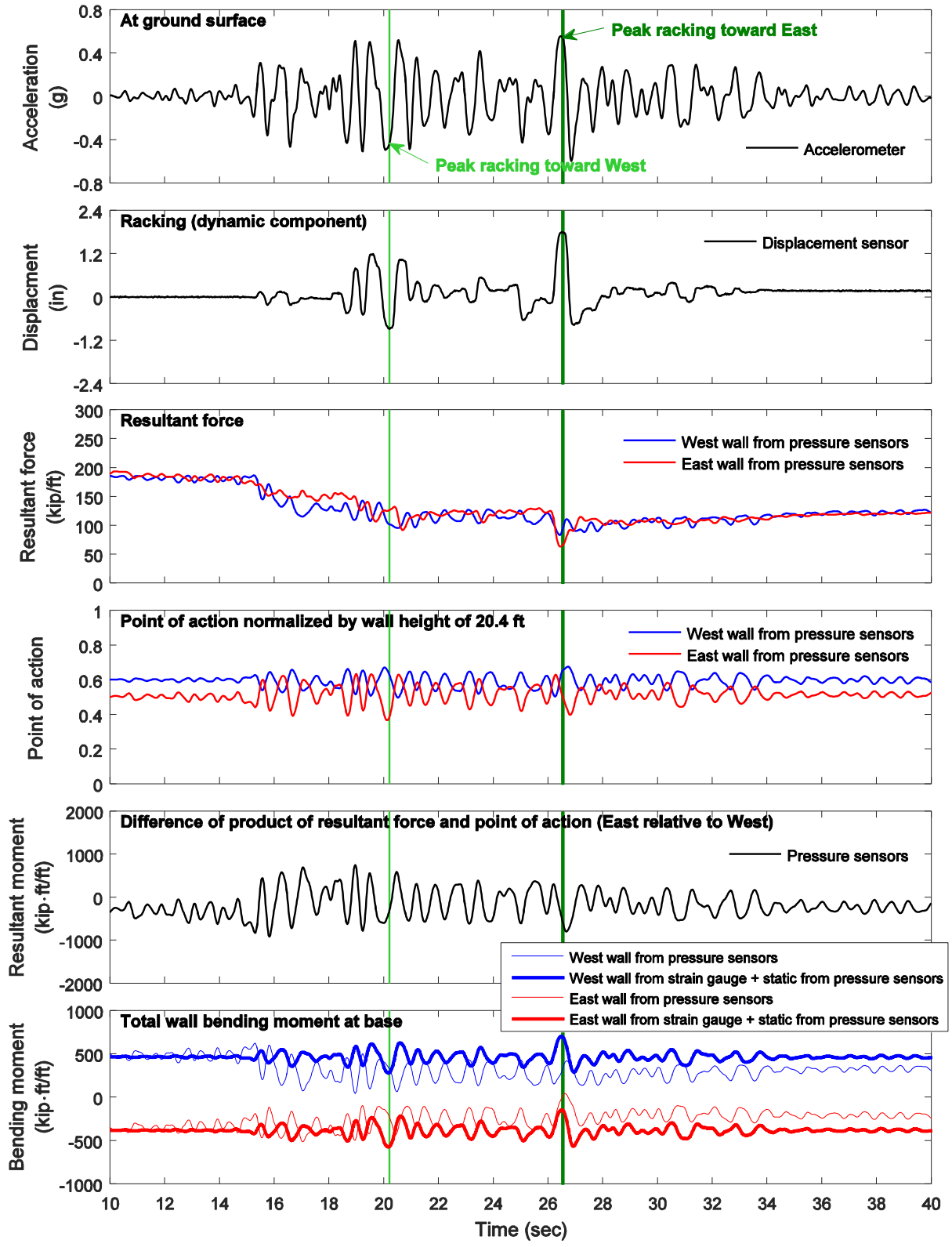

Figure 5–15: Model 1 resultant earth pressure force, point of action, and total wall bending moment at wall base for Nor100PT1 in prototype scale (18 ft overburden soil)

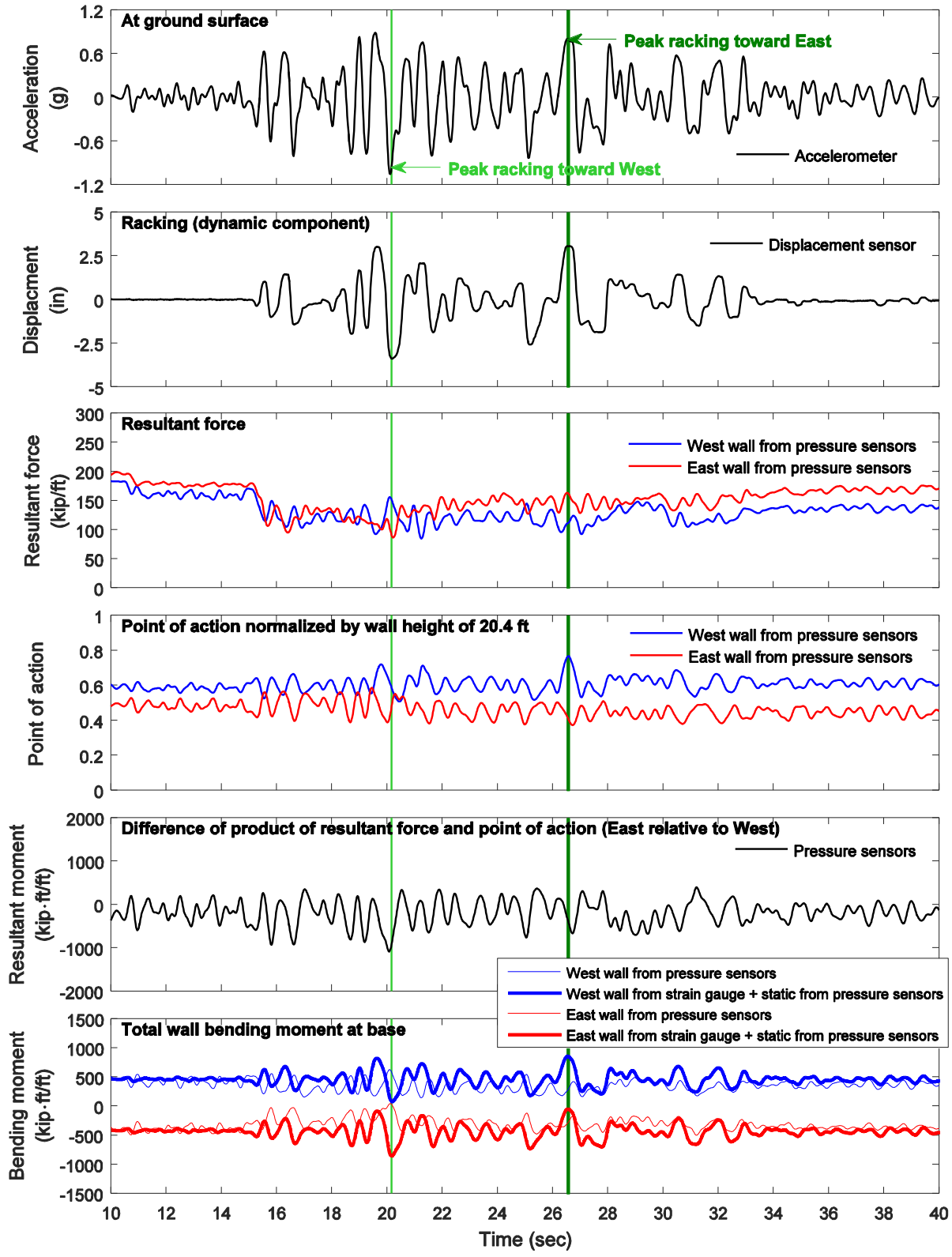

Figure 5–16: Model 1 resultant earth pressure force, point of action, and total wall bending moment at wall base for Nor200PT1 in prototype scale (18 ft overburden soil)

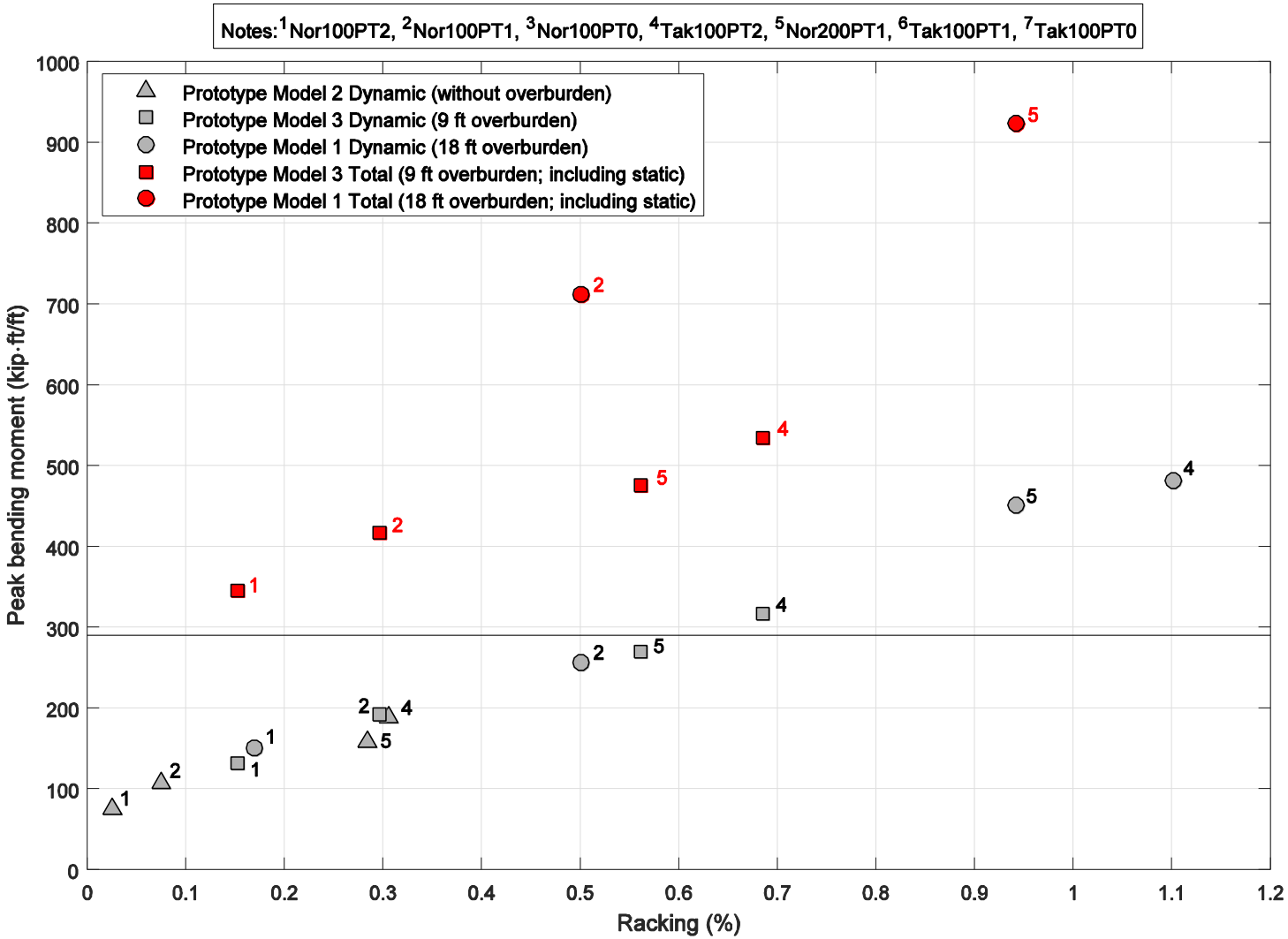

Figure 5–17: Relationship between the peak racking and the peak total wall bending moment for which the dynamic component from the strain gauge and the static value from the pressure sensors (associated resultant force and point of action)

6. FHWA Racking and Bending Moment Estimation

6.1. FHWA step-by-step procedure

This section presents dynamic (seismic) racking and bending moment estimated using the FHWA step-by-step procedure (FHWA 2009). Table 6–1 summarizes the FHWA step-by-step procedure. In this procedure, PGA is used as a main design parameter to derive earthquake-induced shear stress (τ_{max}) at depth of the tunnel base. At this τ_{max}, the resulting shear strain is computed using an average strain-compatible shear modulus (G_m) in the surrounding soil. Once the G_m is obtained, racking is computed using relative stiffness of the tunnel and the surrounding soil (known as flexibility ratio, F_r) as well as racking coefficient (or racking ratio, R_r) according to Wang (1993). To estimate G_m, the EPRI shear modulus reduction curves (EPRI 1993) were used in this study.

6.2. Ground Design Parameters in Model Scale

For use of the FHWA procedure in this study, the tunnel backfill soil was assumed to be compacted at no less than 95% relative compaction according to Caltrans Standard Specification (Caltrans 2015). Earth Mechanics, Inc (EMI 2005) performed an intensive field investigation and characterization of abutment backfill at wide bridges sites in California. EMI (2005) summarized the Standard Penetration Test blow count (N) recorded on the boring logs at a depth of 5 ft with N ranging from 10 to 90, depending on the investigated soil types. In our study, the standard penetration number corrected for field condition (N_{60}) was used rather than N. However, all the correction factors such as hammer efficiency, borehole diameter, and so forth were considered as 1.0 for simplicity (i.e., $N_{60} = N_{SPT}$). Within the range of the N presented in EMI (2005), the backfill properties for the FHWA procedure were determined using N_{60} of 42. As summarized in Table 6–2, N_{60} was used to determine shear wave velocity (converted to low-strain shear modulus) at mid-depth of the tunnel. Furthermore, $(N_1)_{60}$ corrected for overburden pressure was used to determine shear strength (S_u) at 3% shear strain (Table 6-2).

For the design PGA in the FHWA procedure, a range of PGA from 0 to 1.4g was taken into consideration, encompassing recorded PGA from the shake table tests. Three different depths of the tunnel were used as in the test configurations (i.e. depth of overburden soil with 0, 1 and 2 ft in model scale).

To determine F_r and G_m in the FHWA procedure, one of the EPRI shear modulus reduction curves (for depth of 50 ft to 120 ft as shown in Figure 6–1a) was used along with low-strain shear modulus (G_{max}) of 6,730 psi based on N_{60} of 42 (Table 6–2) at the mid-depth of the tunnel wall. This curve was selected because the shear stress at relatively high level of shear strain (3% shear strain in this study) should to be greater than τ_{max} computed from the measured PGA during the test (Table 6–1). S_u was determined using a cohesion (c) of 8.5 psi and a friction angle of 52 degrees (Table 6-2), instead of c of 2 psi measured from the triaxial test as presented earlier in Section 2.3.2. As N_{60} of 42 was used, the measured c of 2 psi still provided a margin of the S_u that was higher than the FHWA τ_{max}. However, as presented in EMI (2005), a wide range of N_{60} represented possible backfill material compacted at D_r of 95% at the depth of our interest. As a lower value of N_{60} was considered, the corresponding S_u at 3% shear strain became lower than the FHWA τ_{max} resulting from a design PGA higher than 0.8g. Thus, the FHWA procedure could not be used to estimate racking. In this regard, the higher c of 8.5 psi allowed systematic application of soil properties in the FHWA procedure, associated with the wide range of studied N_{60} to determine low-strain shear modulus. Further discussion of this range will be presented later.

6.3. Comparison of FHWA estimate to Test Result in Model Scale

6.3.1. Racking

Using the employed soil material properties (Table 6–2), the racking and wall bending moment at base were computed using the FHWA procedure (see the case of N_{60} = 42 in Table 6–3). Compared to the test result, the following observation are drawn:

- Model 1: overburden soil depth of 2 ft
  - The FHWA racking generally agreed with the test results.
- Model 2: without overburden soil
  - The FHWA racking was significantly higher than the test results in all cases (as much as seven times on average).
- Model 3: overburden soil depth of 1 ft
  - The FHWA racking was generally higher than the test result (as much as twice on average)

6.3.2. Sensitivity of backfill material properties in the FHWA procedure

It was found that appropriate selection of the backfill material properties is critical in the FHWA procedure. As such, to further extend this study, the backfill material properties was varied within a range of N_{60} from 25 to 60 (associated shear wave velocity from 456 ft/s to 550 ft/s at depth of 3.3 ft). As presented in EMI (2005), this variation of N_{60} represented possible backfill material compacted at D_r of 95% at the depth of interest in our study. The design PGAs also varied in the range from 0.2g to 1.4g. The resulting racking and wall bending moment in the FHWA procedure are shown in Figure 6–2 through Figure 6–4 for thickness of overburden soil of 2 ft (Model 1), 0 ft (Model 2), and 1 ft (Model 3), respectively. Among these results, the FHWA estimates using backfill based on N_{60} of 25 and 60 are also summarized in Table 6–3 as lower and upper bounds, along with those from N_{60} of 42 as shown earlier. From these plots, the following observation was drawn:

- As the design PGA increased (higher than about 0.6g and the resulting shear strain larger than about 0.1%), the FHWA racking and bending moment significantly varied with the change of the backfill material properties.
- Model 1 with 2 ft overburden soil
  - The test results generally agreed with the range of FHWA racking estimates
  - As stiffness of the backfill material increased (towards N_{60} of 60), the FHWA racking tended to be underestimated in comparison to the test results.
- Model 2 without overburden soil
  - The FHWA procedure overestimated racking.
  - As stiffness of the backfill material increased (towards N_{60} of 60), the degree of the overestimation from the FHWA procedure decreased.
  - It was noted that the backfill behind the tunnel wall in the test model was compacted at D_r of 85%. As such, the test result was associated with a relatively compliant soil (less than N_{60} of 25). In this case, the degree of overestimation further increased.
- Model 3 with 1ft overburden soil depth
  - The FHWA racking was higher than the test result under relatively weak-moderate earthquake excitations (PGA less than 0.6g).

- The FHWA racking was close to the test results under relatively strong earthquake excitation (PGA higher than 0.6 g), except for the cases where the PGA exceeded 1g.
- Similar to Model 2, the backfill was compacted at D_r of 85% in the test model. If the relatively soft material was included in the FHWA procedure (N_{60} less than 25), the FHWA overestimation was noticeable in all the cases studied.

6.3.3. Discussion of wall bending moment

Although the racking estimates from the FHWA procedure (using N_{60} of 42; the average value to represent backfill with 95% relative compaction) was higher than the test result, the FHWA bending moment estimates were relatively lower as shown in Figure 6–2 through Figure 6–4. In the FHWA procedure, the bending moment was computed by imposing the FHWA racking in an additional frame analysis under two different pseudo-static lateral force conditions (Figure 6–5). Under the pseudo-triangular pressure distribution along both walls (Figure 6–5b), higher bending moment was obtained in this study.

As discussed earlier in Section 4, the lateral earth pressure distribution was asymmetric on both sides of the tunnel with the following deformation mechanisms:

1. 1 ft overburden soil (D_r of 85%),
   - The high primary (or governing) resultant force and point of action were high.
   - On the other side of the tunnel, the corresponding resultant force and point of action were low (this was the main contribution).
2. 2 ft overburden soil (D_r of 99%),
   - The governing resultant force was low but associated point of action was high.
   - The other resultant force was high but associated point of action was low.
   - Upward and downward shift of point of action of the resultant forces was a main reason for the tunnel deformation rather than the increase of the resultant force.

As such, the above aspects may be worth taking into consideration when developing a simplified procedure, depending on the thickness of overburden soil (or burial depth of tunnel).

6.4. Comparison of FHWA estimates to Test Results in Prototype Scale

The FHWA procedure was used to estimate racking and wall bending moments for the prototype structure (scaled by a geometric scaling factor of 9). It is noted that the two input motions of Nor100PT2 and Tak100PT2 were appropriately scaled to represent earthquake frequency

content for the prototype scale (the time duration was compressed by a factor of 5.2). As conducted for the model scale, identical material properties for tunnel backfill were used (Table 6–2). For depth of the tunnel in prototype scale, τ_{max} derived from the design PGA appeared to be higher than the shear stress using the EPRI shear modulus reduction curve for depth from 250 ft to 500 ft. As such, this EPRI curve was modified to increase shear strength at shear strain of 3% as shown in Figure 6–6. This modification was performed using the pseudo-reference strain hyperbolic (PRHS) model (Gingery and Elgamal 2013).

Table 6–4 summarizes the racking and wall bending moment computed using the FHWA procedure, along with the test results in prototype scale for comparison. As mentioned earlier in Section 6.2, the backfill material properties varied with N_{60} from 25 to 60. The corresponding FHWA estimates are shown in Figure 6–7 through Figure 6–9, for different thickness of overburden soil such as 18 ft (Model 1), 0 ft (Model 2), and 9 ft (Model 3), respectively. In general, very similar observations to the model scale scenario are noted.

6.5. Summary

Racking and wall bending moment were computed using the FHWA procedure and compared to the test results in model and prototype scale. To represent the actual backfill condition at a tunnel site, standard penetration blow count corrected for field conditions (N_{60} of 42) was considered. It appeared that the FHWA procedure was sensitive to the employed backfill material properties. As such, a wide range of backfill material properties (representing the backfill compacted at 95% relative density) was taken into consideration. It was difficult to find a trend in the FHWA estimates in the light of over-/under-estimation for seismic racking and bending moment. However, the following observations could be drawn and may be considered towards improvements in the current procedure:

- As the earthquake intensity increased (PGA higher than about 0.6g), the FHWA procedure tended to be relatively sensitive to the backfill material properties. This sensitivity resulted from a wide variation in shear strain in the surrounding soil between the top and bottom elevation of the tunnel. As such, the FHWA procedure should be applied with caution for strong earthquake shaking scenarios.

- For the relatively deep tunnel scenario in this study, the FHWA procedure predicted to some extent adequate degree of racking compared to the test result. As the tunnel was placed at relatively shallower depths, conservatism of the FHWA was noticeable.
- In the FHWA procedure, the wall bending moment was essentially dictated by the resulting racking (linear-elastic model). The application of the recommended pseudo-static lateral force model in the FHWA procedure produced conservatism in racking and even more so in estimating bending moment. As observed in the tests, the loading mechanism in terms of asymmetric resultant force and different location of the associated point of action on both sides of the tunnel may be worth considering in an updated simplified procedure. For this purpose, further analysis shall be needed to quantify seismic loading distribution under various conditions of the backfill materials, burial depth, earthquake characteristics, and so forth.

Table 6–1: Summary of FHWA (2009) step-by-step procedure for racking analysis of rectangular tunnels

Step 1	Estimate the free-field ground strains γ_m (along the tunnel height); determine free-field relative displacement ($\Delta_{free\text{-}field}$) corresponding to the top and the bottom elevation of the tunnel i) On the basis of *PGA*- $\Delta_{free\text{-}field} = H\,\gamma_m$, where $\gamma_m = \tau_m / G_m$, $\tau_m = (PGA/g)\sigma_v R_d$, $\sigma_v = \gamma_t$ (h+H)
Step 2	Determine the racking stiffness (K_s) of the box structure from a structural frame analysis
Step 3	Determine the flexibility ratio $F_r = (G_m/K_s)$ (W/H)
Step 4	Determine the racking coefficient, R_r $R_r = \frac{4(1-\nu_m)F_r}{3-4\nu_m+F_r}$ for no-slip interface condition $= \frac{4(1-\nu_m)F_r}{2.5-3\nu_m+F_r}$ for full-slip interface condition
Step 5	Determine the racking deformation of the tunnel, $\Delta_s = R_r\,\Delta_{free\text{-}field}$
Step 6	Obtain the seismic demand in terms of internal forces (and material strains) by imposing Δ_s in a frame analysis

*H = Height of the box structure
W = Width of the box structure
G_m = Effective strain-compatible shear modulus of ground surrounding tunnel
ν_m = Poisson's ratio of the surrounding soil (in our study, ν_m of 0.4 was used)
τ_{max} = Maximum earthquake-induced shear stress (ksf)
σ_v = Total vertical soil overburden pressure at invert elevation of tunnel (ksf)
γ_t = Total soil unit weight (kcf)
h = Soil cover thickness measured from ground surface to tunnel crown (ft)
R_d = Depth dependent stress reduction factor; Rd = 1.174 – 0.00814z for 30 ft < z < 75 ft, z = depth (ft) from ground surface to the invert elevation of the tunnel and is represented by z = (h+H)

Table 6–2: FHWA design parameters for tunnel located at depth of 5.3 ft

Design Parameter	Value
Site Class[1]	D
N_{60}	42
Depth of middle of tunnel wall	3.67 ft
Unit weight, γ	120 pcf
Shear wave velocity, V_s[2]	510 ft/s (155 m/s)
Low-shear modulus, G_{max}[3]	6730 psi
Friction angle, ϕ[4]	52 degrees
Shear strength, S_u[5]	10 psi

[1]Caltrans/NEHRP soil profile type based on SPT N-value

[2]$V_s = 30\ N_{60}^{0.23}\ \sigma_v^{0.23}$ (Wair et al. 2012) where $\sigma_v = \gamma z$ in kPa and z = depth of middle of tunnel wall.

[3]$G_{max} = V_s^2 \rho$ where ρ is soil density = γ/g

[4]$\phi = (15.4\ (N_1)_{60})^{0.5} + 20$ where $(N_1)_{60}$ = corrected N value to a standard value of σ_o (13.9 psi), $(N_1)_{60} = C_N N_{60}$ and $C_N = 2/(1+\sigma_v')$ in normally consolidated sands for fine sands of medium density where σ_v' = effective overburden pressure in ton/ft^2 or kg/cm^2 or kPa/100 (Skempton 1986). In this study, $C_N = 1.65$ and $\sigma_v' = 21$ kPa (3.1 psi)

[5]$S_u = c + \sigma_m \sin(\phi)$ where c is cohesion (c = 8.5 psi) and σ_m is confining stress at depth of middle of tunnel wall ($\sigma_m = 2.1$ psi); $\sigma_m = (\sigma_v + 2\sigma_h)/3$ where σ_v = vertical stress and σ_h = horizontal stress, $K_o\sigma_v$, $K_o = \nu/(1-\nu)$, ν = Poisson's ratio (0.35 in this study);

Table 6–3: Racking and wall bending moment estimated using FHWA step-by-step procedure (FHWA 2009) as well as the test results in model scale

Model[1]	Shaking	EQ	PGA (g)	FHWA[2] (2009)												Test (model scale)	
				N_{60} = 42				N_{60} = 25				N_{60} = 60				Racking (%)	Moment[3] (kip·ft)
				Racking		Moment[3]		Racking		Moment[3]		Racking		Moment[3]			
				Drift (%)	Ratio[4]	kip·ft	Ratio[4]	Drift (%)	Ratio[4]	kip·ft	Ratio[4]	Drift (%)	Ratio[4]	kip·ft	Ratio[4]		
1	1	Nor100PT1	0.60	0.17	0.94	0.47	1.44	0.22	1.27	0.64	1.94	0.13	0.76	0.38	1.16	0.18	0.33
	2	Nor200PT1	1.06	0.50	1.55	1.44	2.38	0.77	2.37	2.20	3.65	0.36	1.09	1.02	1.68	0.33	0.60
	3	Nor100PT0	0.90	0.33	0.83	0.95	1.44	0.53	1.32	1.51	2.28	0.26	0.65	0.75	1.13	0.40	0.66
	4	Tak100PT1	0.88	0.32	0.67	0.91	1.15	0.50	1.05	1.43	1.81	0.25	0.53	0.72	0.91	0.48	0.79
	5	Tak100PT0	0.79	0.26	0.70	0.75	0.96	0.38	1.03	1.10	1.41	0.20	0.55	0.59	0.75	0.38	0.78
	6	Nor100PT2	0.42	0.10	1.93	0.28	1.39	0.13	2.53	0.36	1.83	0.08	1.60	0.23	1.16	0.05	0.20
	7	Tak100PT2	0.75	0.24	0.64	0.68	1.03	0.33	0.89	0.95	1.44	0.19	0.51	0.54	0.82	0.38	0.66
	Average of ratios				**1.04**		**1.40**		**1.49**		**2.05**		**0.81**		**1.09**		
2	1	Nor100PT2	0.64	0.15	17.51	0.44	4.25	0.20	22.81	0.57	5.54	0.13	14.55	0.36	3.53	0.01	0.10
	2	Nor100PT1	0.96	0.30	11.84	0.85	6.02	0.45	17.67	1.28	8.99	0.24	9.59	0.69	4.88	0.03	0.14
	3	Nor100PT0	1.19	0.50	4.67	1.44	5.70	0.65	6.07	1.87	7.40	0.38	3.50	1.08	4.27	0.11	0.25
	4	Tak100PT2	0.90	0.27	2.62	0.77	3.26	0.39	3.79	1.11	4.71	0.22	2.14	0.62	2.65	0.10	0.24
	5	Nor200PT1	1.27	0.58	6.12	1.66	7.68	0.72	7.56	2.05	9.48	0.44	4.63	1.25	5.80	0.09	0.22
	6	Tak100PT1	0.82	0.23	2.81	0.65	2.66	0.32	3.91	0.90	3.71	0.18	2.28	0.53	2.16	0.08	0.24
	7	Tak100PT0	0.92	0.28	3.66	0.79	3.35	0.40	5.32	1.16	4.88	0.23	2.97	0.65	2.73	0.08	0.24
	Average of ratios				**7.03**		**4.70**		**9.59**		**6.39**		**5.67**		**3.72**		
3	1	Nor100PT2	0.52	0.12	2.37	0.34	1.91	0.16	3.13	0.45	2.52	0.10	1.98	0.29	1.60	0.05	0.18
	2	Nor100PT1	0.78	0.23	2.33	0.66	2.50	0.32	3.21	0.91	3.45	0.18	1.87	0.53	2.01	0.10	0.26
	3	Nor100PT0	1.04	0.41	1.77	1.19	2.70	0.63	2.66	1.79	4.07	0.31	1.30	0.88	2.00	0.23	0.44
	4	Tak100PT2	0.80	0.24	1.05	0.69	1.59	0.34	1.49	0.97	2.25	0.19	0.84	0.55	1.27	0.23	0.43
	5	Nor200PT1	1.11	0.49	2.60	1.39	3.76	0.71	3.77	2.02	5.46	0.35	1.85	0.99	2.68	0.19	0.37
	6	Tak100PT1	0.83	0.25	0.99	0.73	1.45	0.37	1.45	1.06	2.12	0.20	0.79	0.58	1.16	0.26	0.50
	7	Tak100PT0	0.80	0.24	1.08	0.69	1.46	0.34	1.53	0.97	2.07	0.19	0.86	0.55	1.17	0.22	0.47
	Average of ratios				**1.74**		**2.19**		**2.46**		**3.13**		**1.36**		**1.70**		

[1]Overburdent soil thickness, Model 1 = 2 ft, Model 2 = 0 ft, Mode 3 = 1 ft

[2]See Table 6–1 for FHWA step-by-step procedure

[3]Bending moment per unit wall length of 1 ft

[4]Ratio of FHWA estimates to the test result

Table 6–4: Racking and wall bending moment estimated using FHWA step-by-step procedure (FHWA 2009) as well as the test results in prototype scale

Model[1]	Shaking	EQ	PGA (g)	FHWA[2] (2009)												Test (prototype scale)	
				N_{60} = 42				N_{60} = 25				N_{60} = 60				Racking (%)	Moment[3] (kip·ft)
				Racking		Moment[3]		Racking		Moment[3]		Racking		Moment[3]			
				Drift (%)	Ratio[4]	kip·ft	Ratio[4]	Drift (%)	Ratio[4]	kip·ft	Ratio[4]	Drift (%)	Ratio[4]	kip·ft	Ratio[4]		
1	1	Nor100PT1	0.60	0.38	0.71	261	1.09	0.52	0.99	361	1.51	0.30	0.58	212	0.89	0.53	239
	2	Nor200PT1	1.06	1.12	1.15	779	1.77	1.52	1.57	1056	2.41	0.84	0.86	584	1.33	0.98	440
	3	Nor100PT0	0.90	0.78	0.65	544	1.13	1.15	0.96	798	1.66	0.61	0.50	421	0.87	1.20	483
	4	Tak100PT1	0.88	0.74	0.52	514	0.89	1.10	0.77	764	1.33	0.58	0.41	406	0.70	1.43	577
	5	Tak100PT0	0.79	0.61	0.54	420	0.74	0.88	0.78	613	1.08	0.48	0.43	335	0.59	1.13	568
	6	Nor100PT2	0.42	0.22	1.46	151	1.05	0.29	1.93	201	1.39	0.18	1.22	126	0.88	0.15	144
	7	Tak100PT2	0.75	0.56	0.49	386	0.80	0.79	0.71	551	1.15	0.44	0.39	302	0.63	1.13	480
	Average of ratios				**0.79**		**1.07**		**1.10**		**1.50**		**0.63**		**0.84**		
2	1	Nor100PT2	0.64	0.47	17.72	324	4.30	0.63	23.82	434	5.79	0.37	14.24	260	3.46	0.03	75
	2	Nor100PT1	0.96	0.99	13.13	689	6.68	1.25	16.48	865	8.38	0.79	10.36	545	5.27	0.08	104
	3	Nor100PT0	1.19	1.41	4.39	981	5.35	1.65	5.13	1149	6.25	1.20	3.73	831	4.54	0.32	184
	4	Tak100PT2	0.90	0.88	2.86	608	3.55	1.13	3.72	788	4.62	0.68	2.22	473	2.76	0.31	171
	5	Nor200PT1	1.27	1.55	5.47	1078	6.86	1.79	6.31	1250	7.92	1.33	4.72	927	5.92	0.28	157
	6	Tak100PT1	0.82	0.73	3.00	507	2.85	0.98	4.05	681	3.84	0.57	2.36	399	2.24	0.24	179
	7	Tak100PT0	0.92	0.91	4.02	635	3.68	1.17	5.15	813	4.72	0.72	3.14	497	2.88	0.23	173
	Average of ratios				**7.23**		**4.75**		**9.24**		**5.93**		**5.83**		**3.87**		
3	1	Nor100PT2	0.52	0.31	1.71	218	1.38	0.42	2.78	295	2.24	0.26	1.71	181	1.38	0.15	131
	2	Nor100PT1	0.78	0.62	1.69	433	1.81	0.89	3.02	620	3.24	0.50	1.69	348	1.81	0.30	192
	3	Nor100PT0	1.04	1.13	1.23	783	1.89	1.46	2.08	1016	3.19	0.87	1.23	603	1.89	0.70	320
	4	Tak100PT2	0.80	0.65	0.76	454	1.15	0.94	1.37	653	2.08	0.52	0.76	363	1.15	0.69	315
	5	Nor200PT1	1.11	1.27	1.77	883	2.56	1.61	2.87	1117	4.15	0.99	1.77	691	2.56	0.56	270
	6	Tak100PT1	0.83	0.70	0.72	483	1.05	1.01	1.31	701	1.92	0.56	0.72	387	1.05	0.77	366
	7	Tak100PT0	0.80	0.65	0.78	454	1.06	0.94	1.41	653	1.91	0.52	0.78	363	1.06	0.67	343
	Average of ratios				**1.24**		**1.56**		**2.12**		**2.67**		**1.24**		**1.56**		

[1]Overburdent soil thickness, Model 1 = 18 ft, Model 2 = 0 ft, Mode 3 = 9 ft

[2]See Table 6–1 for FHWA step-by-step procedure

[3]Bending moment per unit wall length of 1 ft

[4]Ratio of FHWA estimates to the test result

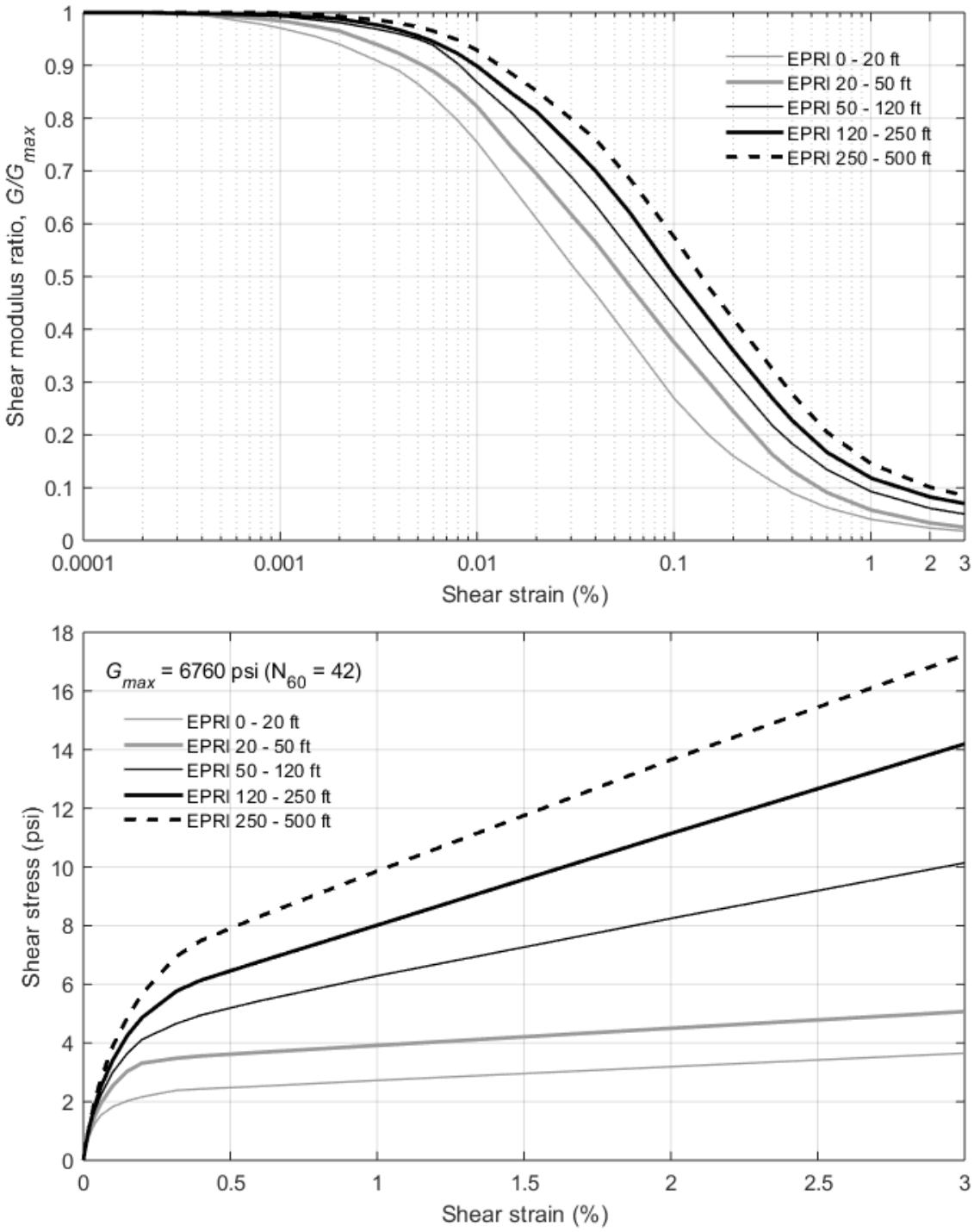

Figure 6–1: EPRI shear modulus reduction curves (above) and shear stress-strain relationship along with G_{max} of 6760 psi using N_{60} of 42 (below) for ground in model scale

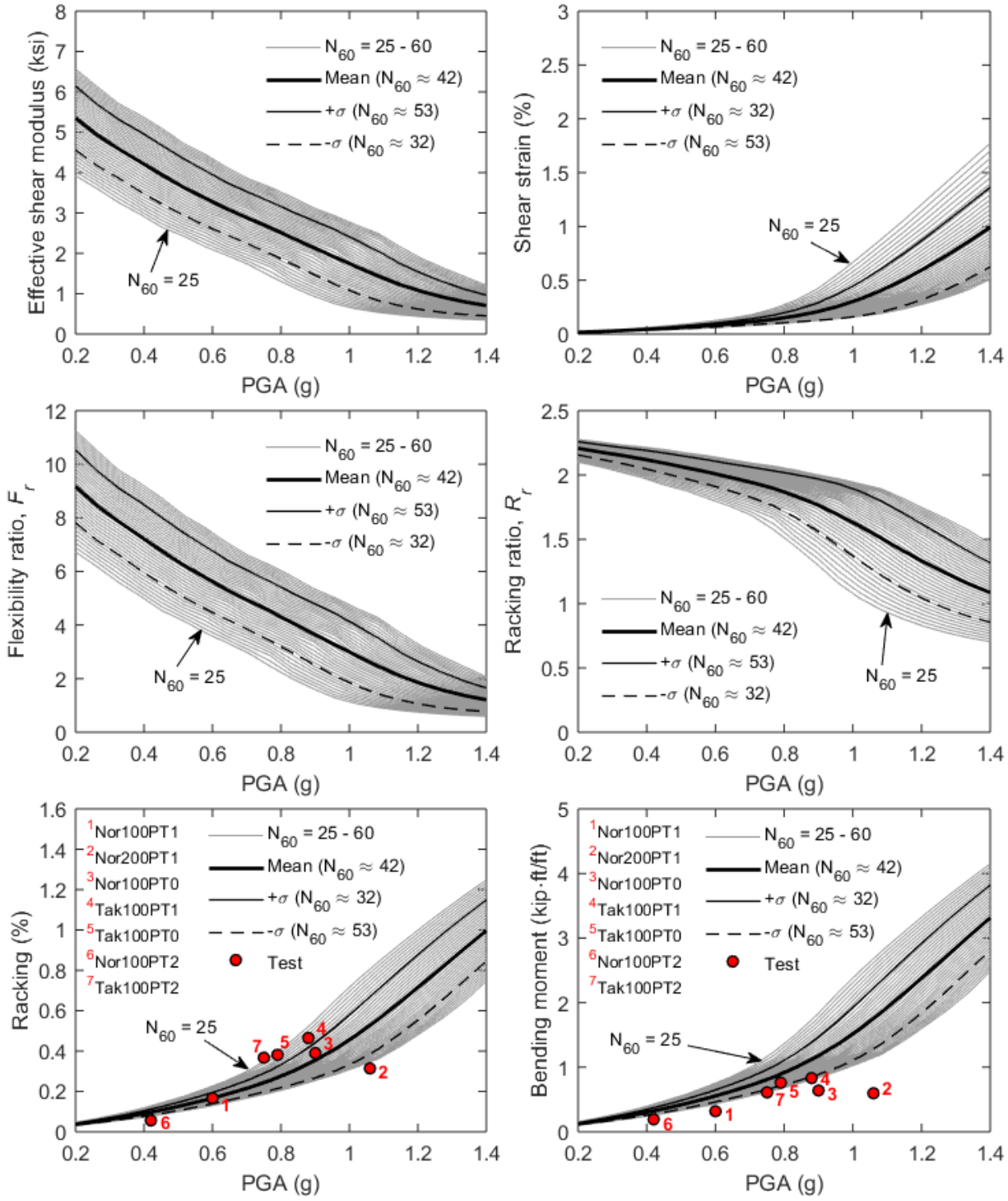

Figure 6–2: Model 1 with overburden soil depth of 2 ft: variation of FHWA parameters varied with N_{60} from 25 to 60 along with test results (marked in red dots) in model scale

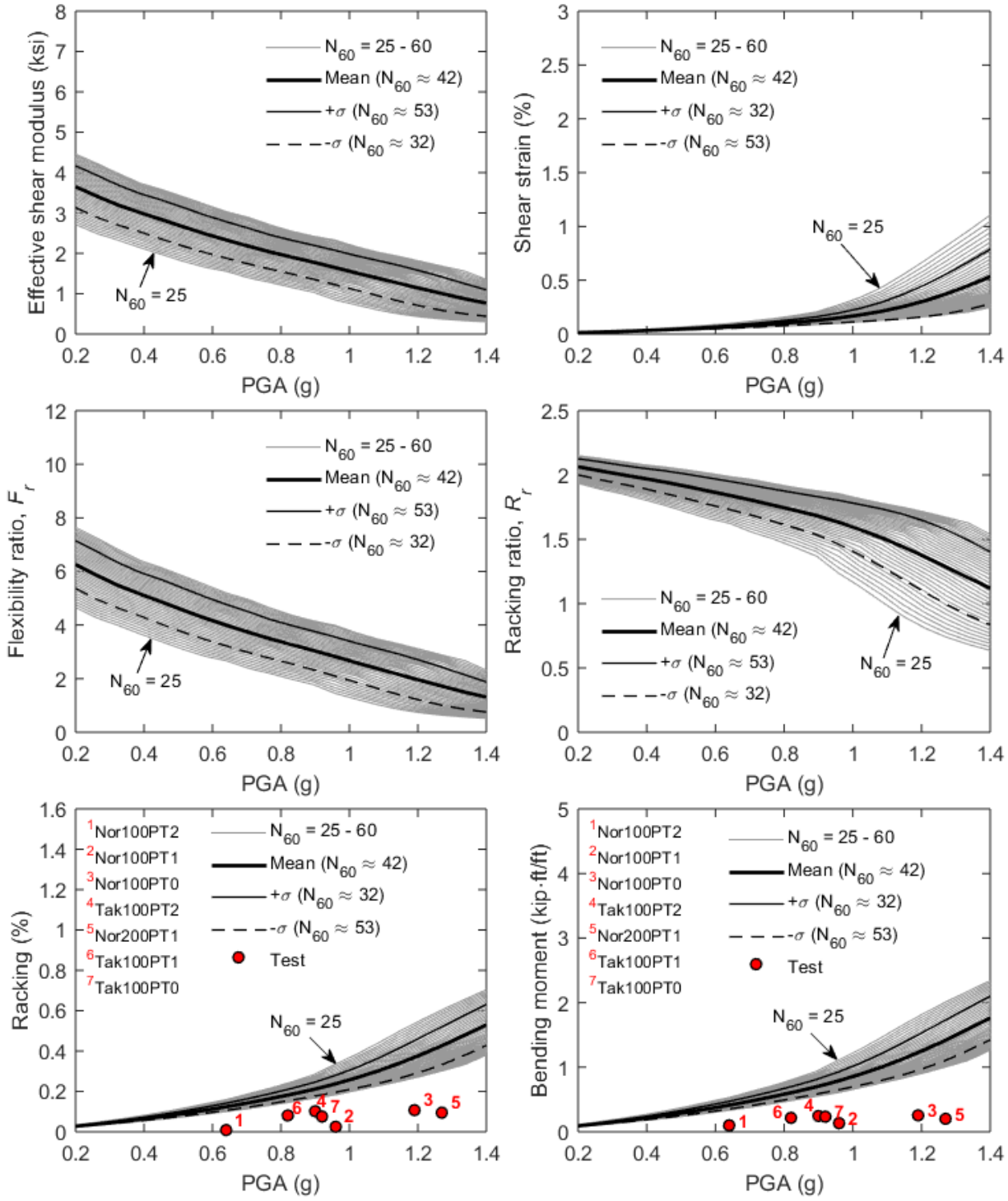

Figure 6–3: Model 2 without overburden soil: variation of FHWA parameters varied with N_{60} from 25 to 60 along with test results (marked in red dots) in model scale

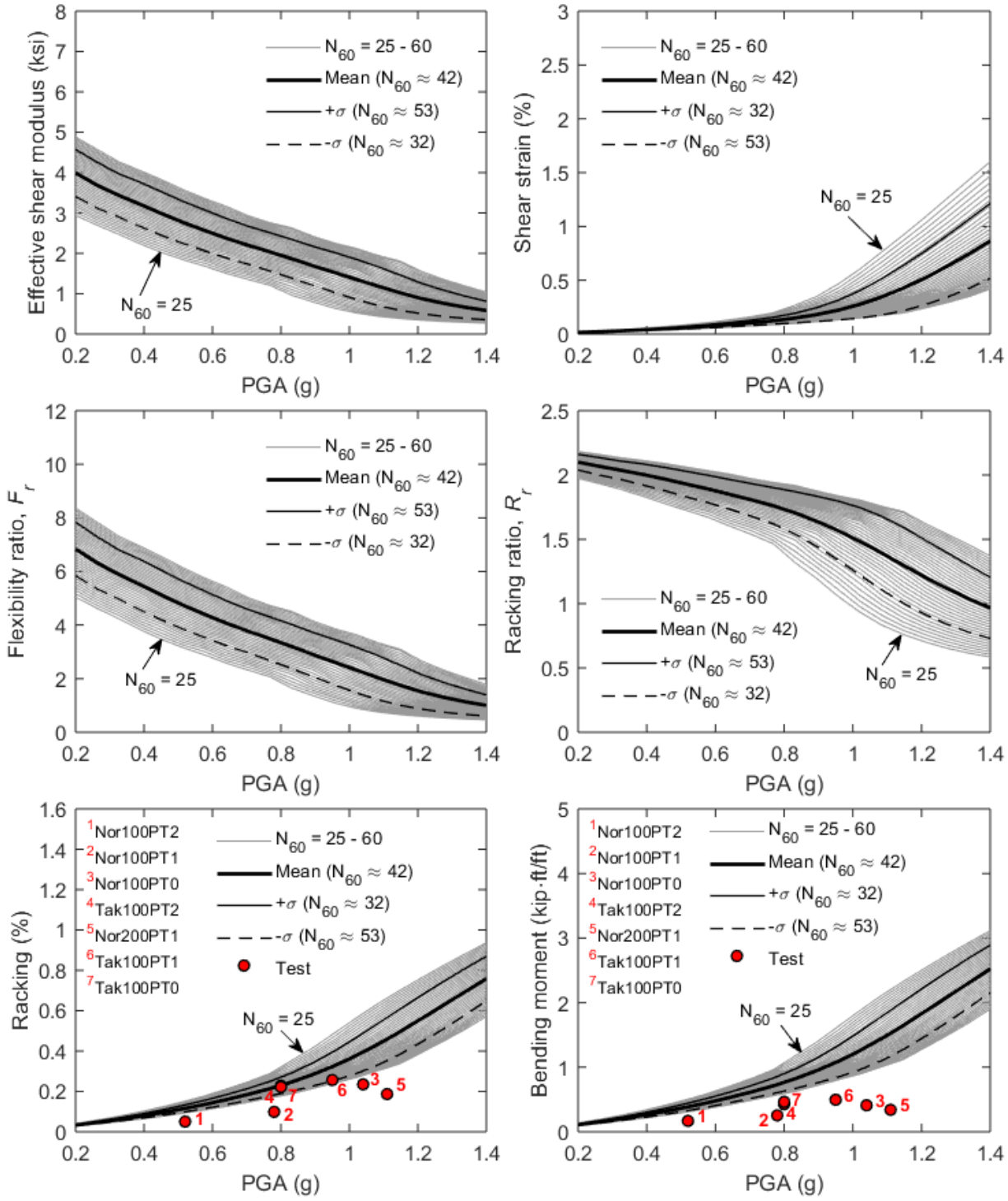

Figure 6–4: Model 3 with overburden soil depth of 1 ft: variation of FHWA parameters varied with N_{60} from 25 to 60 along with test results (marked in red dots) in model scale

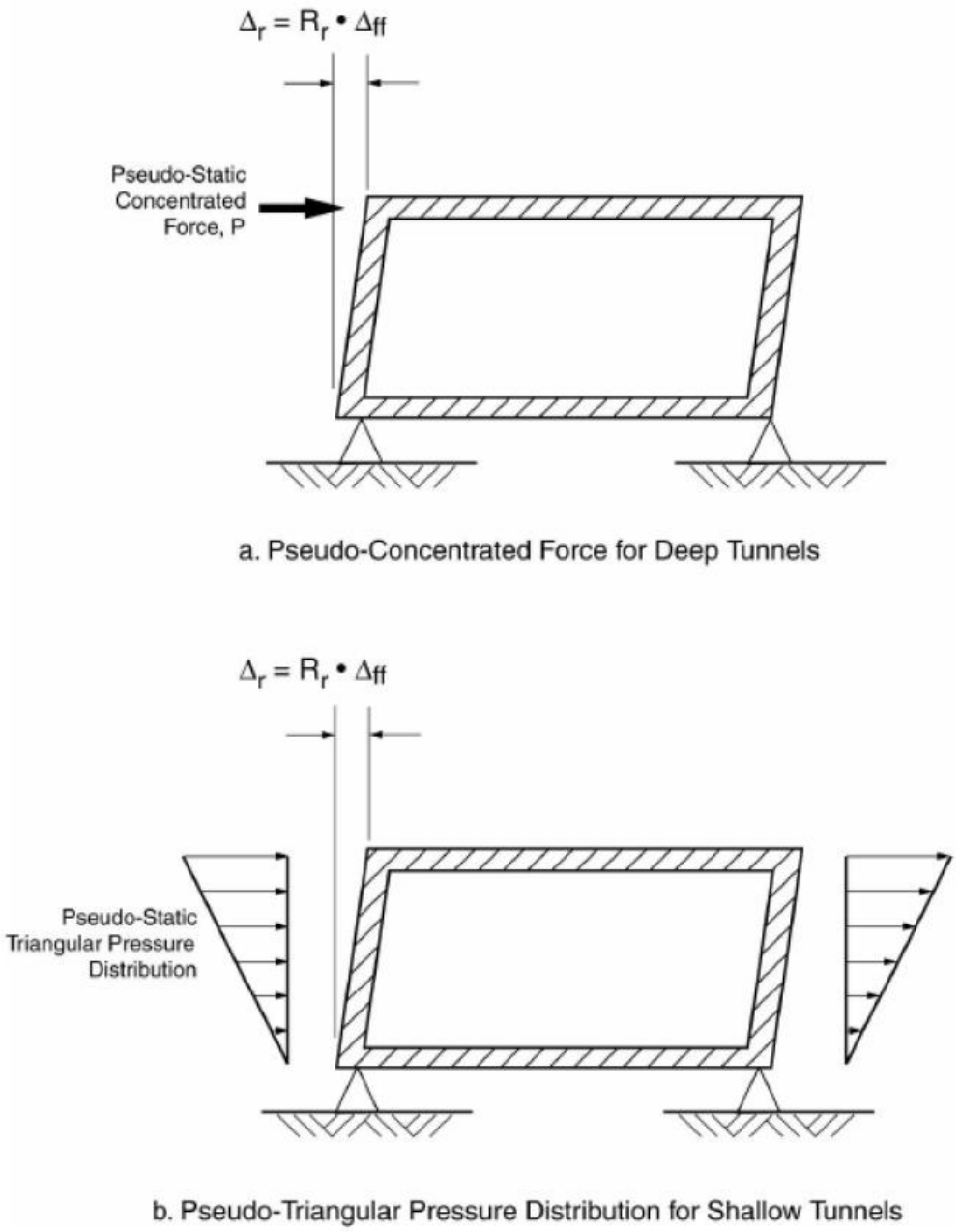

Figure 6–5: Simplified racking frame analysis of a rectangular tunnel (FHWA 2009)

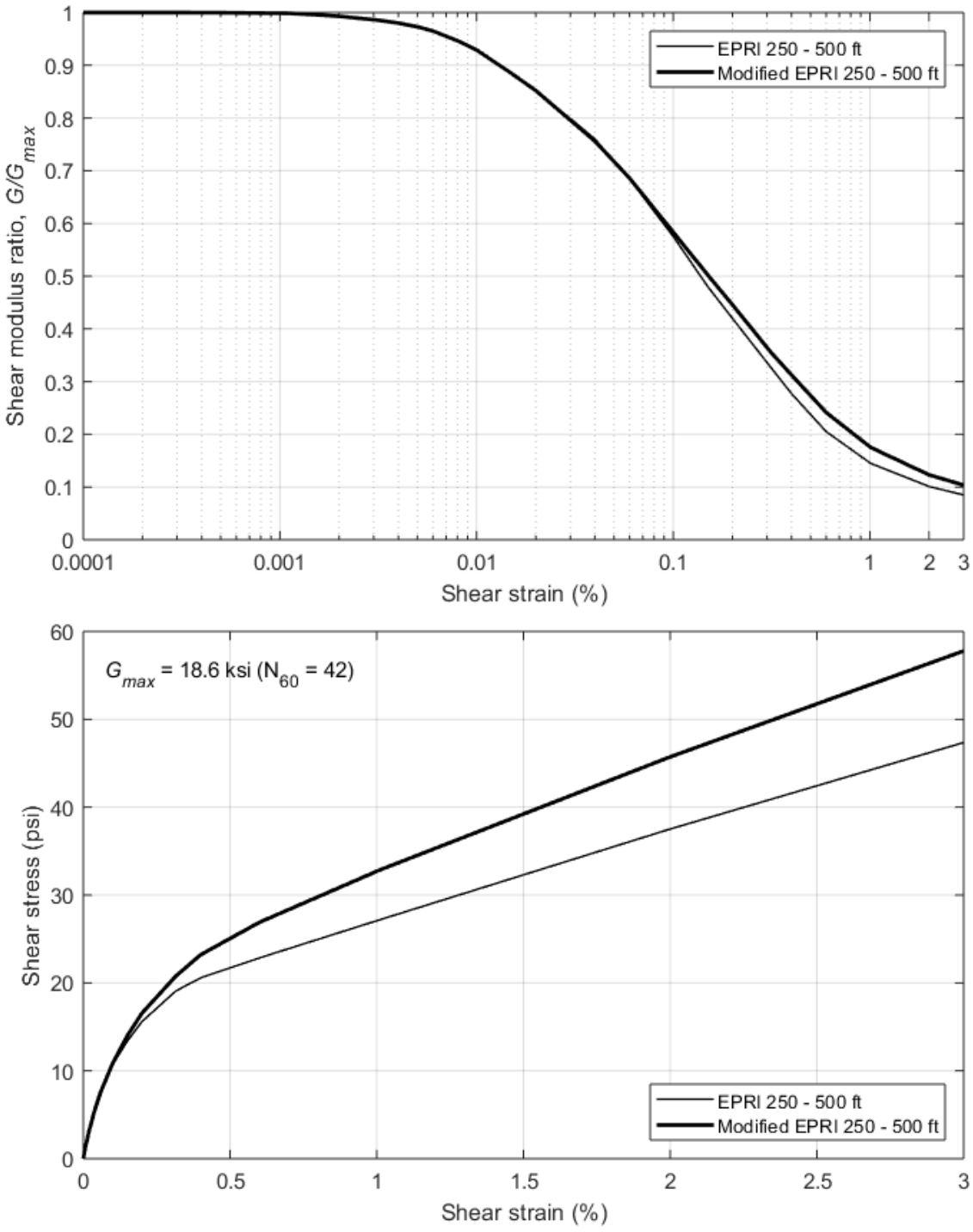

Figure 6–6: Modified EPRI shear modulus reduction curve for depth from 250 ft to 500 ft (above) and shear stress-strain relationship along with G_{max} of 18.6 ksi using N_{60} of 42 (below) for ground in prototype scale

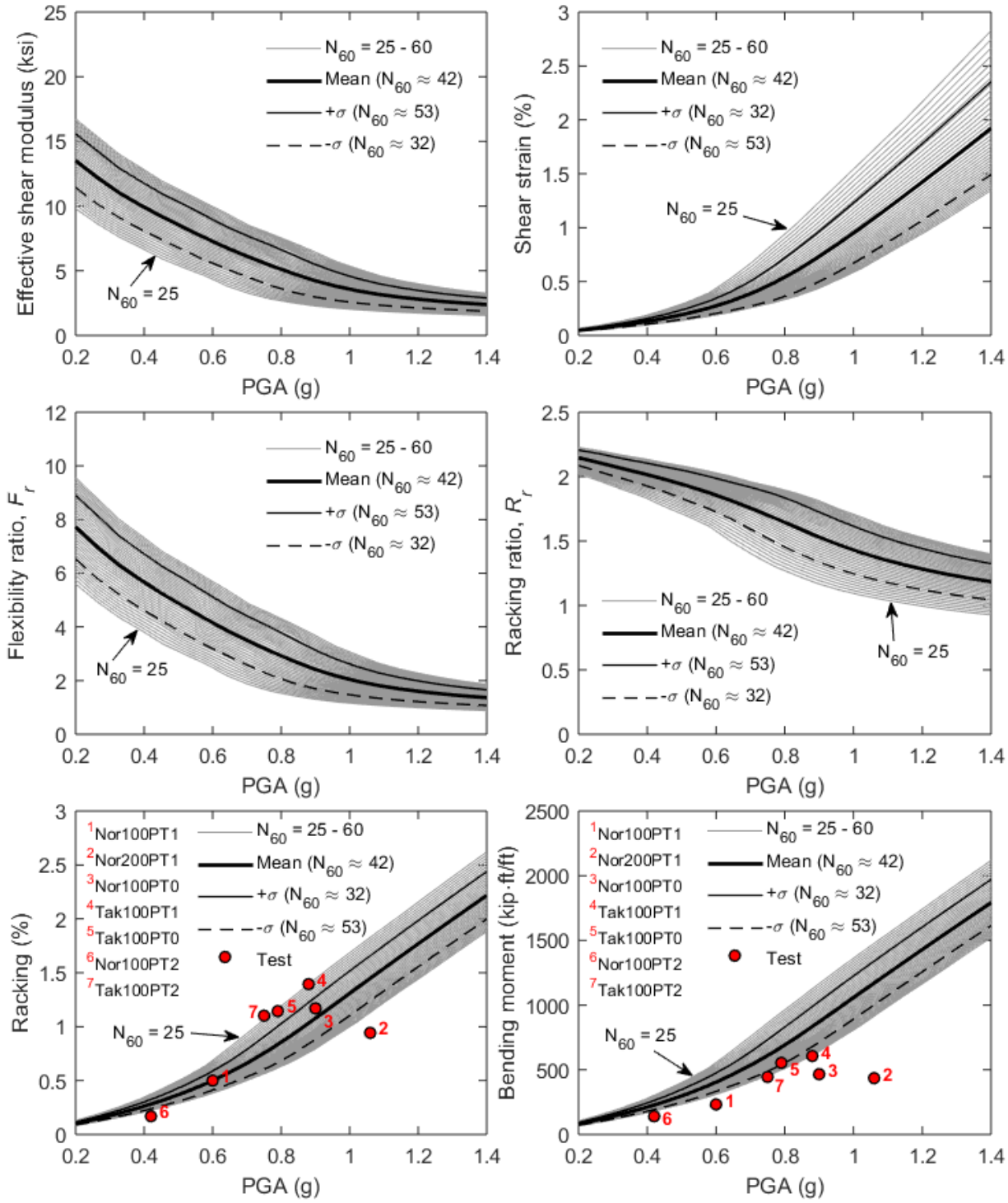

Figure 6–7: Model 1 with overburden soil depth of 18 ft: variation of FHWA parameters varied with N_{60} from 25 to 60 along with test results (marked in red dots) in prototype scale

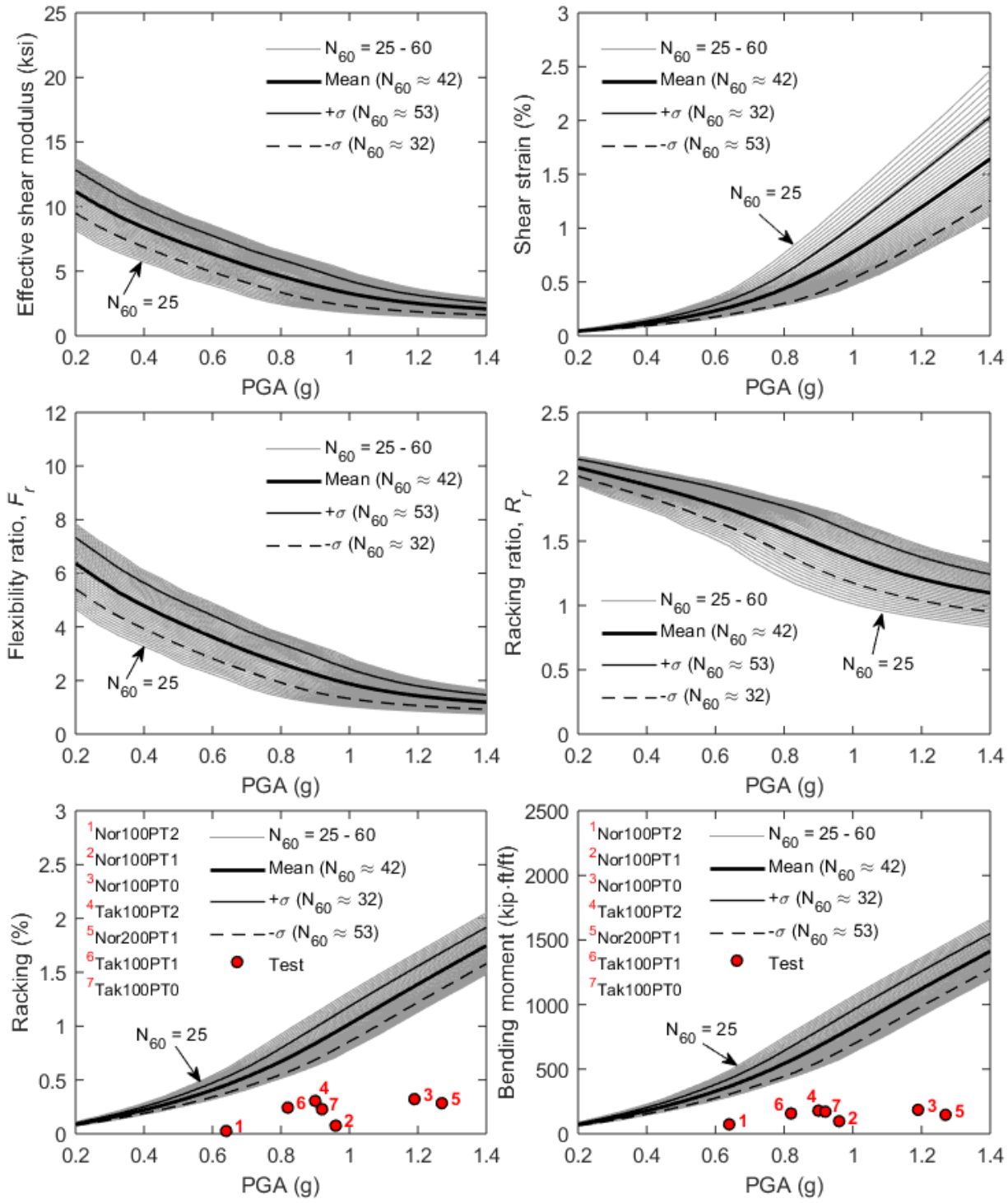

Figure 6–8: Model 2 without overburden soil: variation of FHWA parameters varied with N_{60} from 25 to 60 along with test results (marked in red dots) in prototype scale

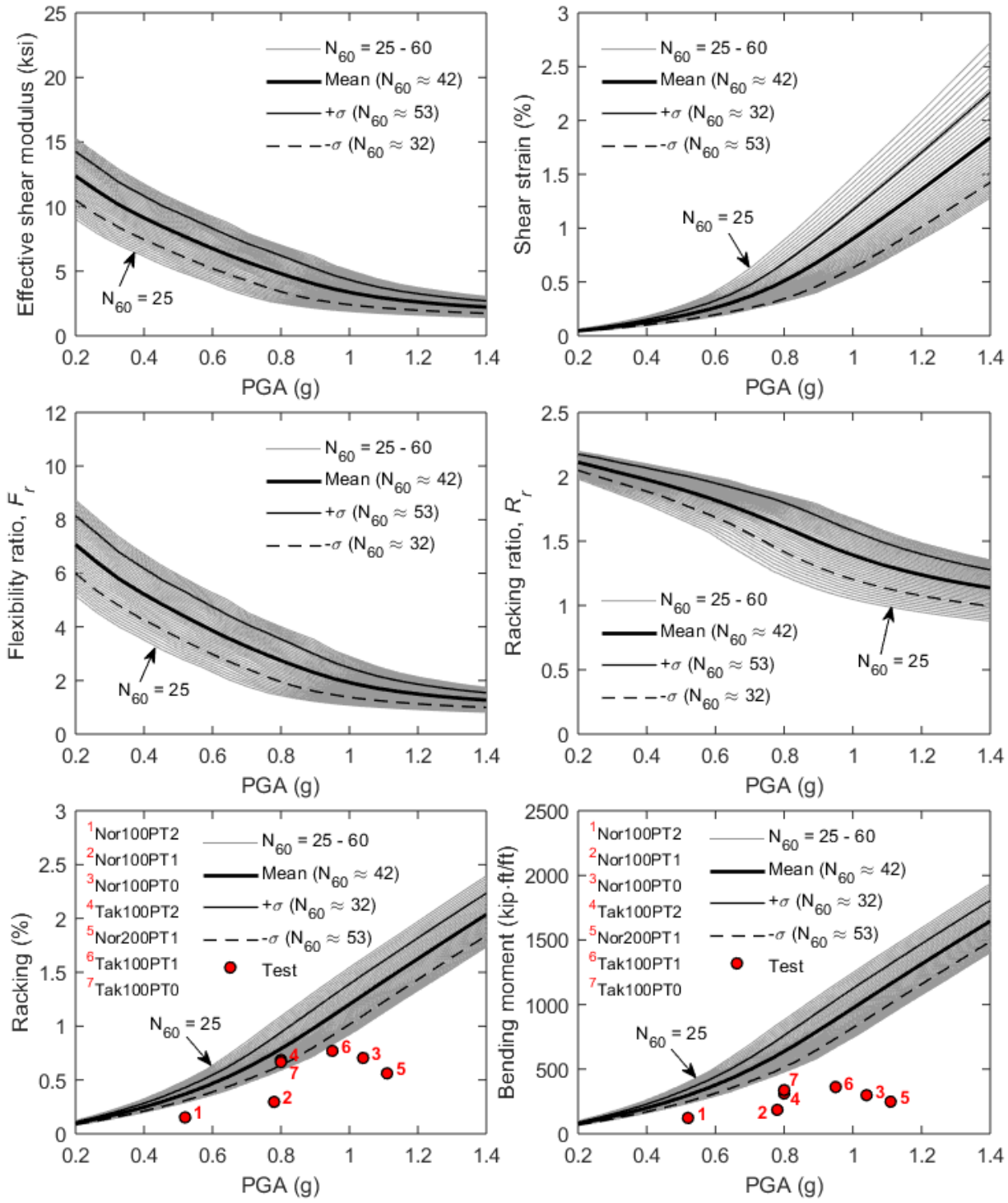

Figure 6–9: Model 3 with overburden soil depth of 1 ft: variation of FHWA parameters varied with N_{60} from 25 to 60 along with test results (marked in red dots) in prototype scale

7. Concluding Remarks

7.1. Summary of Shake Table Test Results

From the shake table tests for three test models under different backfill conditions and thickness of overburden soil (associated with burial depth), peak dynamic response was summarized in the 1/9 scale model and the actual full-scale dimensions. At peak lateral deformation (racking), lateral earth pressure measured from the pressure sensors was presented and discussed. Particularly, the earth pressure was expressed in terms of resultant force and point of action associated with the tunnel deformation.

Main findings from the overall testing results are as follows:

1. Peak racking occurred generally in the neighborhood of PGA and PGV in each test model.
2. Under the same earthquake excitation for the different test models, PGA slightly decreased with increasing thickness of overburden soil. In spite of the lower PGA, peak racking noticeably increased with increasing thickness of overburden soil.
   - This trend was associated with a low level of the strain softening.
   - This softening affected the relative stiffness between the tunnel and the surrounding soil: As the softening increased, the extent of the relative stiffness of the tunnel to the soil increased. Consequently, the tunnel suffered less deformation relative to the soil as shown in the test model without overburden soil.
3. Peak racking was caused by the relative difference between resultant forces and associated point of action on both sides of the tunnel. For instance, generally at peak racking eastwards, the following mechanisms were involved:
   1) For 9ft overburden soil in prototype scale (1 ft overburden in mode scale) compacted at about 85% relative density
      - The resultant force and point of action on the West wall were high, and
      - The resultant force and point of action on the East wall were low,
      - Reduction of the resultant force on the East wall was a main reason for the observed peak racking (rather than the increase of the resultant force on the West wall).
   2) For 18 ft overburden soil in prototype scale (2 ft overburden in model scale) compacted at about 99% relative density
      - The resultant force on the West wall was low but associated point of action was high, and

- The resultant force on the East wall was high but associated point of action was low,
- Upward and downward shift of the resultant forces on the West and the East wall, respectively, was a main reason for the observed peak racking (rather than the increase of the resultant force on the West wall)

In addition to the above overall summaries, the following observations were drawn from the individual testing scenarios:

1. Model configuration without overburden soil (D_r of 85%):
   - Despite large soil deformation associated with PGAs of up to about 1.5g and shear strain of about 2%, resulting peak racking was less than 0.15% in terms of drift.
2. Model configuration with 9 ft (1 ft in model scale) overburden soil (D_r of 85%):
   - For PGAs of 0.8 g and higher, the dynamic excitation can more than double the moments experienced by the wall due to the post-construction static state of stress.
3. Model configuration with 18 ft (2 ft in model scale) overburden soil (D_r of 99%):
   - Due to the post-construction static state of stress associated with relative density of 99%, resultant forces and additional increments of wall bending moments associated with peak racking were likely to be lower than the static values, even for PGAs of up to about 1g.

7.2. Summary of Comparison Study to FHWA Step-by-step Procedure

Racking and wall bending moment were computed using the FHWA procedure and compared to the test results in model and prototype scale. From this study, the following observation could be drawn and may be considered in improving the current simplified procedure.

- As the earthquake intensity increased (PGA higher than about 0.6g), the FHWA procedure tended to be relatively sensitive to the backfill material properties for soils with high relative compaction of about 95 percent. This sensitivity resulted from wide variation of shear strain in the surrounding soil between the top and bottom elevation of the tunnel. As such, the FHWA procedure must be applied with caution for relatively strong earthquake scenarios.
- For the relatively deep tunnel in this study (18 ft overburden soil above top face of the tunnel), the FHWA procedure predicted to some extent adequate degree of racking compared to the test result.

- For the relatively shallow tunnel (in the case without overburden soil), conservatism of the FHWA was noticeable in comparison to the test results.
- In the FHWA procedure, wall bending moment was essentially dictated by the resulting racking based on a linear-elastic frame model. As the pseudo-static lateral distribution (inverted triangular shape) was used in computing the seismic demand in terms of bending moment, more conservatism was noted. From the test, it was found that there was a considerable reduction of the lateral earth pressure (dynamic component) near the tunnel base in the shape of the asymmetric distribution on both sides of the tunnel. As such, a more realistic loading mechanism representative of asymmetric resultant force and point of action on both sides of the tunnel may be considered in updates of simplified analysis procedures. For this purpose, further analysis is needed to quantify seismic loading distribution under various conditions of the backfill material, burial depth, earthquake characteristics, and so forth.

7.3. Tunnels with a wall-roof hinge connection

Using a Finite Element model calibrated by the test results, a preliminary numerical investigation was conducted to assess the influence of a potential hinge connection between the tunnel walls and the roof. In general, the numerical response matched well with the recorded response during the Nor100PT1 input excitation. To evaluate seismic capacity of the tunnel with respect to change in the tunnel stiffness, wall-roof hinge connections were prescribed on both sides of the tunnel. Using this modified tunnel model, the numerical results showed that the reduced tunnel stiffness increased the displacement demand by as much as 75%. However, no significant change in the wall peak bending moment or shear force were noted. Racking deformation for the pinned connection scenario can thus be potentially estimated by the FHWA (2009) procedure, employing the corresponding reduced tunnel racking stiffness.

References

Bathe, K. J. (2007). “Conserving energy and momentum in nonlinear dynamics: A simple implicit time integration scheme.” Computers and Structures, 85(7–8), 437–445.

Caltrans (2012). Personal communications.

Caltrans (2015). Standard Specifications. California Department of Transportation, Sacramento, CA.

EPRI (1993). Guidelines for determining design basis ground motions, volume I: method and guidelines for estimating earthquake ground motion in eastern North America. Rep. No. TR-102293. Electric Power Research Institute, Palo Alto, CA.

FHWA (2009). Technical manual for design and construction of road tunnels - civil elements. U.S. Department of transportation. Federal Highway Administration. Publication No. FHWA-NHI-10-034, 702 p

Gingery, J. R. and Elgamal, A. (2013). Shear stress-strain curves based on the G/Gmax logic: A procedure for strength compatibility. IACGE 2013: Challenges and Recent Advances in Geotechnical and Seismic Research and Practices: 721-729.

Hashash, Y., Hook, J. J. and Schmidt, B. (2001). Seismic design and analysis of underground structures. Tunnelling and Underground Space Technology 16(4): 247-293.

Iai, S. (1989). Similitude for shaking table tests on soil-structure-fluid model in 1g gravitational field. Soils and Foundations 29(1): 105-118.

Kim, K., Giacalone, C., Elgamal, A. and Shing, P. B. (2015). Racking response of reinforced concrete cut and cover tunnel. SSRP-15-03. Department of Structural Engineering, University of California, San Diego, La Jolla, CA

EMI (2005). Field investigation report for abutment backfill characterization. SSRP-05/02. University of California San Diego, La Jolla, CA.

Mazzoni, S., McKenna, F., Scott, M. H., and Fenves, G. L. (2009). Open system for earthquake engineering simulation user manual, University of California, Berkeley, CA., (http://opensees.berkeley.edu/)

Skempton, A. (1986). Standard penetration test procedures and the effects in sands of overburden pressure, relative density, particle size, ageing and overconsolidation. Geotechnique 36(3): 425-447.

Wair, B., DeJong, J. and Shantz, T. (2012). Guidelines for Estimation of Shear Wave Velocity Profiles. Pacific Earthquake Engineering Research Center, PEER Report 8, UC Berkeley, Berkeley, CA.

Wang, J.-N. (1993). Seismic design of tunnels: a simple state-of-the-art design approach, Parsons Brinckerhoff New York.

Yang, Z., Elgamal, A., and Parra, E. (2003). "Computational Model for Cyclic Mobility and Associated Shear Deformation." Journal of Geotechnical and Geoenvironmental Engineering, 129(12), 1119–1127.

Appendix A Test Model Construction

This appendix presents photographs taken from the test model construction.

Figure A–1: Transportation of the laminar frames to the shake table

Figure A–2: Laminar soil container base on shake table

Figure A–3: Assembly of the laminar soil container frames

Figure A–4: Plastic lining inside the laminar soil container (the wood was removed during backfill)

Figure A–5: Adjusting soil moisture

Figure A–6: Transportation of soil

Figure A–7: Backfilling

Figure A–8: Backfill compaction

Figure A–9: Verification of the achieved soil density during backfilling from sand cone test

Figure A–10: Placement of accelerometer during backfilling

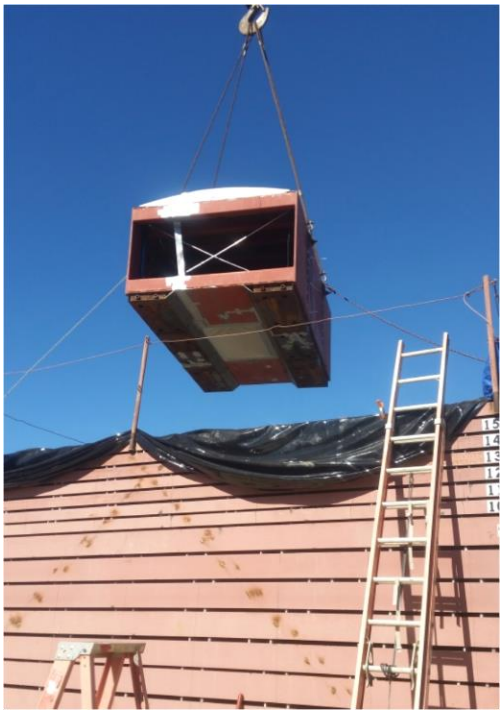

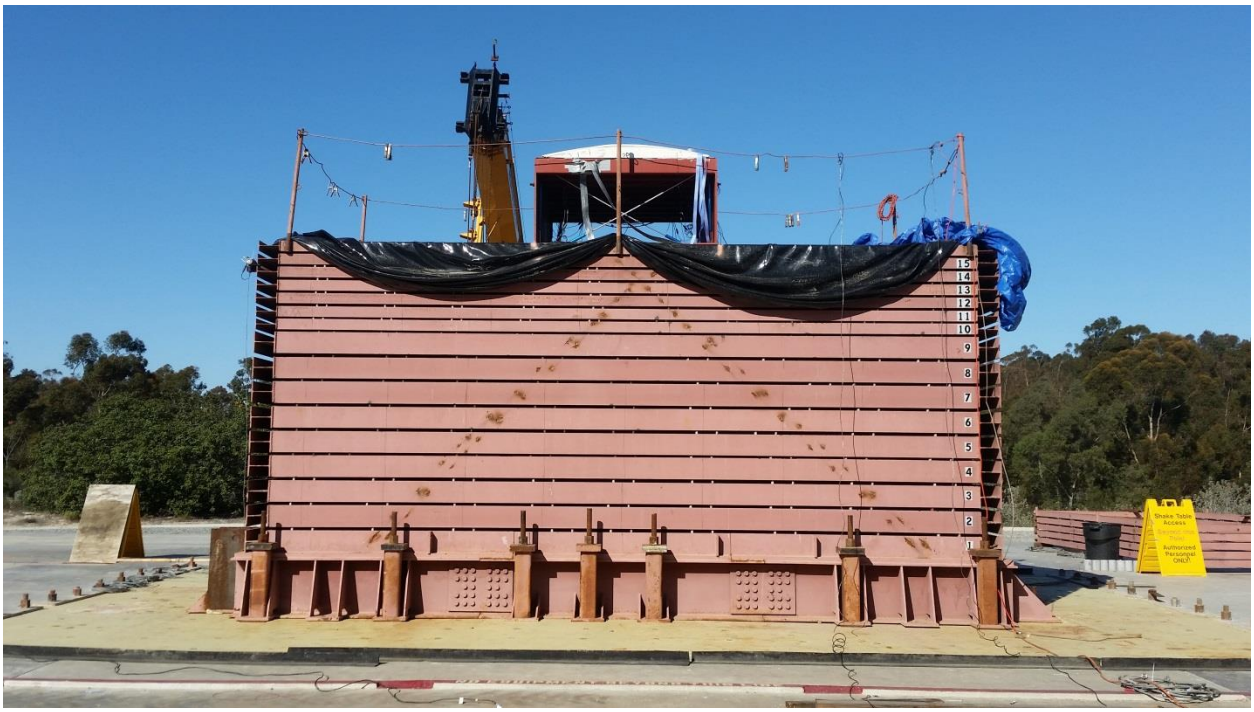

Figure A–11: Transportation of tunnel

Figure A–12: Backfilling

Figure A–13: Replacement of backfill

Appendix B Instrumentation Plan

This appendix presents the detailed instrumentation layout.

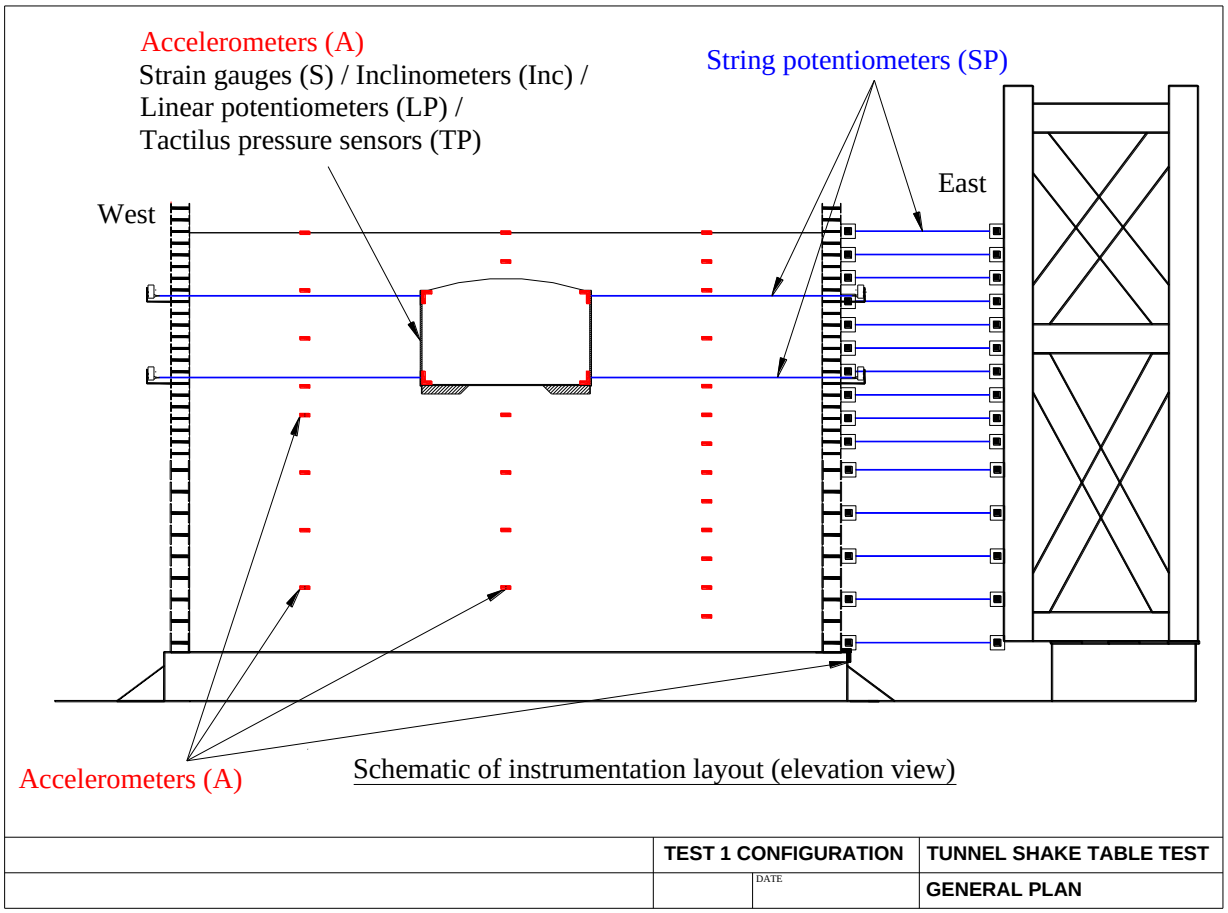

Figure B–1: General plan of the instrumentation

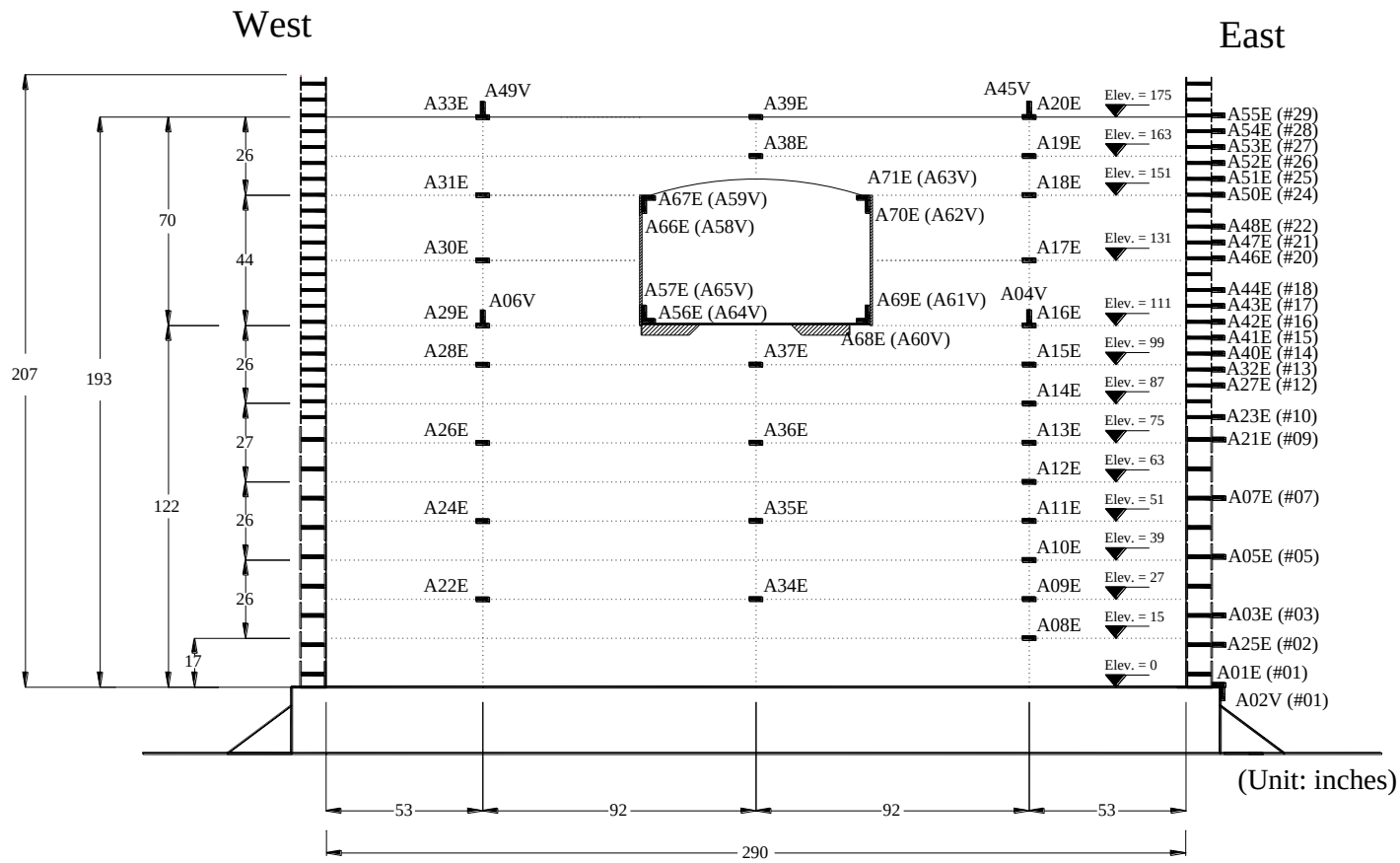

Accelerometer layout (elevation view)

	TEST 1 CONFIGURATION	**TUNNEL SHAKE TABLE TEST**
	DATE	**ACCELEROMETER PLAN**

Figure B–2: Elevation view of accelerometer (A) instrumentation plan for Test Model 1

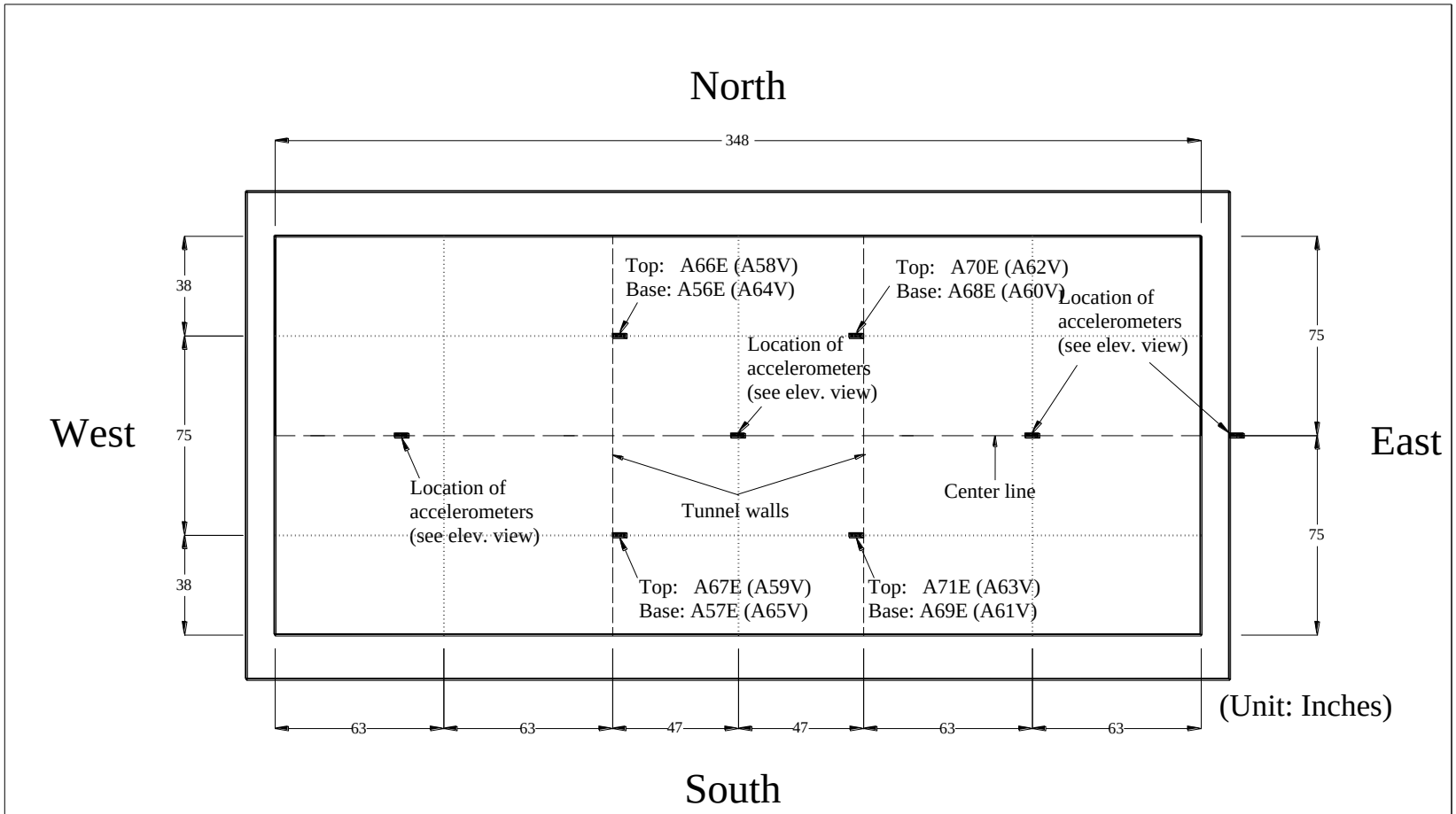

Figure B–3: Plan view of accelerometer (A) instrumentation layout

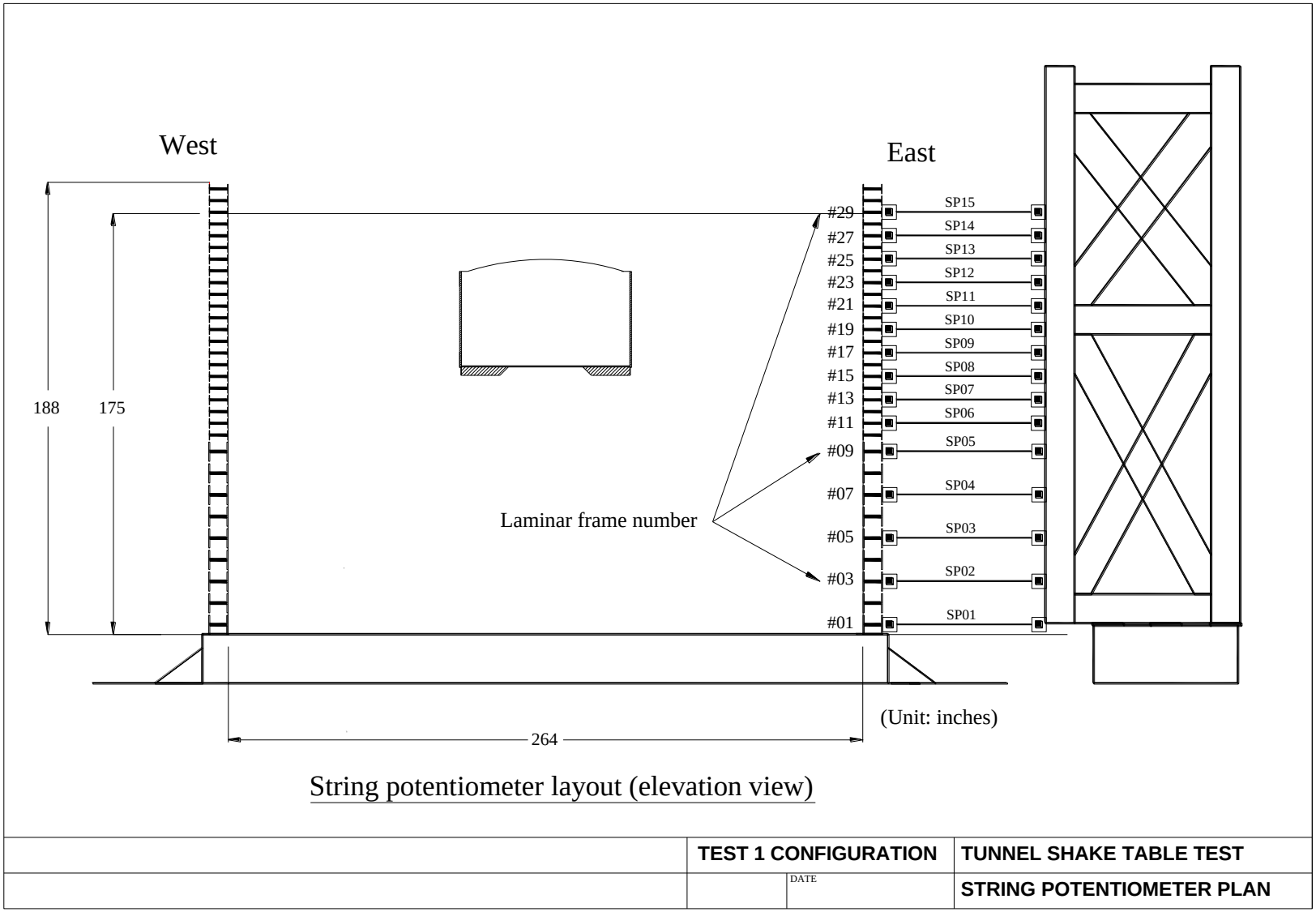

Figure B–4: Elevation view of string potentiometer (SP) layout to measure lateral displacement of the laminar frames

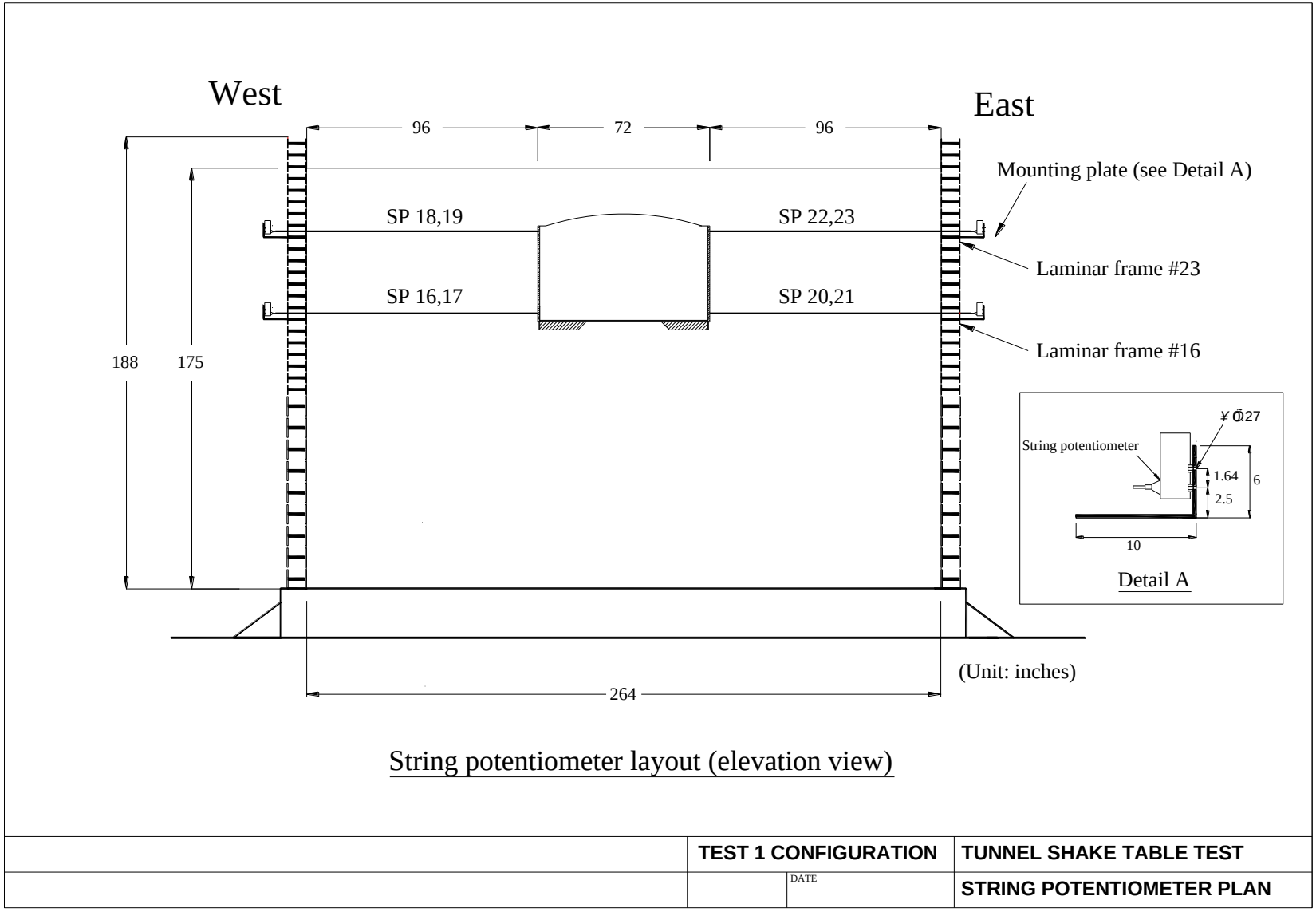

Figure B–5: Elevation view of string potentiometer (SP) layout to measure translation of the tunnel relative to the laminar frames

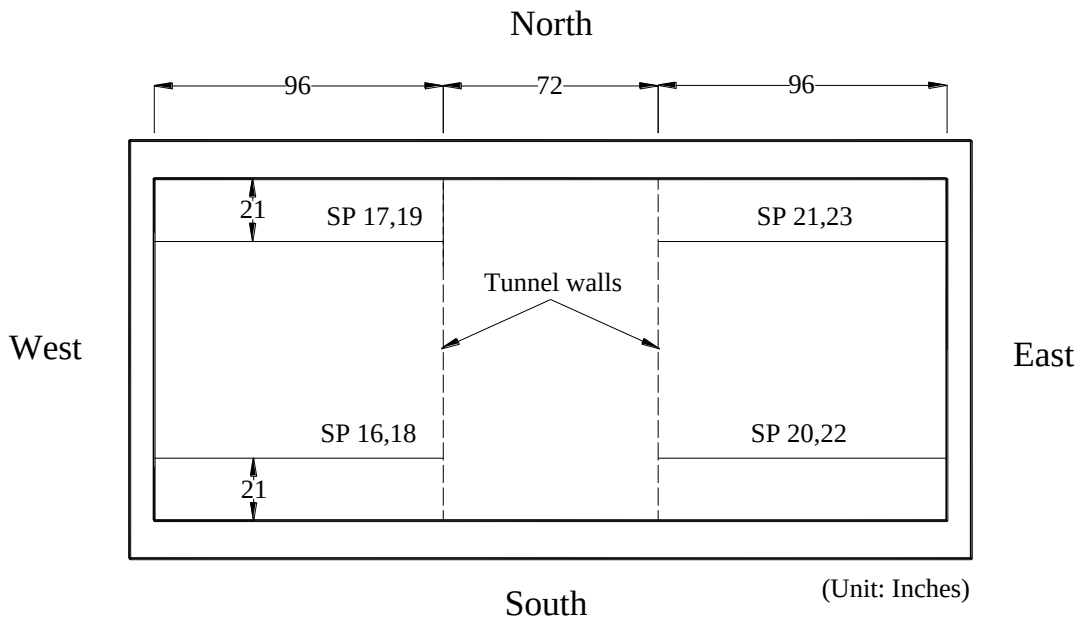

String potentiometer layout (plan view)

	TEST 1 CONFIGURATION	TUNNEL SHAKE TABLE TEST
	DATE	STRING POTENTIOMETER PLAN

Figure B–6: Plan view of string potentiometer (SP) layout to measure translation of the tunnel relative to the laminar frames

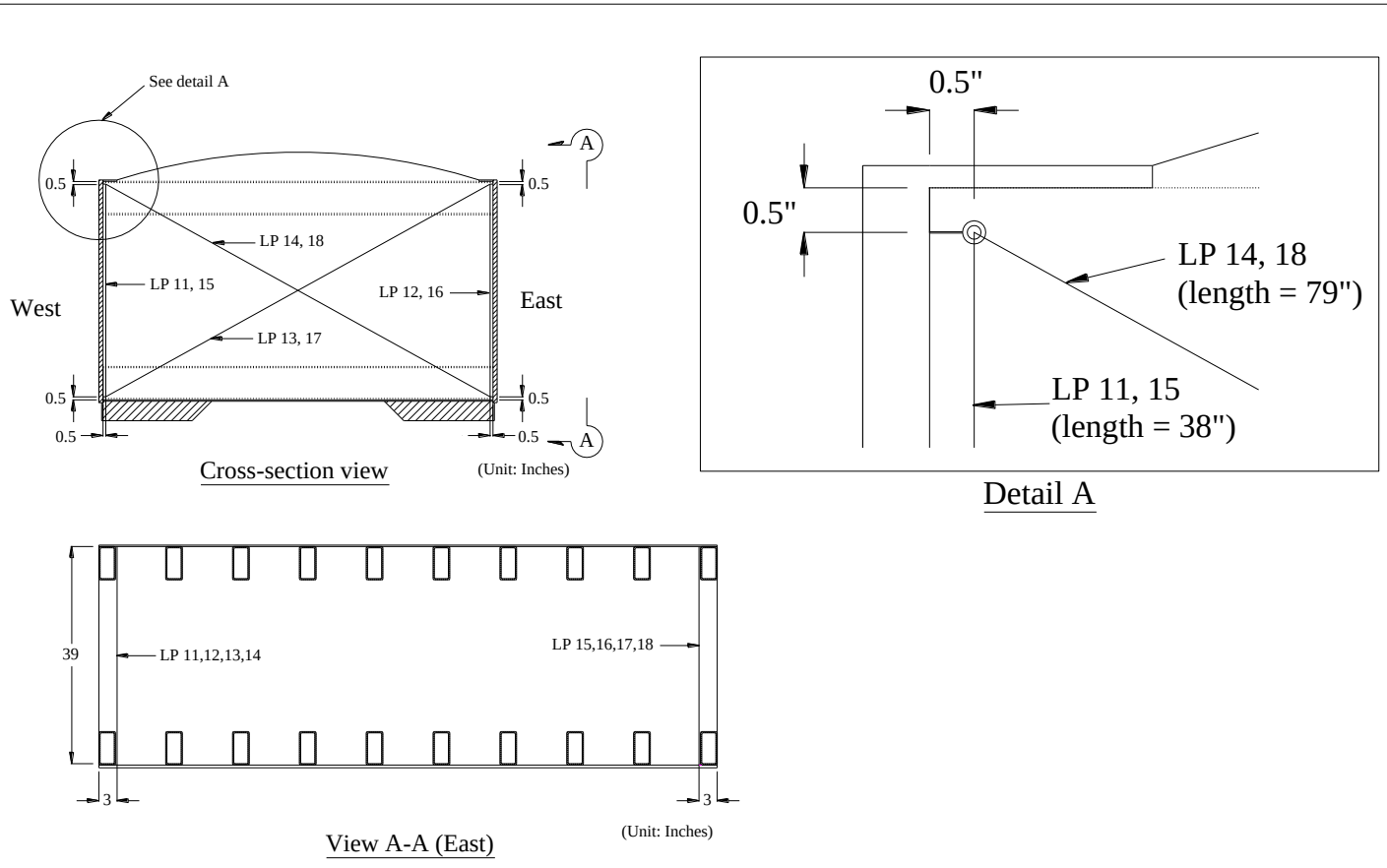

Figure B–7: Linear potentiometer (LP) layout to measure lateral deformation of tunnel

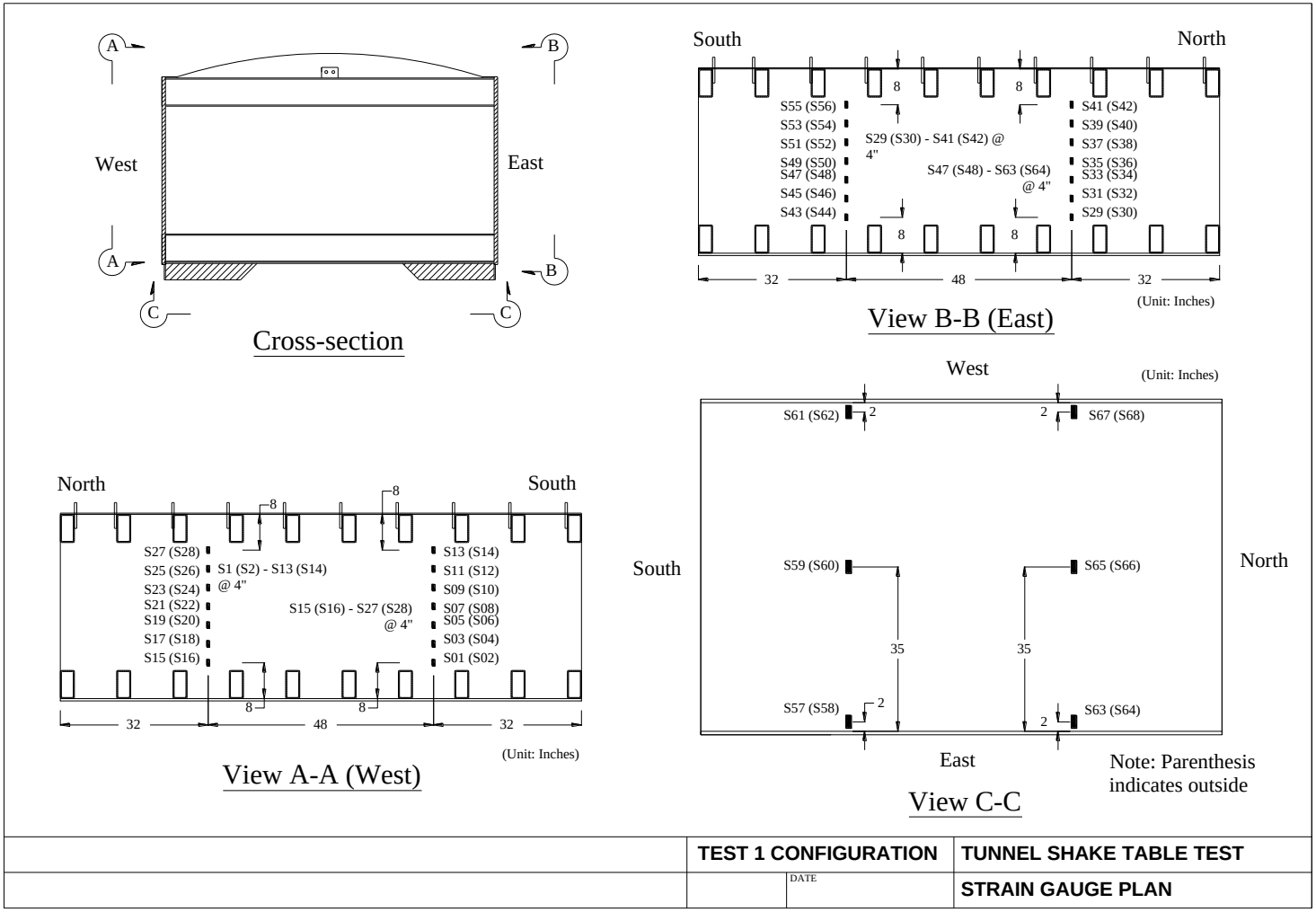

Figure B–8: Strain gauge (S) layout to measure bending strain along the tunnel walls and the base

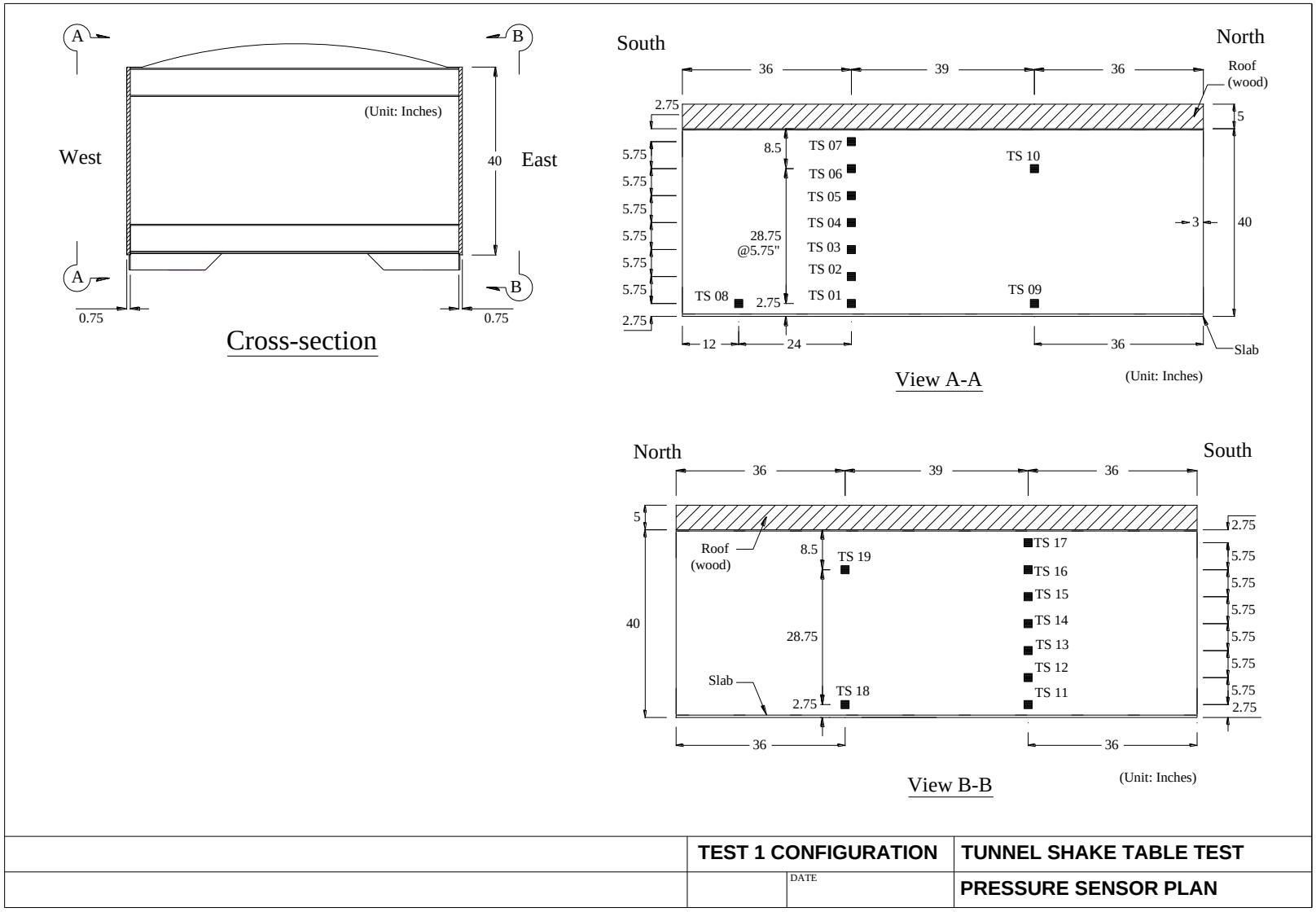

Figure B–9: Tactilus pressure sensor (TS) layout to measure lateral earth pressure along the tunnel walls

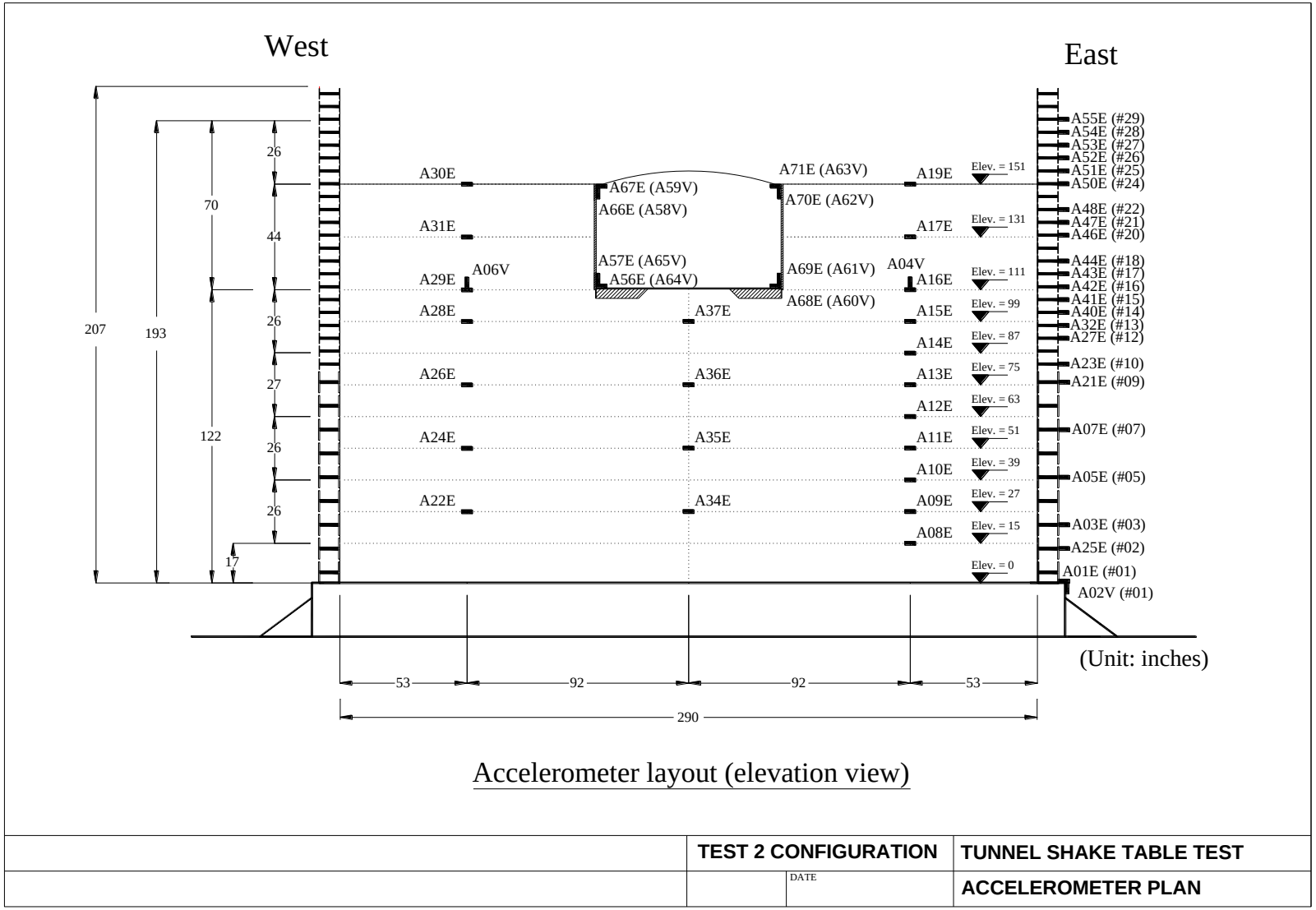

Accelerometer layout (elevation view)

	TEST 2 CONFIGURATION	**TUNNEL SHAKE TABLE TEST**
	DATE	**ACCELEROMETER PLAN**

Figure B–10: Elevation view of accelerometer (A) layout for Test Model 2

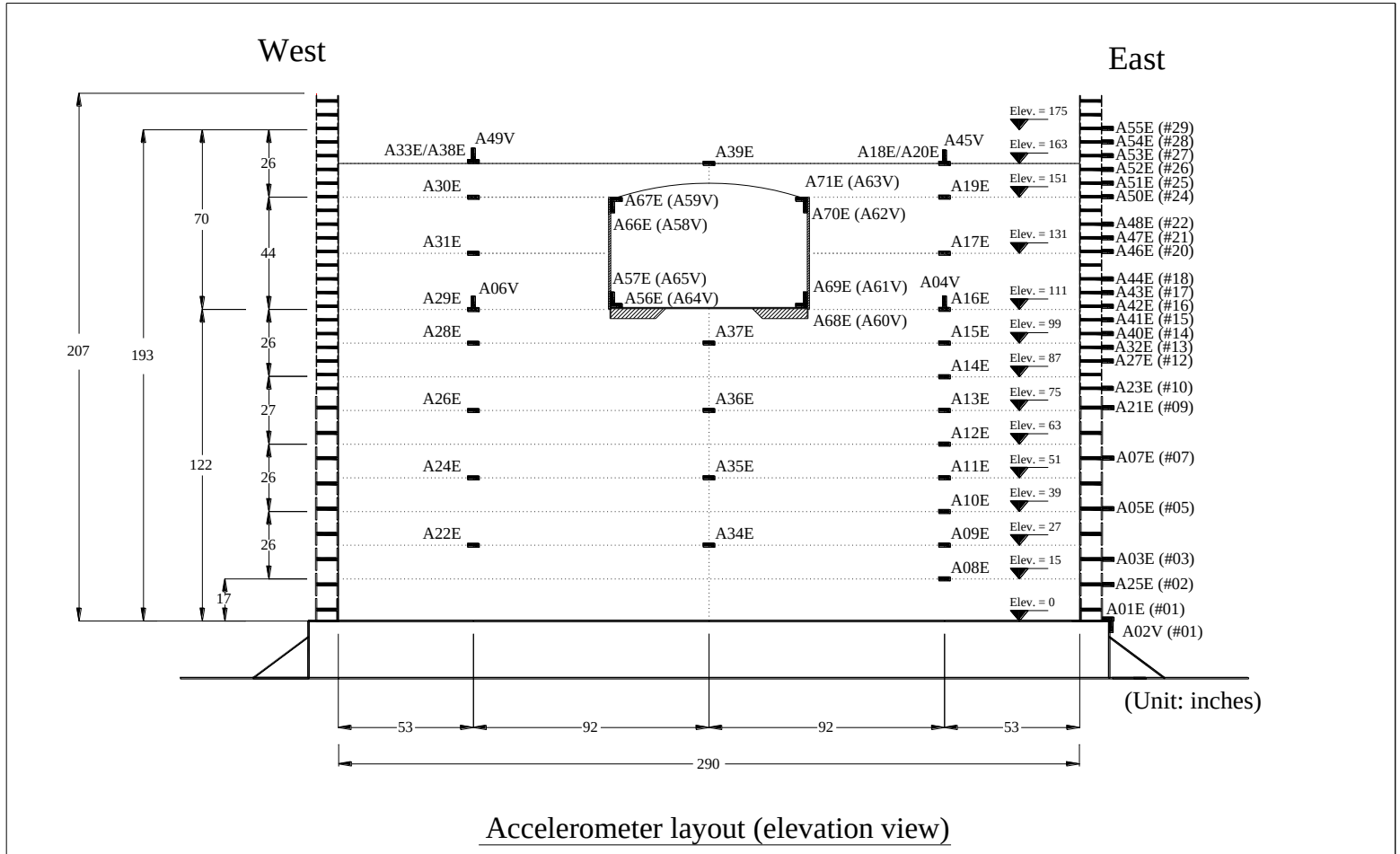

Accelerometer layout (elevation view)

	TEST 3 CONFIGURATION	TUNNEL SHAKE TABLE TEST
	DATE	ACCELEROMETER PLAN

Figure B–11: Elevation view of accelerometer (A) layout for Test Model 3

Appendix C Shake Table Test Response Time Histories in Model Scale

This appendix presents time histories of the main response recorded from the shake table tests in model scale, as discussed earlier in Section 3.3. Model 1 recorded response time histories in the order of the shaking sequence (see Section 2.4.3 for the loading protocol) are shown in Figure C-1 through Figure C-7. Model 2 recorded response is shown in Figure C-8 through Figure C-14. Model 3 response is shown in Figure C-15 through C-21.

The time histories of the lateral earth pressure along the walls as shown earlier in Section 4.2 are presented in Figure C-22 through Figure C-26 from Model 1 and in Figure C-28 through FigureC-32 from Model 3.

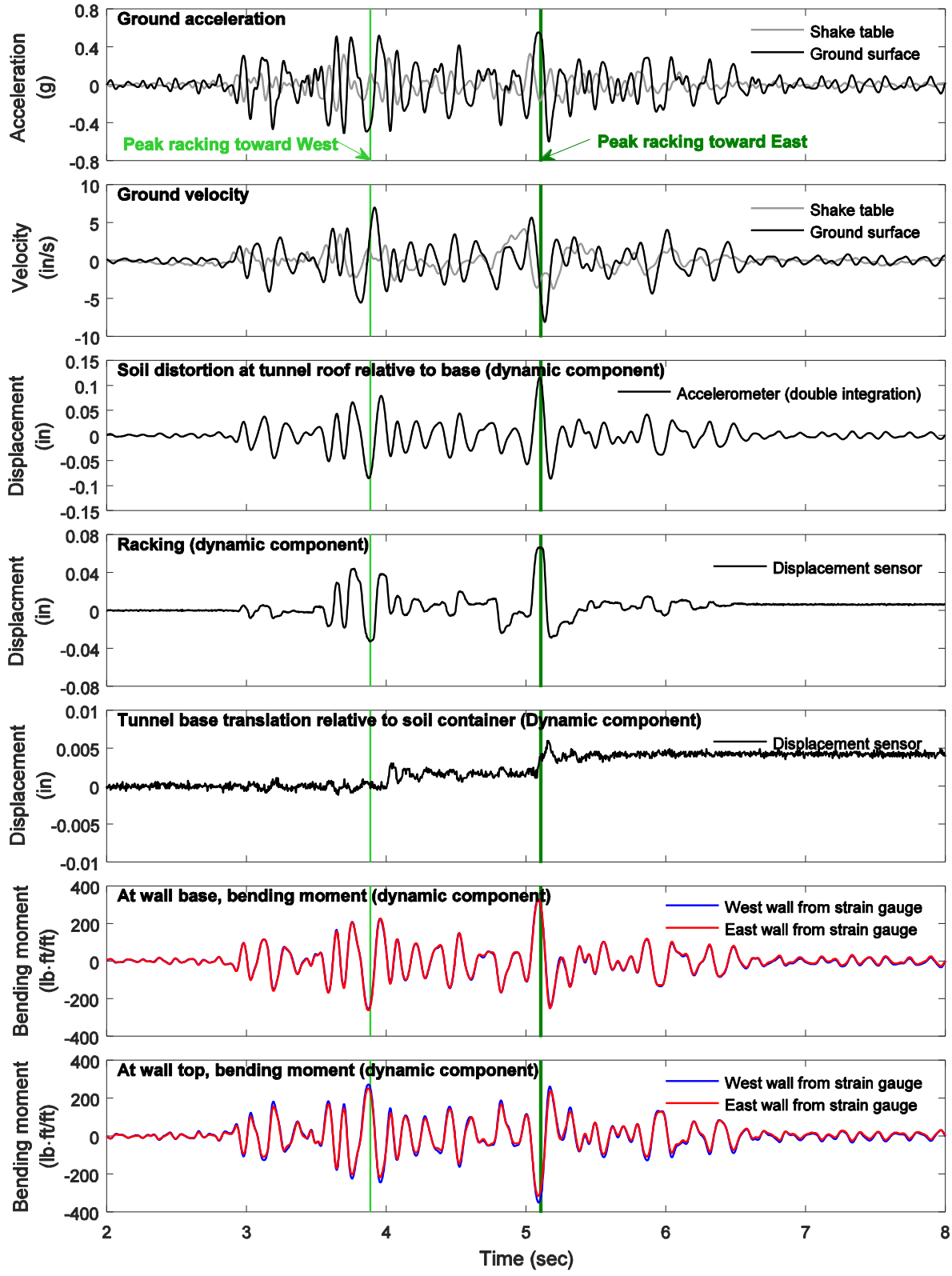

Figure C–1: Model 1 response time histories during Nor100PT1 input excitation in model scale (2 ft overburden soil)

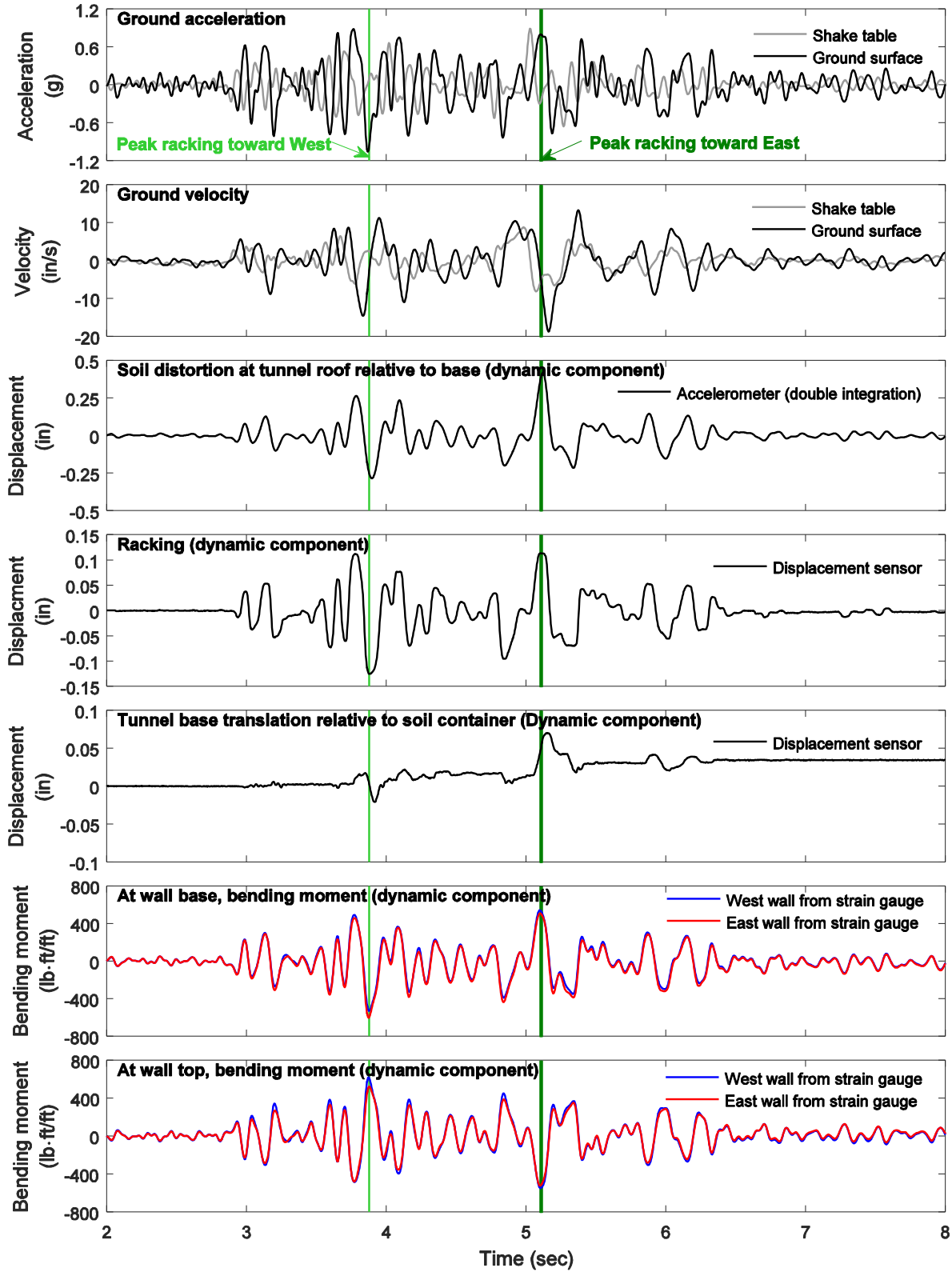

Figure C–2: Model 1 response time histories during Nor200PT1 input excitation in model scale (2 ft overburden soil)

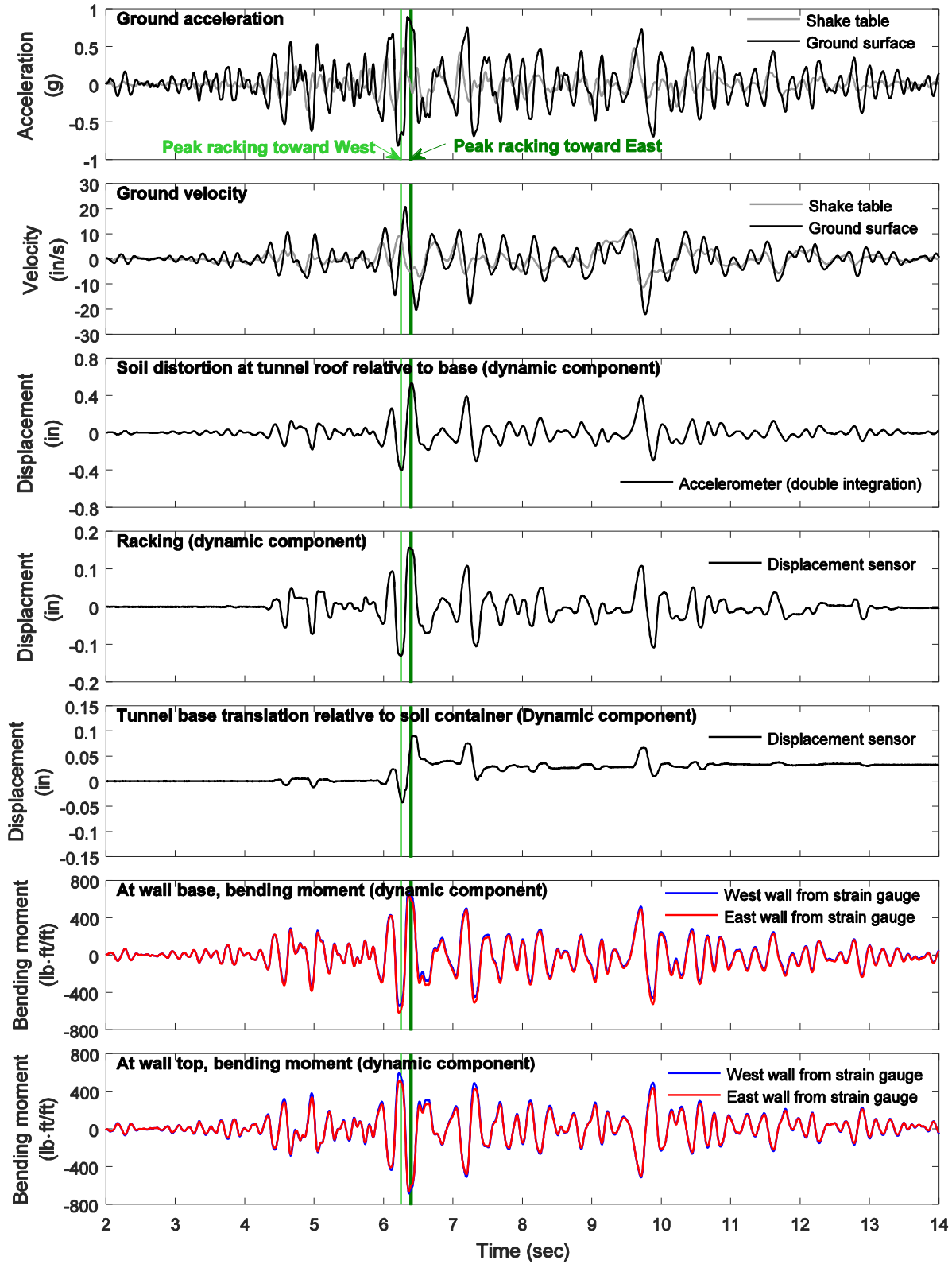

Figure C–3: Model 1 response time histories during Nor100PT0 input excitation in model scale (2 ft overburden soil)

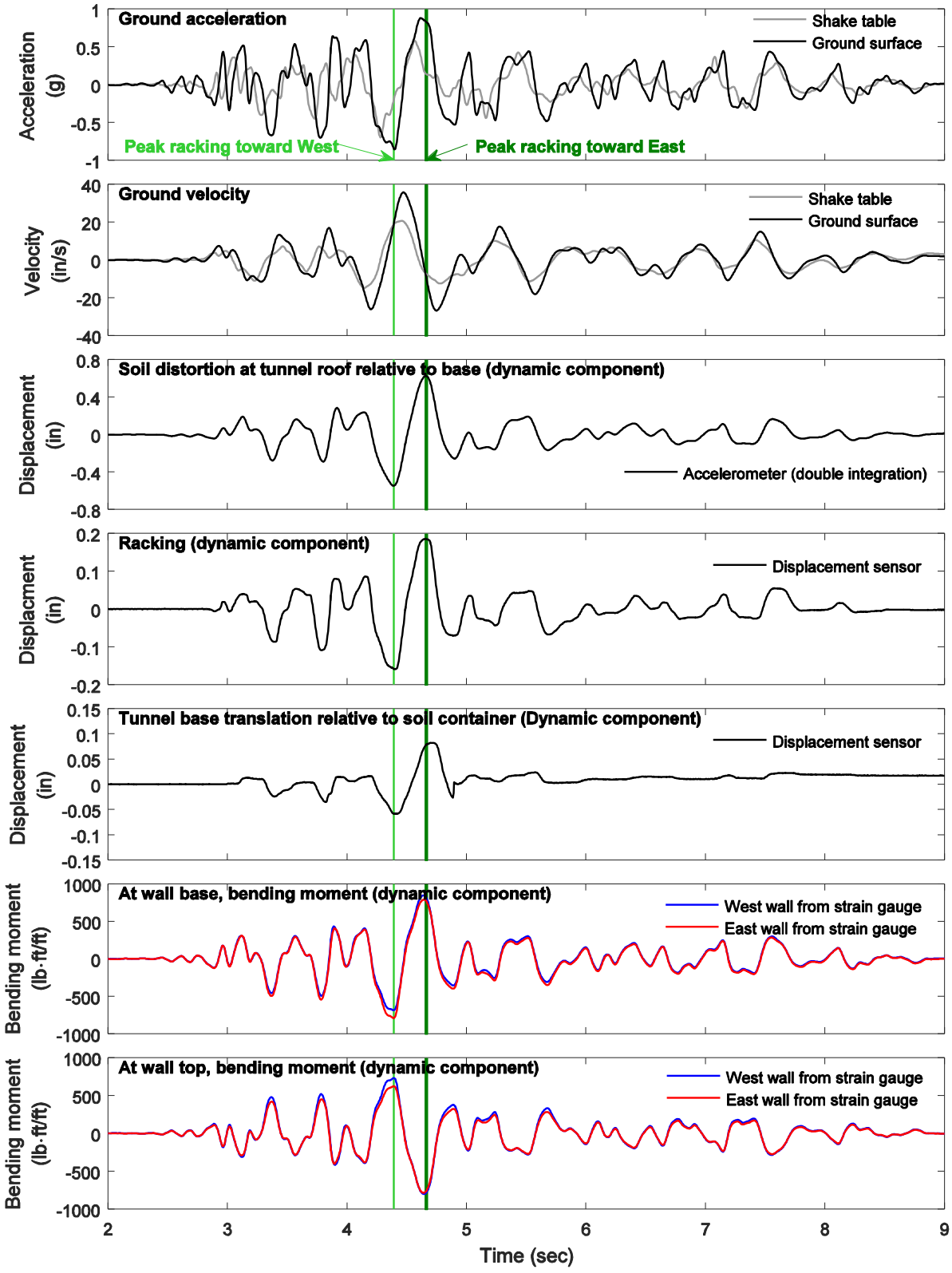

Figure C–4: Model 1 response time histories during Tak100PT1 input excitation in model scale (2 ft overburden soil)

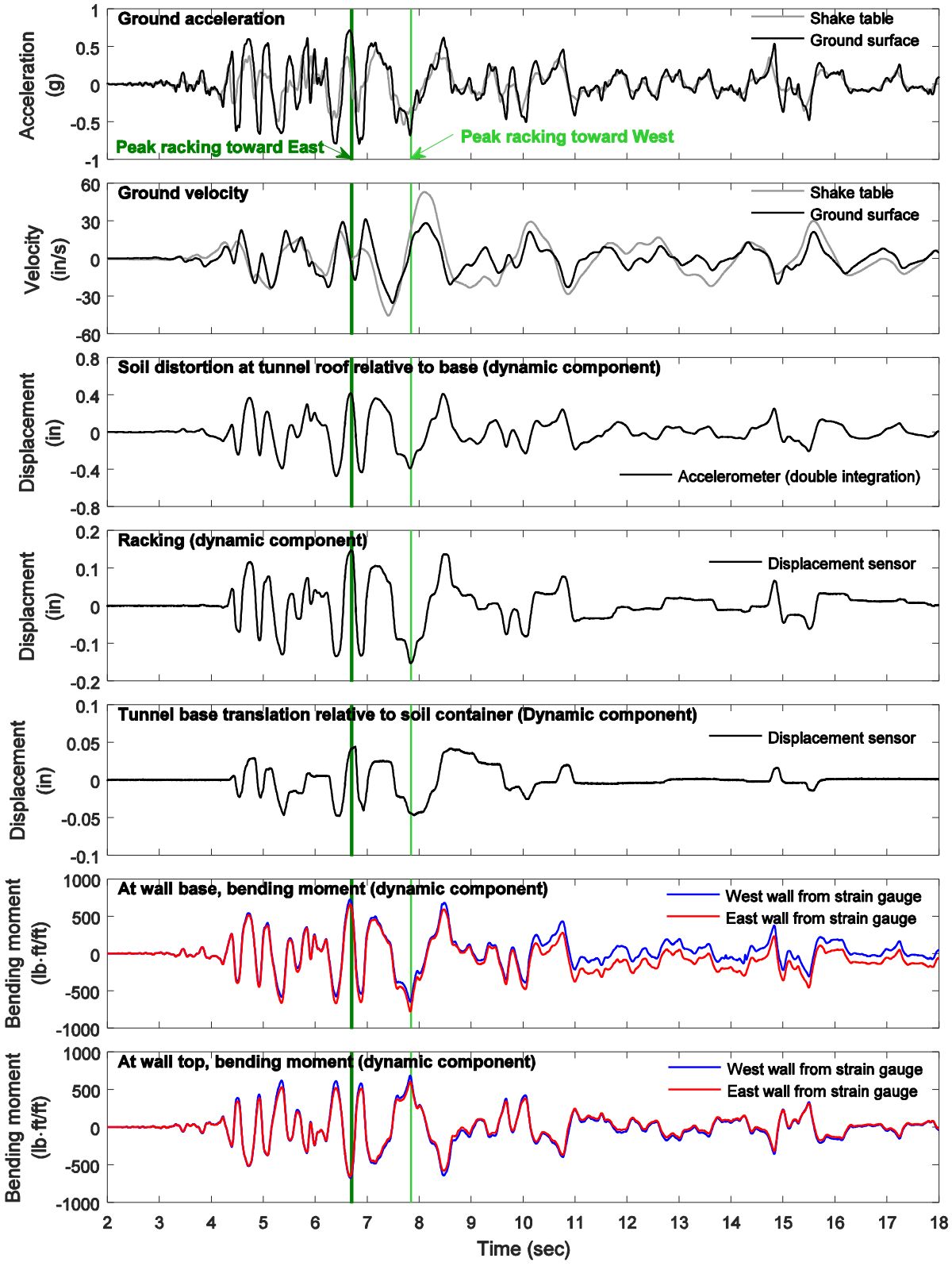

Figure C–5: Model 1 response time histories during Tak100PT0 input excitation in model scale (2 ft overburden soil)

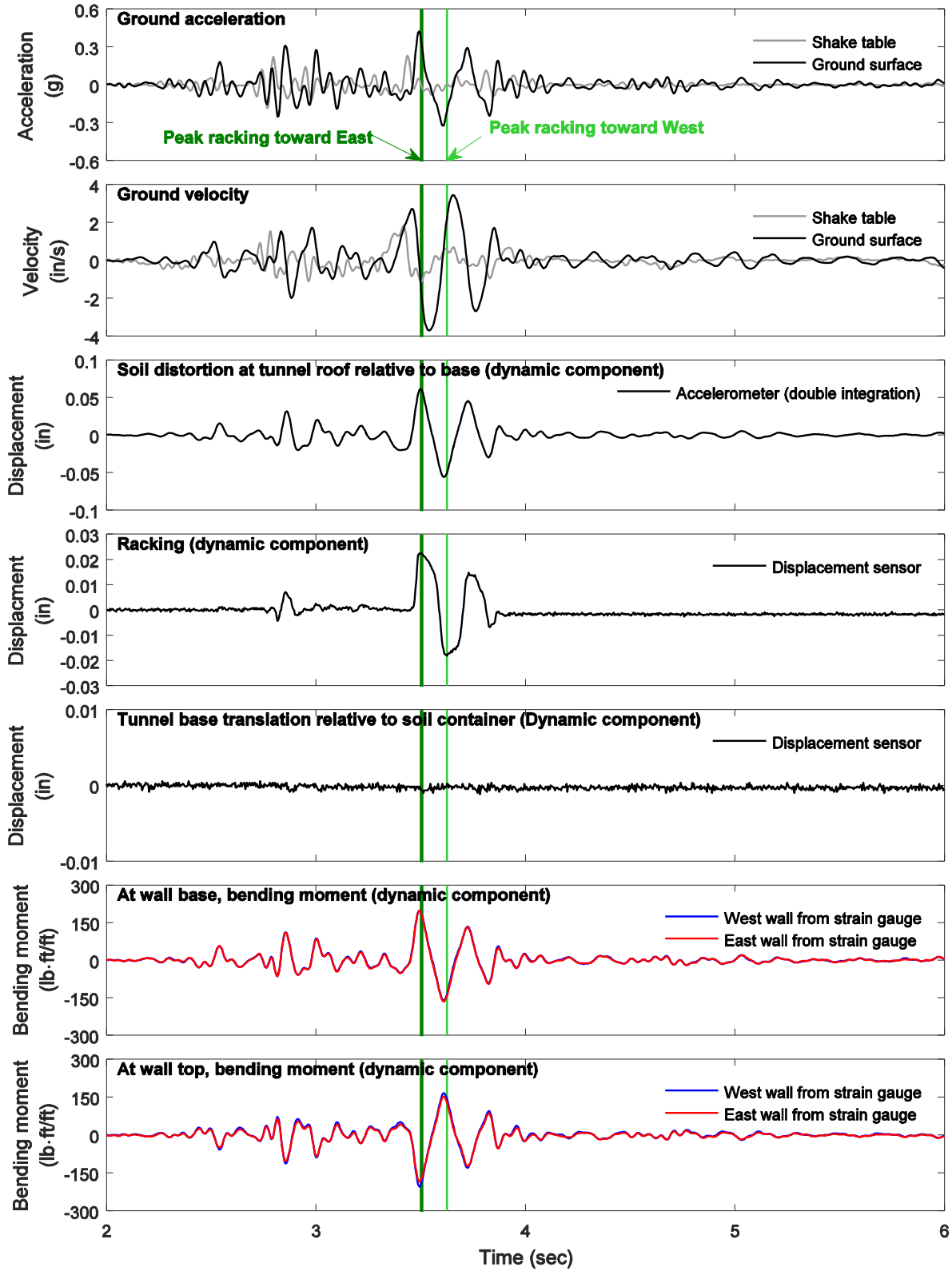

Figure C–6: Model 1 response time histories during Nor100PT2 input excitation in model scale (2 ft overburden soil)

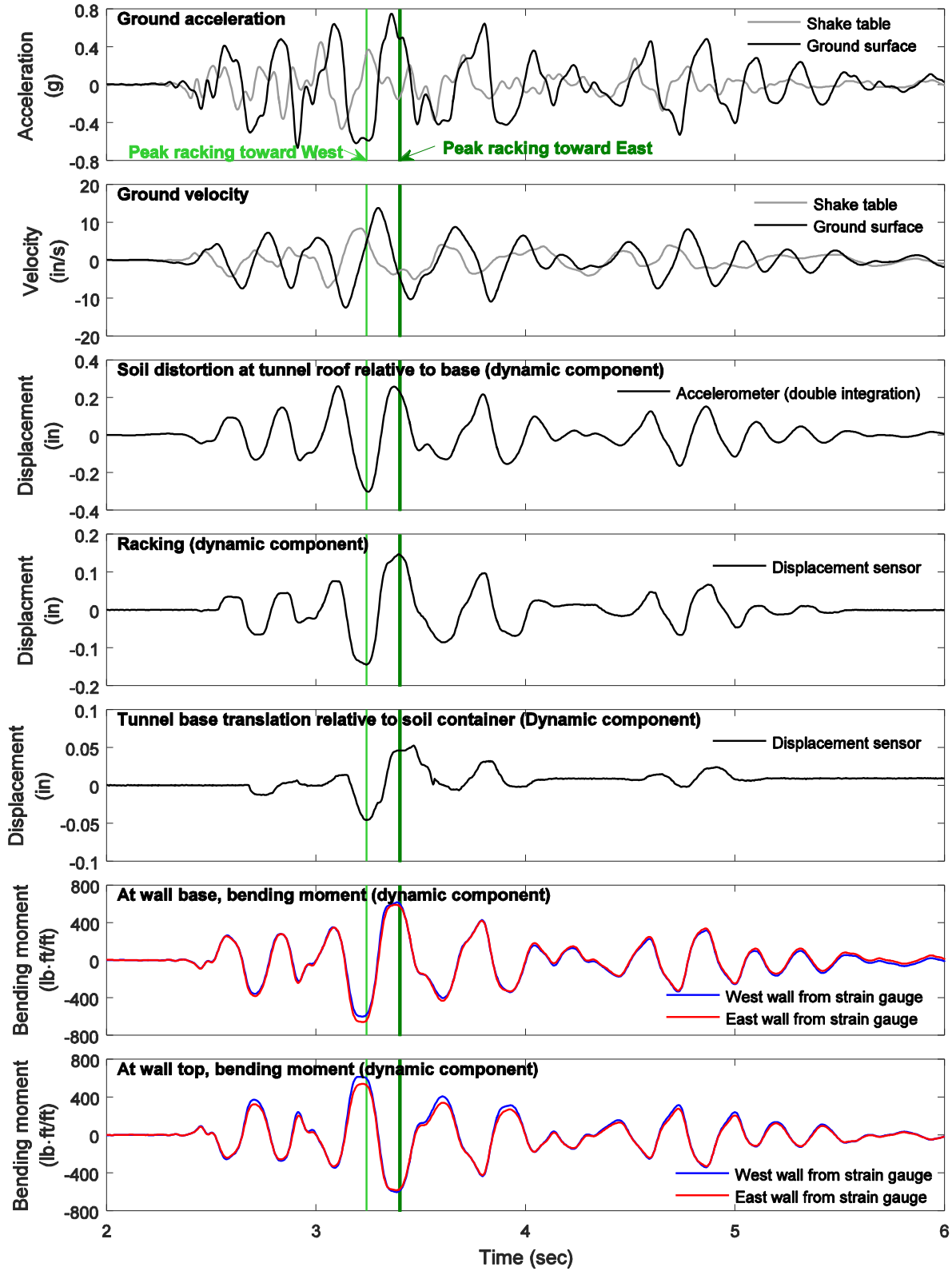

Figure C–7: Model 1 response time histories during Tak100PT2 input excitation in model scale (2 ft overburden soil)

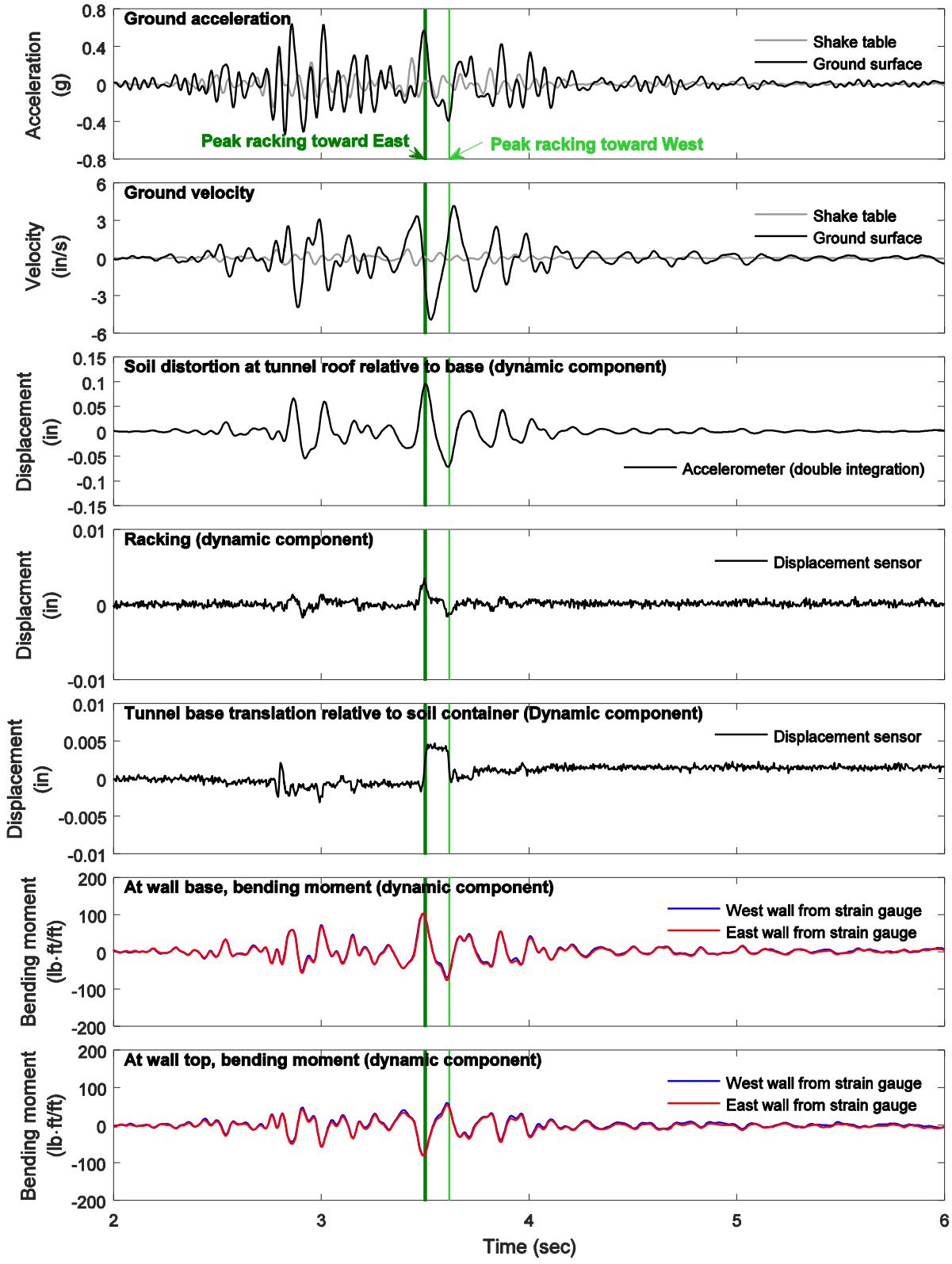

Figure C–8: Model 2 response time histories during Nor100PT2 input excitation in model scale (without overburden soil)

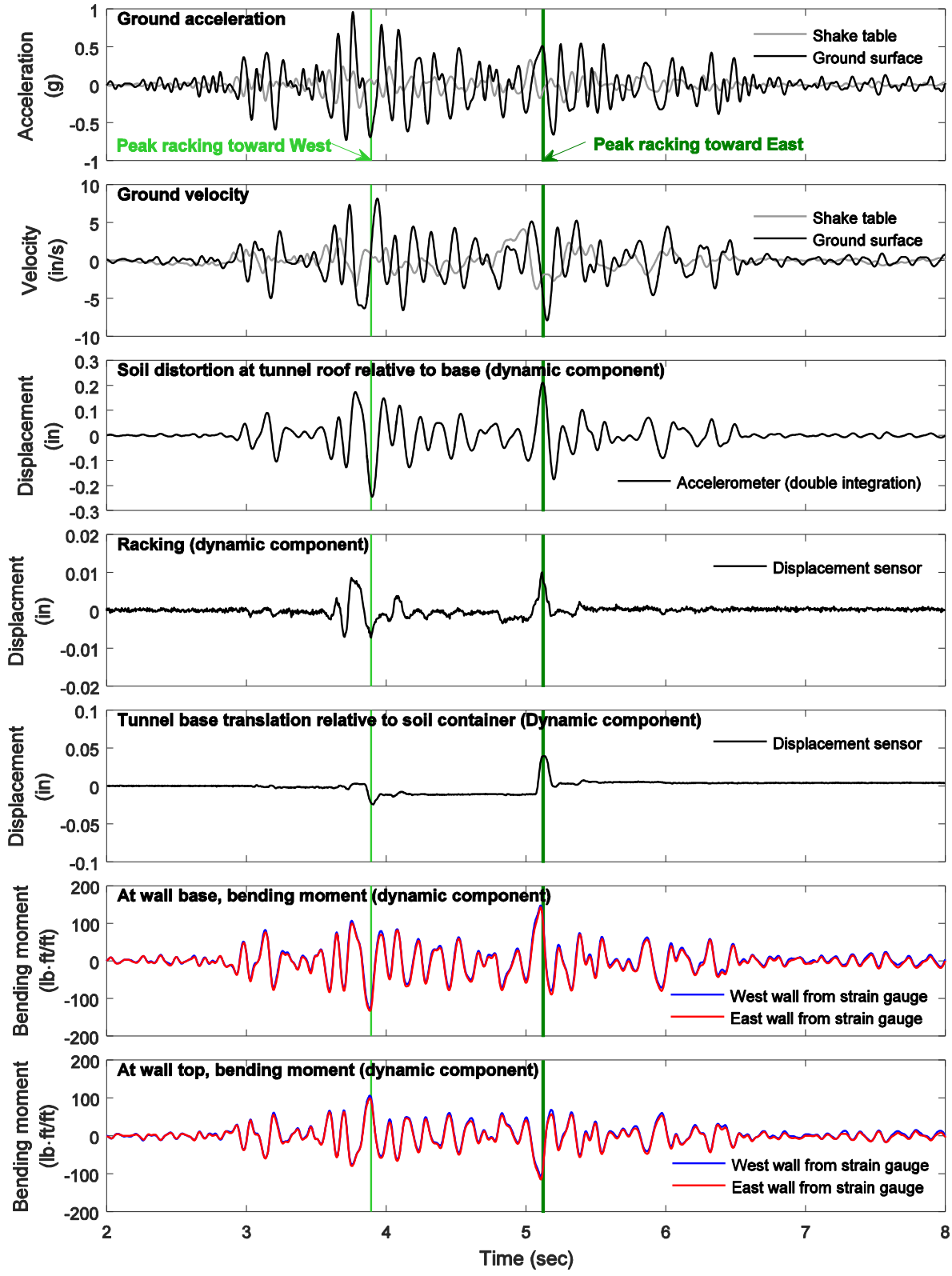

Figure C–9: Model 2 response time histories during Nor100PT1 input excitation in model scale (without overburden soil)

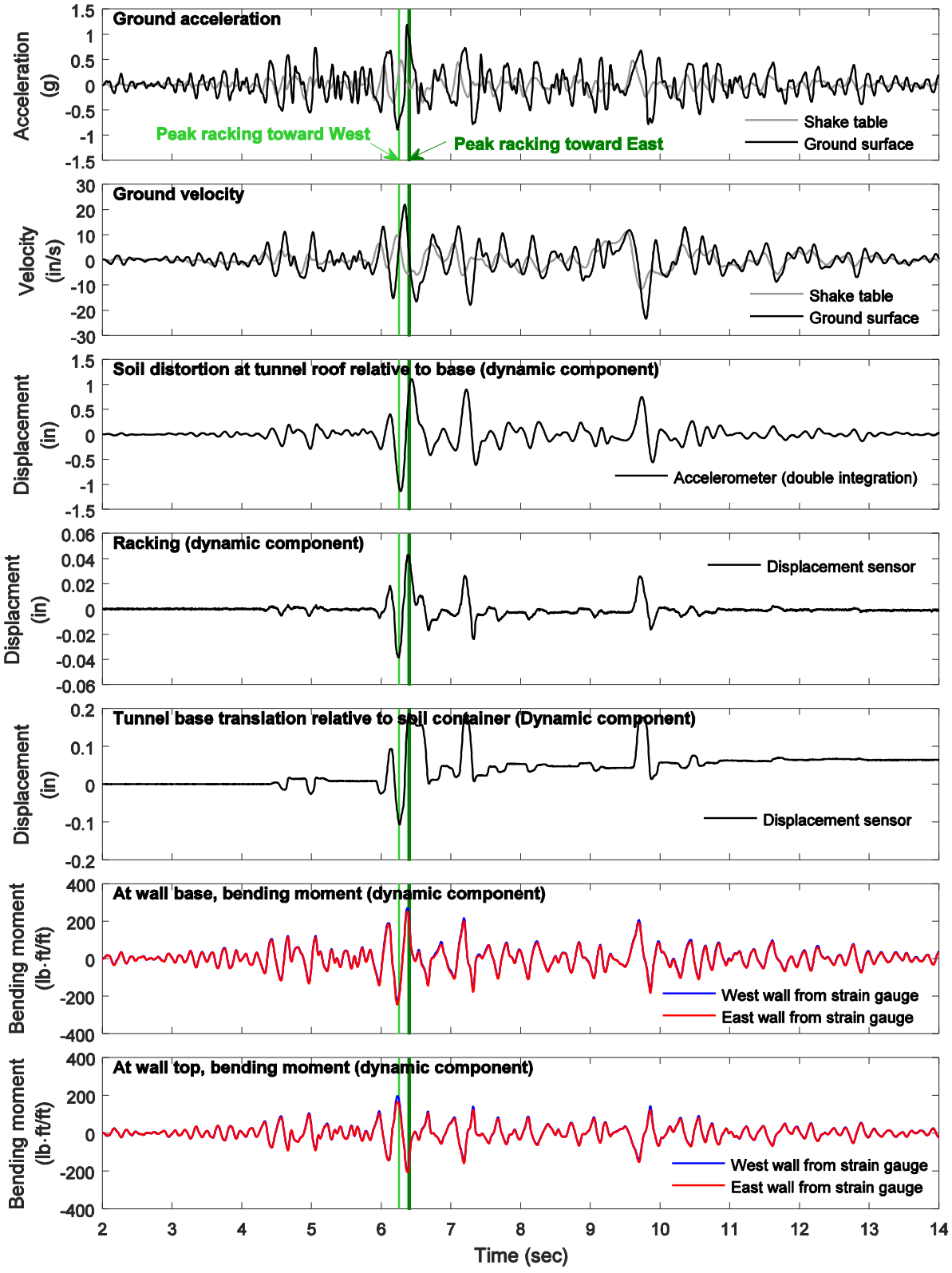

Figure C–10: Model 2 response time histories during Nor100PT0 input excitation in model scale (without overburden soil)

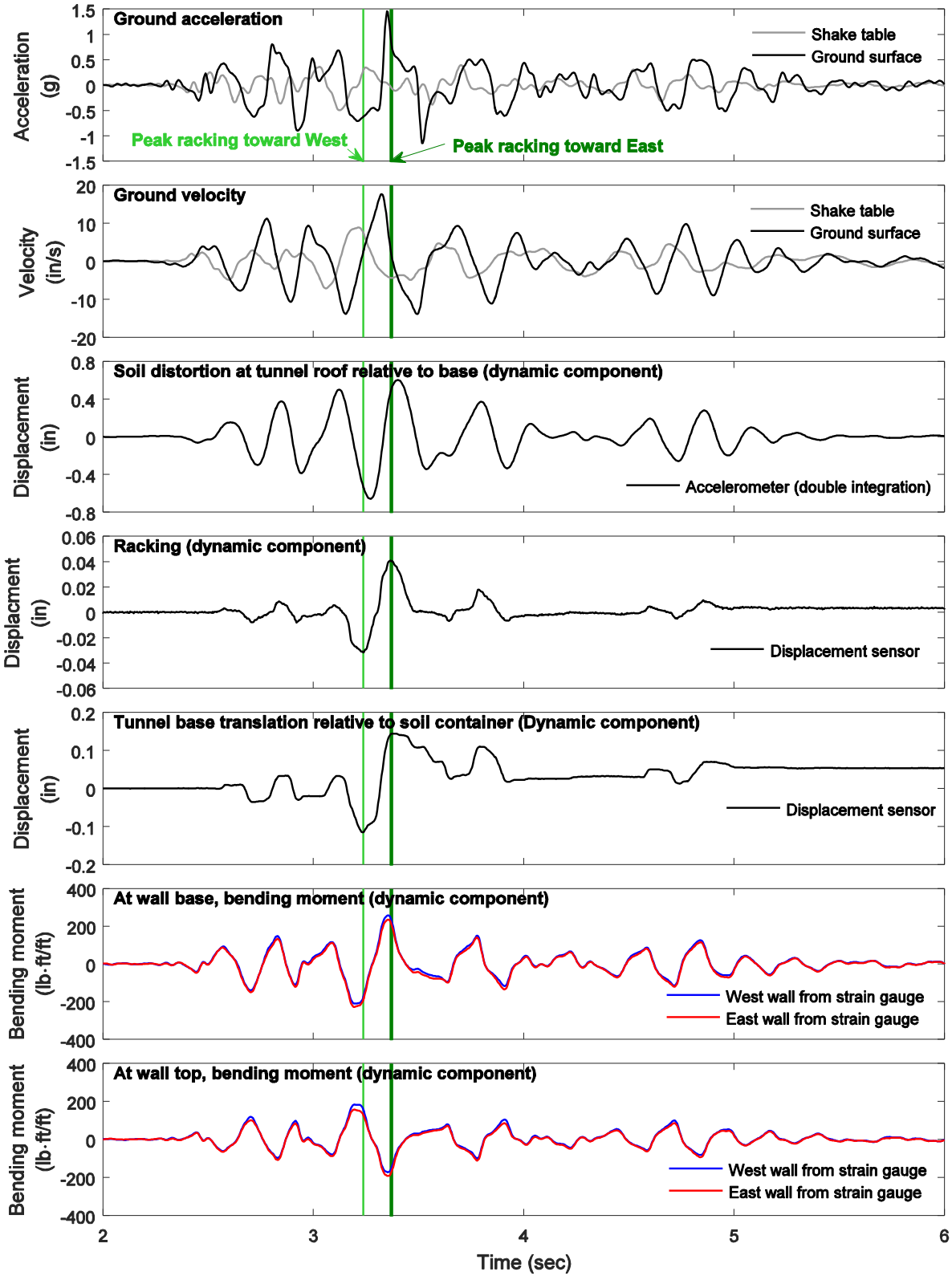

Figure C–11: Model 2 response time histories during Tak100PT2 input excitation in model scale (without overburden soil)

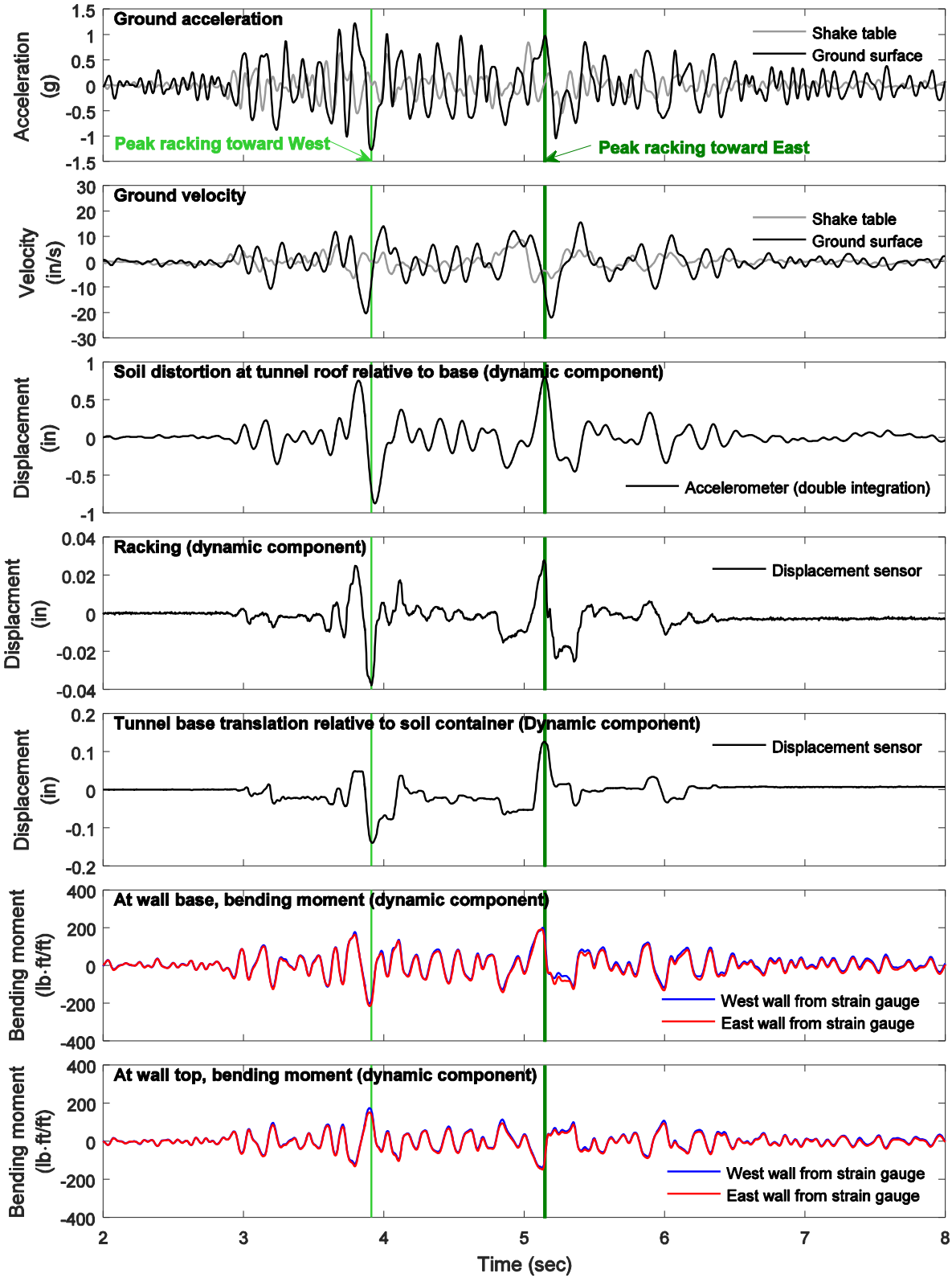

Figure C–12: Model 2 response time histories during Nor200PT1 input excitation in model scale (without overburden soil)

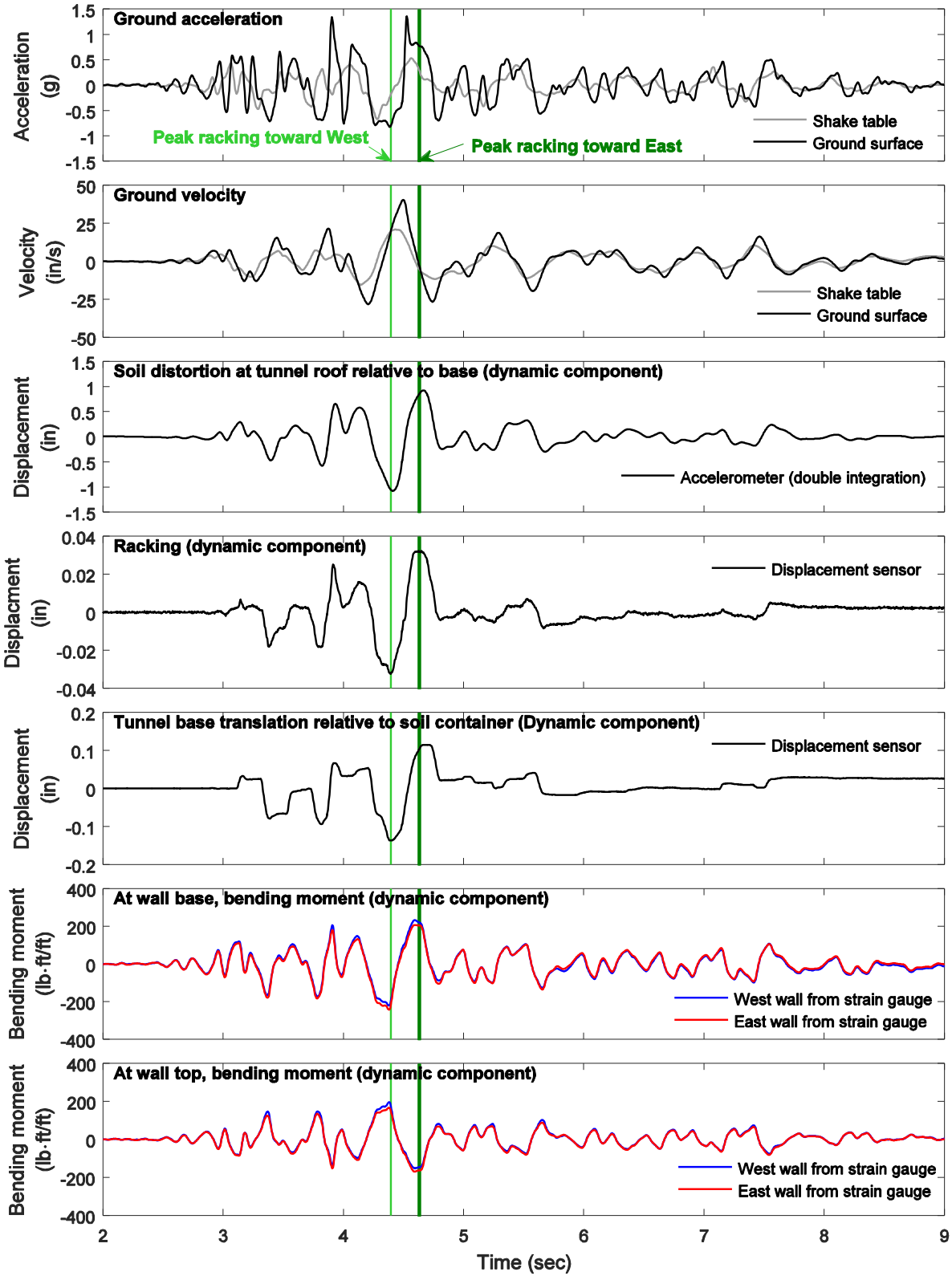

Figure C–13: Model 2 response time histories during Tak100PT1 input excitation in model scale (without overburden soil)

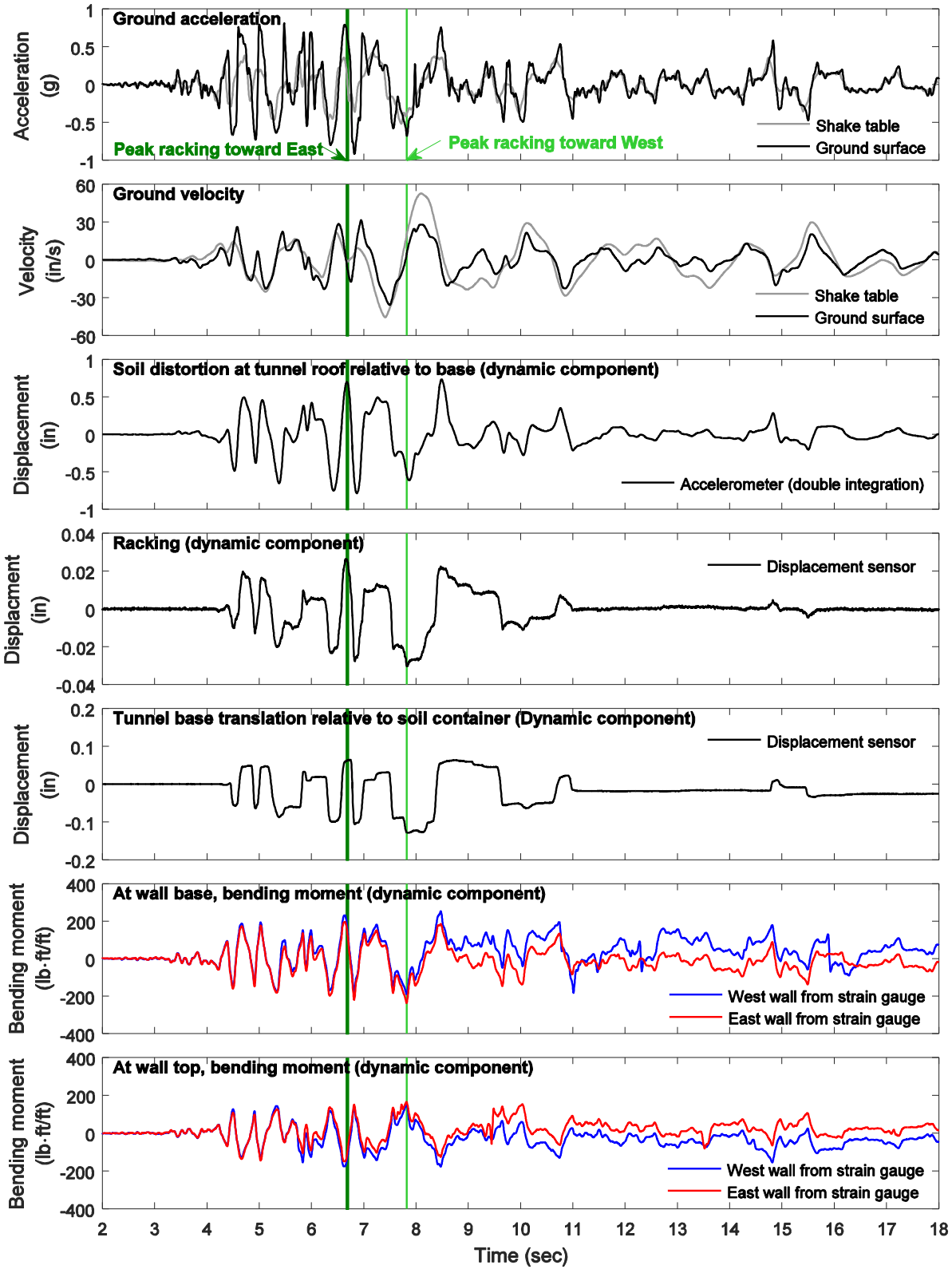

Figure C–14: Model 2 response time histories during Tak100PT0 input excitation in model scale (without overburden soil)

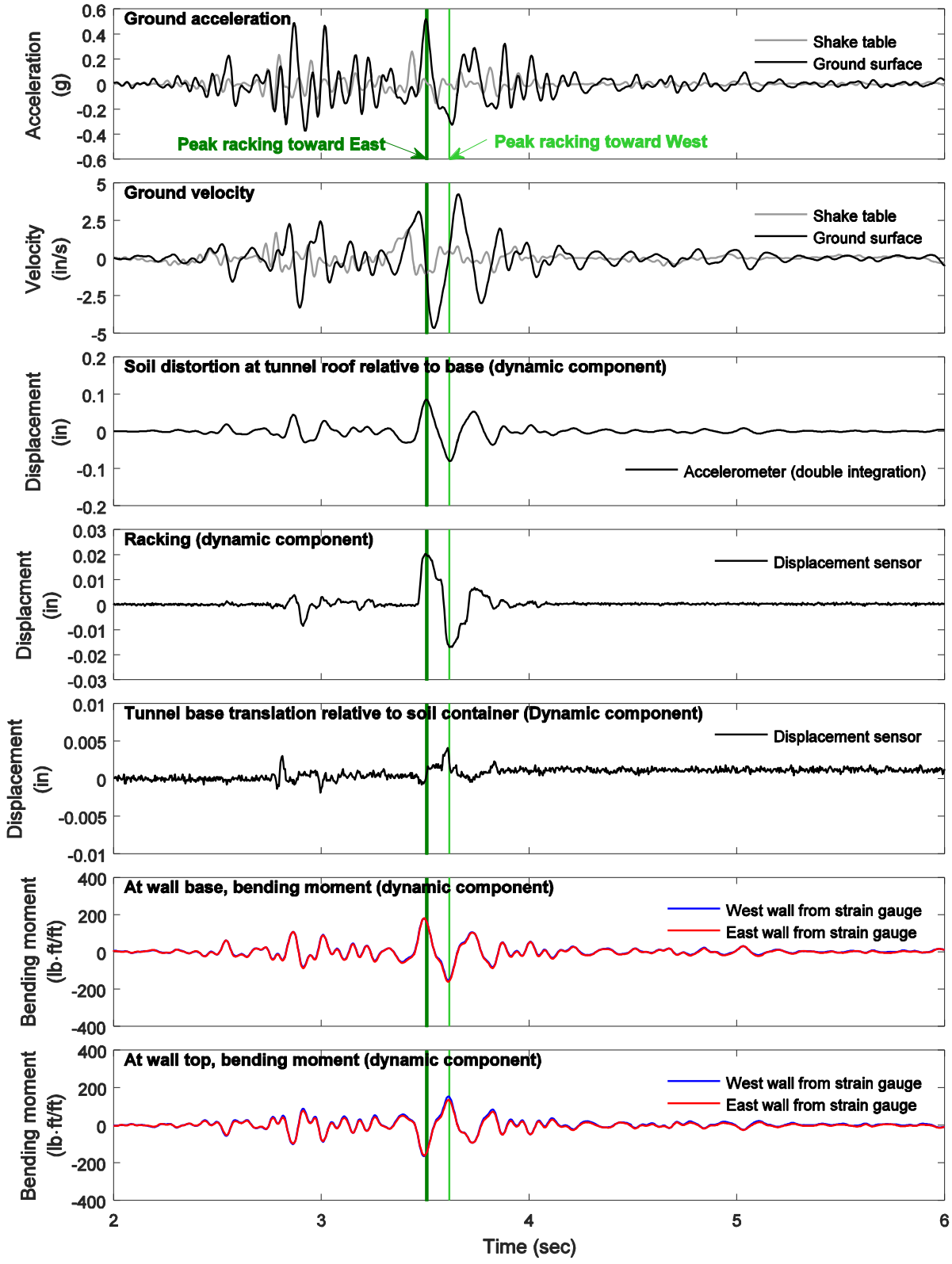

Figure C–15: Model 3 response time histories during Nor100PT2 input excitation in model scale (1 ft overburden soil)

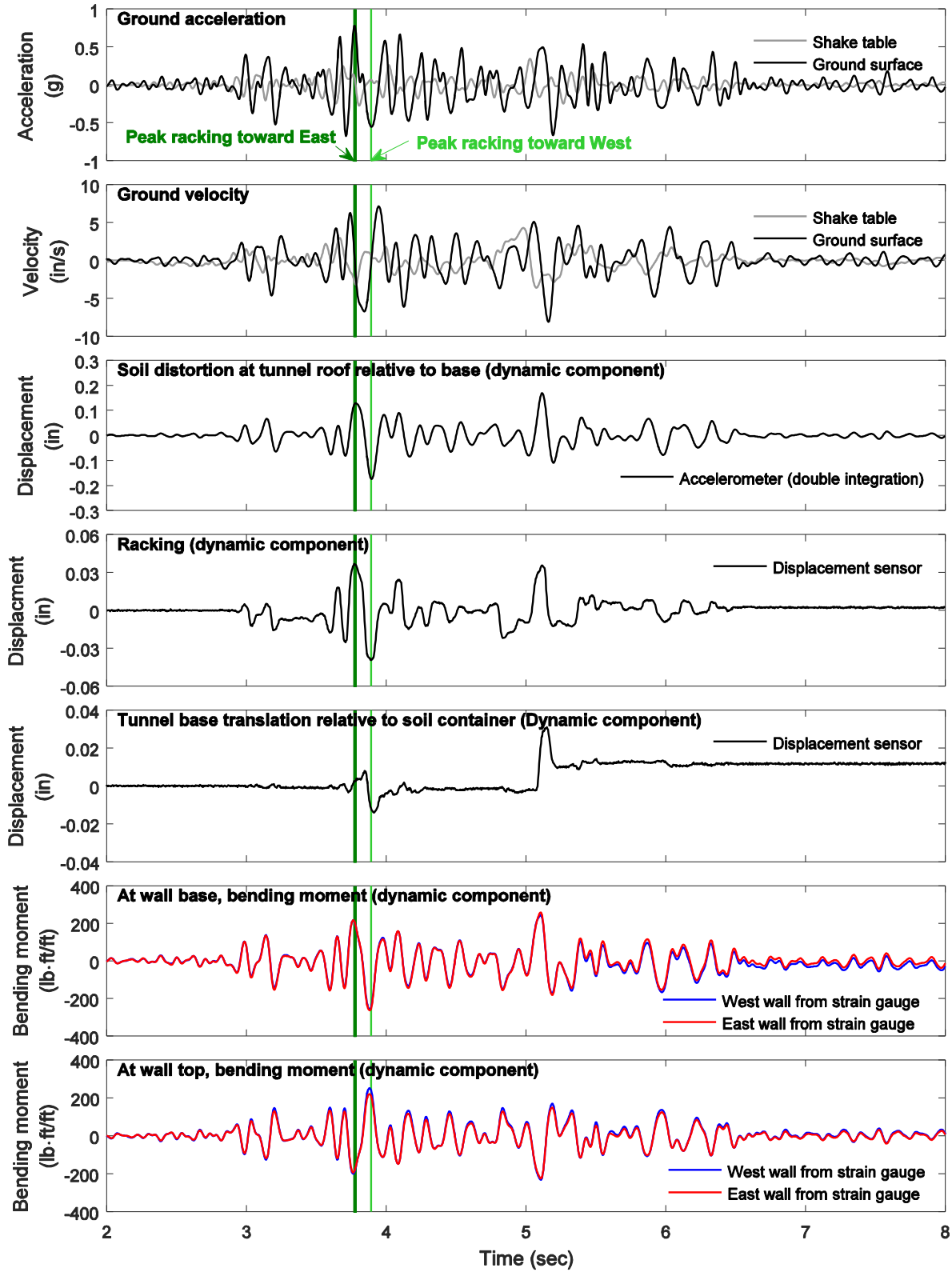

Figure C–16: Model 3 response time histories during Nor100PT1 input excitation in model scale (1 ft overburden soil)

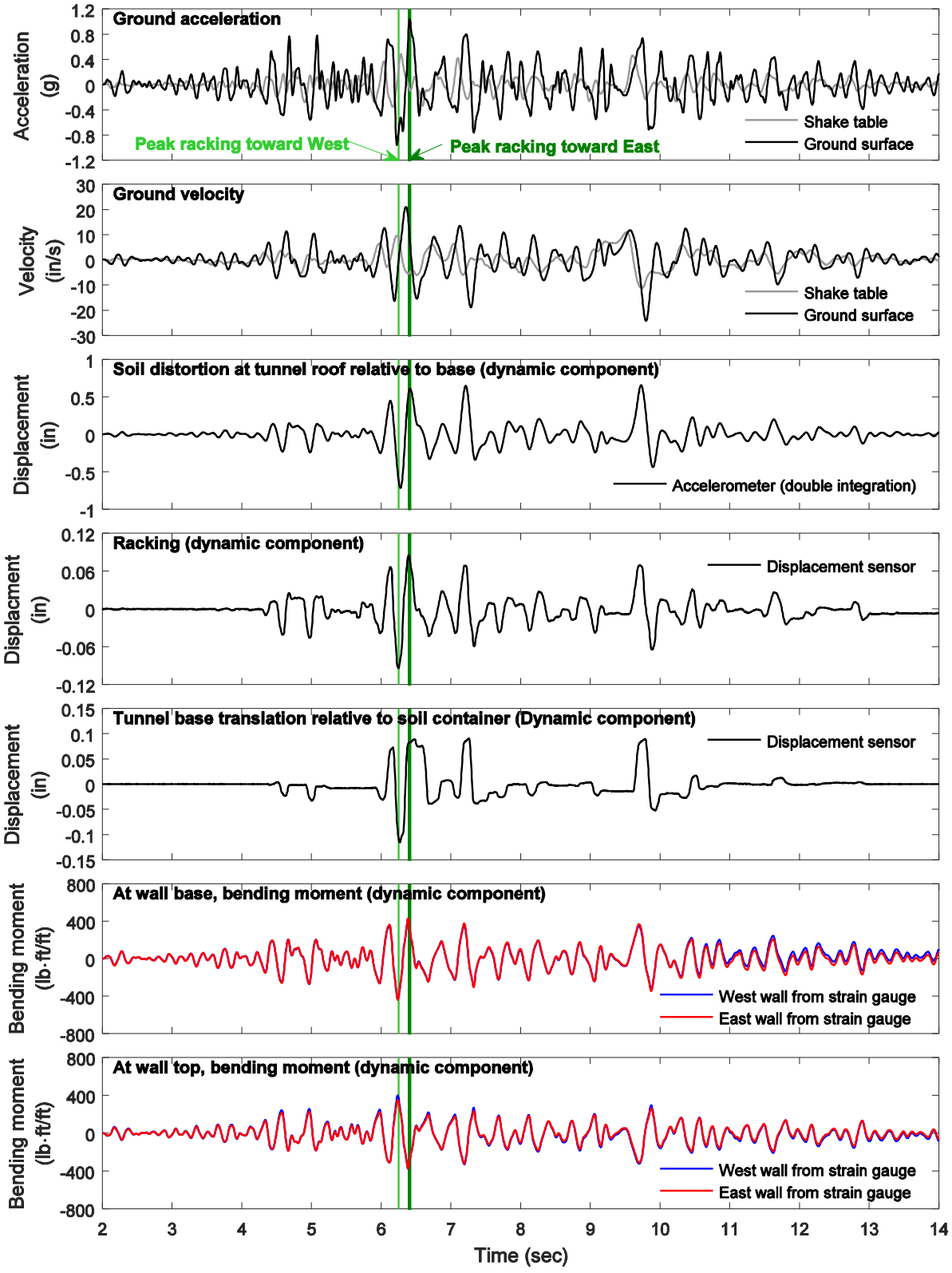

Figure C–17: Model 3 response time histories during Nor100PT0 input excitation in model scale (1 ft overburden soil)

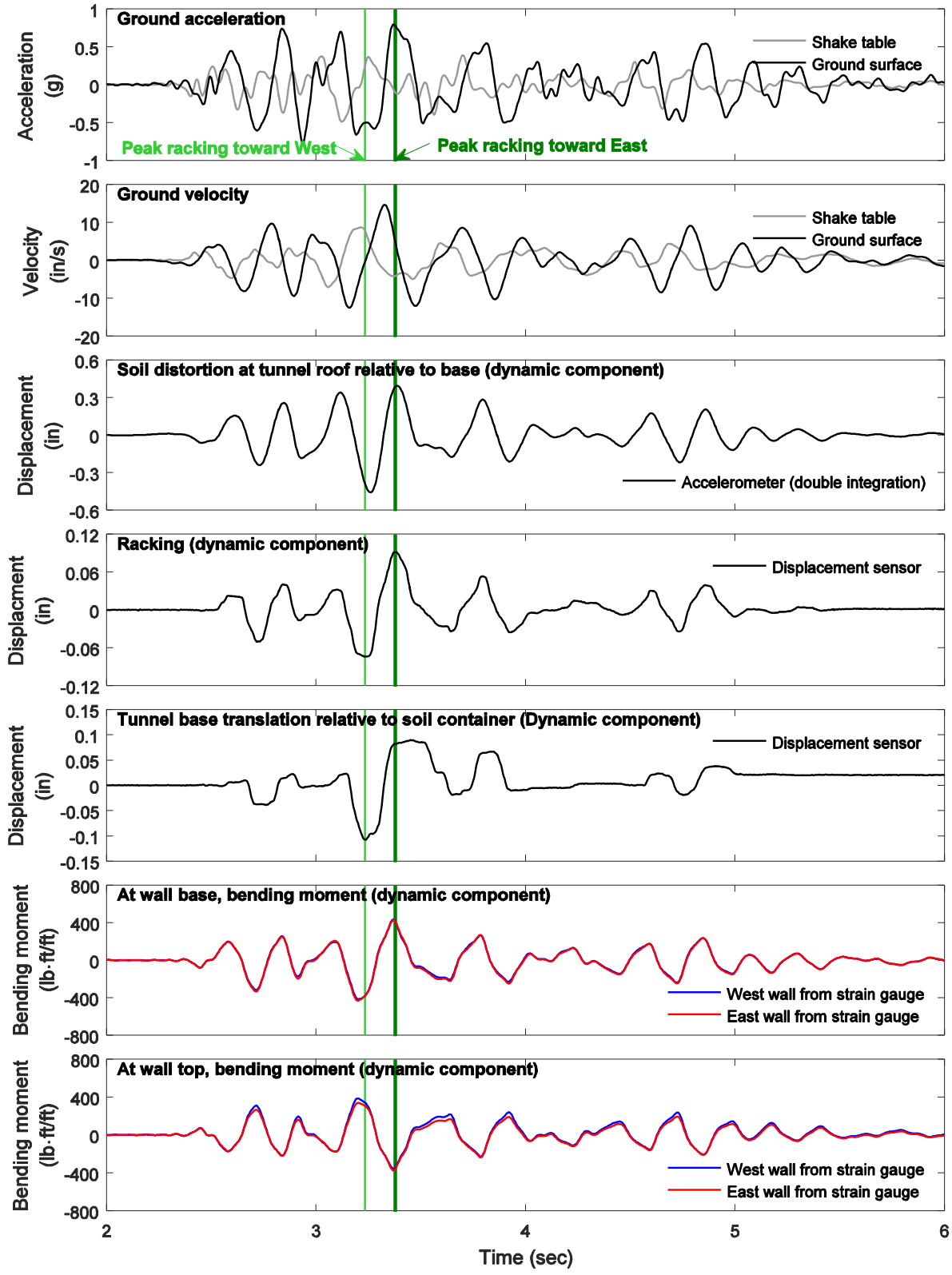

Figure C–18: Model 3 response time histories during Tak100PT2 input excitation in model scale (1 ft overburden soil)

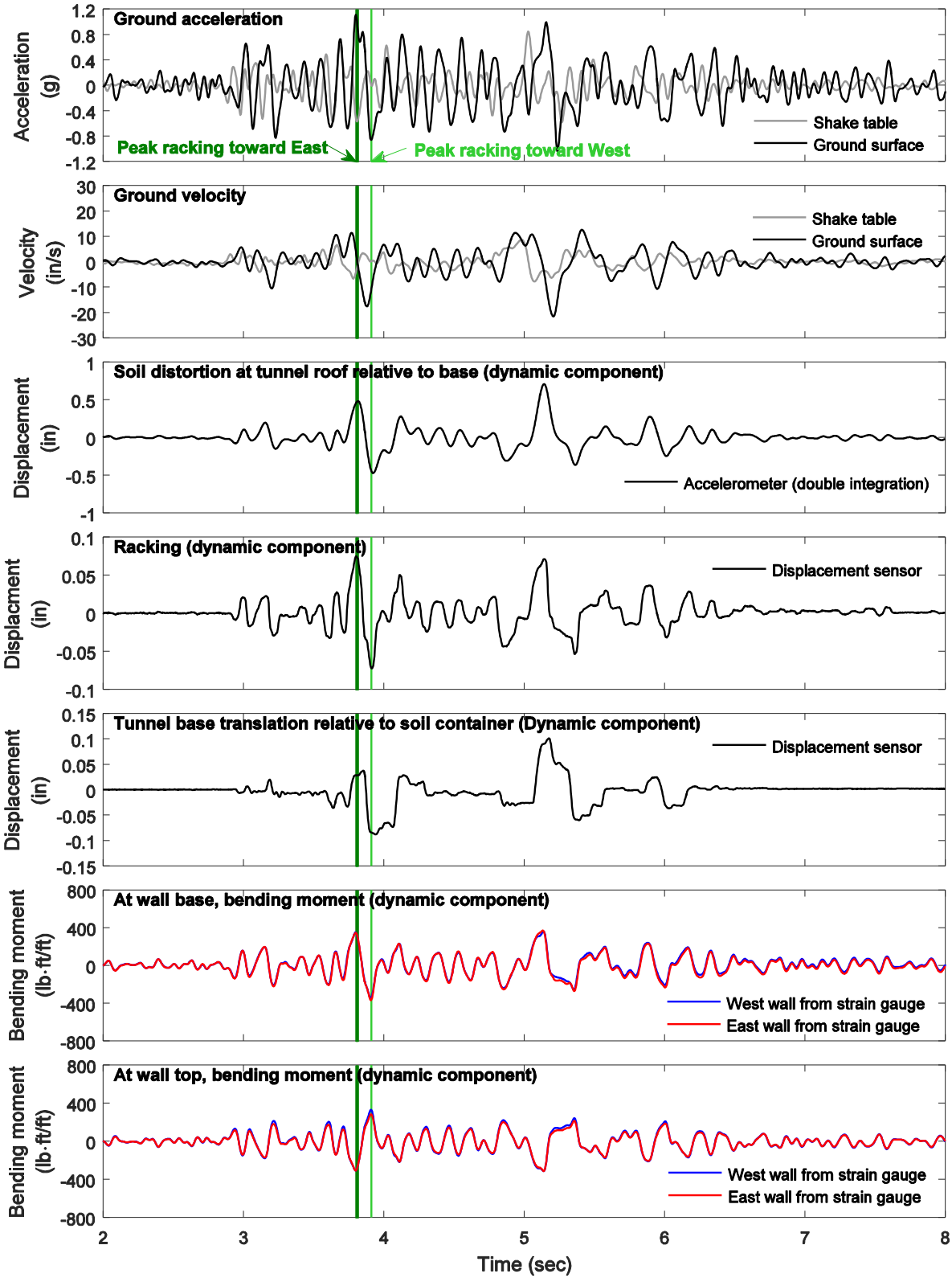

Figure C–19: Model 3 response time histories during Nor200PT1 input excitation in model scale (1 ft overburden soil)

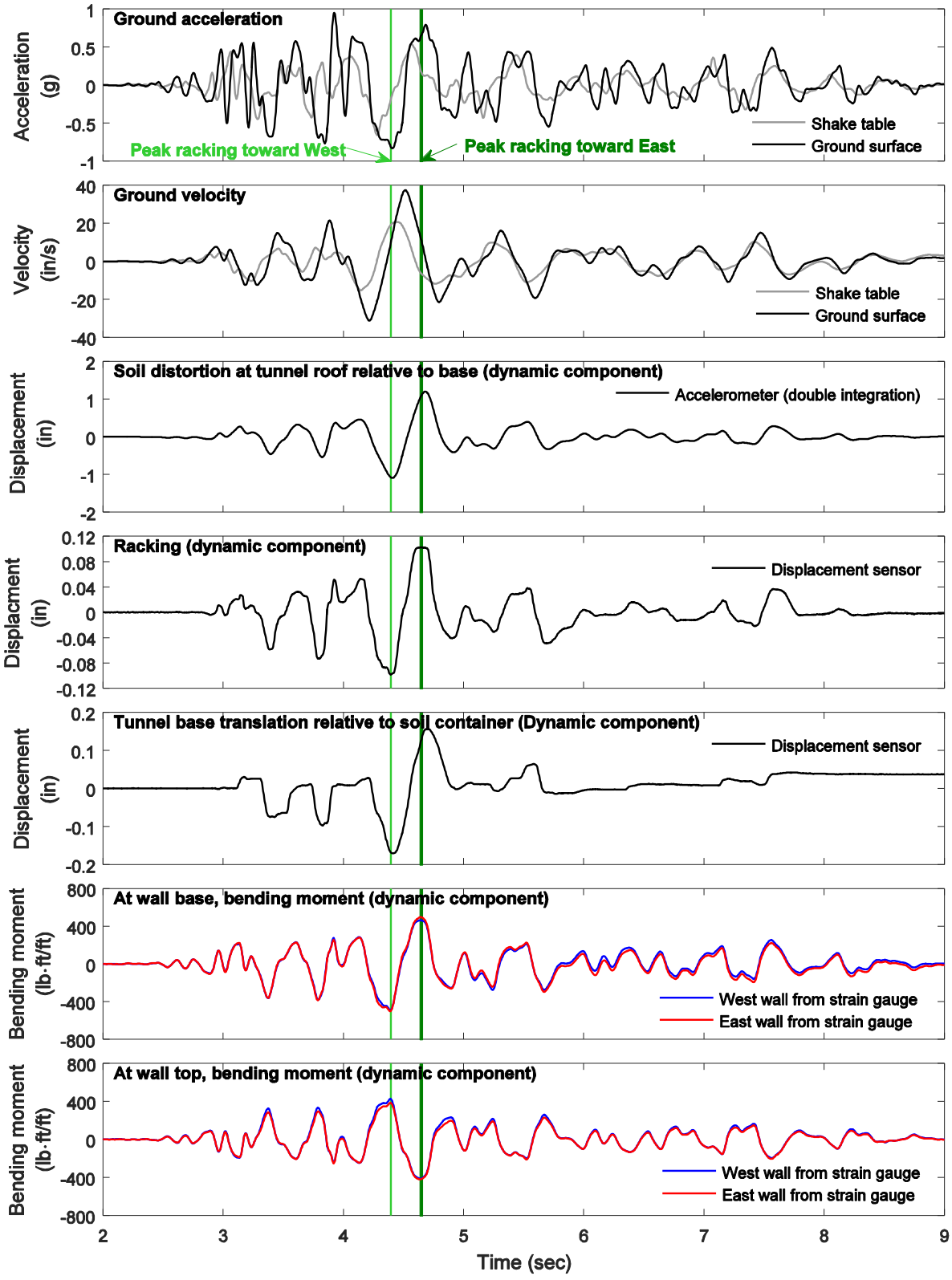

Figure C–20: Model 3 response time histories during Tak100PT1 input excitation in model scale (1 ft overburden soil)

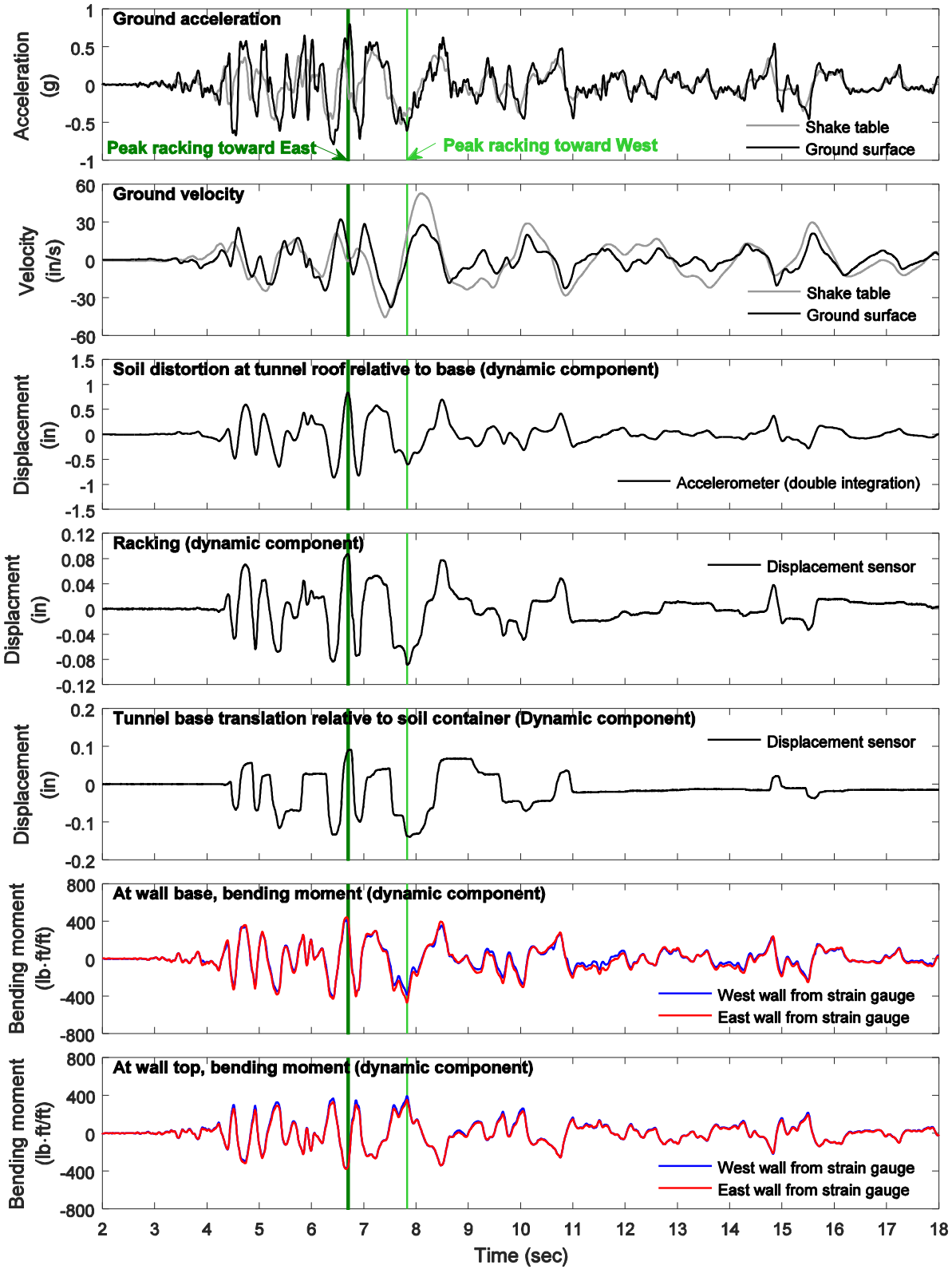

Figure C–21: Model 3 response time histories during Tak100PT0 input excitation in model scale (1 ft overburden soil)

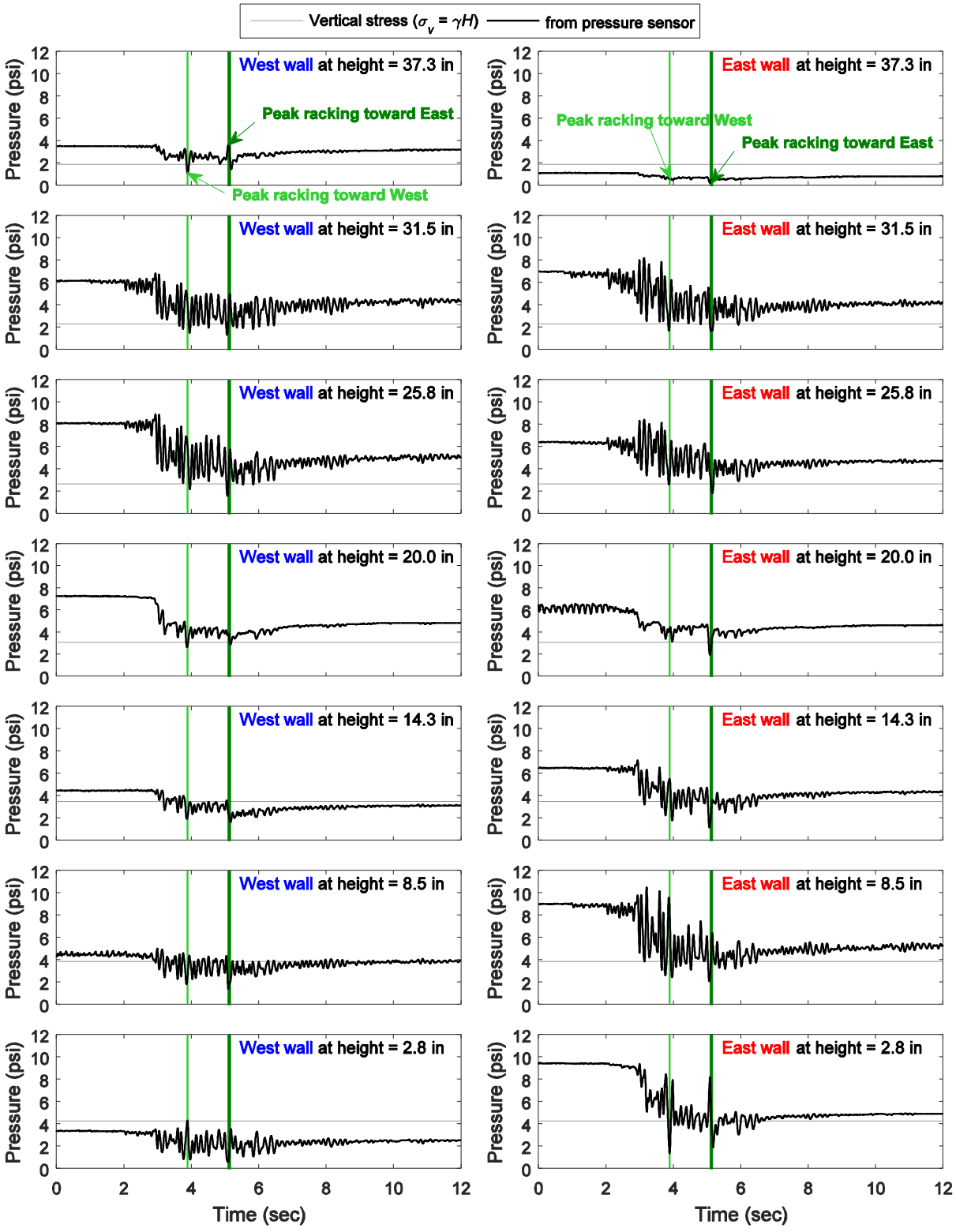

Figure C–22: Model 1 earth pressure time histories along the wall height during Nor100PT1 input excitation (2 ft overburden soil)

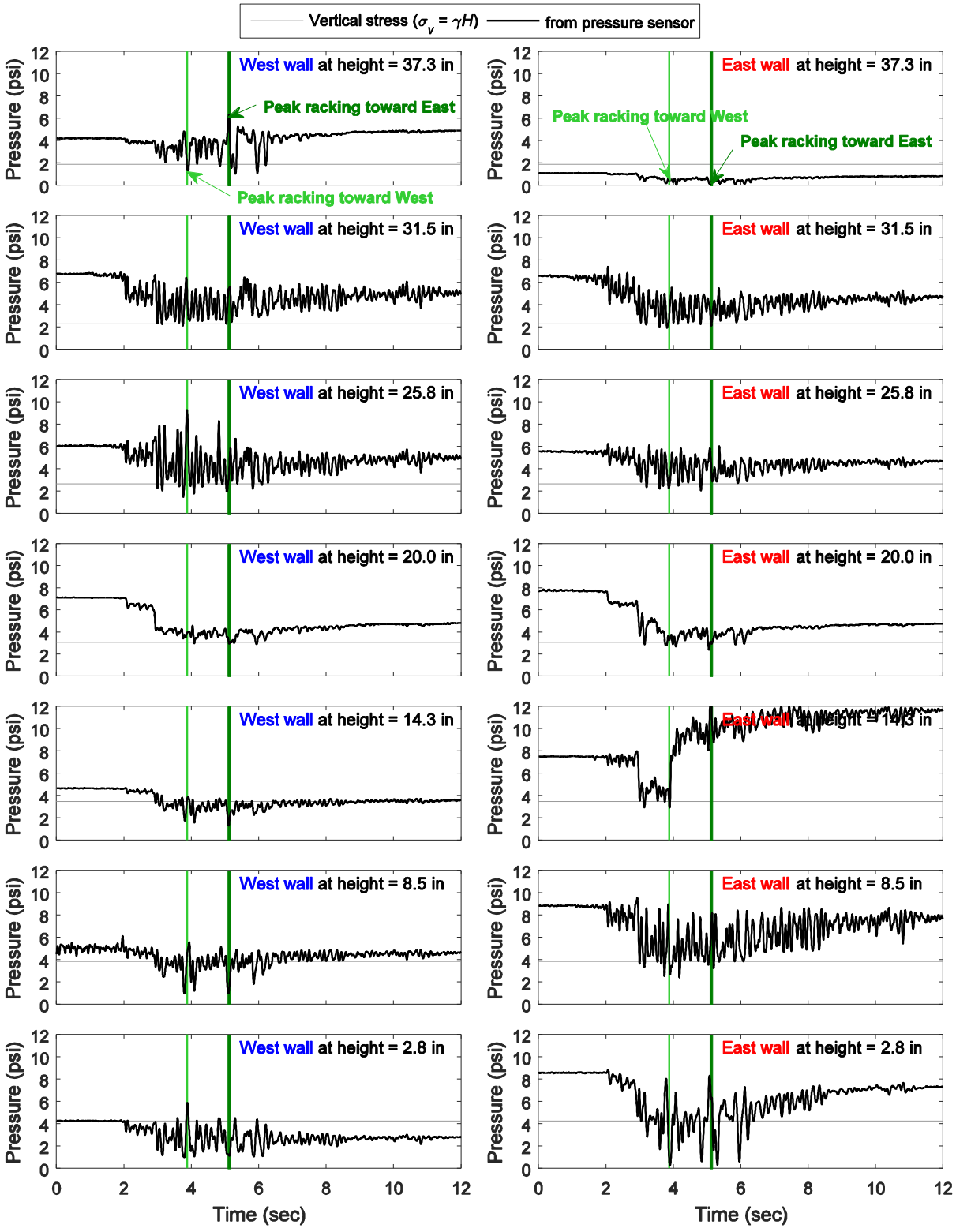

Figure C–23: Model 1 earth pressure time histories along the wall height during Nor200PT1 input excitation (2 ft overburden soil)

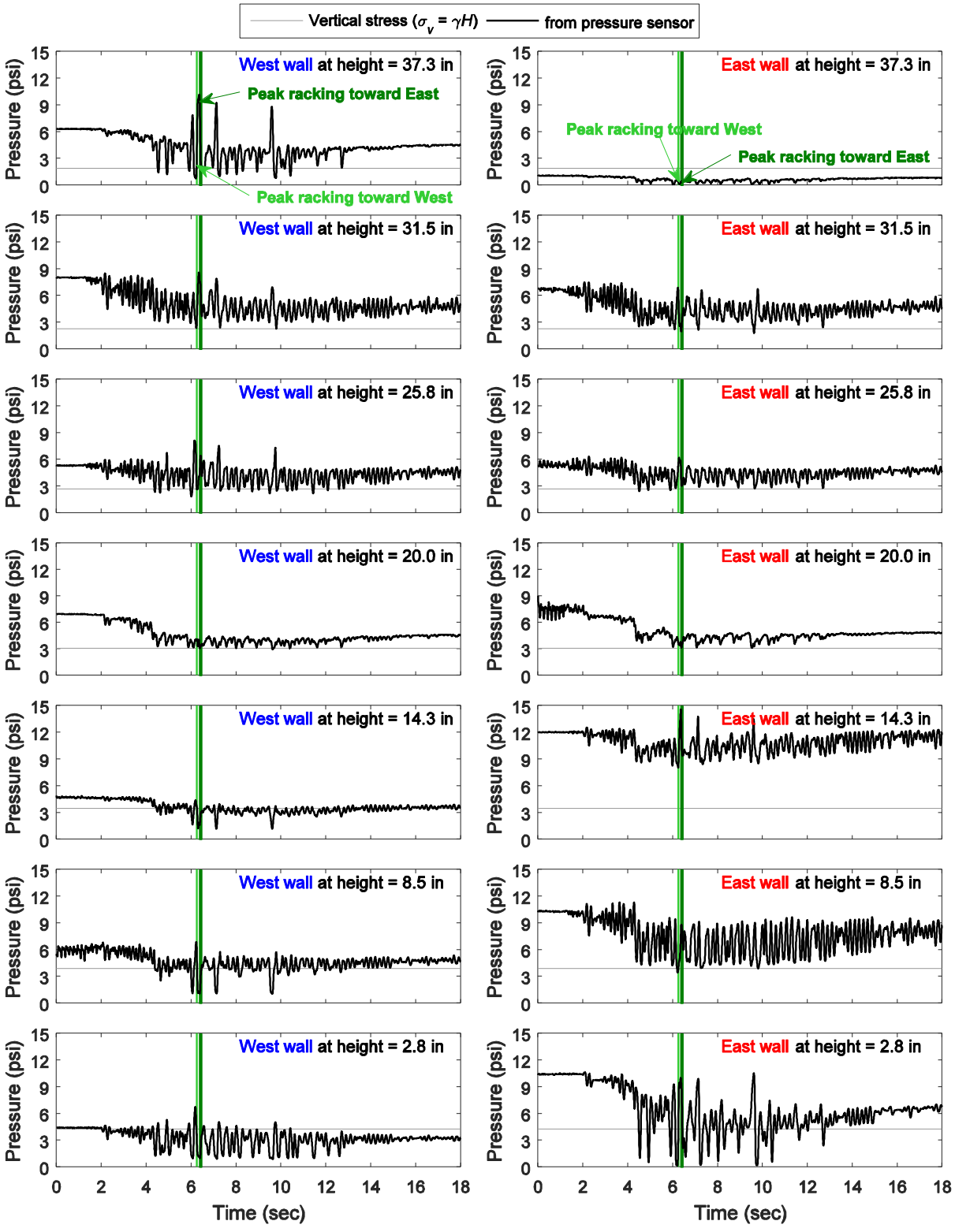

Figure C–24: Model 1 earth pressure time histories along the wall height during Nor100PT0 input excitation (2 ft overburden soil)

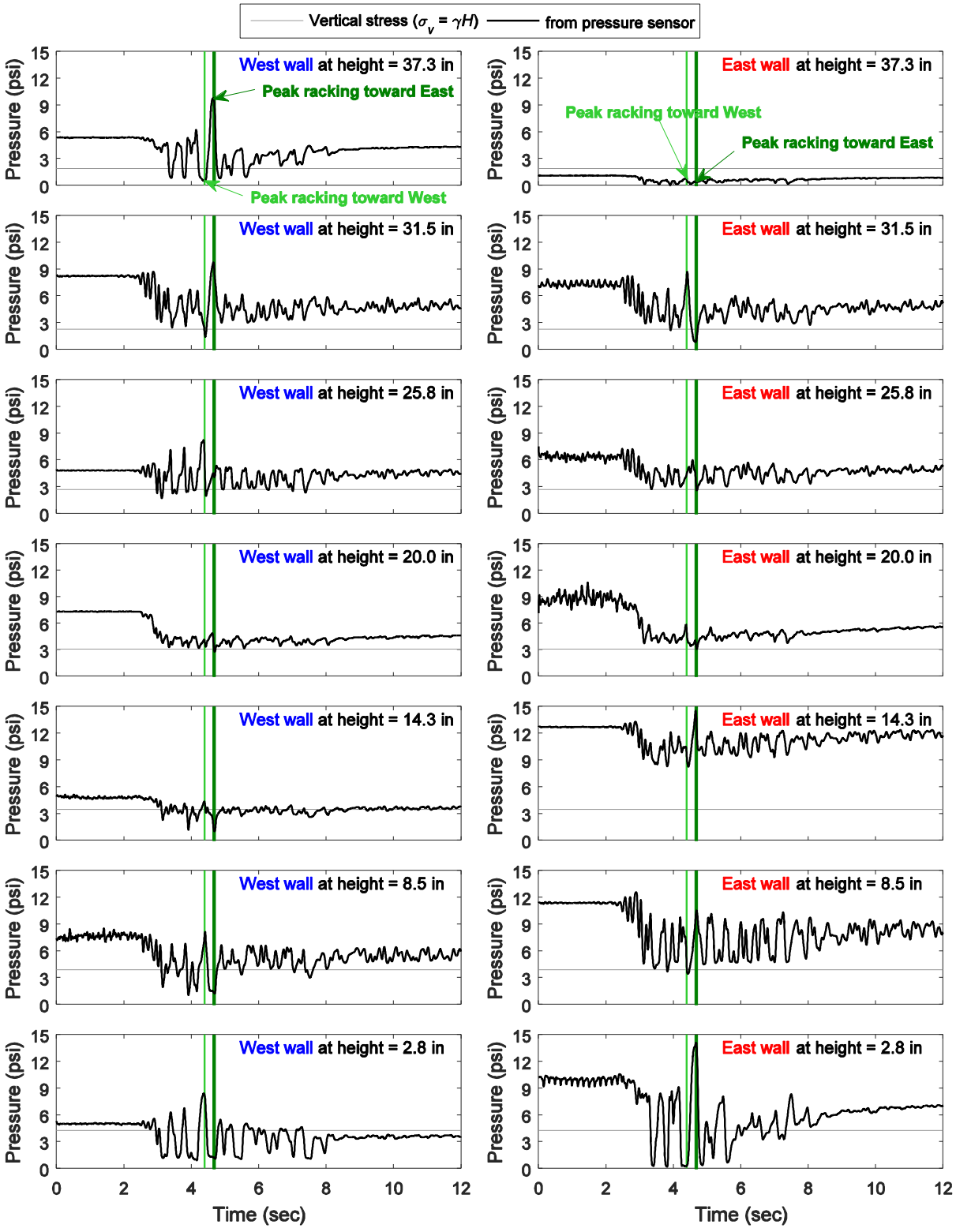

Figure C–25: Model 1 earth pressure time histories along the wall height during Tak100PT1 input excitation (2 ft overburden soil)

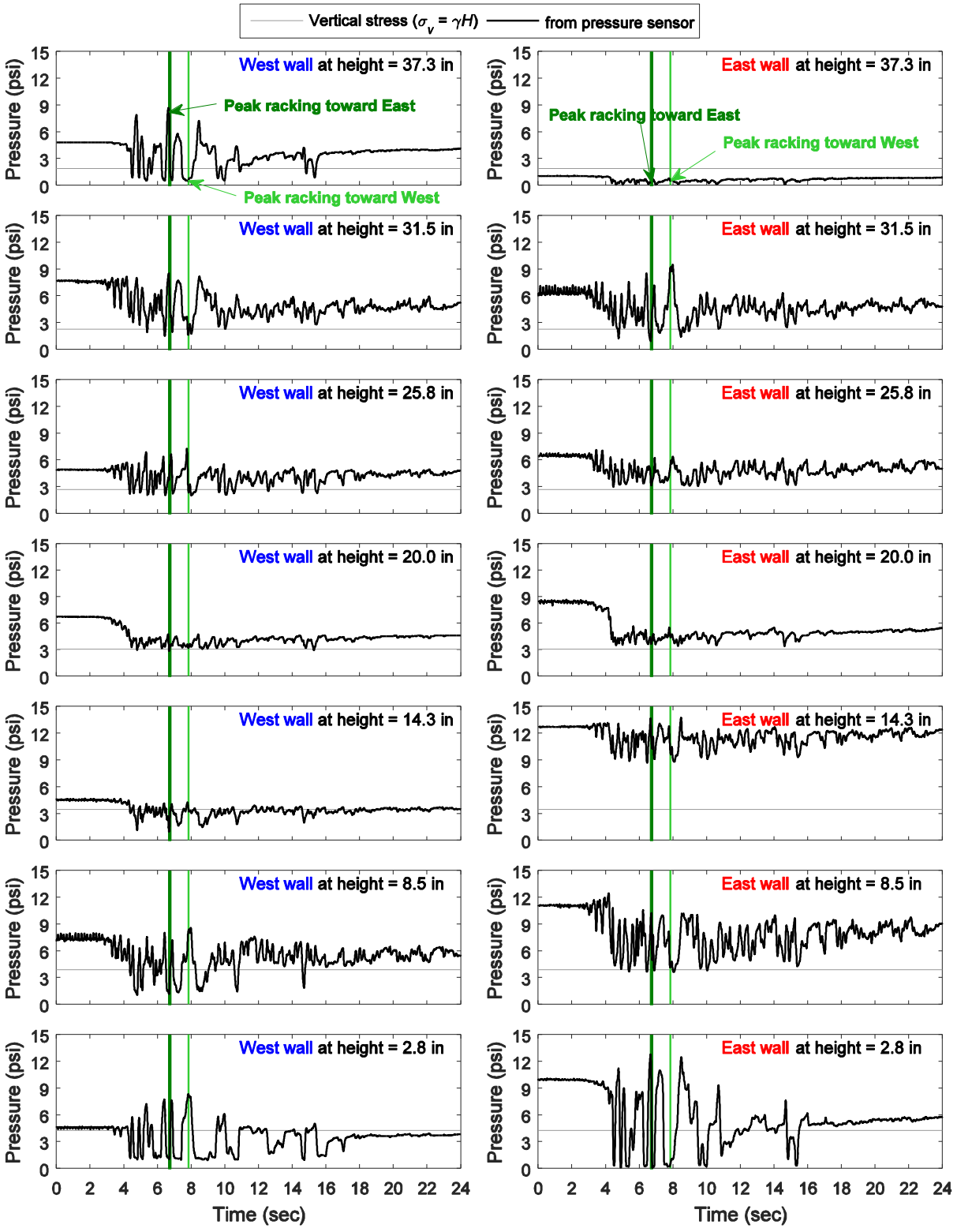

Figure C–26: Model 1 earth pressure time histories along the wall height during Tak100PT0 input excitation (2 ft overburden soil)

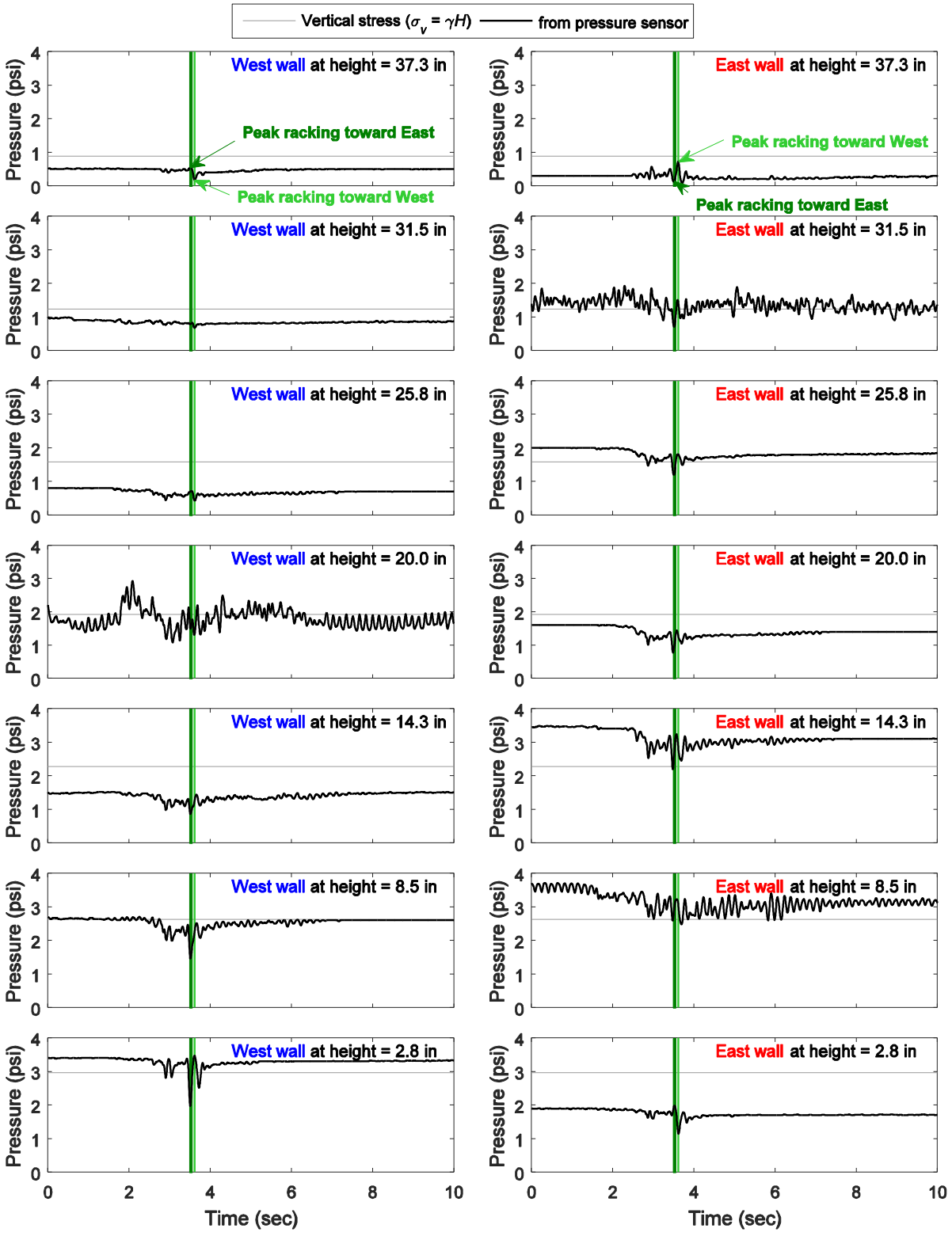

Figure C–27: Model 3 earth pressure time histories along the wall height during Nor100PT2 input excitation (1 ft overburden soil)

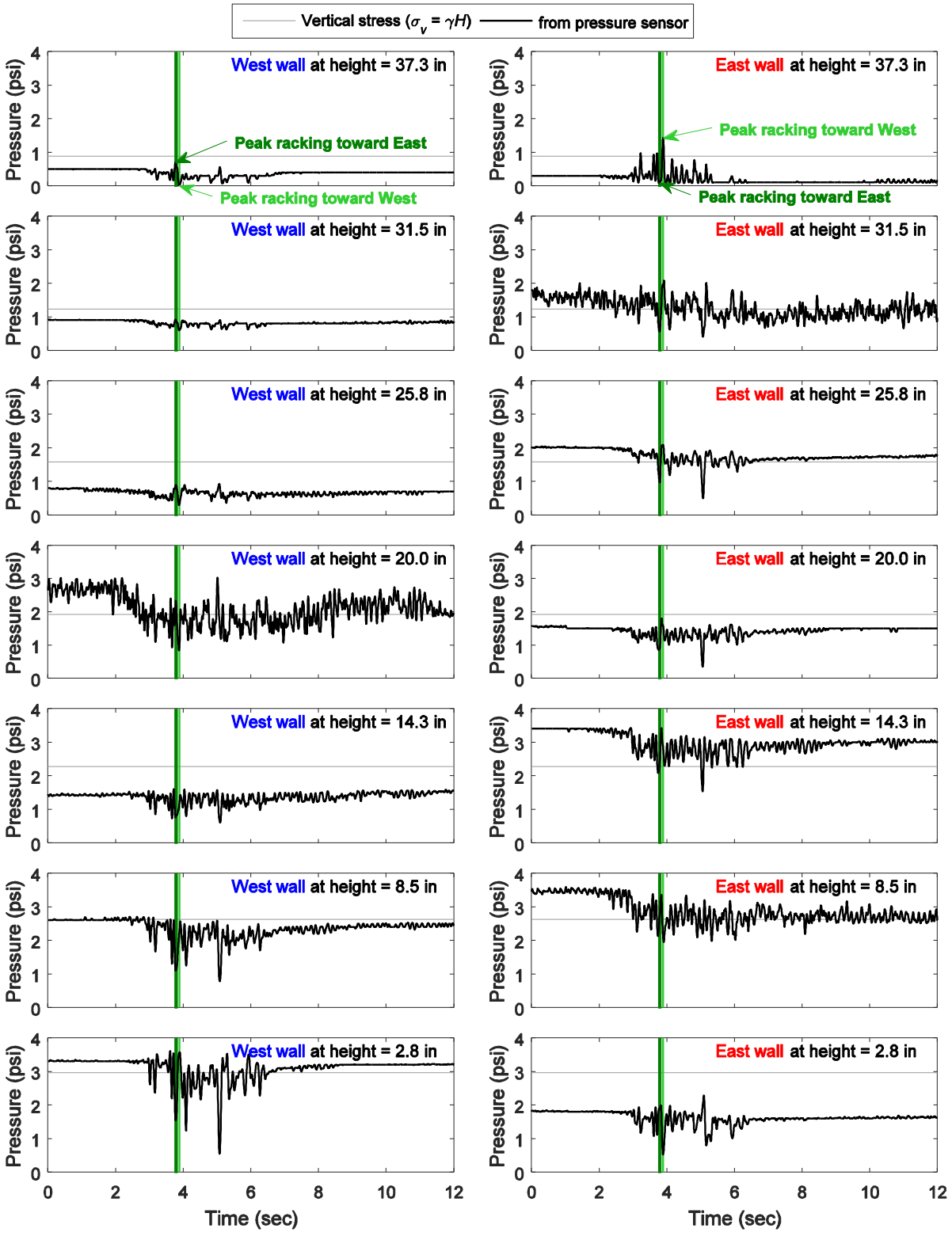

Figure C–28: Model 3 earth pressure time histories along the wall height during Nor100PT1 input excitation (1 ft overburden soil)

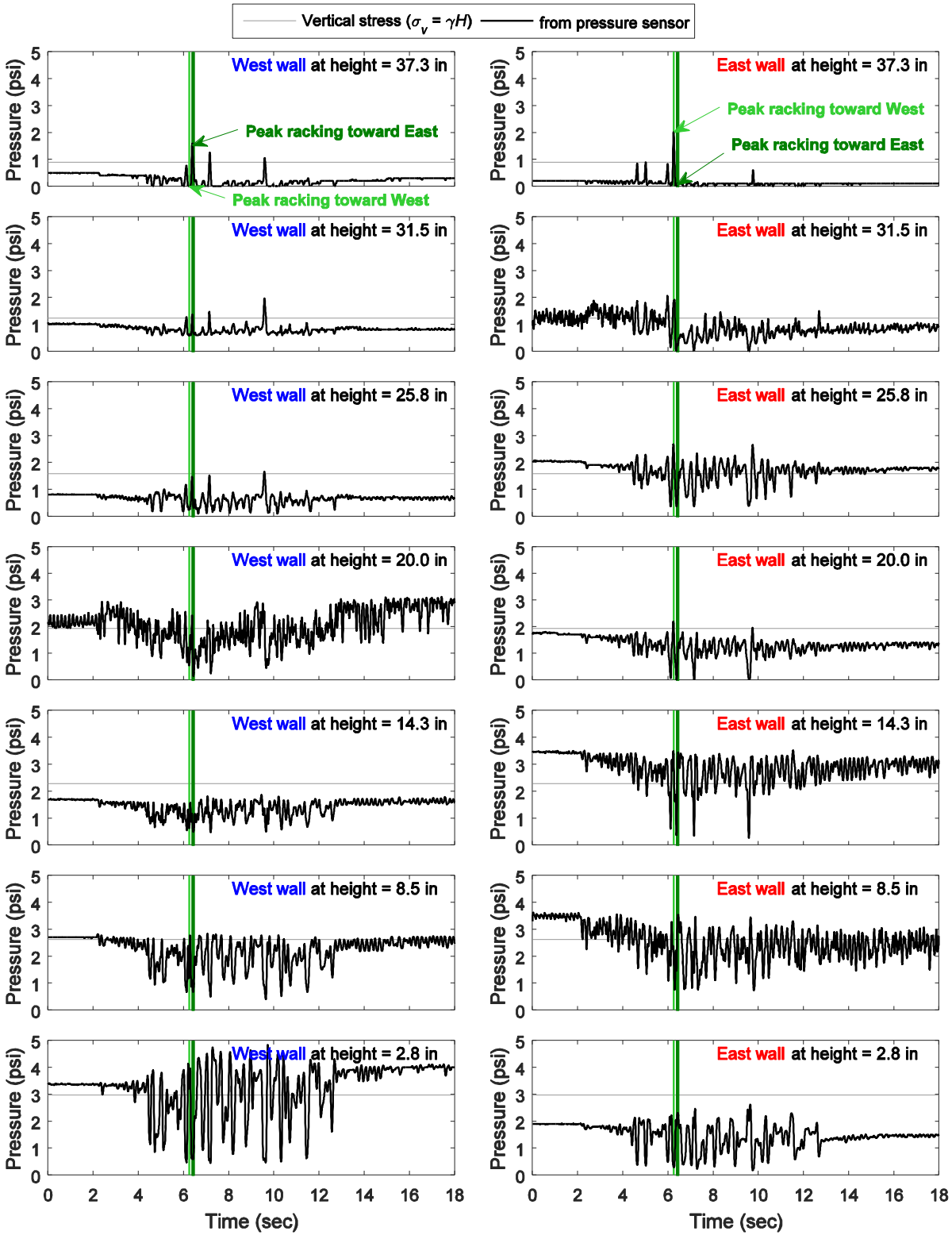

Figure C–29: Model 3 earth pressure time histories along the wall height during Nor100PT0 input excitation (1 ft overburden soil)

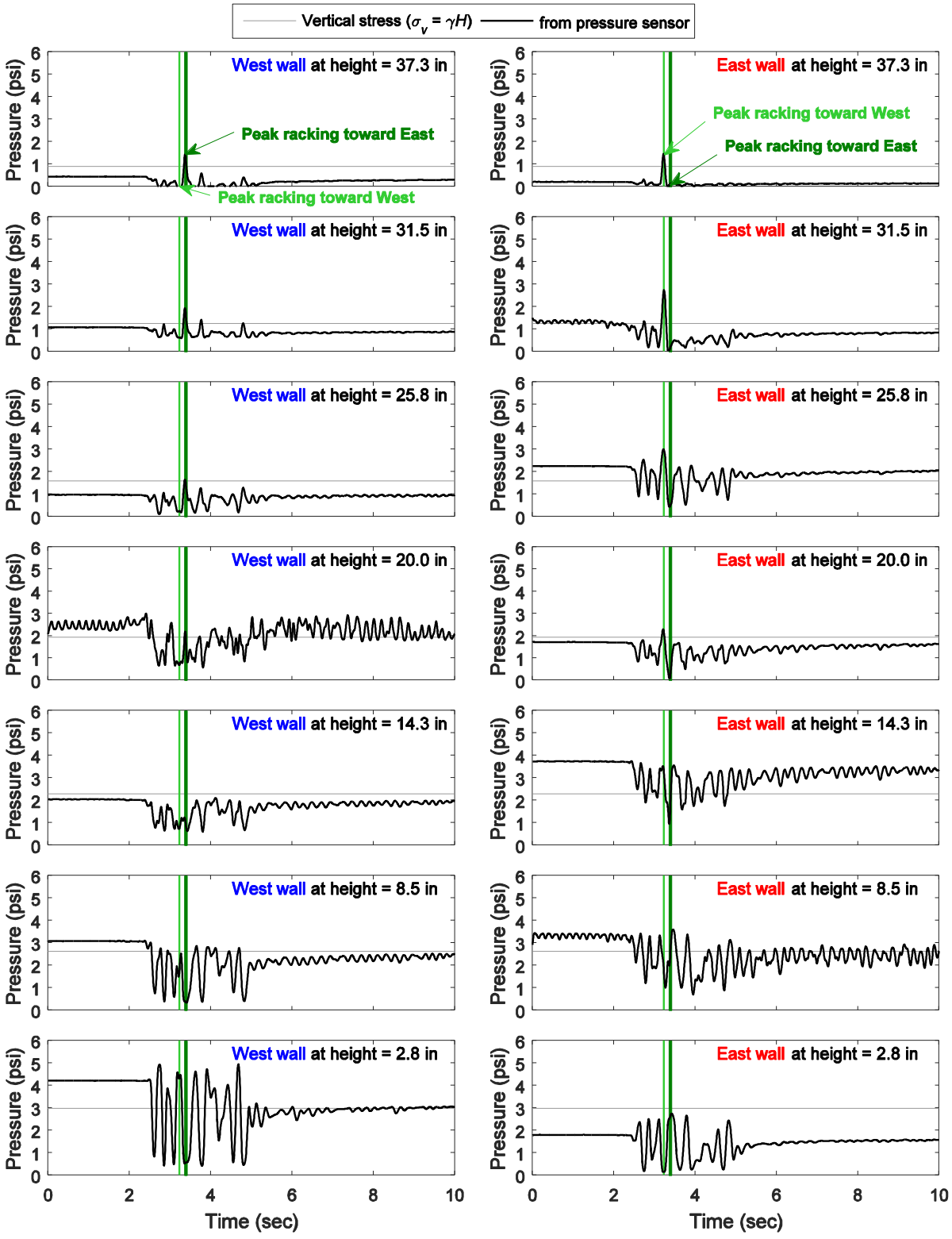

Figure C–30: Model 3 earth pressure time histories along the wall height during Tak100PT2 input excitation (1 ft overburden soil)

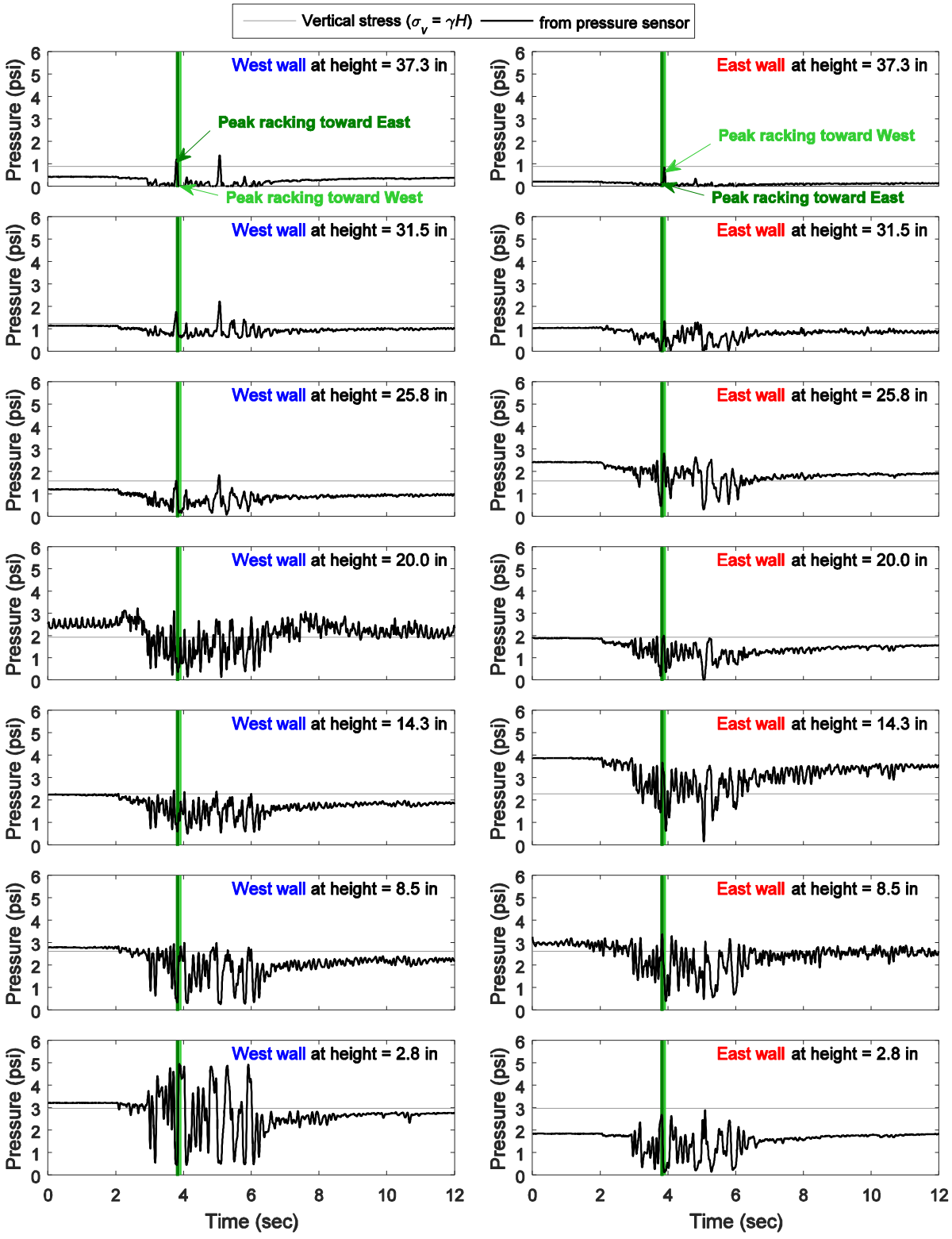

Figure C–31: Model 3 earth pressure time histories along the wall height during Nor200PT1 input excitation (1 ft overburden soil)

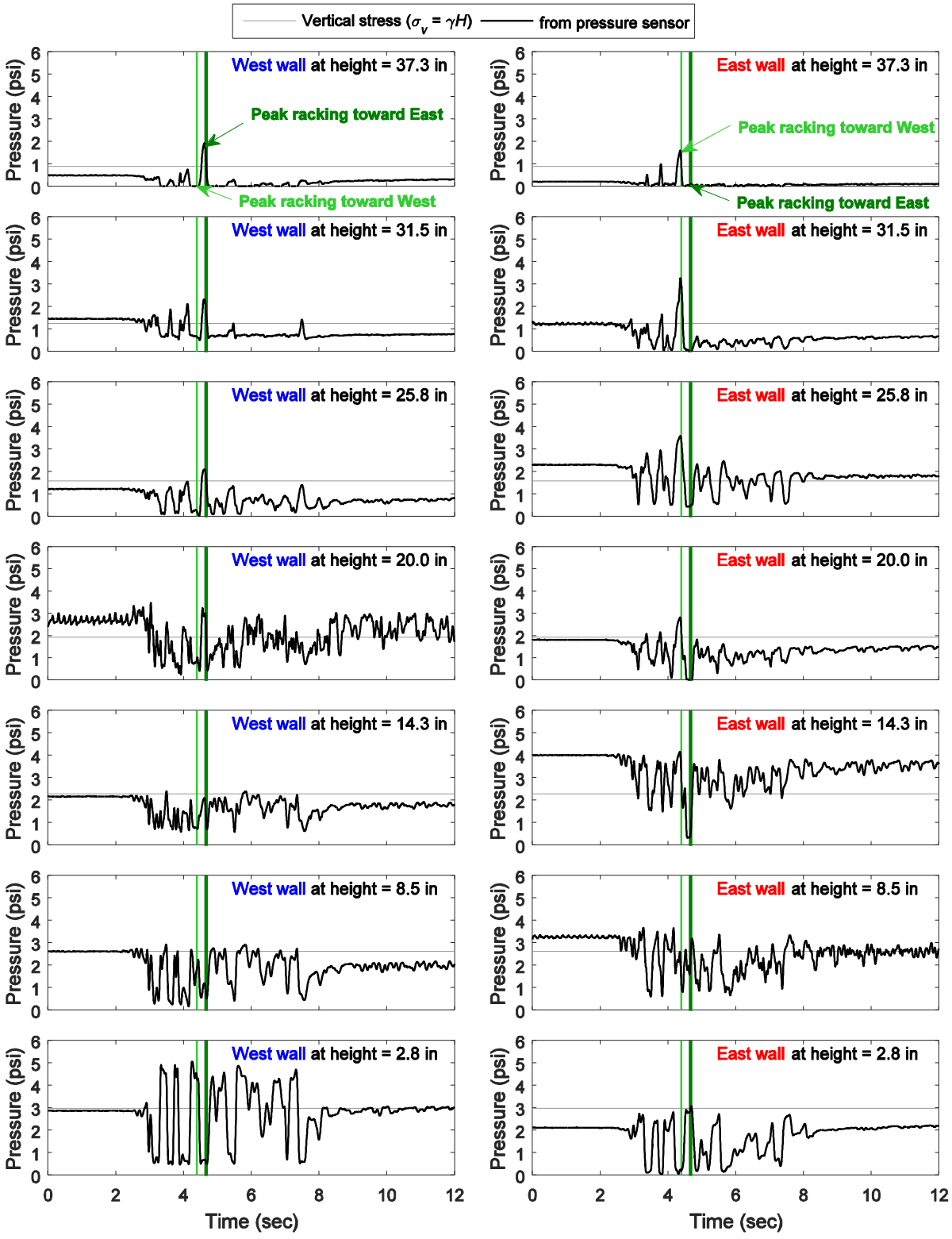

Figure C–32: Model 3 earth pressure time histories along the wall height during Tak100PT1 input excitation (1 ft overburden soil)

Appendix D Scaling Law

For 1g model tests in soil-structure systems, scaling relationships between a model (similitude) and the corresponding prototype are discussed. Since soil is a stress-dependent material, its stress-strain behavior should be appropriately presented by the model as illustrated in Figure D-1. Fundamental laws of mechanics such as equilibrium and mass balance of soil skeleton (dry soil) also need to be satisfied in the similitude through the scaling factors. From governing equations for these principles, the following relations are derived by Iai (1989):

$$\lambda_\sigma/\lambda = \lambda_\rho = \lambda_\rho\lambda_u/\lambda_t^2 \text{ (from equilibrium)} \quad \text{(D-1)}$$

$$\lambda_\varepsilon = \lambda_u/\lambda \text{ (from strain definition)} \quad \text{(D-2)}$$

$$\lambda_\sigma = \lambda_D\lambda_\varepsilon \text{ (from constitutive law)} \quad \text{(D-3)}$$

where λ = geometrical scaling factor (prototype/model)

λ_σ = stress scaling factor (prototype/model)

λ_ε = strain scaling factor (prototype/model)

λ_D = modulus of soil scaling factor (prototype/model)

λ_ρ = density scaling factor (prototype/model)

λ_u = displacement scaling factor (prototype/model)

λ_t = time scaling factor (prototype/model)

Iai (1989) derived the strain scaling factor (λ_ε) from shear wave velocity tests in the model and prototype such as:

$$\lambda_\varepsilon = \lambda\left[\frac{(V_s)_m}{(V_s)_p}\right]^2 \quad \text{(D-4)}$$

where $(V_s)_m$ and $(V_s)_p$ denote shear wave velocities of soil deposits in the model and prototype, respectively. If the preliminary data for stress-dependent behavior of soil in the model are not available, it is assumed that the shear modulus at small strain of 10^{-6} is proportional to the square roof of the confining pressures. Consequently, this assumption leads to the following relation:

$$\lambda_\varepsilon = \lambda^{0.5} \quad \text{(D-5)}$$

In practice, as the density of the soil in the model is the same as that in the prototype, the density scaling factor is unity ($\lambda_\rho = 1$). Table D-1 summarizes the main scaling factors derived by Iai (1989). The scaling factors for structures as a beam (e.g. a sheet pile) are also shown in Table D-1. For such a structure in two dimensions (2D), its dimensions and cross-sections are generally specified per unit length (i.e. an axis out-of plane in Figure D-1). Thus, the scaling factors shown in Table E-1 are specified per unit length.

Table D-1: Main scaling factors for 1g model tests (Iai 1989)

Quantity	**Scaling factor (prototype to 1/9 scale)**		
	Generalized scaling factors	**$\lambda_\varepsilon = \lambda^{0.5}$, λ_ρ=1**	**CASE of λ = 9**
Length	λ	λ	9
Density	λ_ρ	1	1
Time	$(\lambda\lambda_\varepsilon)^{0.5}$	$\lambda^{0.75}$	5.2
Acceleration	1	1	1
Velocity	$(\lambda\lambda_\varepsilon)^{0.5}$	$\lambda^{0.75}$	5.2
Displacement	$\lambda\lambda_\varepsilon$	$\lambda^{1.5}$	27
Stress	$\lambda\lambda_\rho$	λ	9
Strain	λ_ε	$\lambda^{0.5}$	3
Stiffness	$\lambda\lambda_\rho/\lambda_\varepsilon$	$\lambda^{0.5}$	3
EI*	$\lambda^4\lambda_\rho/\lambda_\varepsilon$	$\lambda^{3.5}$	2187
EA*	$\lambda^2\lambda_\rho/\lambda_\varepsilon$	$\lambda^{1.5}$	27
Moment*	$\lambda^3\lambda_\rho$	λ^3	729
Shear*	$\lambda^2\lambda_\rho$	λ^2	81
Axial Force*	$\lambda^2\lambda_\rho$	λ^2	81

*specified per unit breadth of the tunnel along its longitudinal axis (based on 2D Plane Strain)

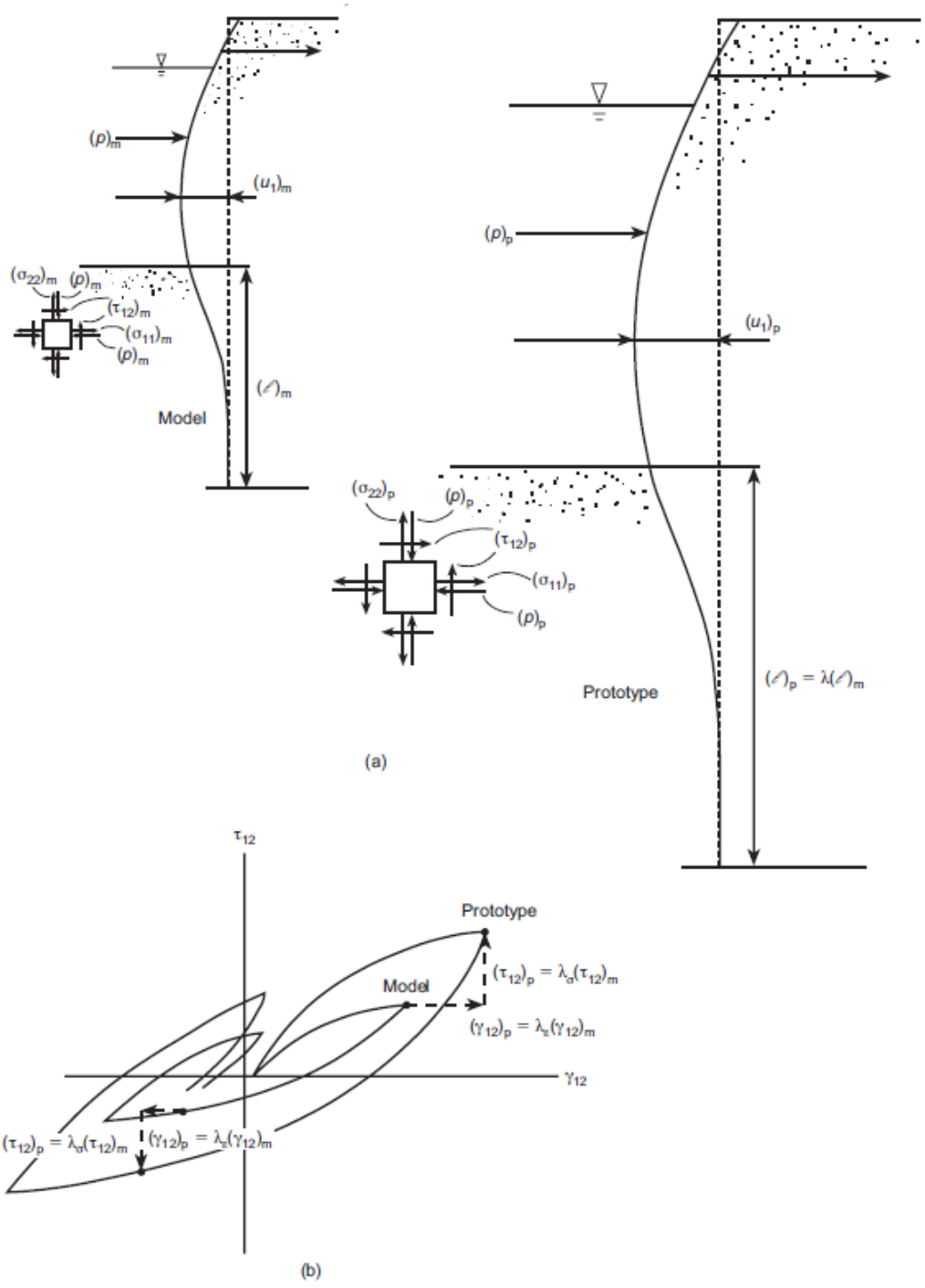

Figure D-1: Illustrative example of model and prototype (Iai, 1989): (a) relevant quantities of prototype and model and (b) stress-strain relations of soils in prototype and model

Appendix E Shake Table Test Response Time Histories in Prototype Scale

This appendix presents time histories of the main response recorded from the shake table tests in prototype scale, as discussed earlier in Chapter 5. The recorded response time histories from Model 1 by order of the shaking sequence (see Section 2.4.3 for the loading protocol) are shown in Figure E-1 through Figure E-5. The similar plots from Model 2 are shown in Figure E-6 through Figure E-10. The similar plots from Model 3 are shown in Figure E-11 through E-15.

The time histories of the lateral earth pressure along the walls as shown earlier in Section 4.2 are presented in Figure E-16 through Figure E-19 from Model 3 and in Figure E-20 and Figure E-21 from Model 3.

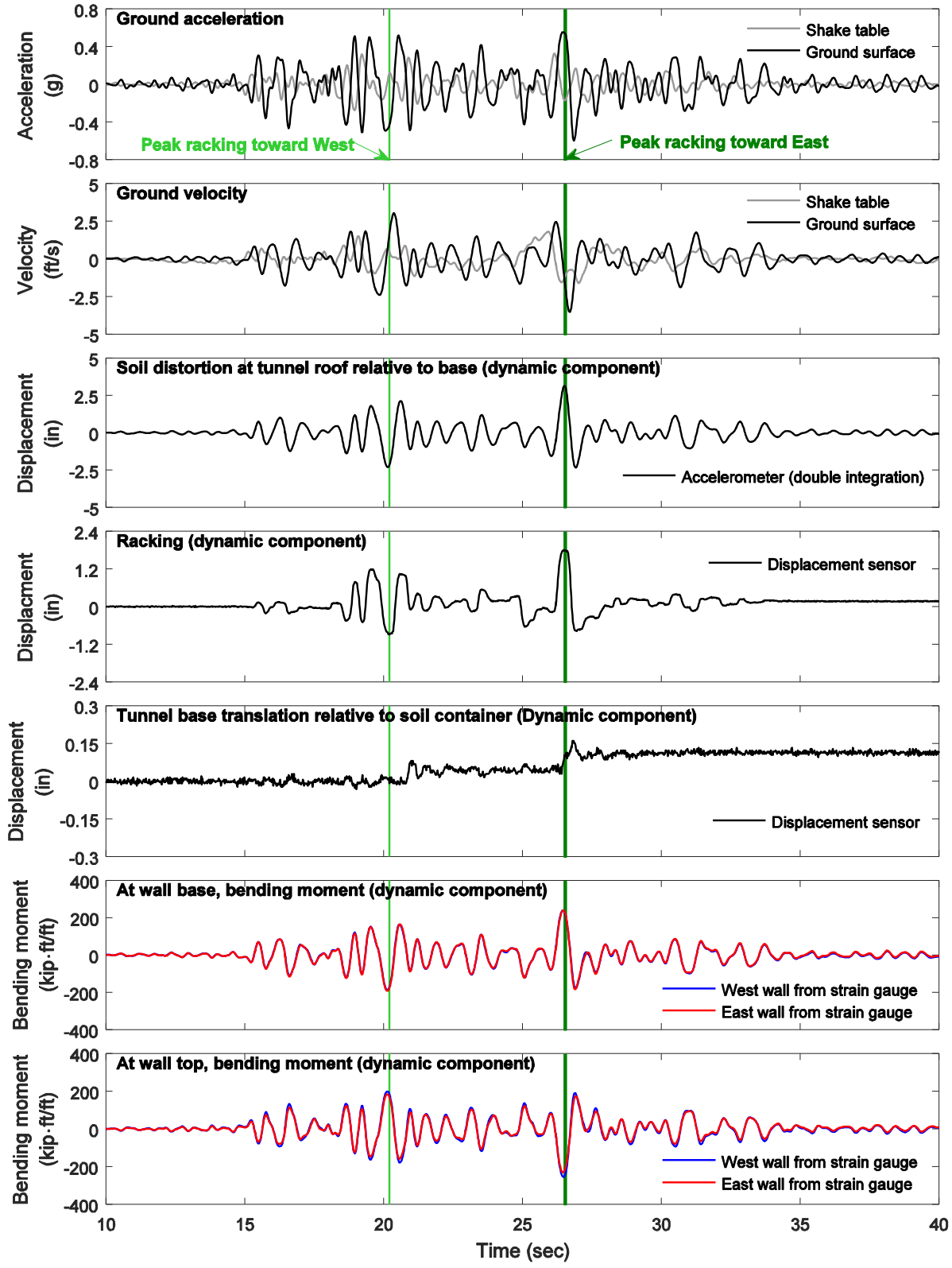

Figure E–1: Model 1 response time histories during Nor100PT1 input excitation in prototype scale (18 ft overburden soil)

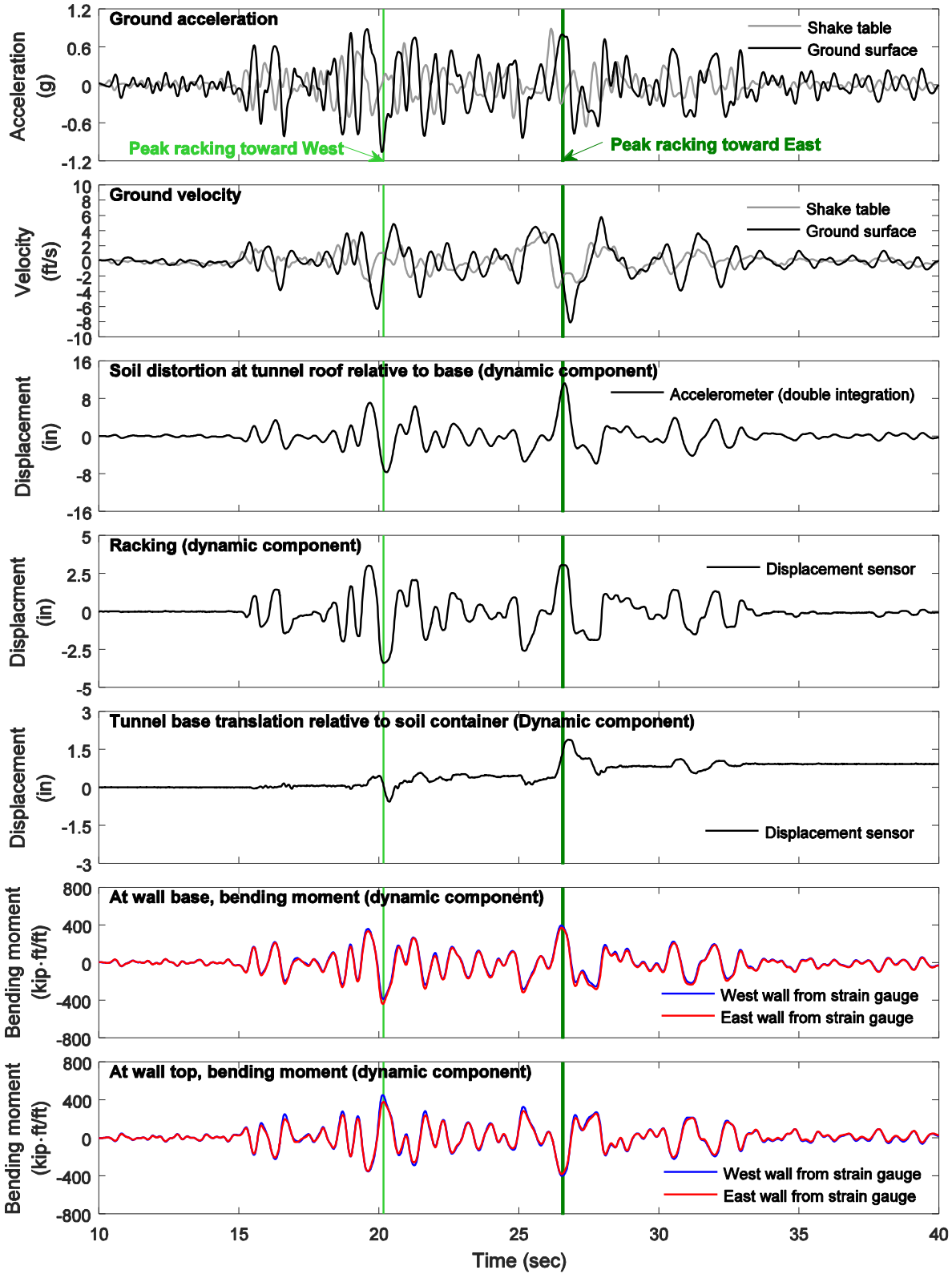

Figure E–2: Model 1 response time histories during Nor200PT1 input excitation in prototype scale (18 ft overburden soil)

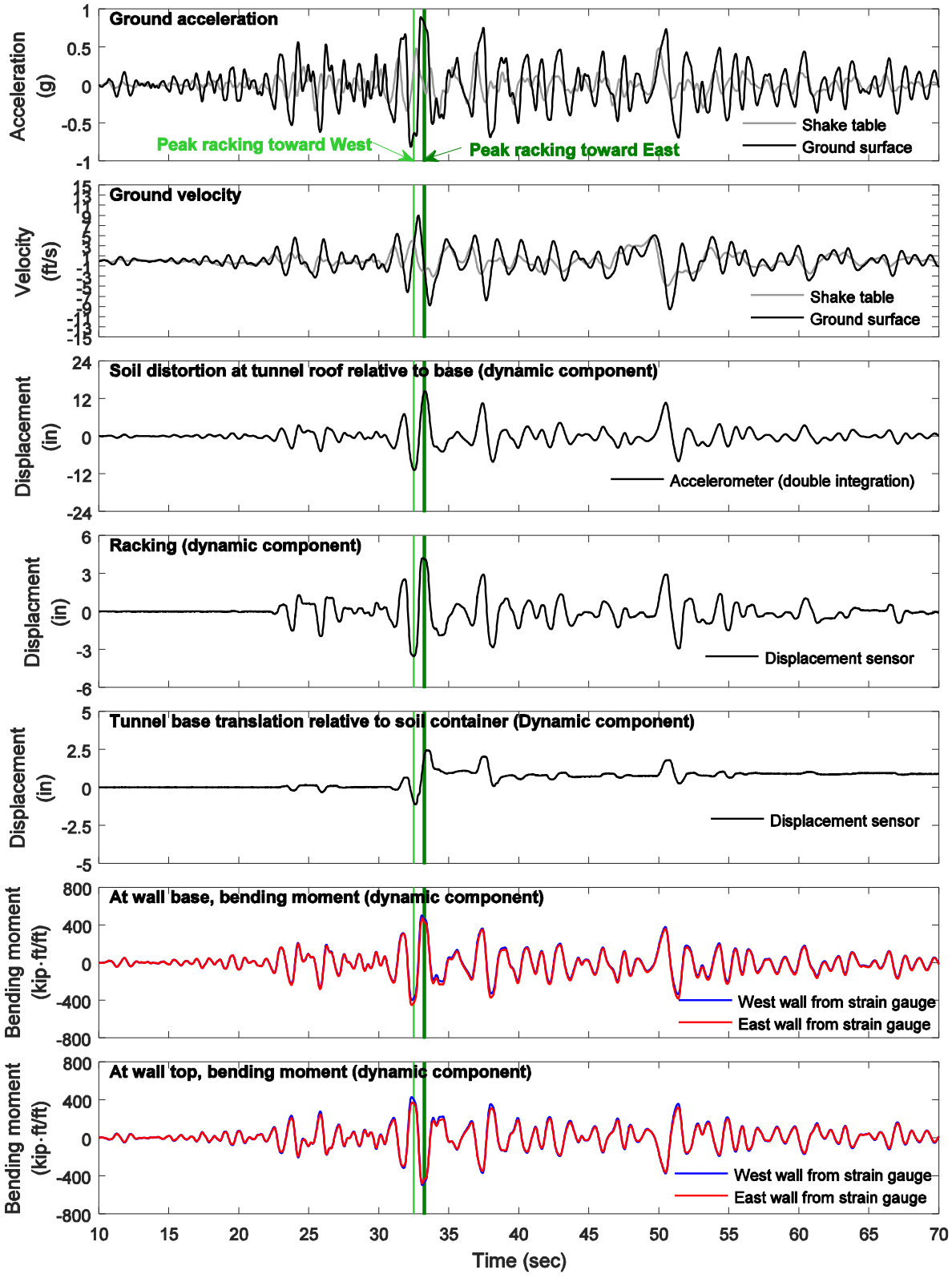

Figure E–3: Model 1 response time histories during Nor100PT0 input excitation in prototype scale (18 ft overburden soil)

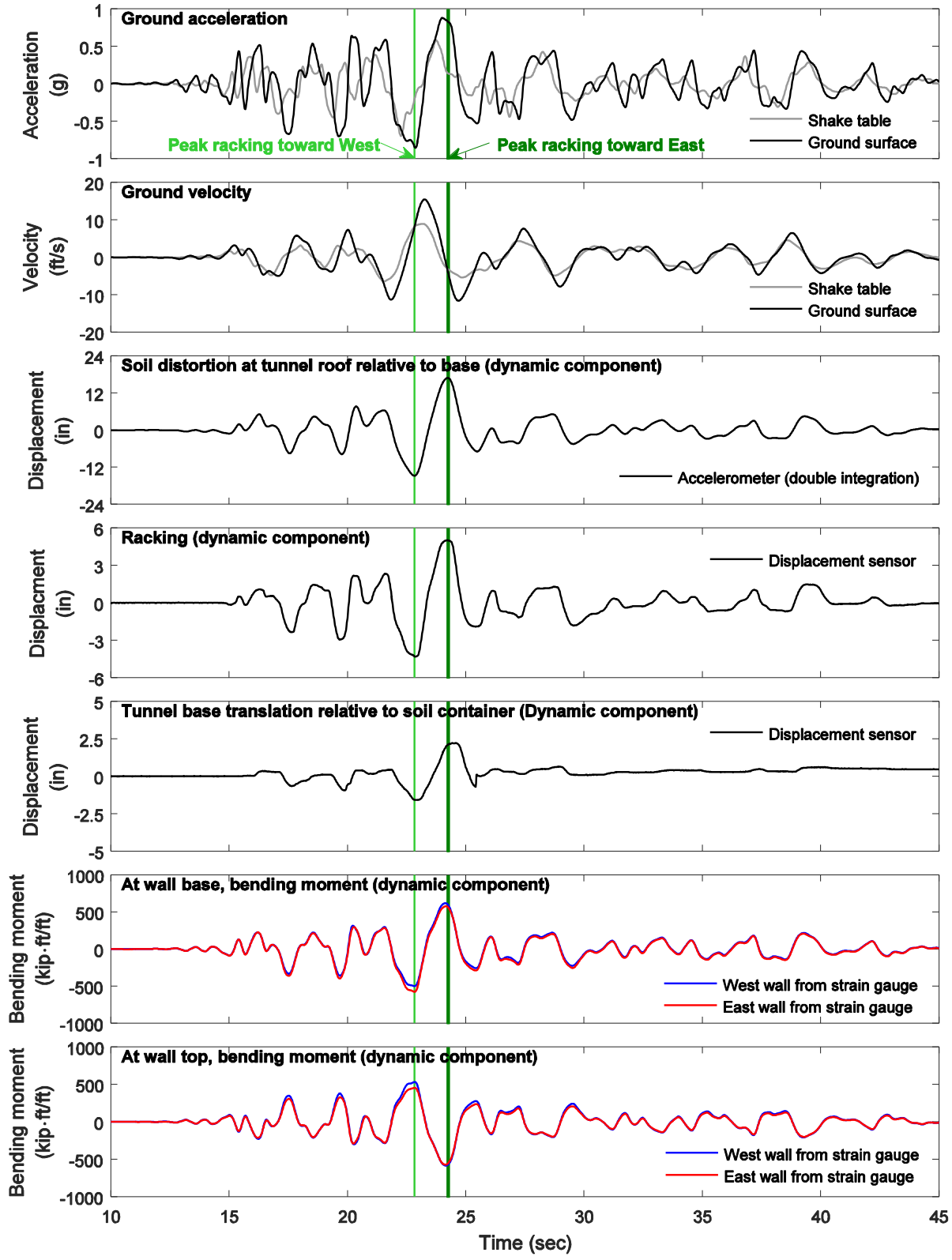

Figure E–4: Model 1 response time histories during Tak100PT1 input excitation in prototype scale (18 ft overburden soil)

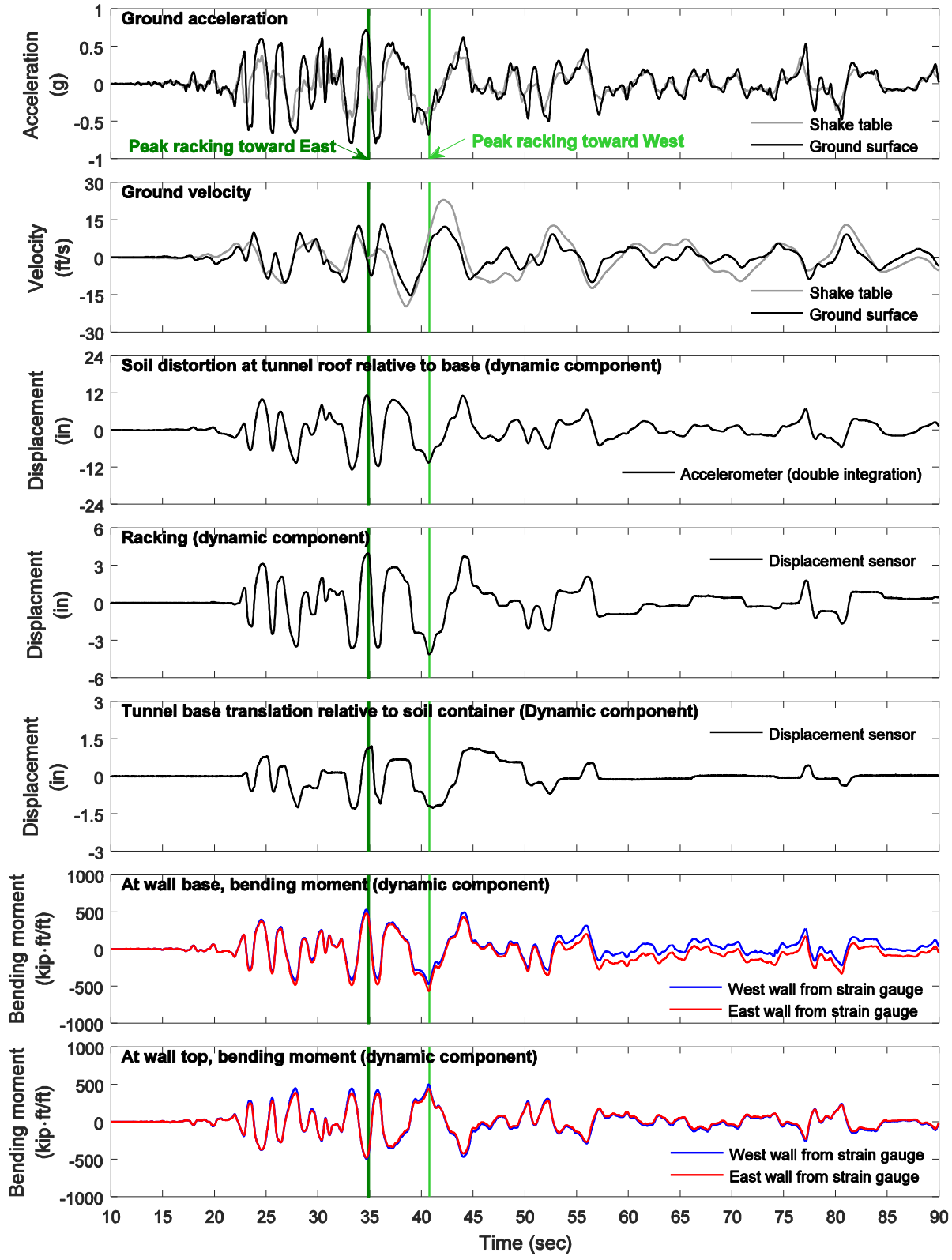

Figure E–5: Model 1 response time histories during Tak100PT0 input excitation in prototype scale (18 ft overburden soil)

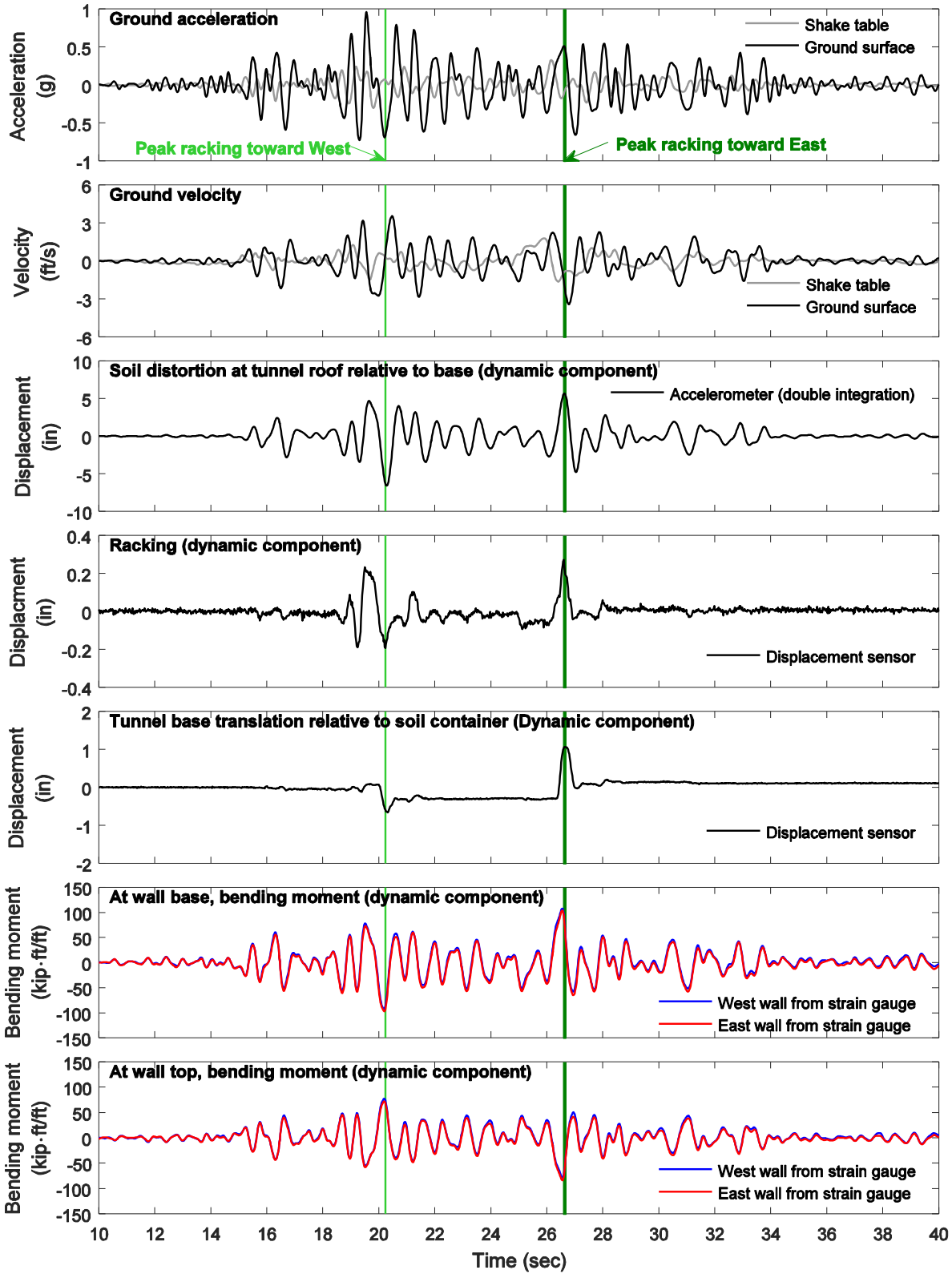

Figure E–6: Model 2 response time histories during Nor100PT1 input excitation in prototype scale (without overburden soil)

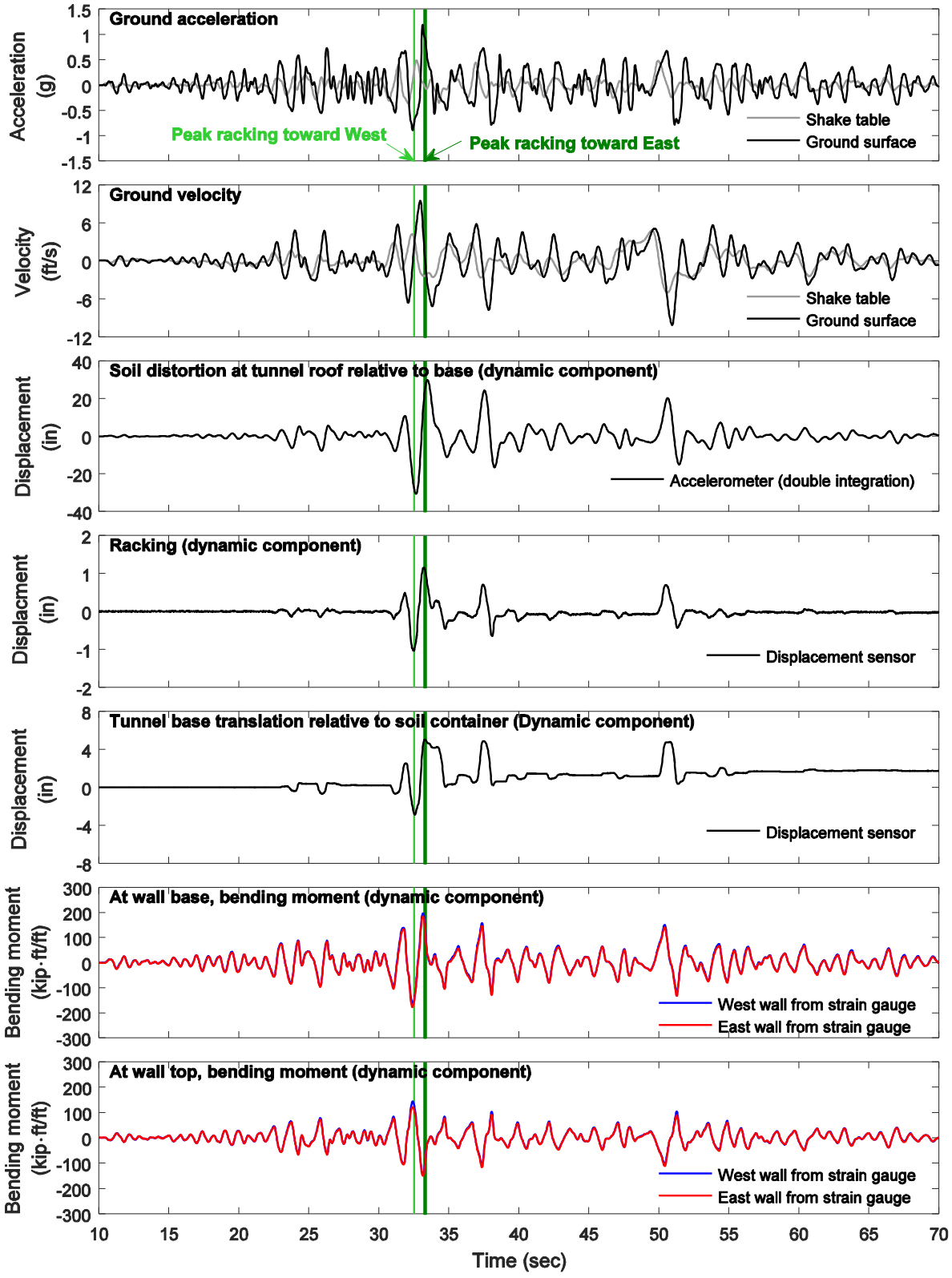

Figure E–7: Model 2 response time histories during Nor100PT0 input excitation in prototype scale (without overburden soil)

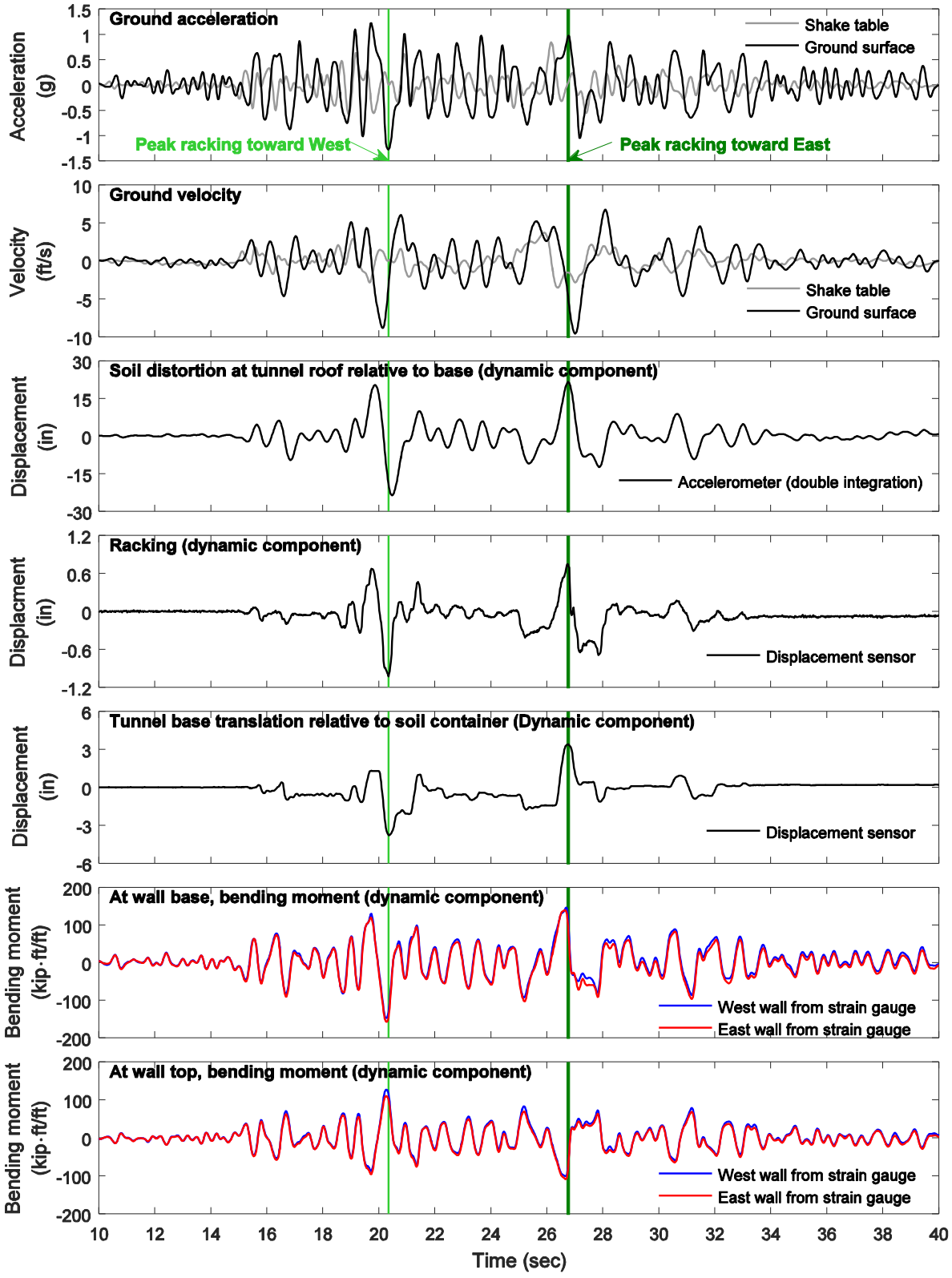

Figure E–8: Model 2 response time histories during Nor200PT1 input excitation in prototype scale (without overburden soil)

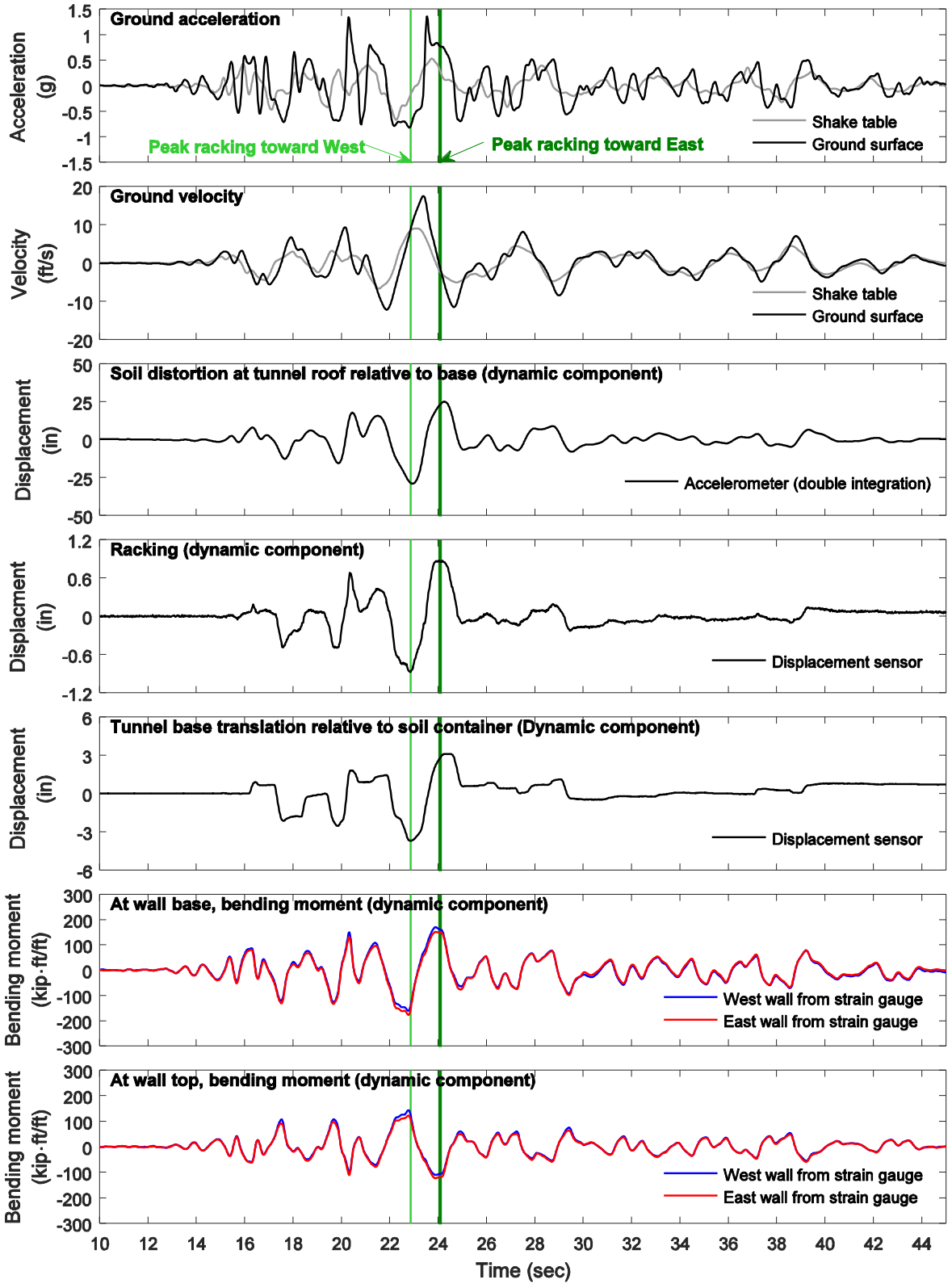

Figure E–9: Model 2 response time histories during Nor100PT1 input excitation in prototype scale (without overburden soil)

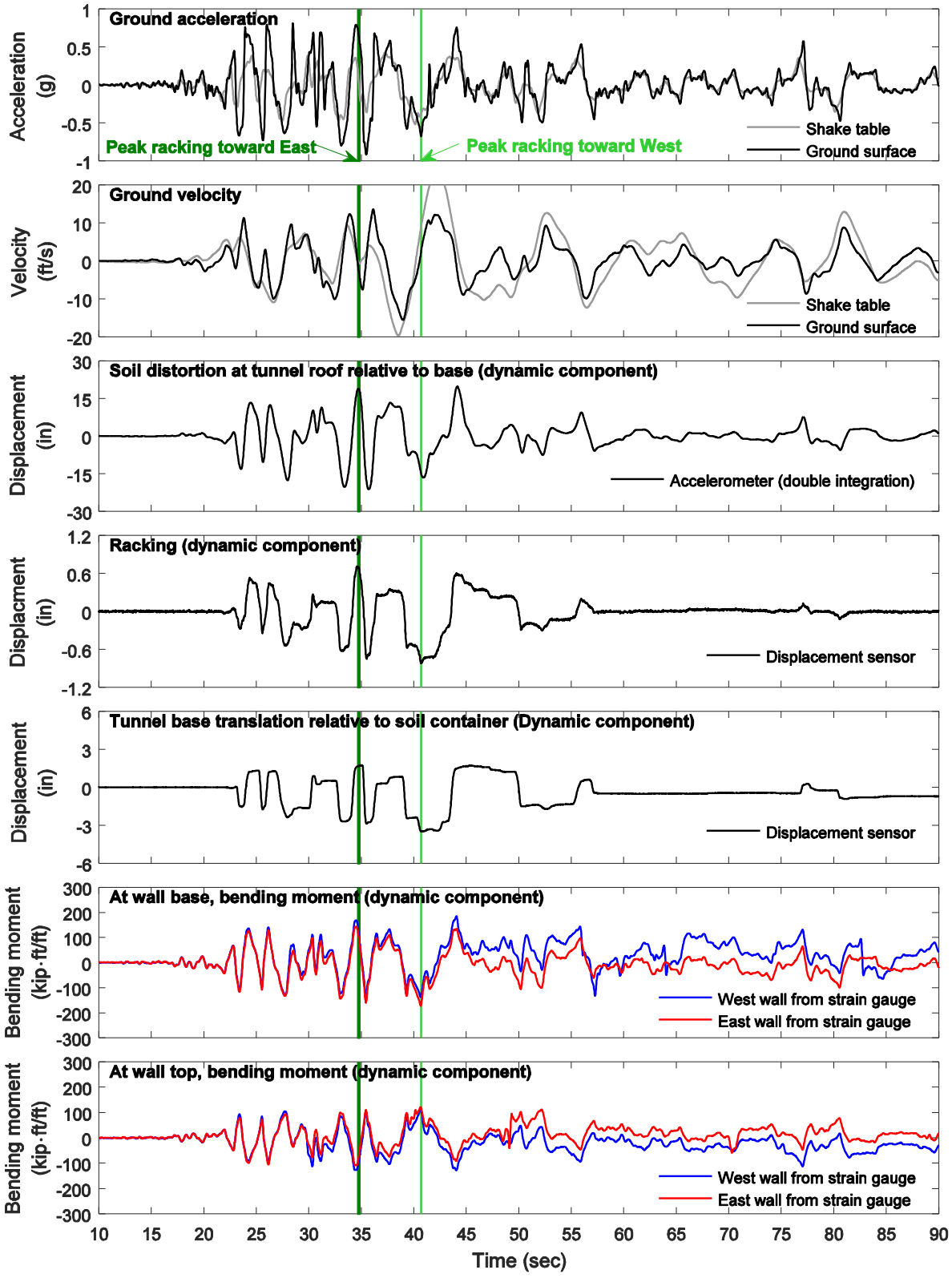

Figure E–10: Model 2 response time histories during Tak100PT0 input excitation in prototype scale (without overburden soil)

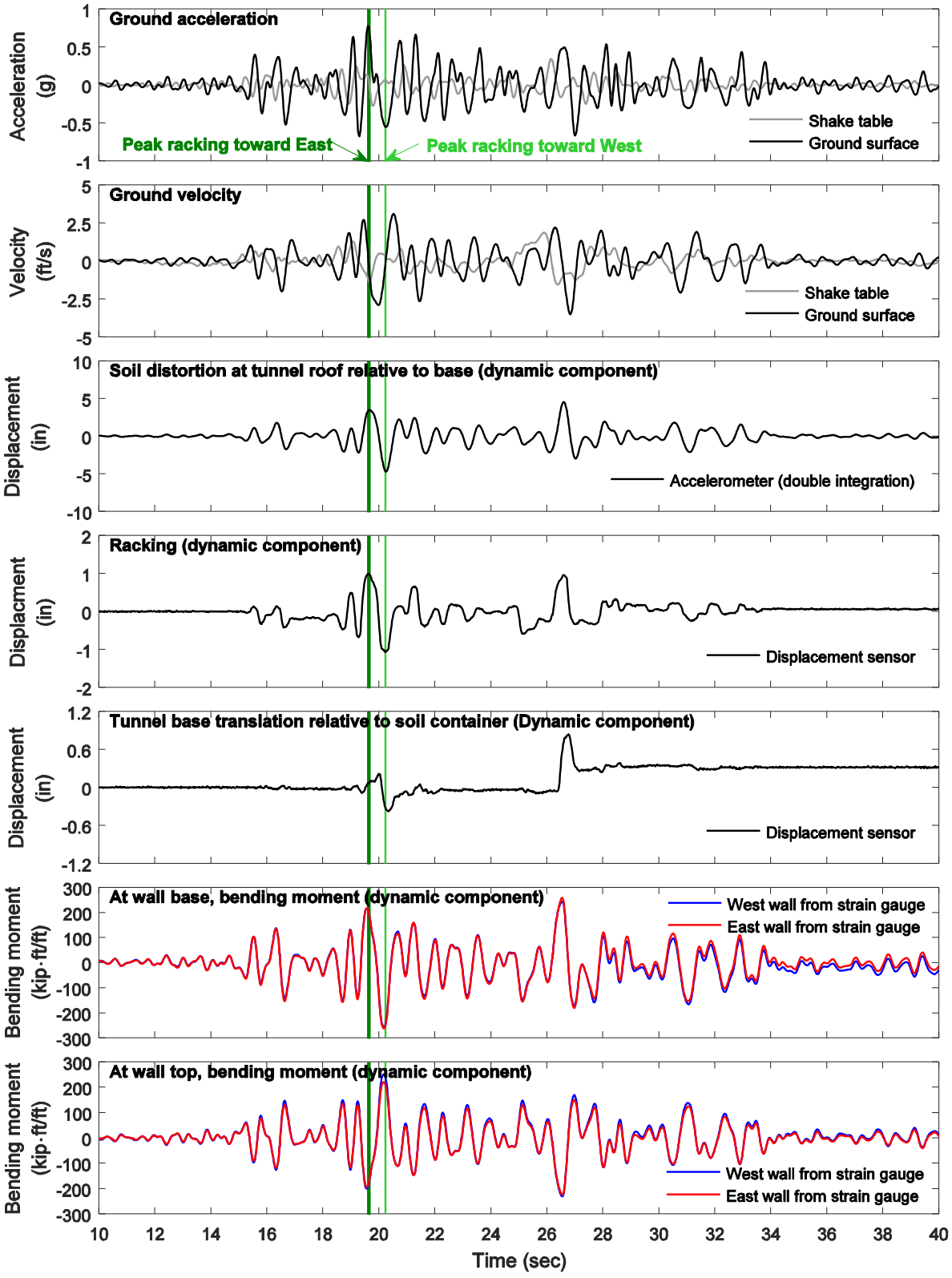

Figure E–11: Model 3 response time histories during Nor100PT1 input excitation in prototype scale (9 ft overburden soil)

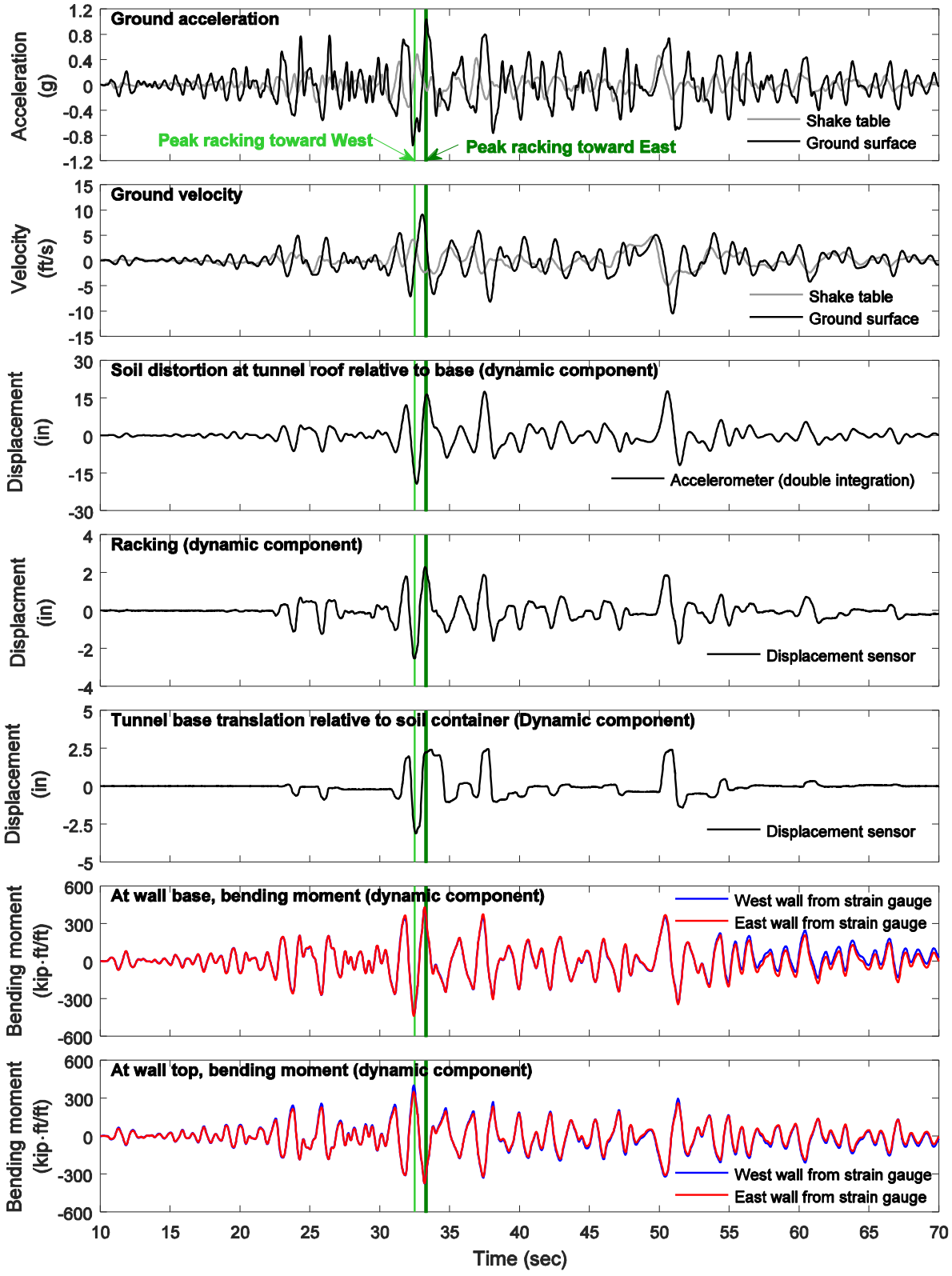

Figure E–12: Model 3 response time histories during Nor100PT0 input excitation in prototype scale (9 ft overburden soil)

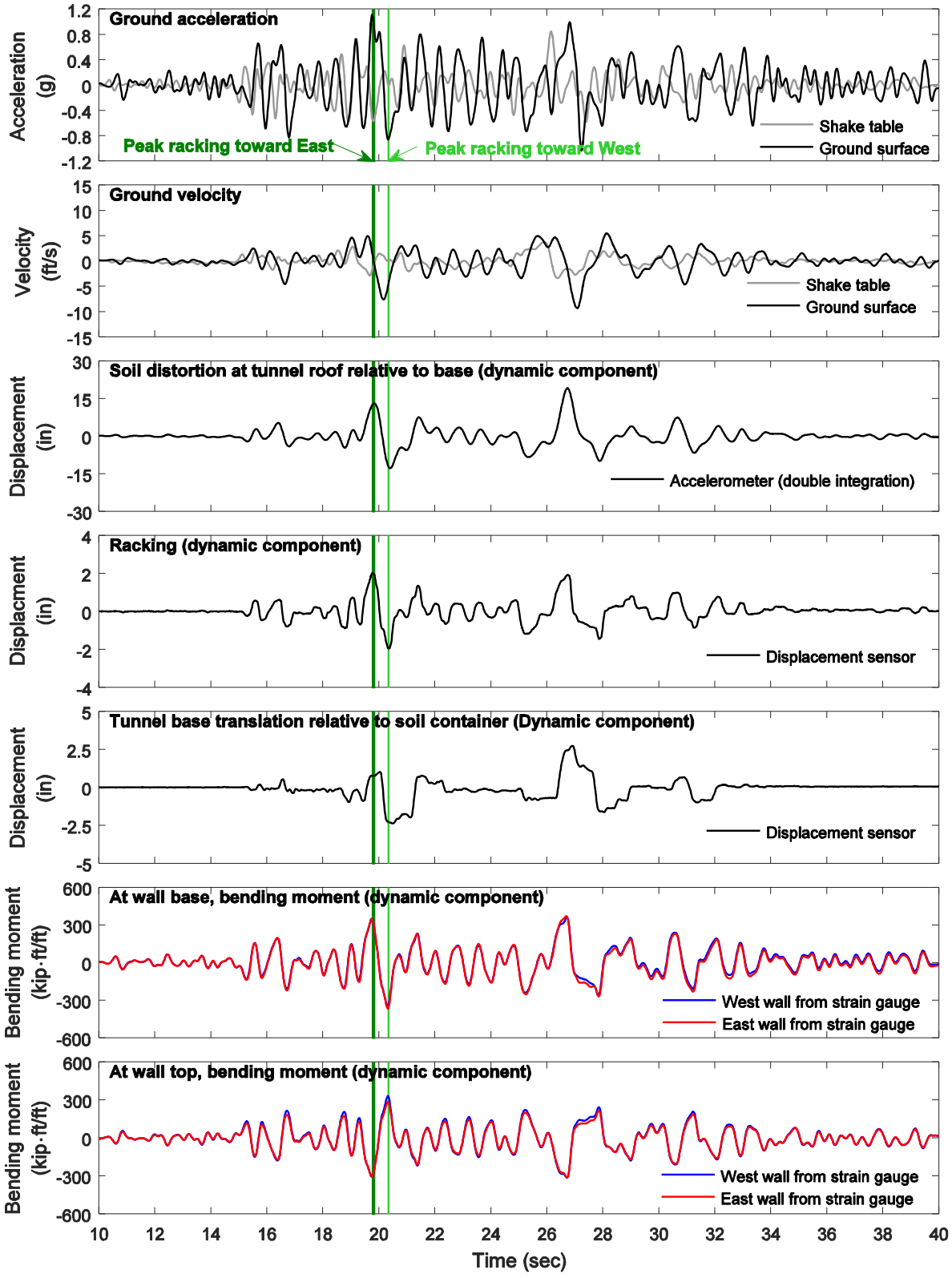

Figure E–13: Model 3 response time histories during Nor200PT1 input excitation in prototype scale (9 ft overburden soil)

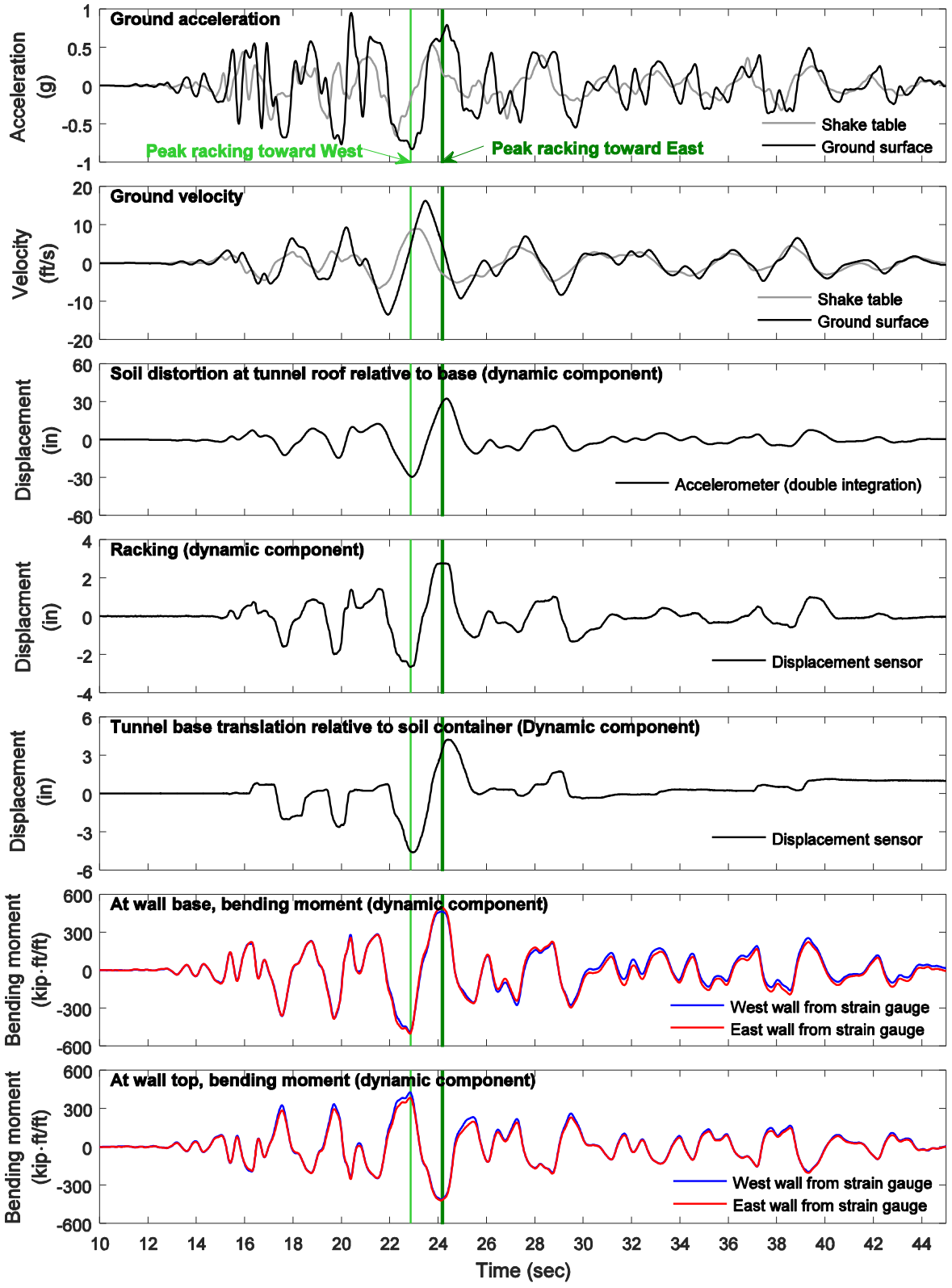

Figure E–14: Model 3 response time histories during Nor100PT1 input excitation in prototype scale (9 ft overburden soil)

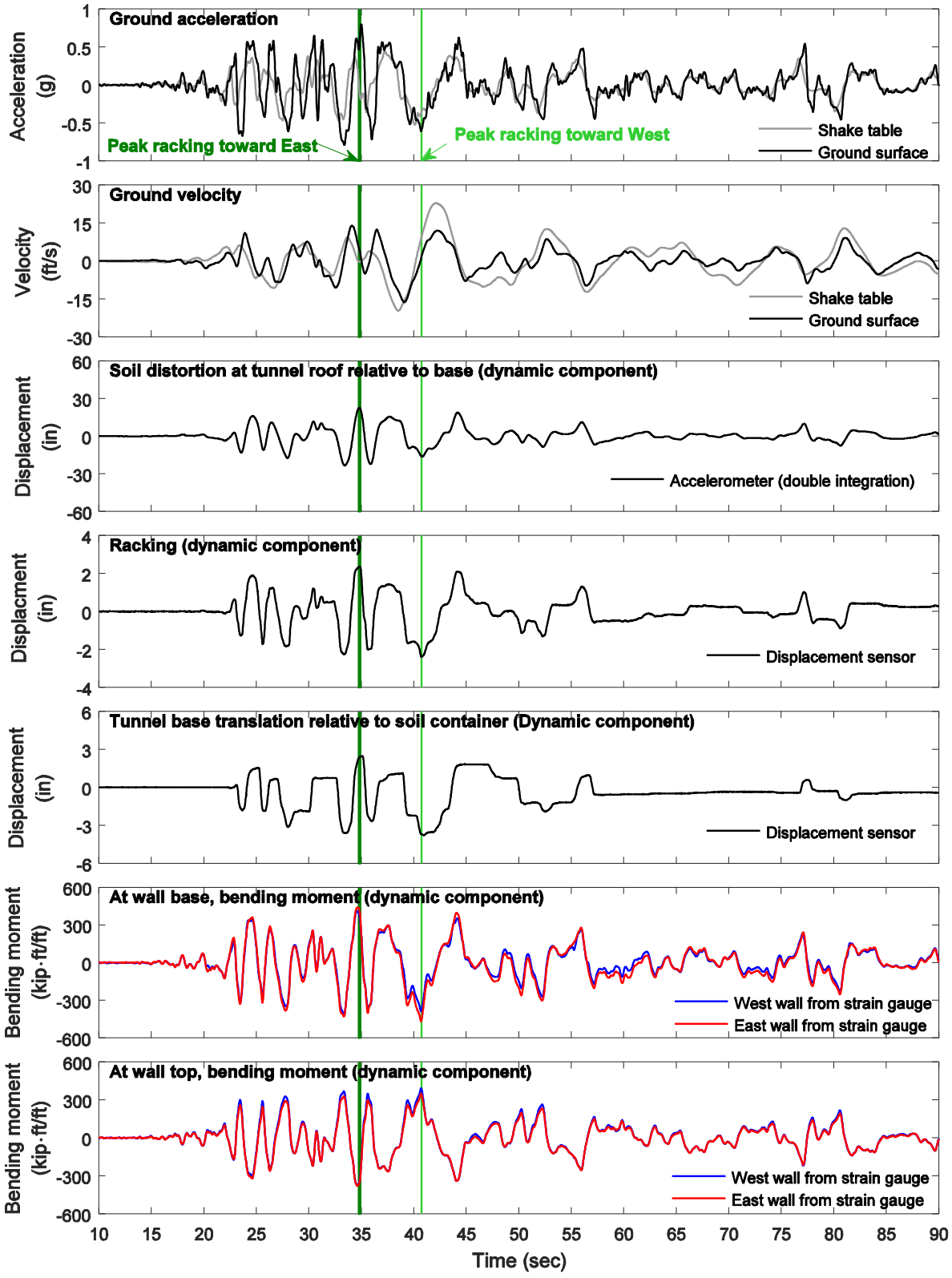

Figure E–15: Model 3 response time histories during Tak100PT0 input excitation in prototype scale (9 ft overburden soil)

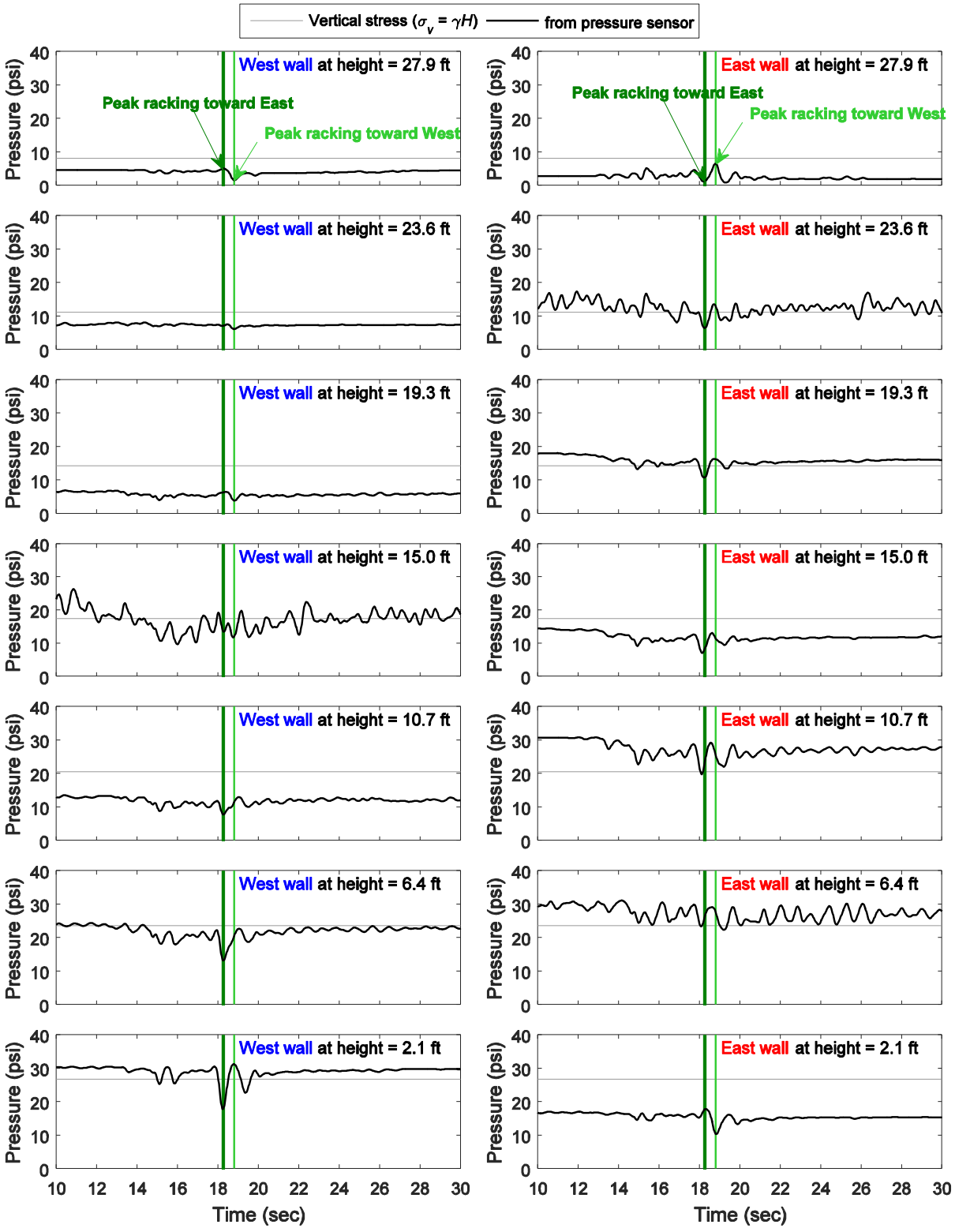

Figure E–16: Model 3 earth pressure time histories along the wall height during Nor100PT2 input excitation in prototype scale (9 ft overburden soil)

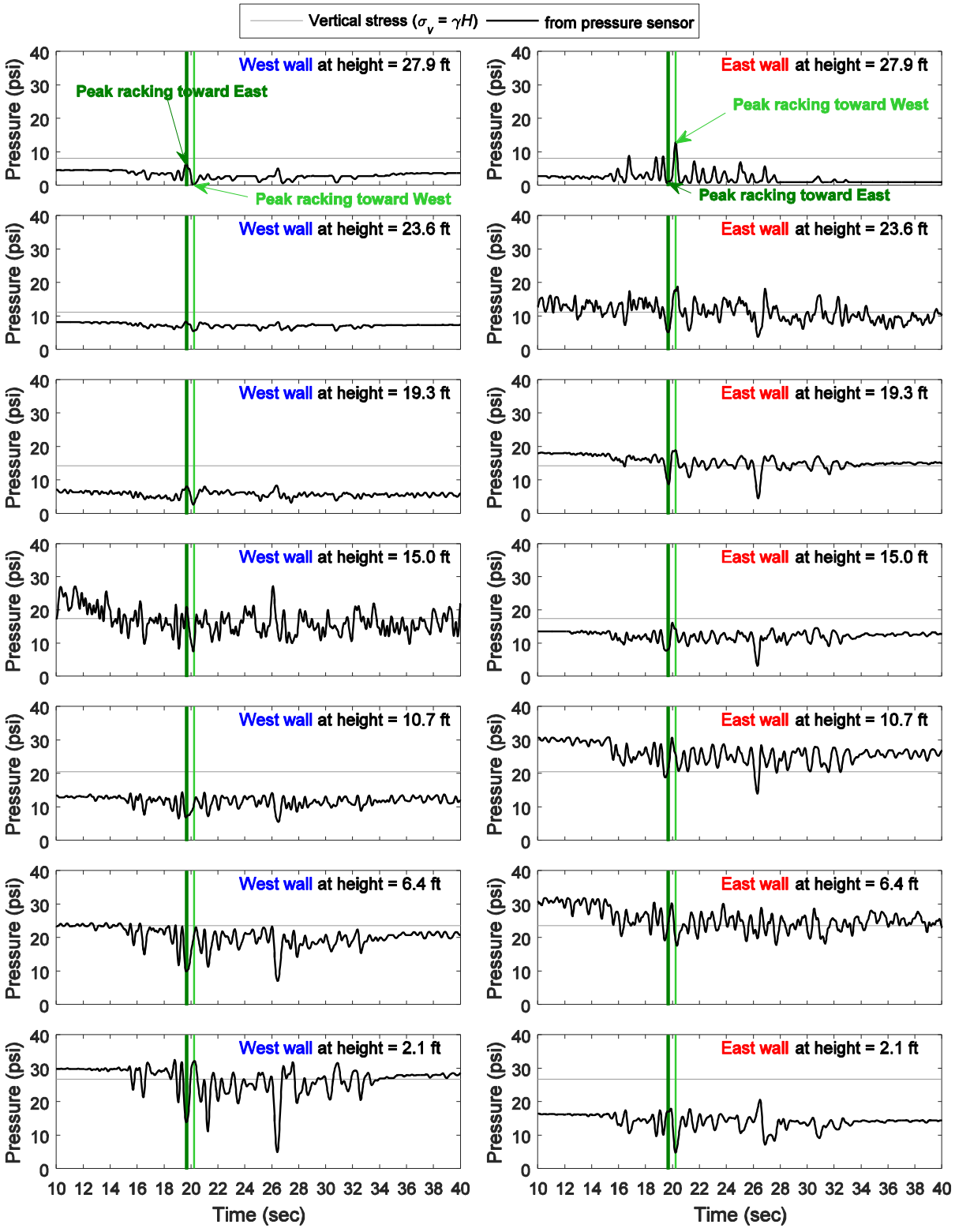

Figure E–17: Model 3 earth pressure time histories along the wall height during Nor100PT1 input excitation in prototype scale (9 ft overburden soil)

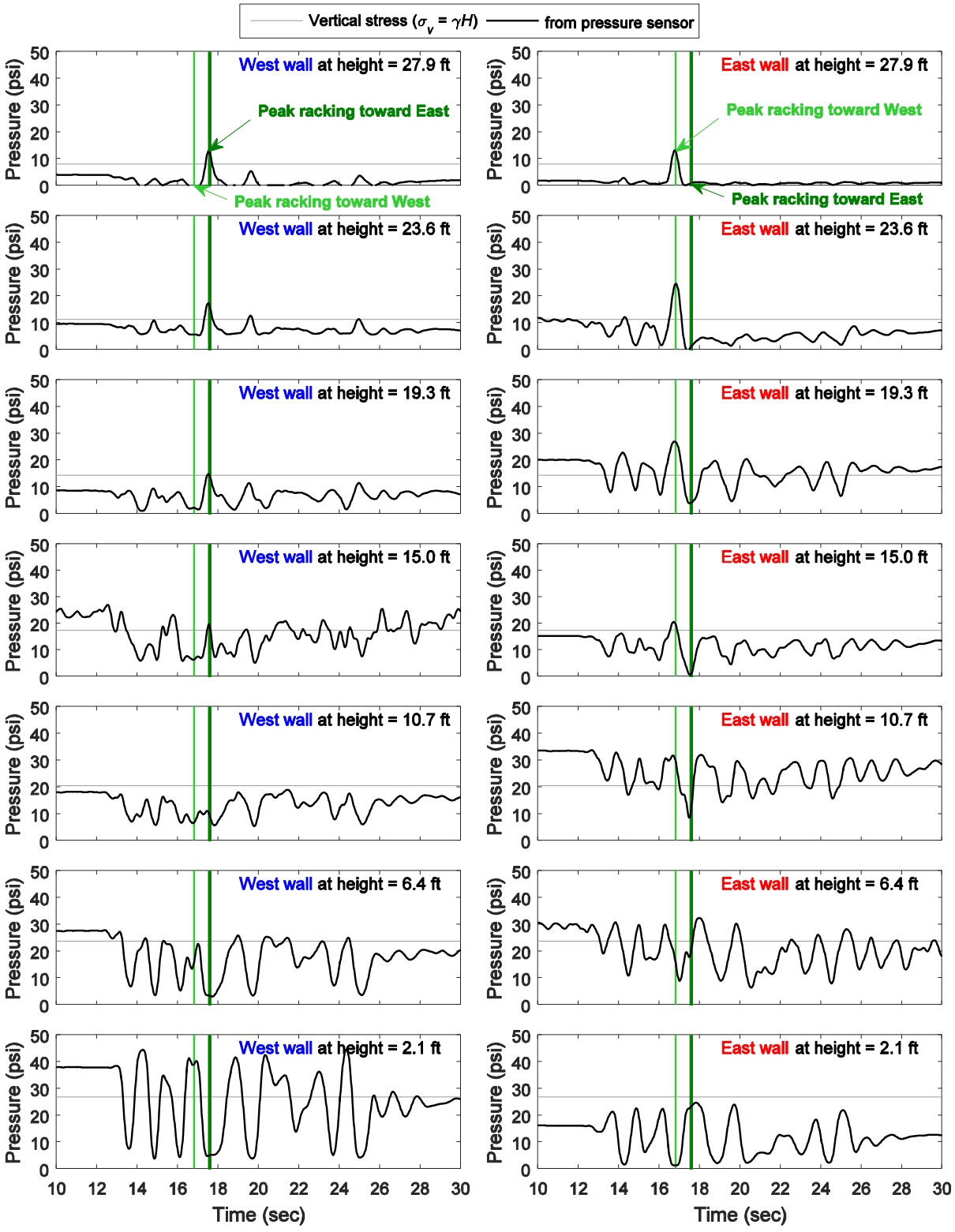

Figure E–18: Model 3 earth pressure time histories along the wall height during Tak100PT2 input excitation in prototype scale (9 ft overburden soil)

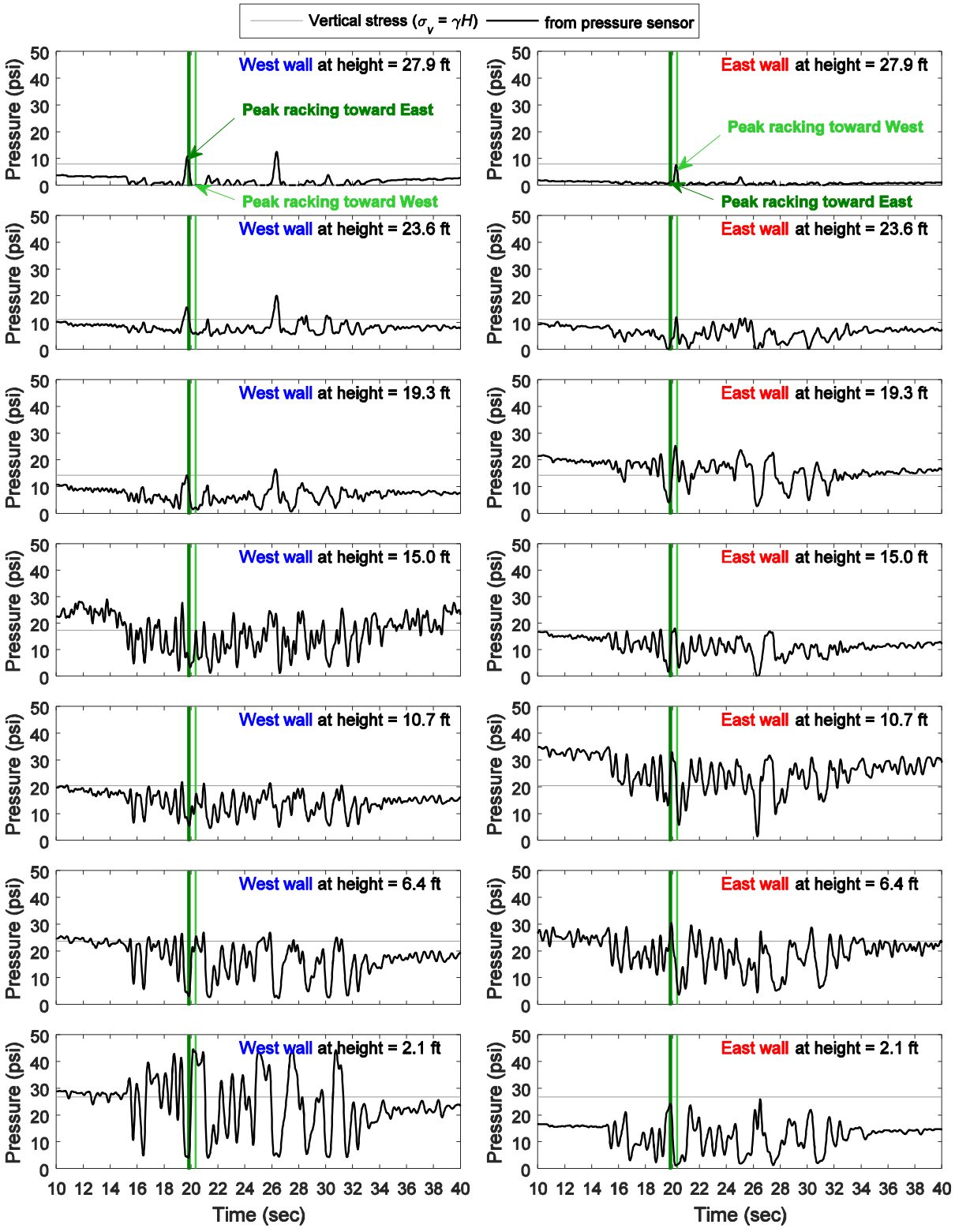

Figure E–19: Model 3 earth pressure time histories along the wall height during Nor200PT1 input excitation in prototype scale (9 ft overburden soil)

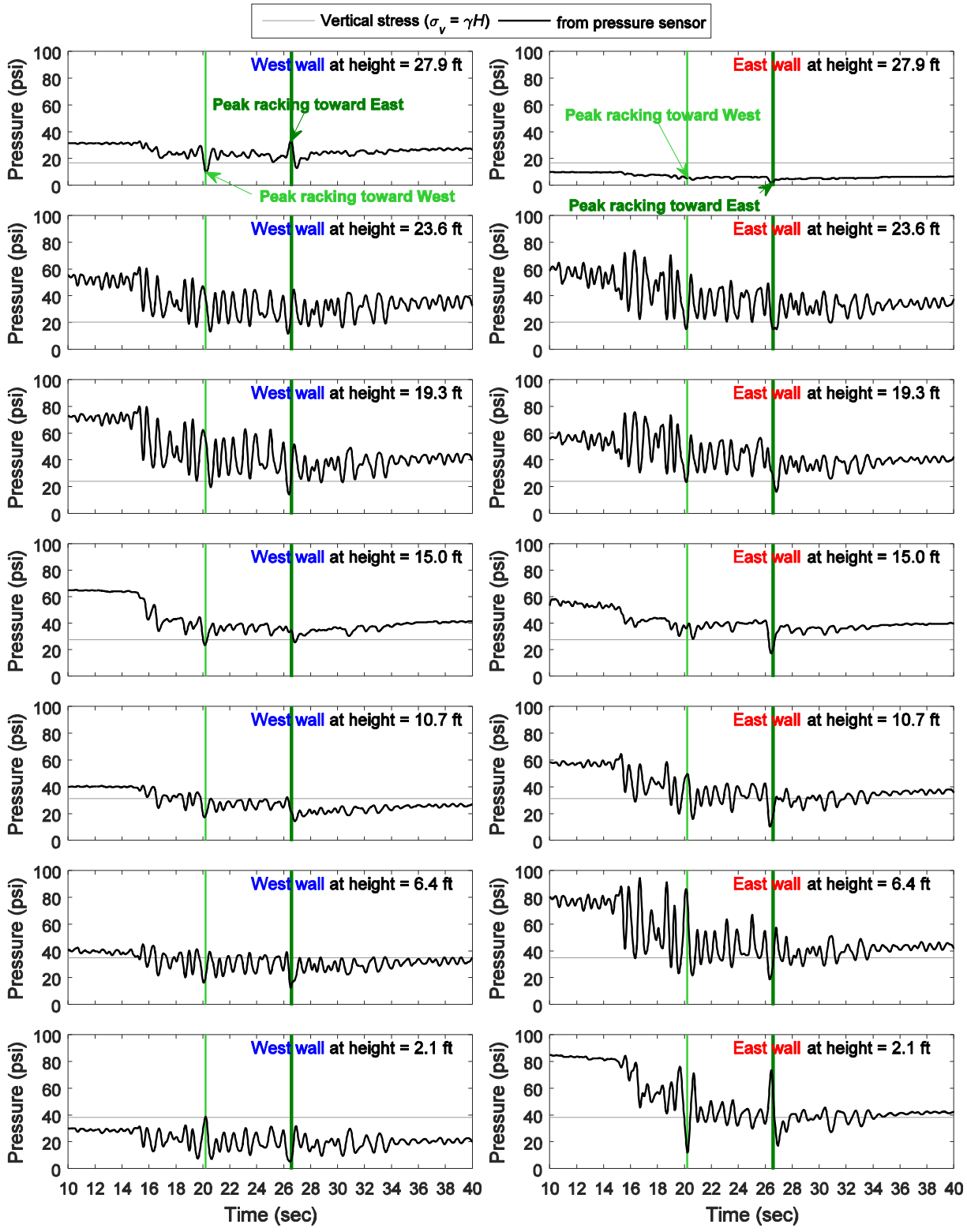

Figure E–20: Model 1 earth pressure time histories along the wall height during Nor100PT1 input excitation in prototype scale (18 ft overburden soil)

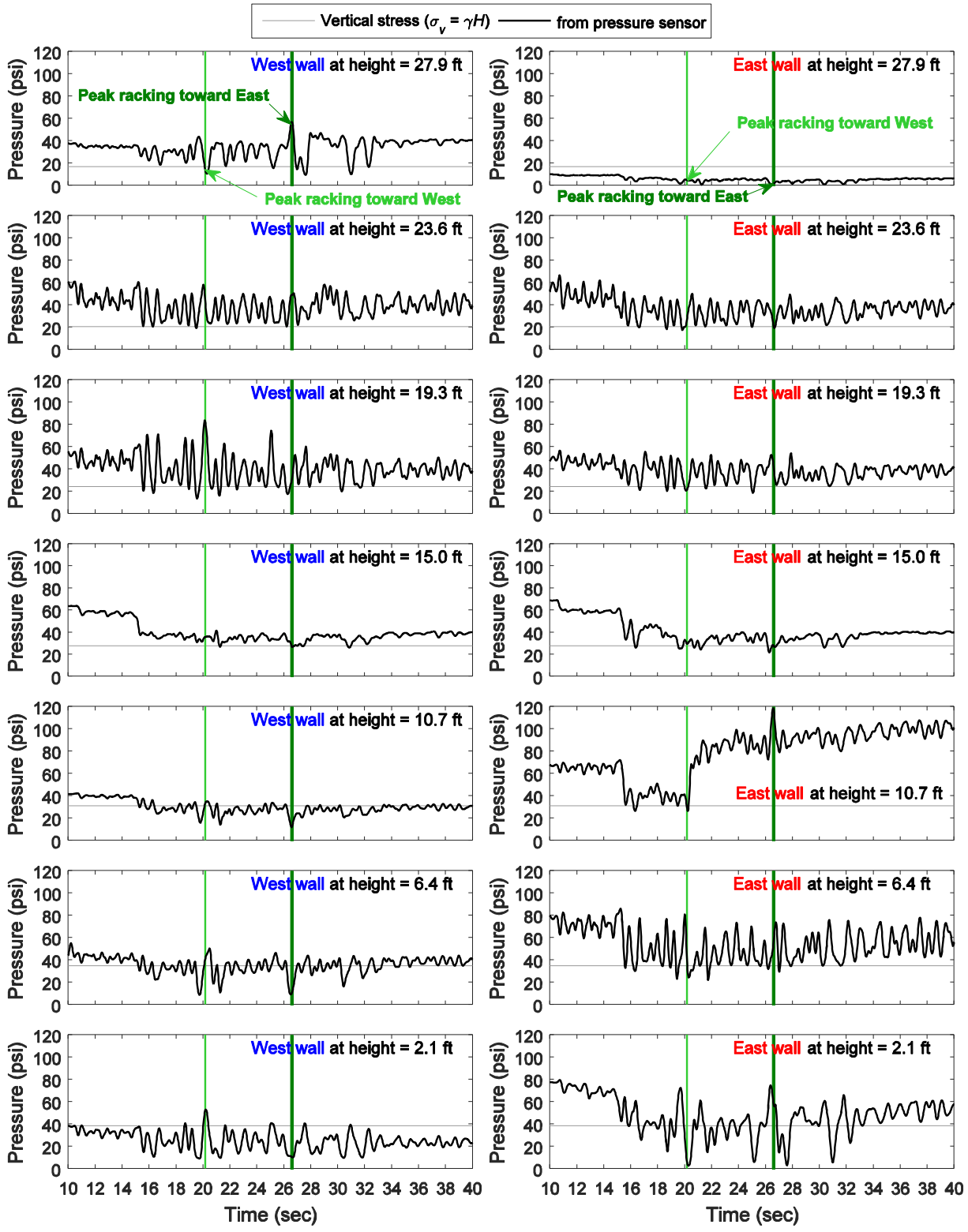

Figure E–21: Model 1 earth pressure time histories along the wall height during Nor200PT1 input excitation in prototype scale (18 ft overburden soil)

Appendix F Numerical Analysis: Pinned Connection Between Tunnel Roof and Side Walls

In this section, two-dimensional (2D) plane-strain finite element (FE) analyses were conducted to model the 1st test configuration (Model 1 with 2 ft overburden soil in model scale). First, the FE simulation in model scale was calibrated using the test records measured during the Nor100PT0 input excitation. Upon completion of this calibration phase, the employed geometric and material properties were scaled up to simulate the full-scale model using the scaling relationships presented by Iai (1989). The full-scale numerical model response was compared to the test results which were also interpreted in full-scale. Finally, the full-scale FE model was employed to further study the influence of possible hinge connection at the interface between wall and roof on both sides of the tunnel.

F.1 FE Model Configuration in Test Scale

System modeling was performed in the 2D plane strain configuration using the OpenSees platform (Mazzoni et al. 2009). Figure F-1 shows the 2D FE mesh representing the shake table test model.

F.1.1 Soil element and material properties

Four-node quadrilateral elements were used to model the backfill soil (Figure F-1a). The PressureDependMultiYield (PDMY) model (Yang et al. 2003) was used to represent the soil material in Model 1 compacted at D_r of 99% (Table F-1). Reference shear modulus (G_r) of 2623 psi at depth of 6 ft was selected to match G_{max} (on average) which was evaluated from the recorded acceleration in the shake table test (average from ground surface to the model base).

F.1.2 Tunnel element and material properties

As shown in Figure F-1b, the tunnel model was composed of two different OpenSees element types:

1) Elastic beam-column element (see Table F-2 for the material properties)

   This element was used to only model the tunnel wall part. Mass of the wall was distributed along the elements. During the entire FE simulation phases (static and shaking), the resulting wall response was dictated by these elements.

2) Quadrilateral elements (see Table F-3 for the material properties)

The quadrilateral element was used to model the geometric configuration for the roof and slab. The corresponding equivalent unit weight (mass density) was defined as the actual weight of the components divided by the corresponding occupied space. As designed, essentially rigid material properties were used for the roof and slab elements throughout.

F.1.3 Boundary conditions

At the interface between the soil and the tunnel walls, Elastic No-Tension (ENT) uniaxial material was employed to allow possible gap opening during shaking in the normal (lateral) direction to the wall (Figure F-2). The corresponding structure and soil nodes were connected using OpenSees zero-Length elements. In the vertical direction, free settlement was allowed (no friction) due to differential settlement of the soil and the structure (noting that the structure was relatively light). Along the wall base, the structure nodes were tied to the soil nodes to enforce identical translation in the horizontal and vertical directions (no separation/friction using equalDOF). Along both sides of the soil mesh, lateral and vertical translations were constrained to be identical (i.e., shear beam response assumption).

Computational procedure

Prior to seismic excitation, gravity induced own-weight was applied. Based on the confinement at any depth, the soil constitutive parameters were systematically defined (Table F-1). The Nor100PT1 input motion measured from the shake table was used as input. This motion was applied to the model base as uniform excitation. Dynamic response of this FE model was computed using the TRBDF2 integrator, a combination of the trapezoidal and 3 point backward Euler schemes (Bathe 2007). This integrator attempts to conserve energy and momentum in the model. The analysis was conducted with a step size of 0.005 sec. Rayleigh damping was employed. For that purpose, the mass and stiffness proportional terms were defined to provide viscous damping of about 5% for the first few modes of the model (in the range of 9.22 Hz – 17.25 Hz).

F.2 FE Analysis Results Compared to Test Records

The computed FE response time histories of Model 1 were compared to the test results in terms of:

1) Acceleration at 7 locations along the depth compared to the records from the West side (Figure F-3) and the East side (Figure F-4)

2) Soil lateral boundary displacement along the depth (i.e., lateral displacement of the laminar soil container) compared to the records measured from string potentiometers (Figure F-5)
3) Racking (Figure F-6)
4) Wall bending moment on both sides of the tunnel (Figure F-7)

As shown in the above figures, the numerical response of soil and wall bending moment generally provided a reasonable match to the recorded response. The numerical racking result showed a good agreement in terms of the peak value rather than overall in-phase response.

F.3 FE Model Configuration in Full-Scale

The geometric configuration of the full-scale FE model was scaled by a factor of 9 (the nodal coordinates of the FE mesh were simply scaled up). Table F-4 summarizes the soil material properties in the full-scale FE model using the scaling relationships by Iai (1989). Similarly, the tunnel material properties were determined by applying the scaling factor as summarized inTable F-5. As in model scale, the quadrilateral elements representing of the tunnel roof and base in model scale were essentially in full-scale as well (Table F-3). The mass of the model changed according to the scaled nodal coordinates. Boundary conditions and the ENT material properties at the interface between the soil and the tunnel wall remained identical.

The time duration of the Nor100PT1 input motion was scaled by a factor of 5.2 ($= 9^{0.75}$) and applied to the full-scale model base. Rayleigh damping of 5% was employed for the updated first few modes of the model in the range of 1.78 Hz – 3.32 Hz which were the outcomes from the full-scale numerical model eigenvalue analysis (scaled values according to the scale factor for frequency). The computational procedure was identical to that employed earlier as presented above in Section 1.2.4.

F.3.1 FE analysis results compared to test results

As presented earlier in Section F.3, the computed FE response time histories of the full-scale Model 1 were compared to the corresponding test results in terms of:

1) Acceleration at 7 locations along the depth compared to the records from the West side (Figure F-8) and the East side (Figure F-9)
2) Soil lateral boundary displacement along the depth compared to the records measured from string potentiometers (Figure F-10)
3) Racking (Figure F-11)

4) Wall bending moment on both sides of the tunnel (Figure F-12)

As observed in the model scale, the full-scale numerical response matches well with the recorded response.

F.4 Inclusion of Pinned Connection in Full-Scale FE Model

As shown in Figure F-13, two pinned connections (hinges) at the interface between the wall top and the roof were defined in the OpenSees tunnel model (full-scale). This modification essentially reduced the racking stiffness by as much as four times, compared to the employed fixed-fixed wall-roof and wall-base configuration scenario of the experimental phase. In this regard, the tunnel with the pinned connections is now represented by the earlier OpenSees FE model (presented in Section F.3). All other numerical considerations such as the soil material properties, boundary conditions, input motions, and so forth remained identical.

F.4.1 Comparison of FE analysis results with fixed and with hinge conditions

Figure F-14 and Figure F-15 show a comparison of soil acceleration (on the West side) and soil displacement along the lateral boundary of the FE mesh. As shown in these plots, the soil response was quite similar, regardless of the tunnel stiffness. As such, the selected nodal locations for this comparison represent a free-field condition (e.g., acceleration at 36 ft away and displacement at 72 ft away from the wall). Similarly, the soil displacement (distortion) at the level of the tunnel roof relative to the base (72 ft away from the wall) was quite similar (Figure F-16a).

Despite this similar soil response, the tunnel racking was significantly affected by the reduction in its lateral stiffness (Figure F-16b). Racking (about 3.3 in) for the pinned connections was higher by as much as 75% compared to the earlier fixed-fixed case (about 1.9 in), as summarized in Table F-6. Associated with the pinned connections, the resulting bending moment was essentially zero near the tunnel roof (Figure F-17). However, bending moment at the wall base was close to that of the earlier fixed-fixed case (Figure F-17).

For a given deflection (δ) at one end of a bending beam under two different boundary conditions: 1) fixed-fixed end (without the hinges) and 2) fixed-free end (with the hinges), the resulting bending moment (M) can be analytically computed as: 1) $M_{\text{fixed-fixed}} = 6EI\delta/h^2$ and 2) $M_{\text{fixed-free}} = 3EI\delta/h^2$ where EI and h are flexural rigidity and length of the beam, respectively. In our study, racking for the pinned connection (δ_{pinned}), which was about 75% larger than that in the

other case ($\delta_{\text{fixed-fixed}} = 1/1.75\ \delta_{\text{pinned}} = 0.57\delta_{\text{pinned}}$), resulted in the bending moment of $3EI\delta_{\text{pinned}}/h^2$, compared to $6EI(0.57\delta_{\text{pinned}})/h^2 = 3.4EI\delta_{pinned}/h^2$ with fixed connection (i.e., about 10% reduction).

Figure F-18 shows shear force time histories along the walls with fixed and with hinge connections. As observed above for bending moment (Figure F-17), shear force at the base was quite similar. The pinned connection resulted in lower shear force near the roof, about 30% of the fixed-fixed model case. In this regard, the additional hinge-induced flexibility mainly affected the displacement demand rather than the internal forces in the tunnel walls.

At peak racking, the resulting soil shear modulus from the fixed-fixed model (from soil elements next to the lateral boundary along the depth) is presented in Figure F-19a. The average soil shear modulus was about 3160 psi. Furthermore, the resulting shear strain was generally constant in the 16 soil layers along the depth from the tunnel roof to the base (about 0.6% as shown in Figure F-19b).

As discussed earlier in Section 6, tunnel racking can be estimated using the FHWA step-by-step procedure (Table 6-1). In this procedure, racking ratio (R_r) is determined by the flexibility ratio (F_r). Racking can then be computed by R_r multiplied by free-field soil distortion (along the tunnel height). As such, F_r and R_r were evaluated from the soil shear modulus (Figure F-19a) and racking stiffness (Figure F-13) as summarized in Table F-7. Without aid of the FHWA procedure, R_r can be directly obtained from the numerical results as shown in Table F-6. It is noted that, as discussed earlier in Section 6, the FHWA estimate is relatively higher that the test results. However, in this section, focus is on quantifying the change in F_r and R_r depending on racking stiffness with the fixed and the hinge connections.

As summarized in Table F-6, the pinned connection induced a higher R_r by as much as 53%, compared to the original fixed-fixed tunnel configuration (observed from the OpenSees FE analysis). This higher R_r consequently resulted in larger tunnel racking deformation without significant change in the wall bending moment as well as the soil response. Similarly, R_r estimated using F_r as presented in FHWA (2009), became about 50% higher than that with the fixed connection (Table F-7). As such, the above observation illustrates that tunnel racking with respect to soil deformation (i.e., R_r) can be determined by the relative stiffness between the tunnel and the surrounding soil (i.e., F_r).

F.5 Summary

Using a Finite Element model calibrated by the test results, a preliminary numerical investigation was conducted to assess the influence of a potential hinge connection between the tunnel walls and the roof. In general, the numerical response matched well with the recorded response during the Nor100PT1 input excitation. To evaluate seismic capacity of the tunnel with respect to change in the tunnel stiffness, wall-roof hinge connections were prescribed on both sides of the tunnel. Using this modified tunnel model, the numerical results showed that the reduced tunnel stiffness increased the displacement demand by as much as 75%. However, no significant change in the wall peak bending moment or shear force were noted. Racking deformation for the pinned connection scenario can thus be potentially estimated by the FHWA (2009) procedure, employing the corresponding reduced tunnel racking stiffness.

Table F-1: OpenSees soil material properties (PressureDependMultiYield) for Model 1 in model scale

Model parameter	**Parameter value**	
	Below tunnel base	**Above tunnel base**
Unit weight (pcf)	120	
Reference shear modulus, G_r (psi)	2623	
Reference shear wave velocity (ft/s)	318	
Poisson's ratio	0.4	
Reference bulk modulus, B_r (psi)	12,241	
Reference confining stress, p'_r (psi)	4.3	
Peak shear strain	0.03	
Friction angle (degrees)	41	46

Table F-2: OpenSees beam-column element material properties of tunnel wall (based on 1 in plane strain FE model thickness)

Unit weight (γ)	490 pcf
Young's modulus (E)	25,164 ksi
Moment of inertia (I)	0.0352 in^4
Sectional area (A)	0.75 in^2

Table F-3: OpenSees quadrilateral element material properties of tunnel structure

Part	Slab	Roof (HSS sections)	Wood
Unit weight (γ)	160 pcf	39 pcf	6 pcf
Young's modulus (E)	Essentially rigid for the entire analysis phases (static and shaking)		
Poisson's ratio (v)	0.3		

Table F-4: OpenSees soil material properties (PressureDependMultiYield) for Model 1in prototype scale

Model parameter	**Parameter value**	
	Below tunnel base	**Above tunnel base**
Unit weight (pcf)	120	
Reference shear modulus, G_r (psi)	7,869 (scaled by a factor of $9^{0.5} = 3$)	
Reference shear wave velocity (ft/s)	551 (scaled by a factor of $9^{0.25} = 1.73$)	
Poisson's ratio	0.4	
Reference bulk modulus, B_r (psi)	36,723 (scaled by a factor of $9^{0.5} = 3$)	
Reference confining stress, P'_r (psi)	38.7 (scaled by a factor of 9)	
Peak shear strain	0.09 (scaled by a factor of $9^{0.5} = 3$)	
Friction angle (degrees)	41	46

Table F-5: OpenSees beam-column element material properties of tunnel wall per unit length of 1 inch in prototype scale

Unit weight (γ)	490 pcf
Young's modulus (E)	75,492 ksi (scaled by a factor of $9^{0.5} = 3$)
Moment of inertia (I)	25.66 in^4 (scaled by a factor of $9^3 = 729$)
Sectional area (A)	6.75 in^2 (scaled by a factor of 9)

Table F-6: OpenSees FE analysis results with fixed and with hinge boundary condition

Parameter	**Original model configuration (fixed condition)**	**Modified model configuration (with hinges)**
Soil distortion (in)	1.96	2.17
Racking (in)	1.92	3.25
Racking ratio, R_r	0.98	1.50

Table F-7: Comparison of flexibility and racking ratios resulting from OpenSees FE analyses with fixed and with hinge boundary condition

Parameter	**Fixed condition**	**With hinges**	
		G_m from original model config.	**G_m from modified model config.**
Effective shear modulus, G_m (psi)	3,155	3,155	3,028
Racking stiffness, K_s (psi)	2,995	767	767
Flexibility ratio, F_r (FHWA 2009)	1.88	7.35	7.06
Racking ratio, R_r (FHWA 2009)	1.42	2.04	2.03

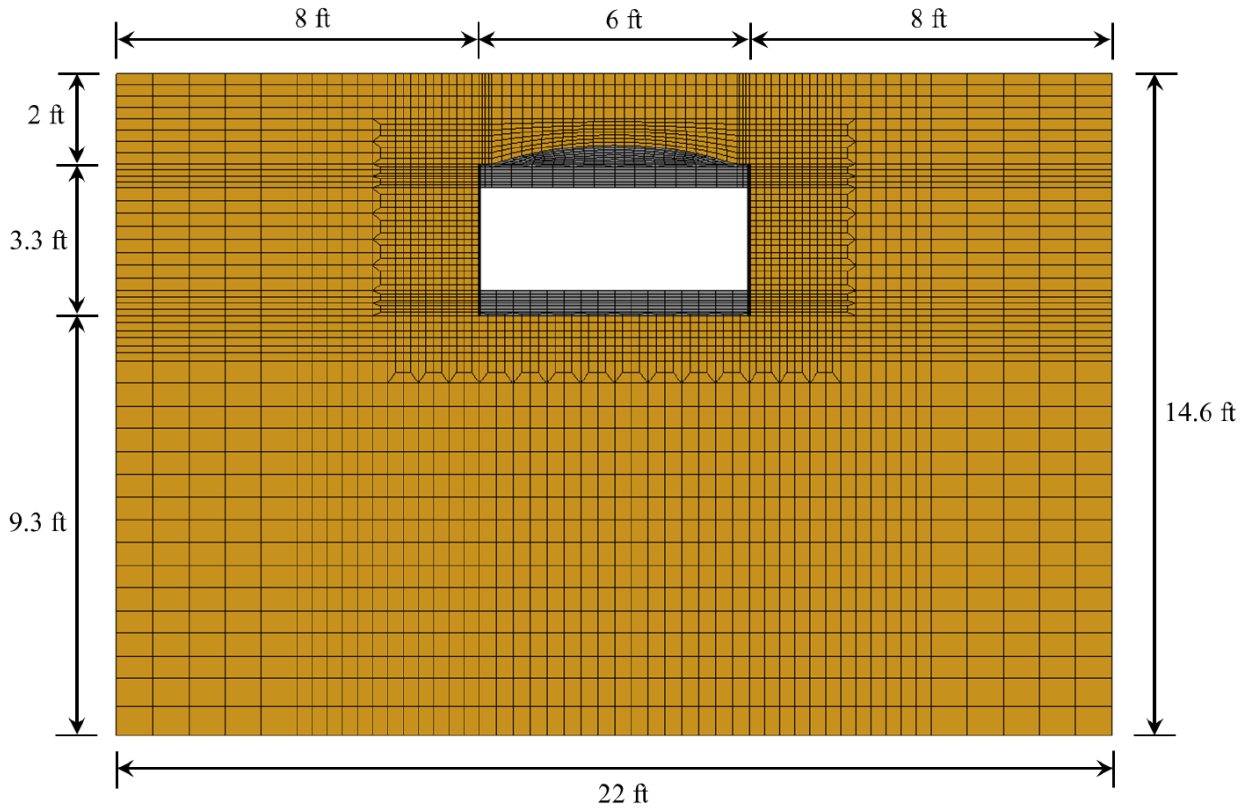

(a)

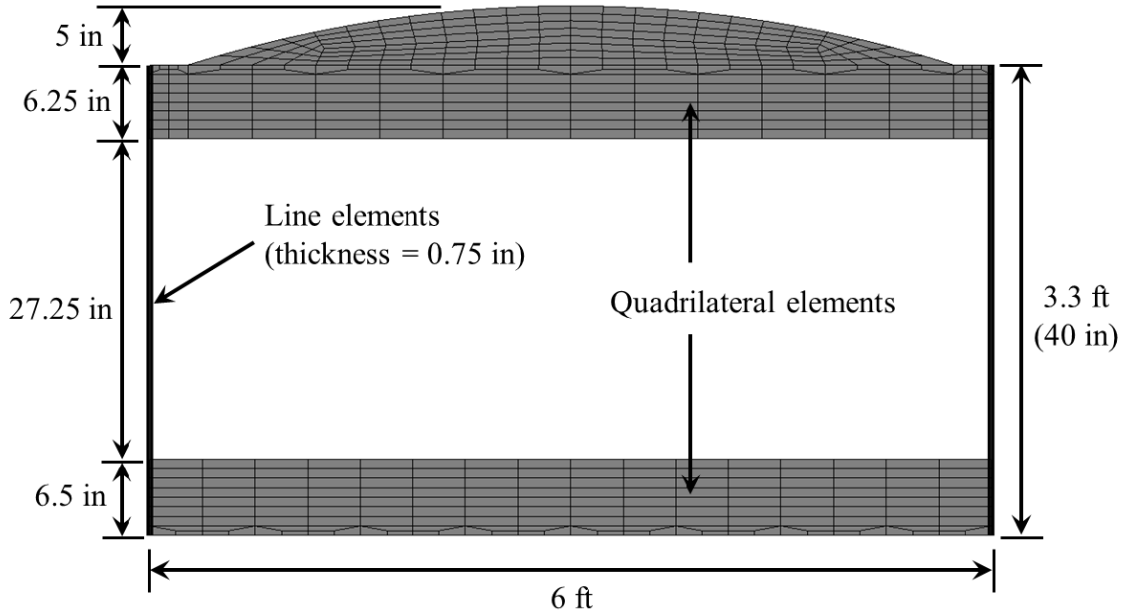

(b)

Figure F–1: OpenSees mesh for shake table test model: (a) entire tunnel-ground model and (b) tunnel model

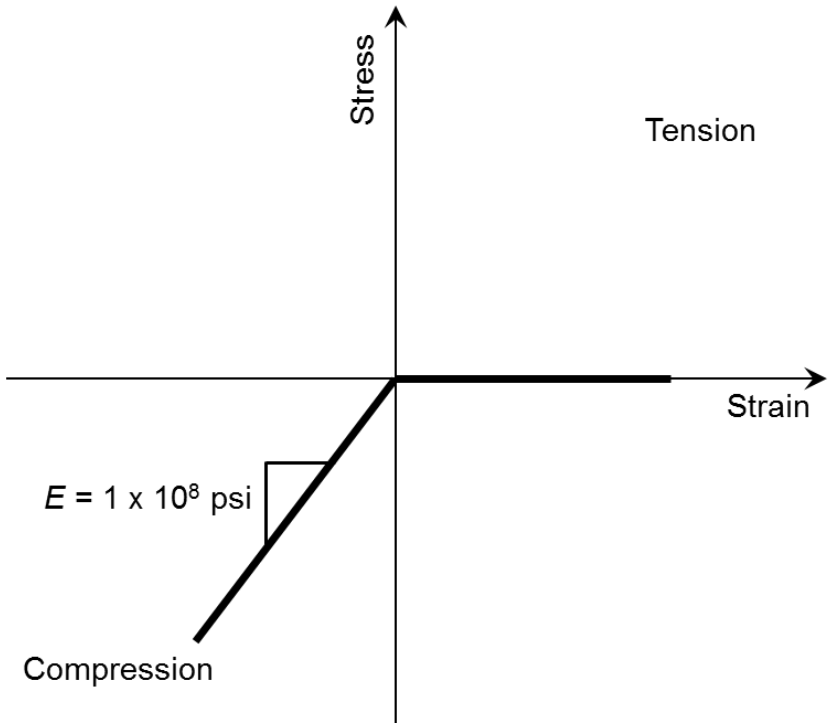

Figure F–2: Elastic no-tension (ENT) uniaxial material backbone curve

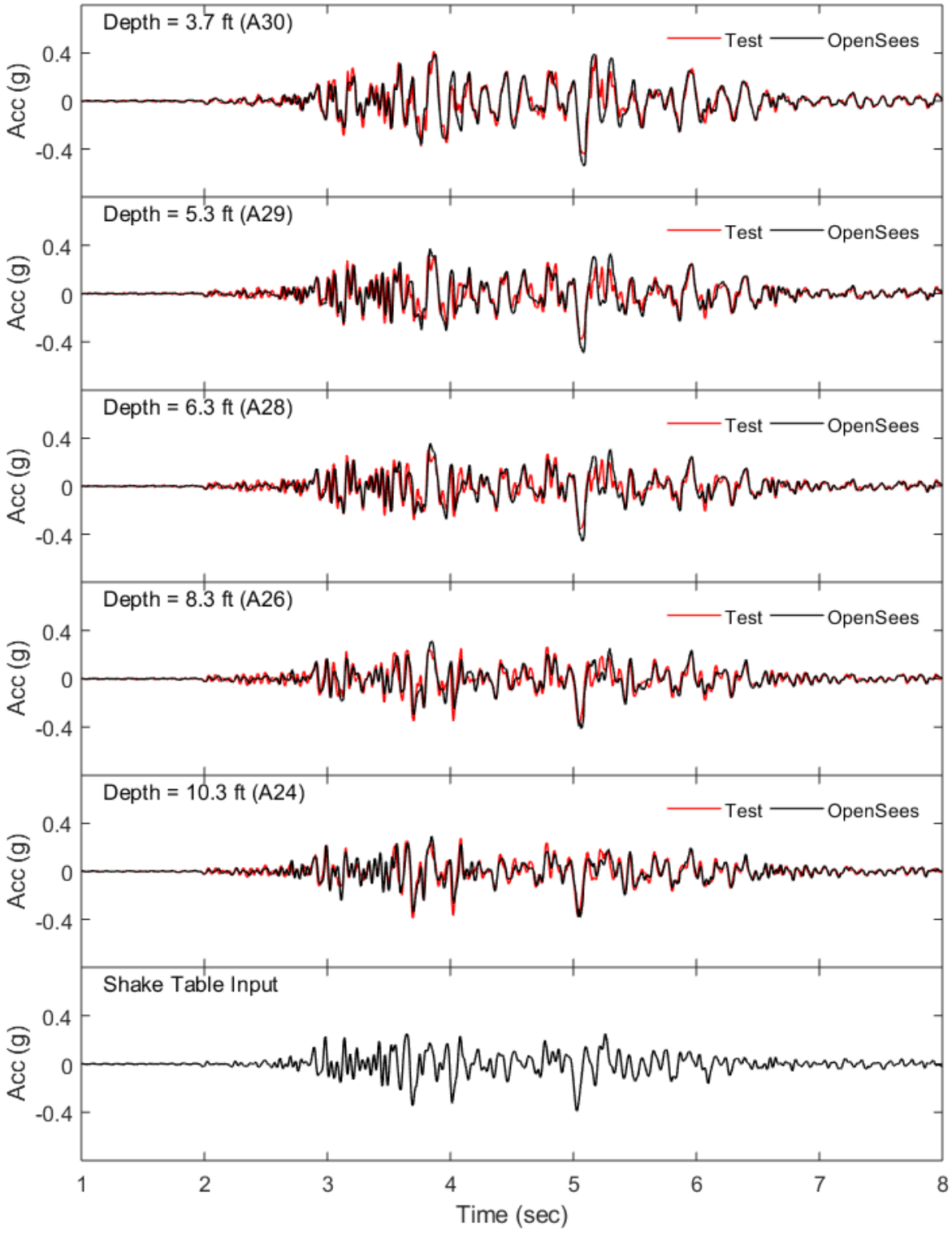

Figure F–3: Soil acceleration time histories on the West soil from Model 1 Nor100PT1

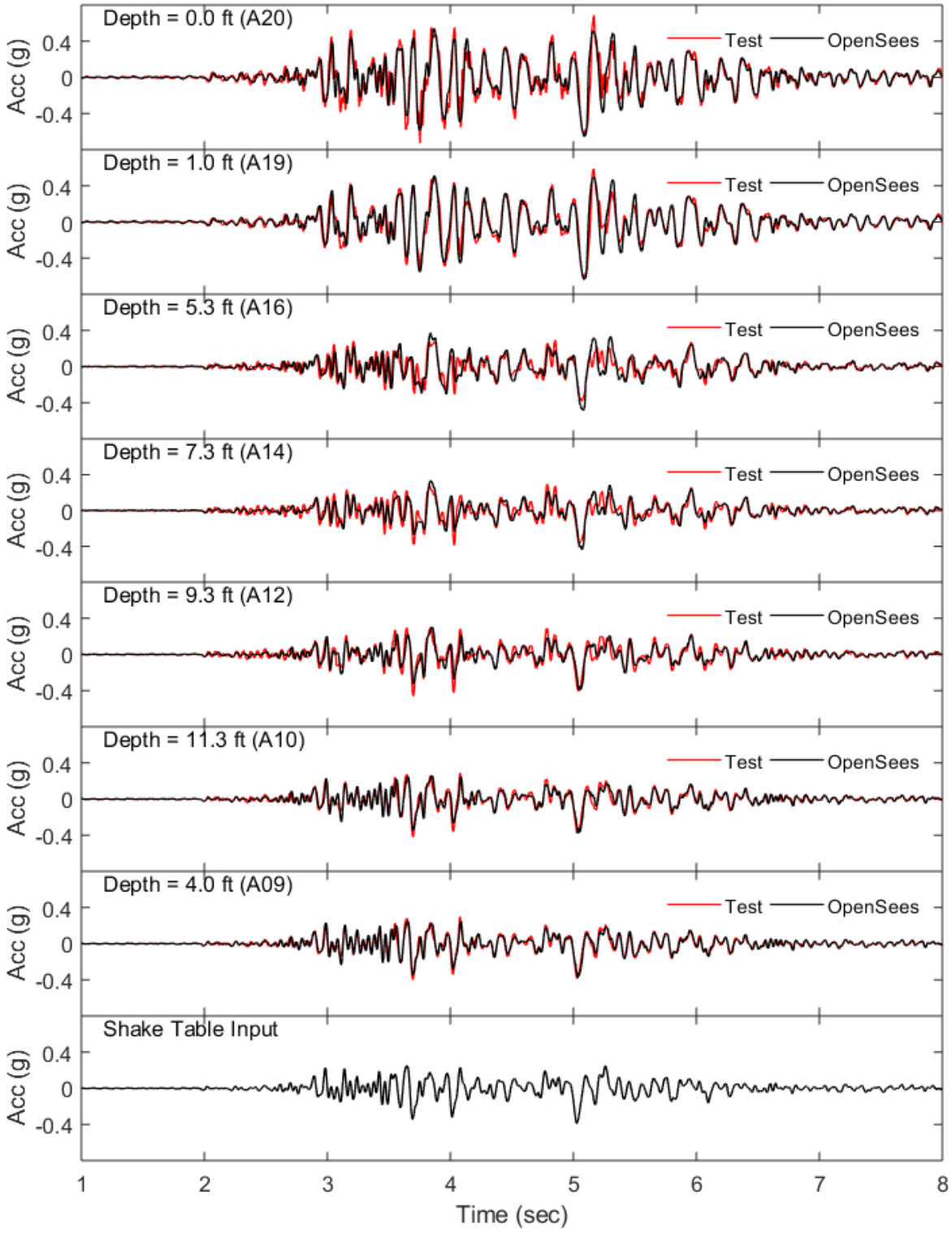

Figure F–4: Soil acceleration time histories on the East soil from Model 1 Nor100PT1

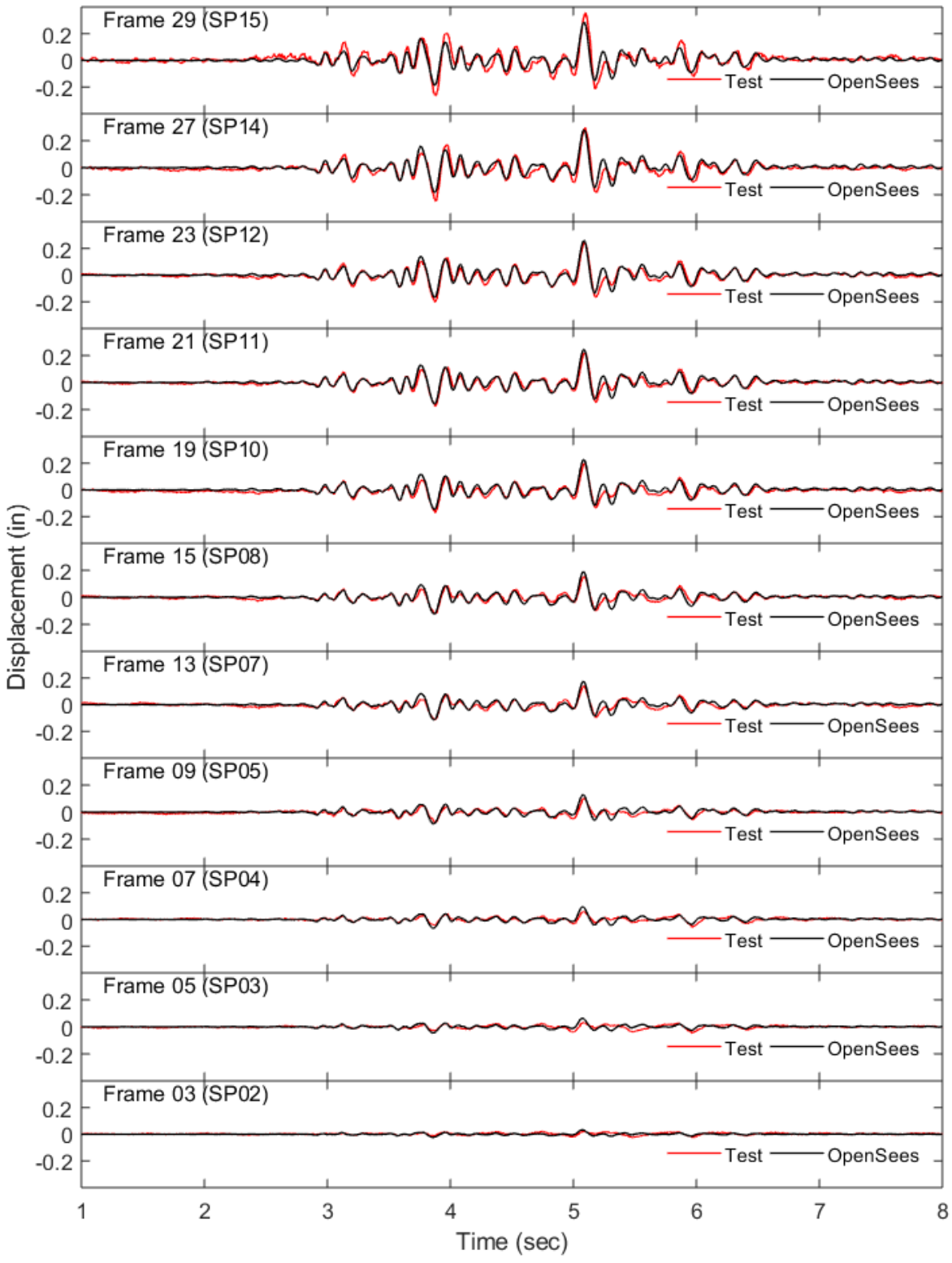

Figure F–5: Soil displacement along depth (side boundary) relative to the base from Model 1 Nor100PT1

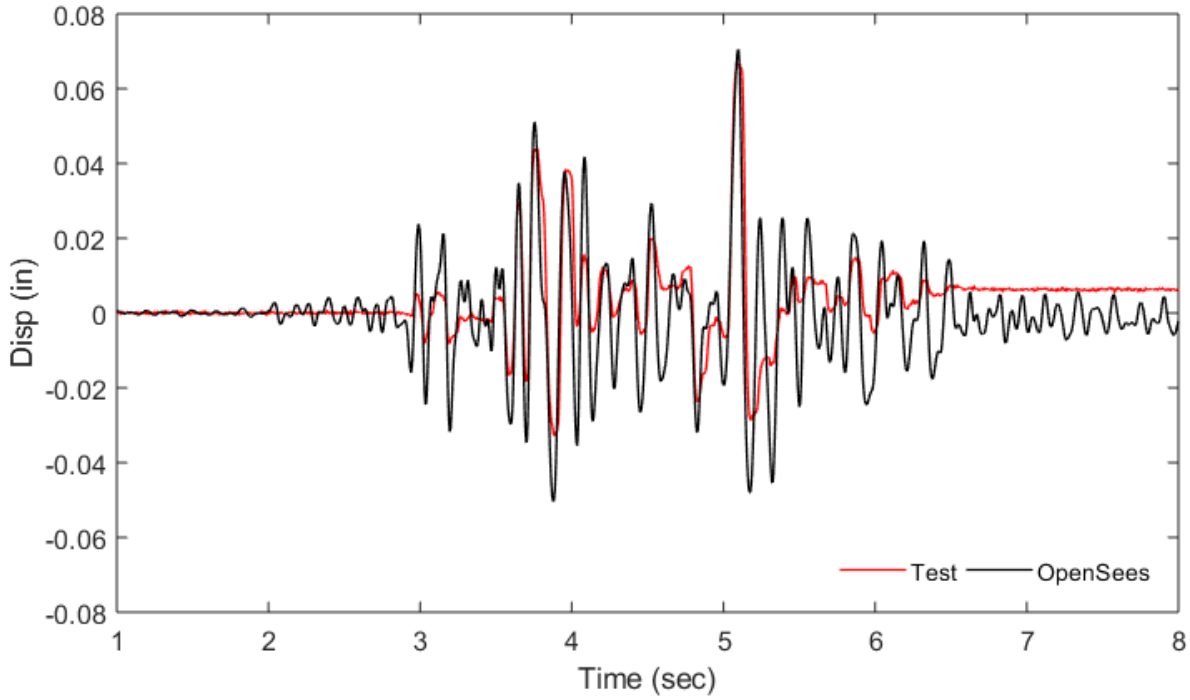

Figure F–6: Racking time history from Model 1 Nor100PT1

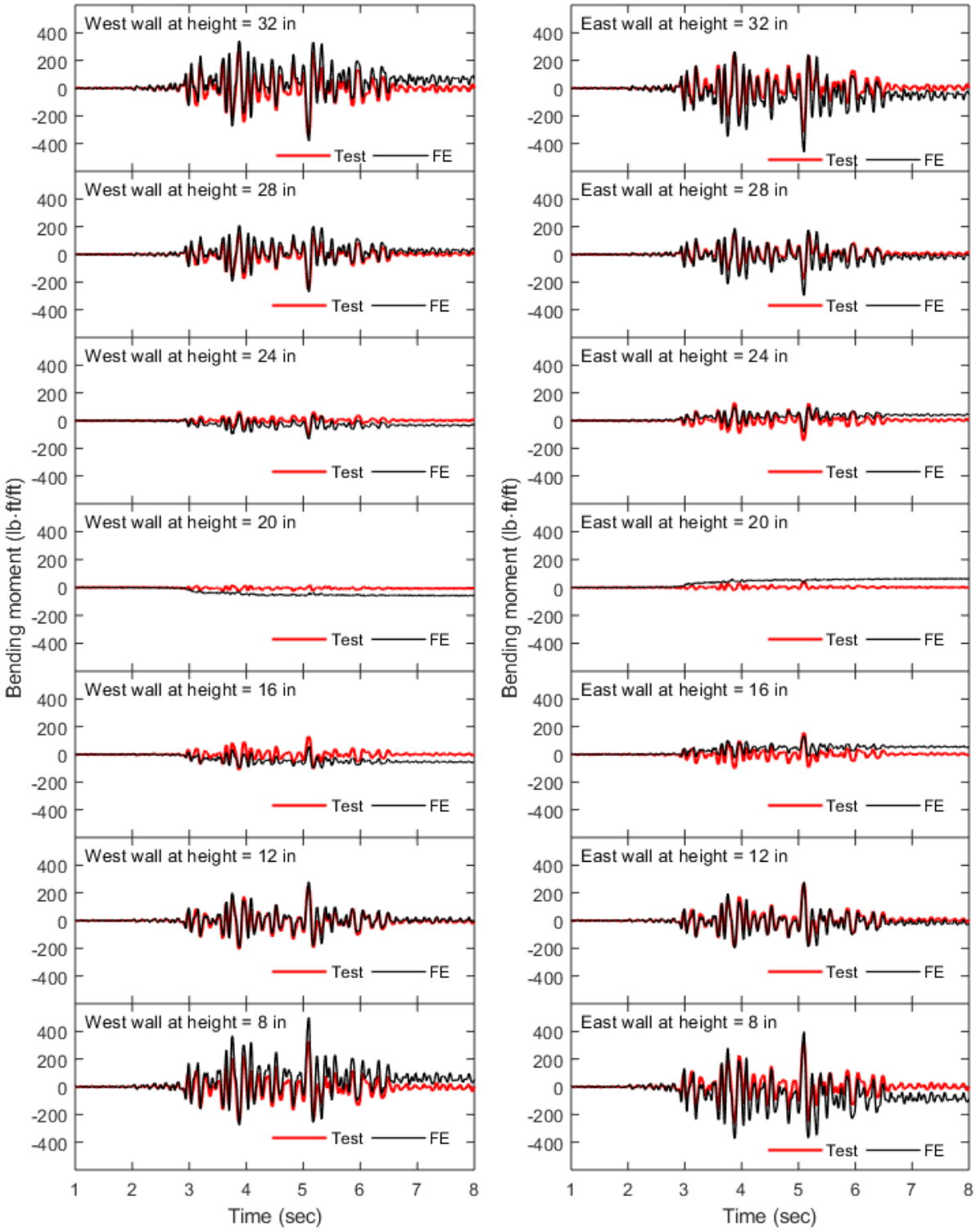

Figure F–7: Wall bending moment time histories from Model 1 Nor100PT1

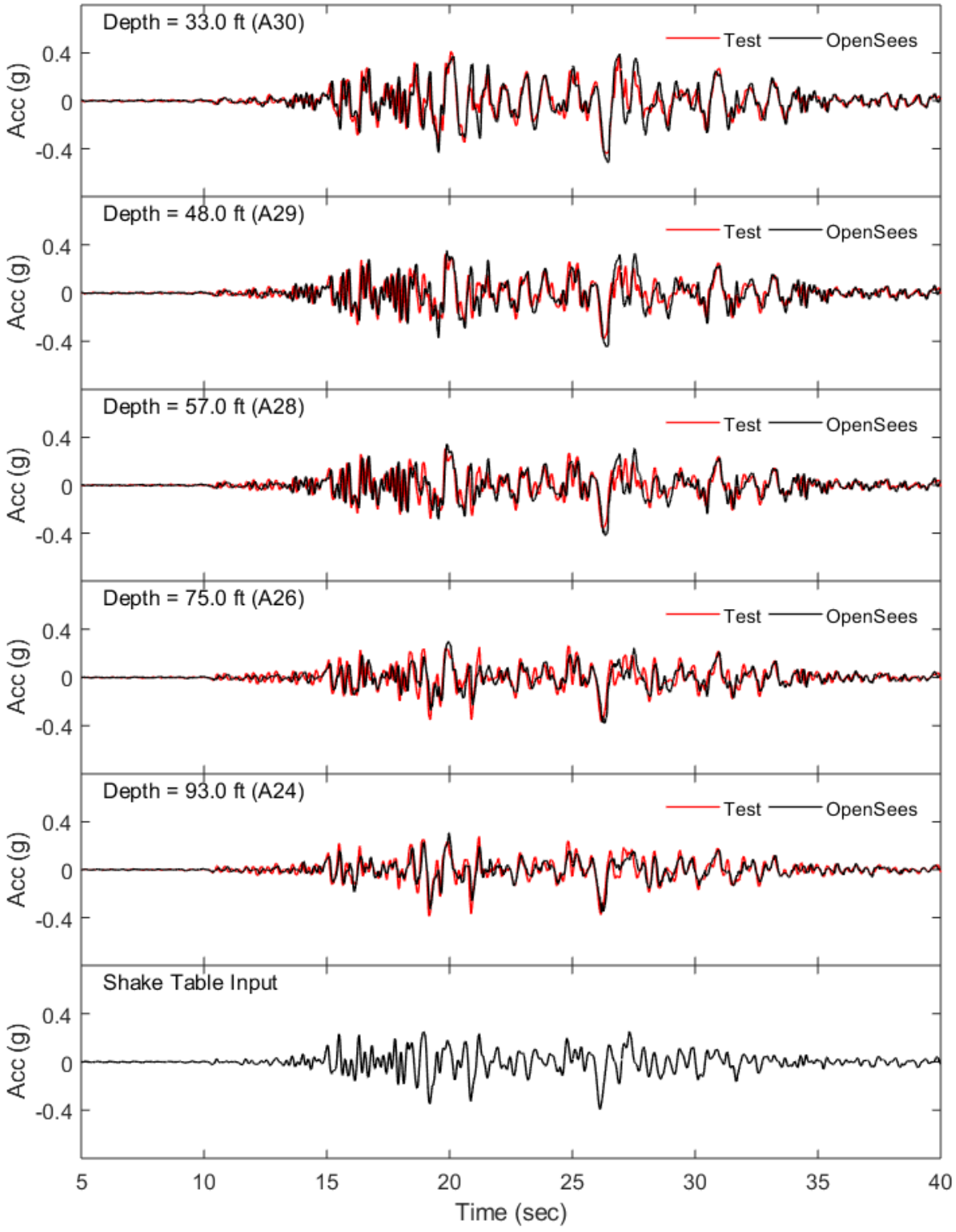

Figure F–8: Soil acceleration time histories on the West soil from Model 1 Nor100PT1 in prototype scale

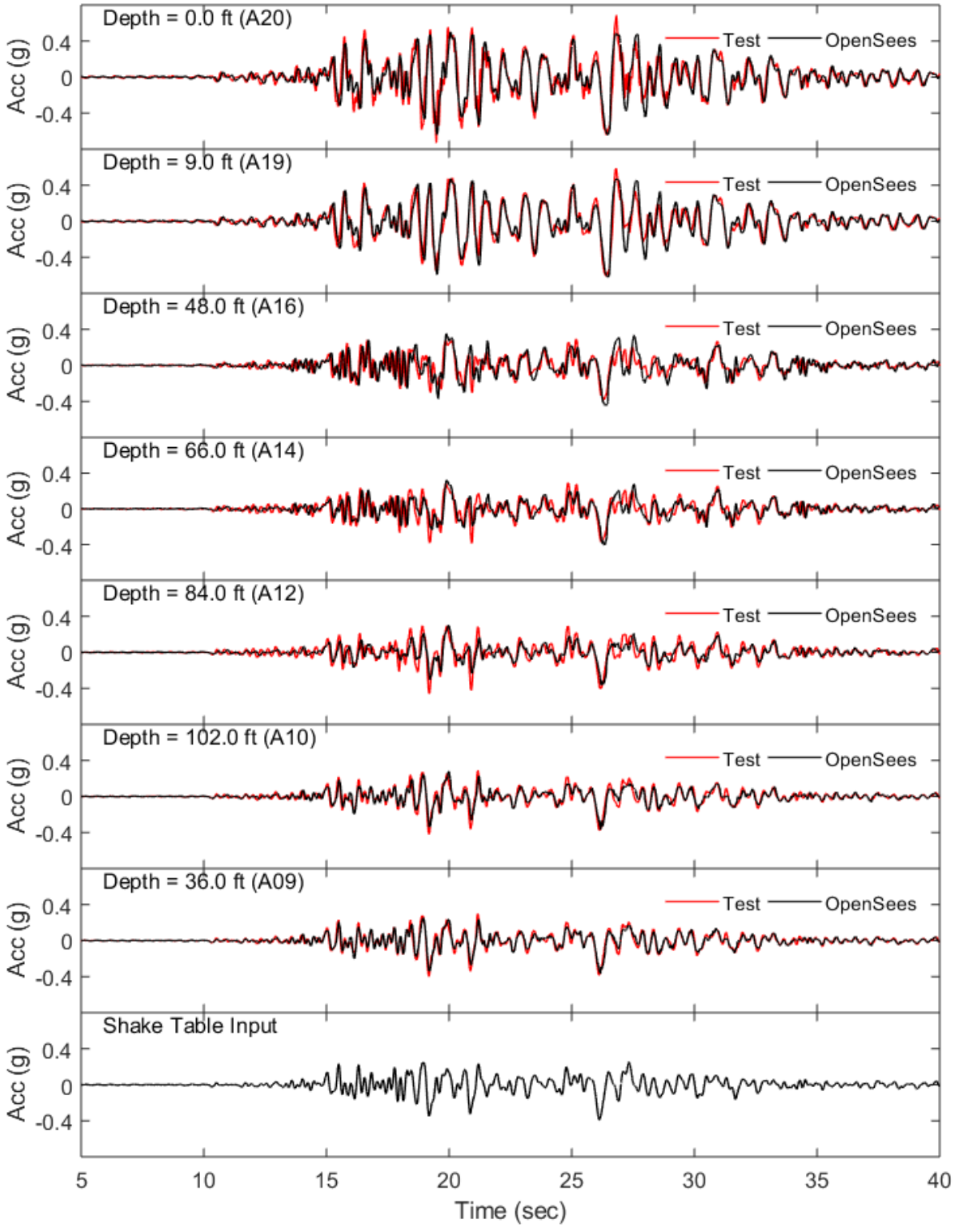

Figure F–9: Soil acceleration time histories on the East soil from Model 1 Nor100PT1 in prototype scale

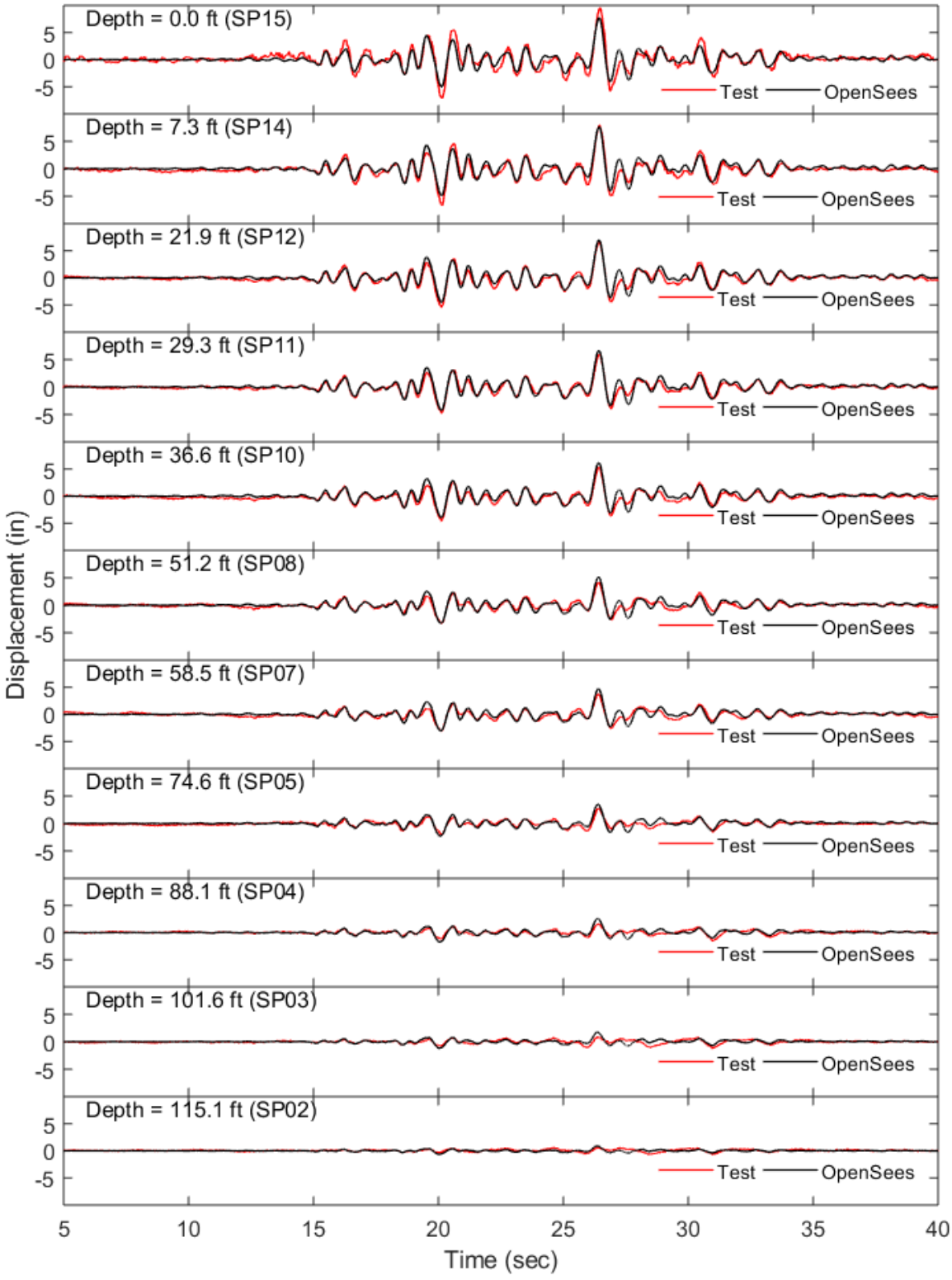

Figure F–10: Soil displacement along depth (side boundary) relative to the base from Model 1 Nor100PT1 in prototype scale

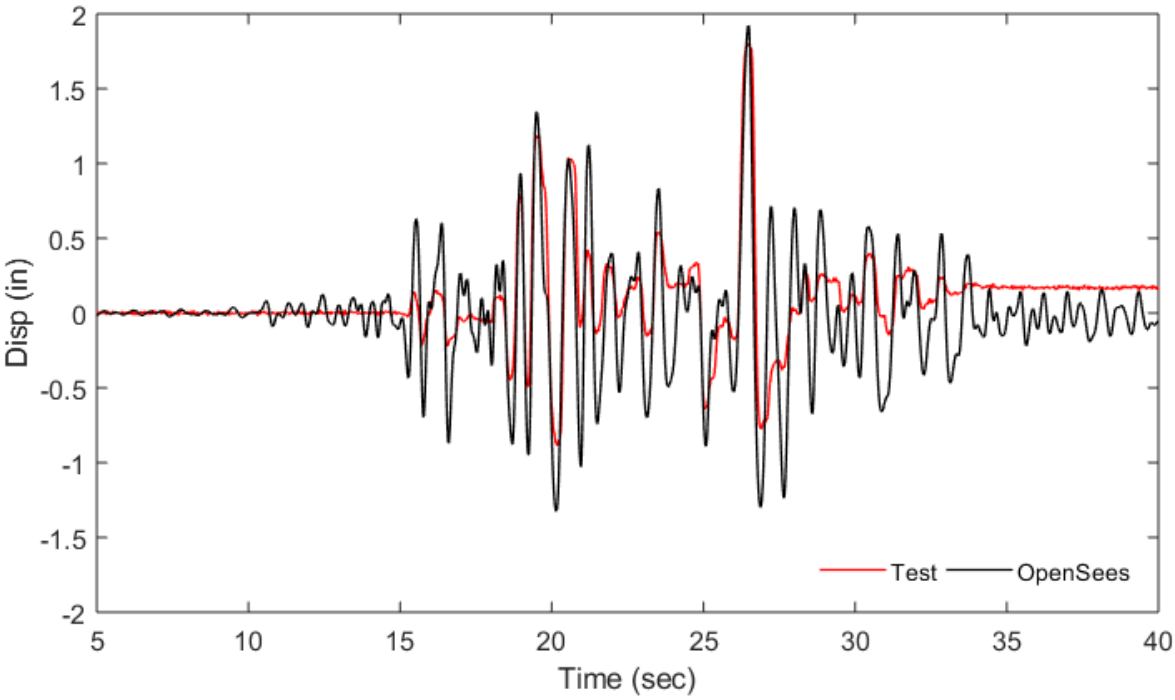

Figure F–11: Racking time history from Model 1 Nor100PT1 in prototype scale

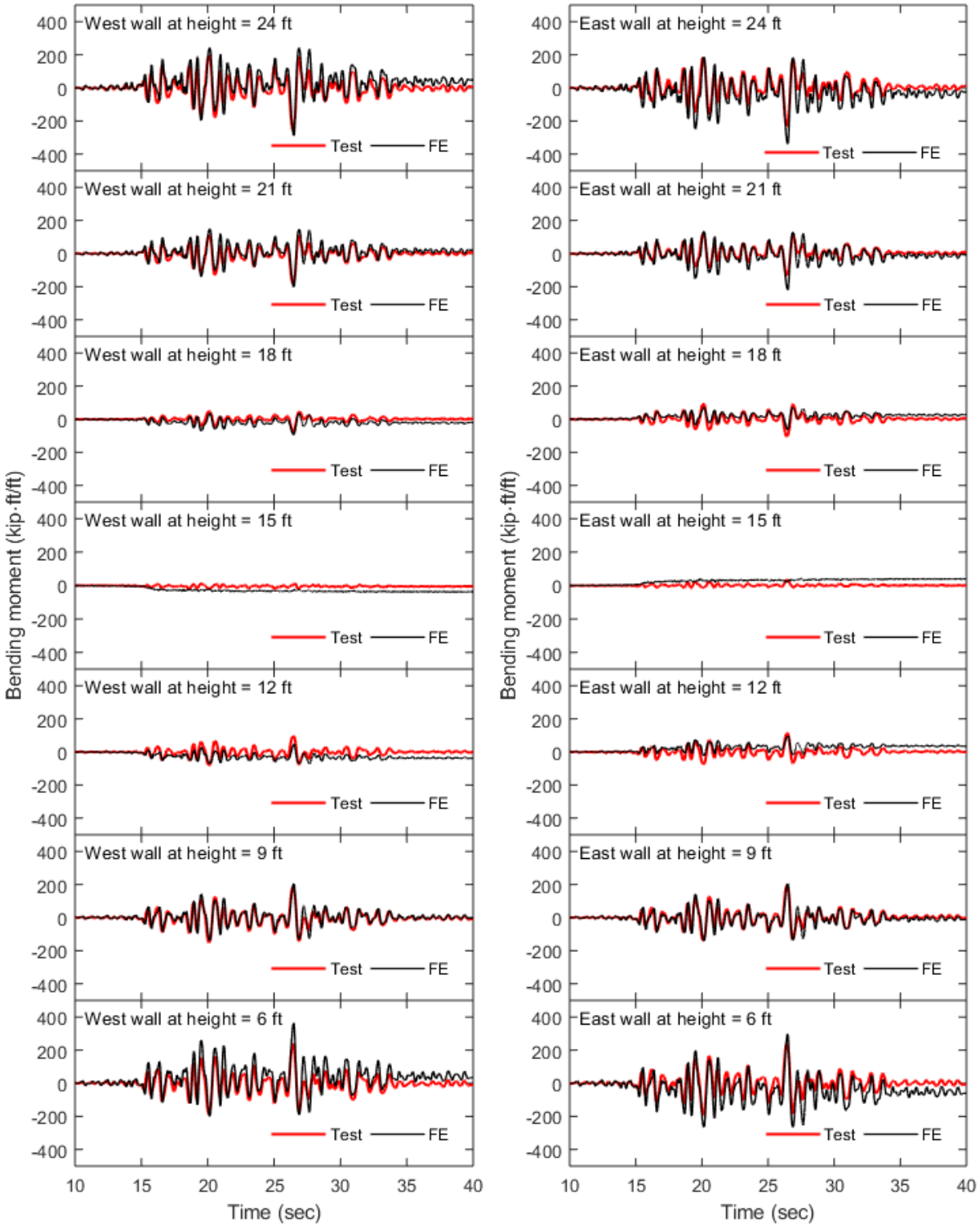

Figure F–12: Wall bending moment time histories from Model 1 Nor100PT1 in prototype scale

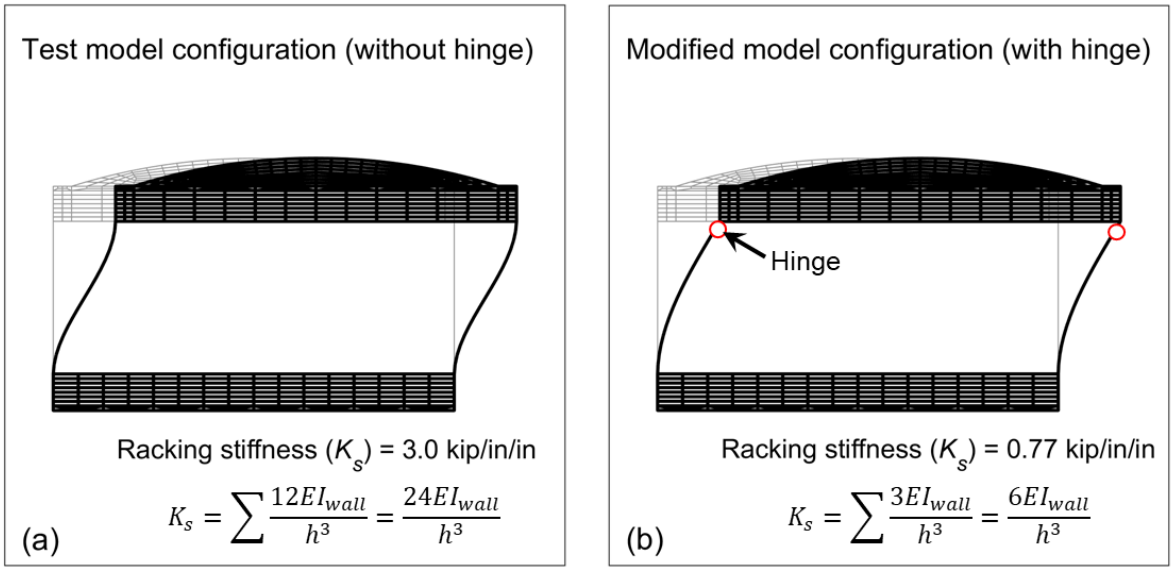

Figure F–13: Deformed configuration of OpenSees tunnel model subjected to unit displacement at the wall top with fixed and with hinge boundary condition

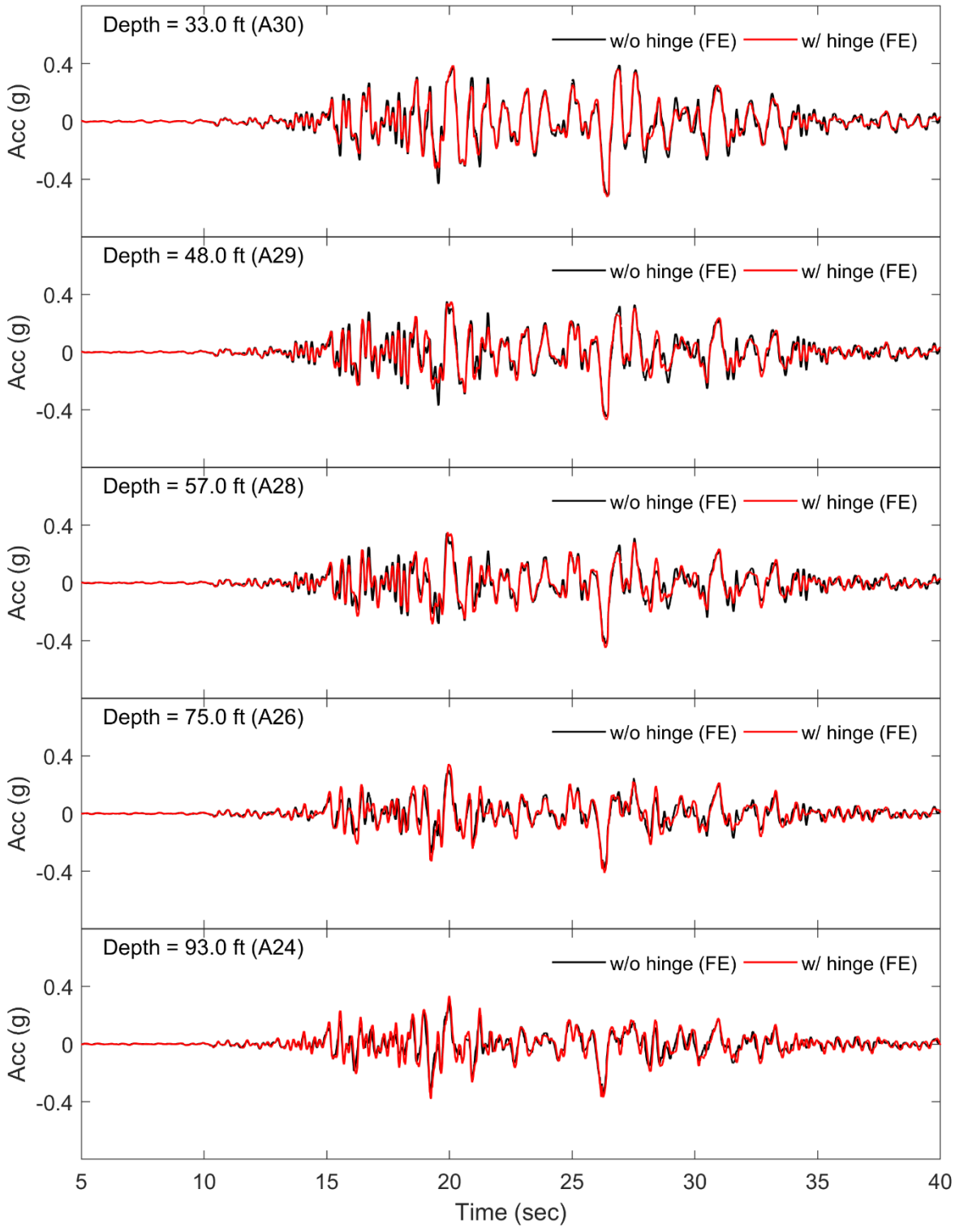

Figure F–14: OpenSees soil acceleration time histories on the West soil from Model 1 Nor100PT1 with fixed and with hinge boundary condition in prototype scale

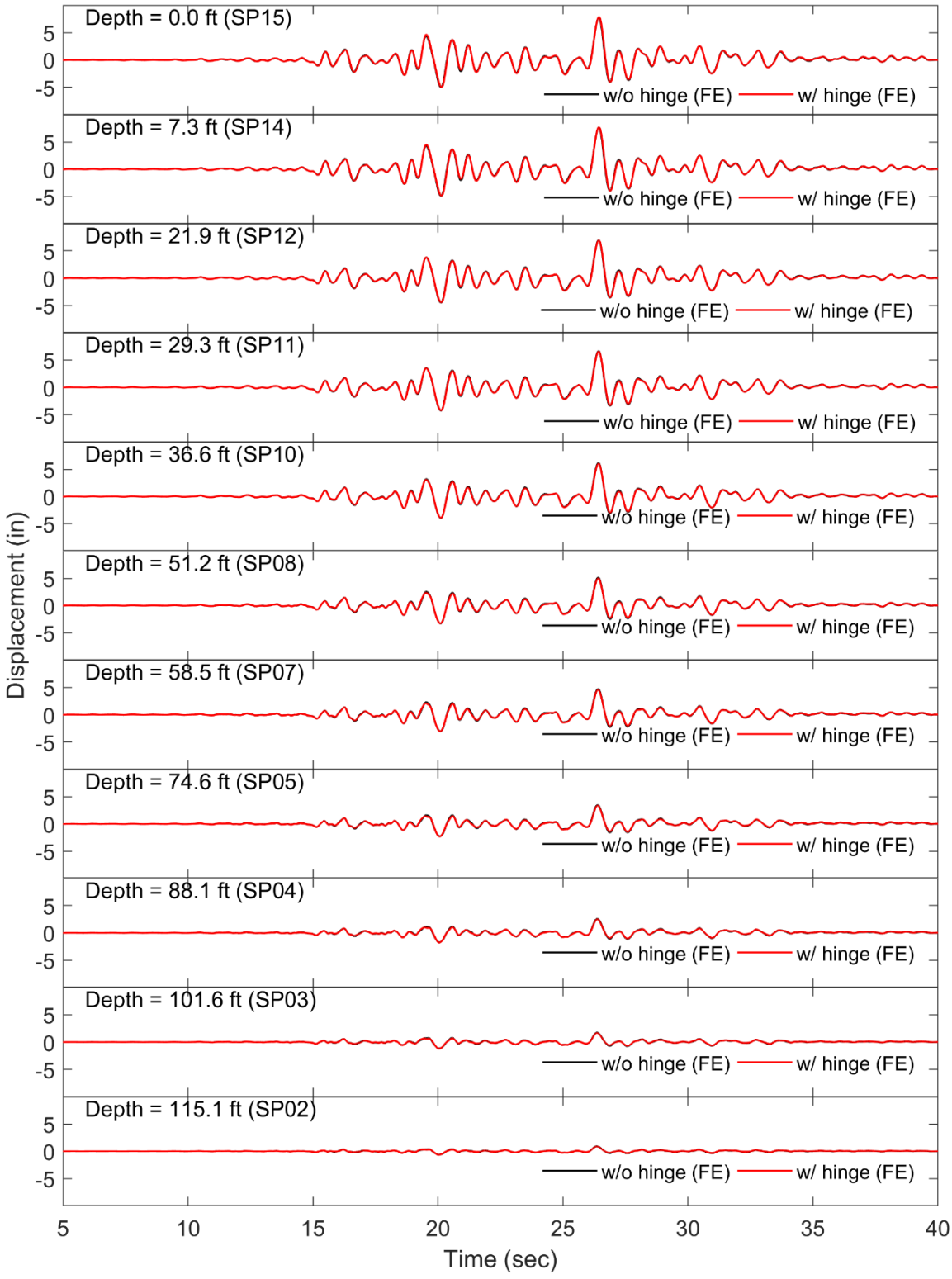

Figure F–15: OpenSees soil displacement along depth (side boundary) relative to the base from Model 1 Nor100PT1 with fixed and with hinge boundary condition in prototype scale

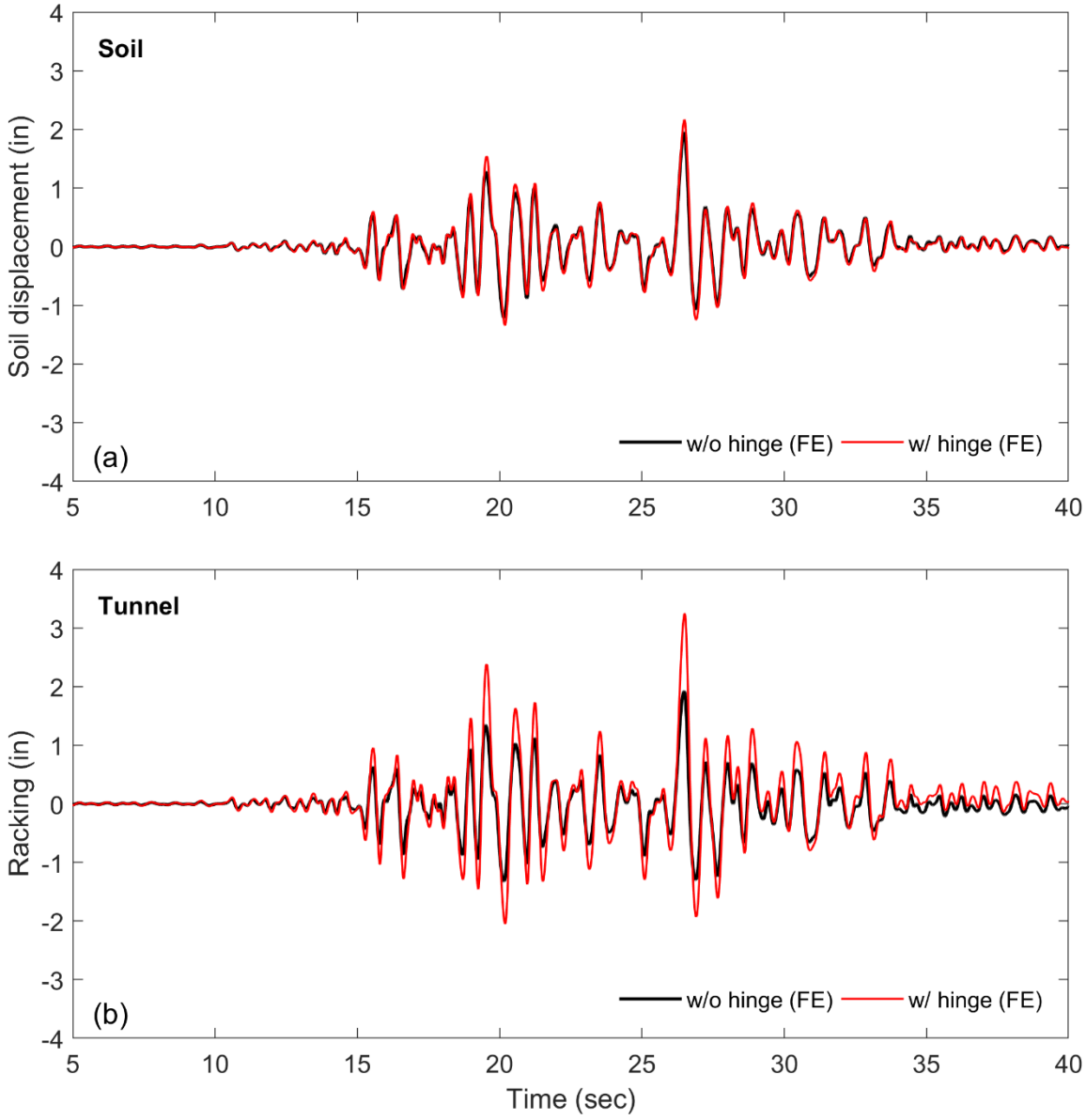

Figure F–16: OpenSees soil displacement at level of the tunnel top relative to the base (a) and racking (b) from Model 1 Nor100PT1 with fixed and with hinge boundary condition in prototype scale

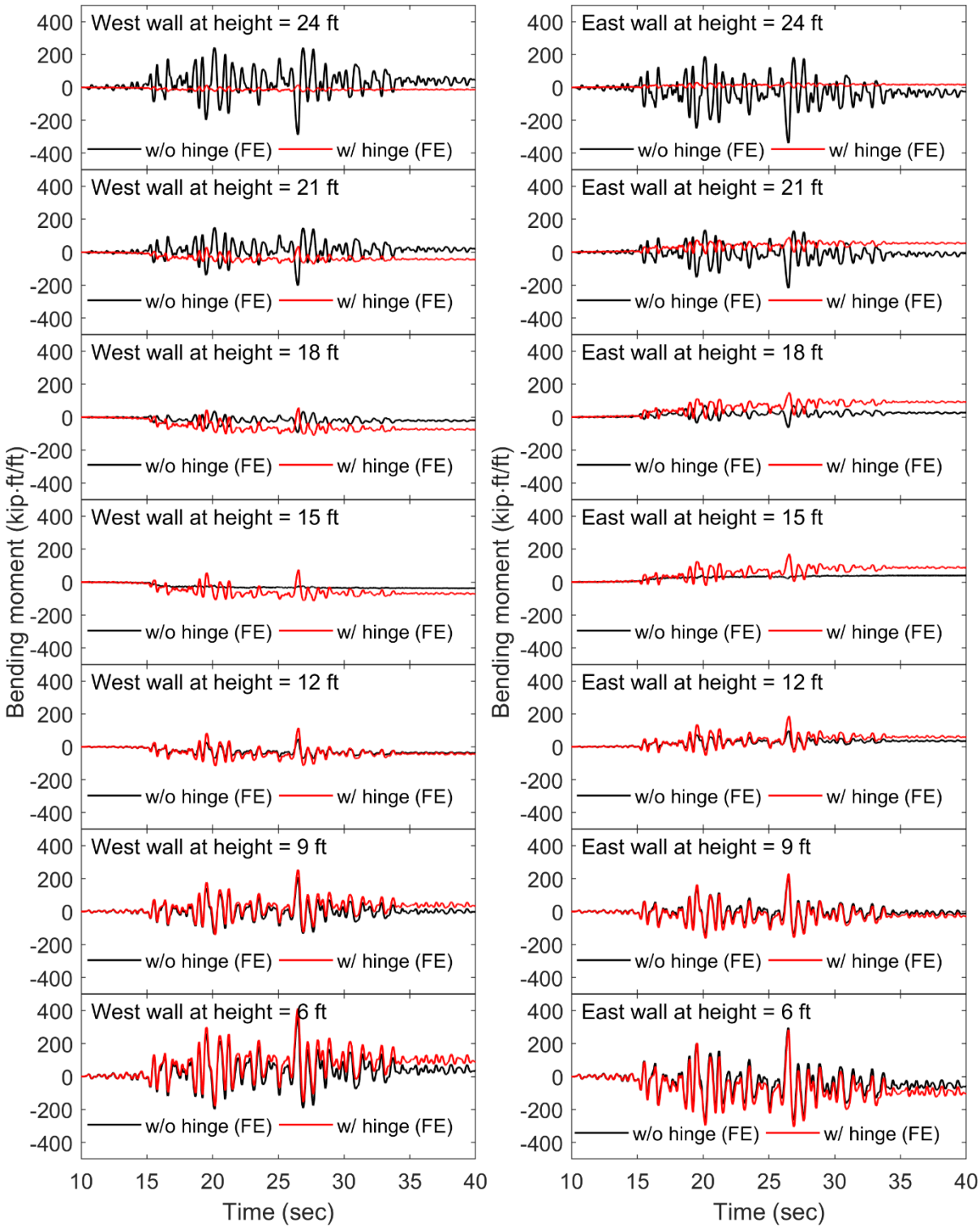

Figure F–17: OpenSees wall bending moment time histories (per unit wall length of 1 ft) from Model 1 Nor100PT1 with fixed and with hinge boundary condition in prototype scale

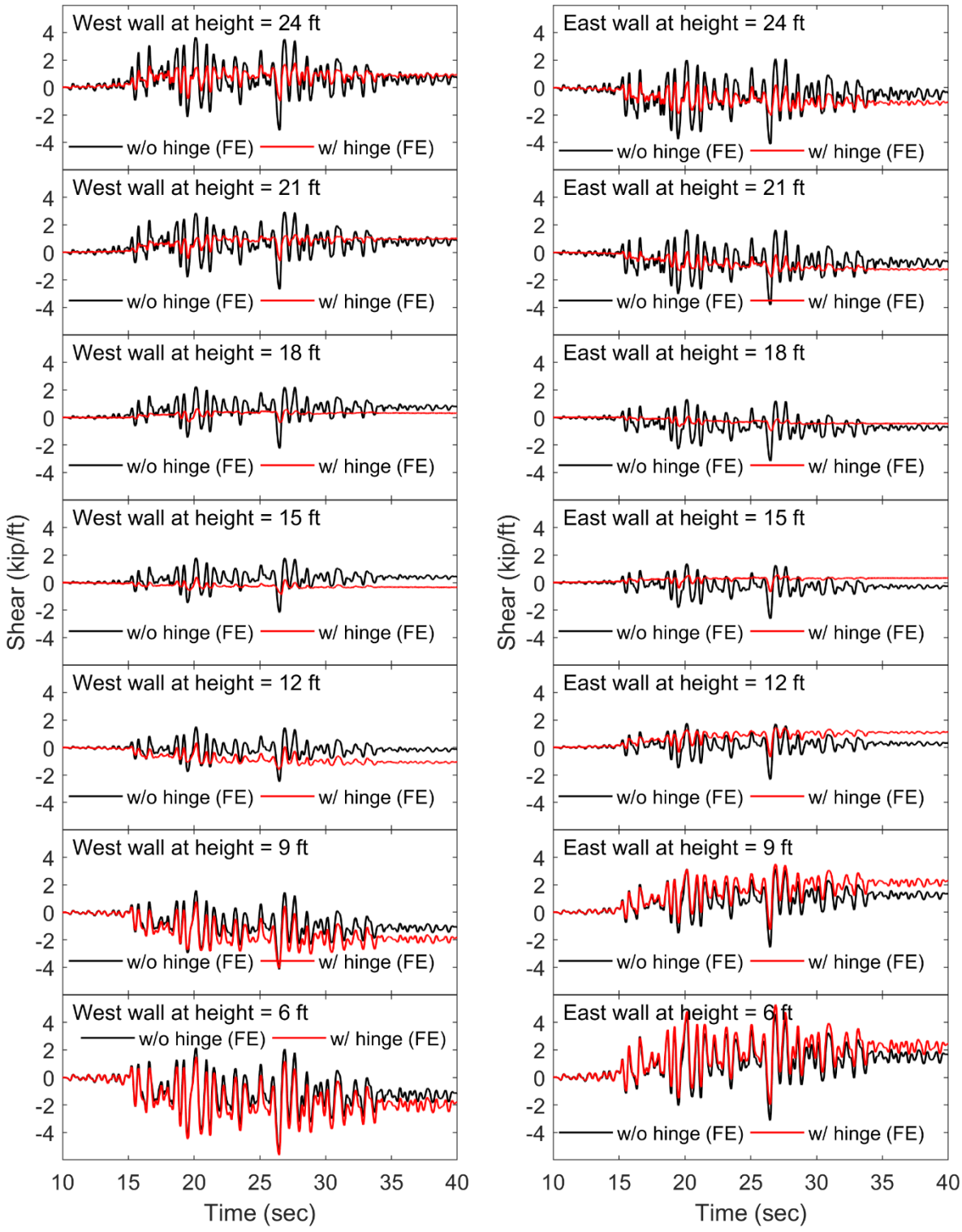

Figure F–18: OpenSees wall shear force time histories (per unit wall length of 1 ft) from Model 1 Nor100PT1 with fixed and with hinge boundary conditions in prototype scale

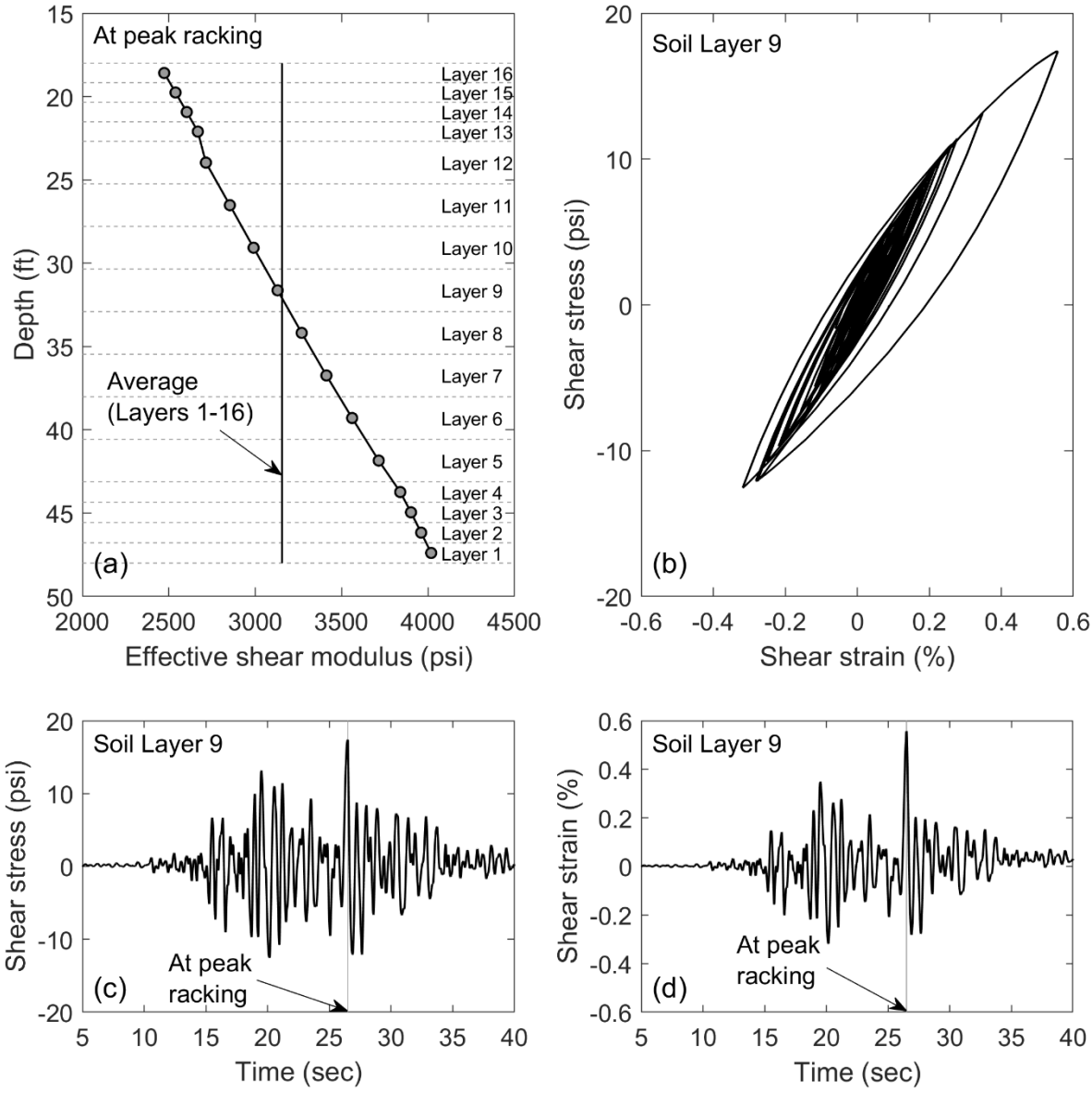

Figure F–19: OpenSees soil response from Model 1 Nor100PT1 in prototype scale: (a) effective shear modulus profile along the tunnel wall height; (b) shear stress vs strain from the soil layer at the middle height of tunnel wall; (c) shear stress time history; (d) shear strain time history

Appendix G : Summary of Reinforced Concrete Tunnel Test

This appendix presents a summary of the 1/3 scale reinforced concrete tunnel test under quasi-static cyclic loading. Full description of the test results were reported in the previous Caltrans report (Kim et al. 2015).

Figure F-1b shows the test model that was idealized from the Doyle Drive battery tunnel (see Figure F-1a for the typical cross section). The photograph and drawing of the test setup are shown in Figure F-2 and Figure F-3, respectively. Under the control of the lateral displacement at the top of the tunnel (Figure F-4), the relationship of the lateral force and displacement in model scale is shown in Figure F-5. This test result was interpreted in the full scale (Figure F-6).

A numerical effort was made to simulate the lateral force-displacement behavior of the 1/3 scale RC tunnel using the OpenSees platform (Figure F-7 and Figure F-8). On this basis, the actual scale model was built and the moment-curvature response of the wall section in the full scale is shown in Figure F-9.

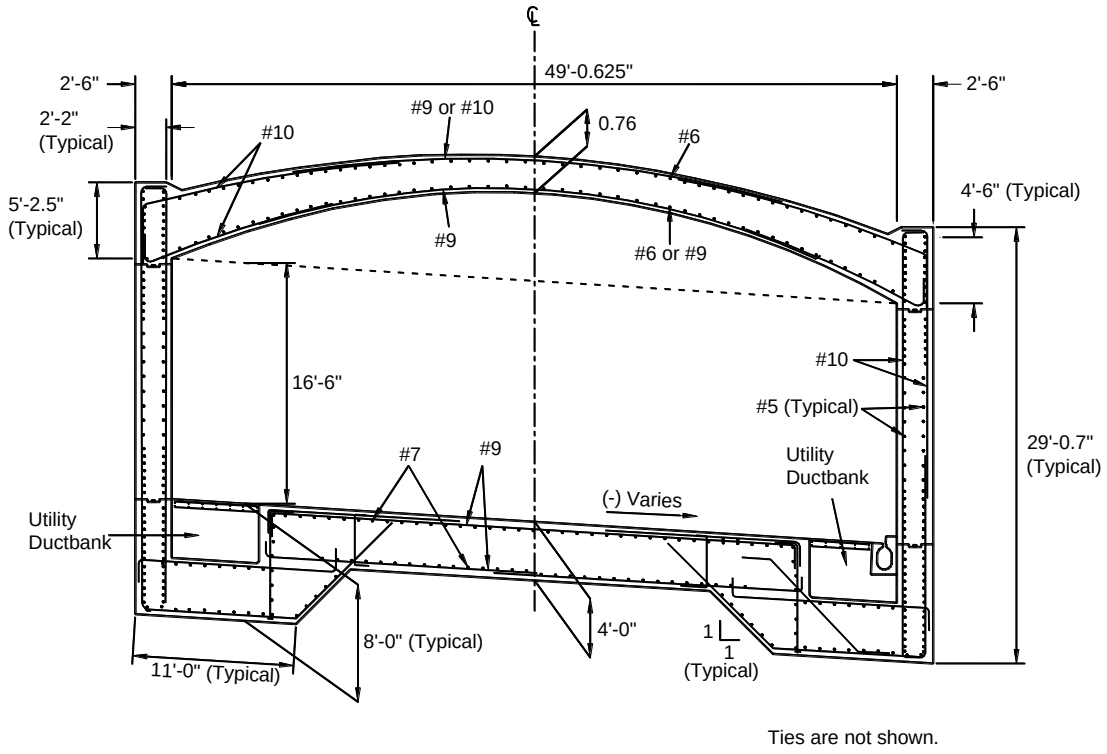

(a)

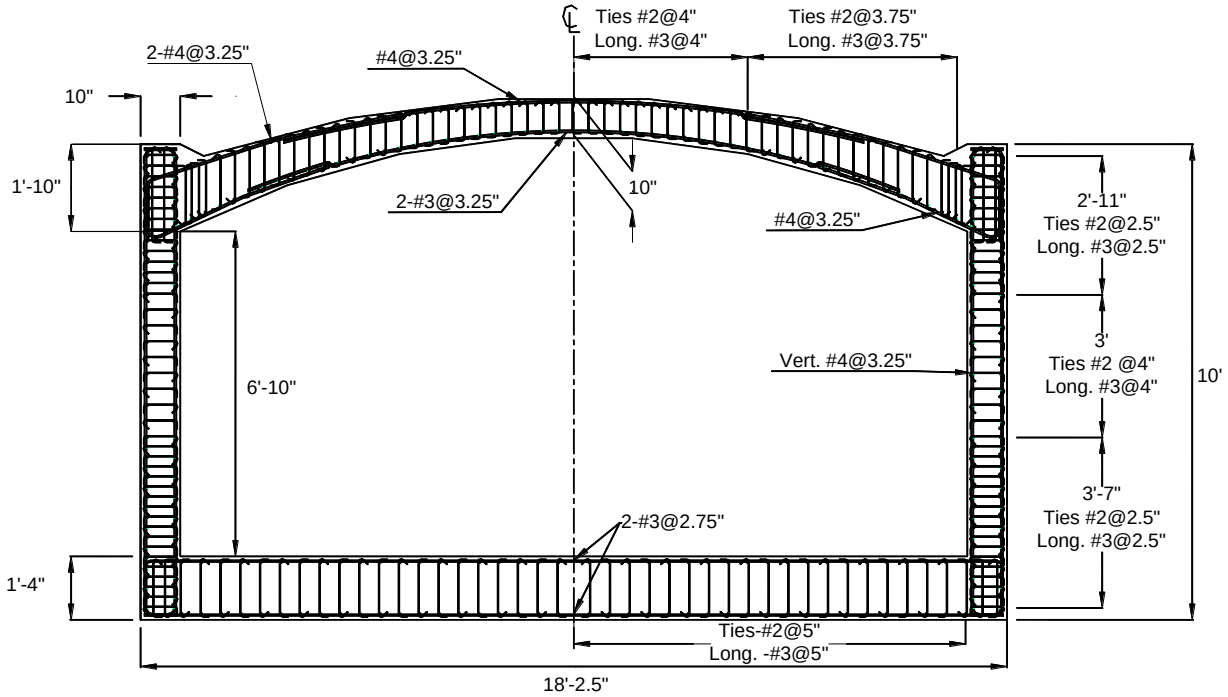

(b)

Figure G–1: Reinforced concrete tunnel: (a) typical cross-section of the Doyle Drive Battery Tunnel (Caltrans, 2012); (b) 1/3 scale test model at UCSD

(a) Test setup

(b) Loading frame North-Top connection

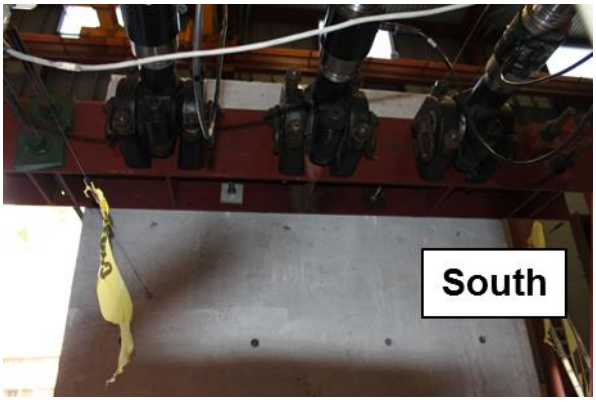

(c) Location of the actuators (South-Top)

Figure G–2: Photograph of the test setup

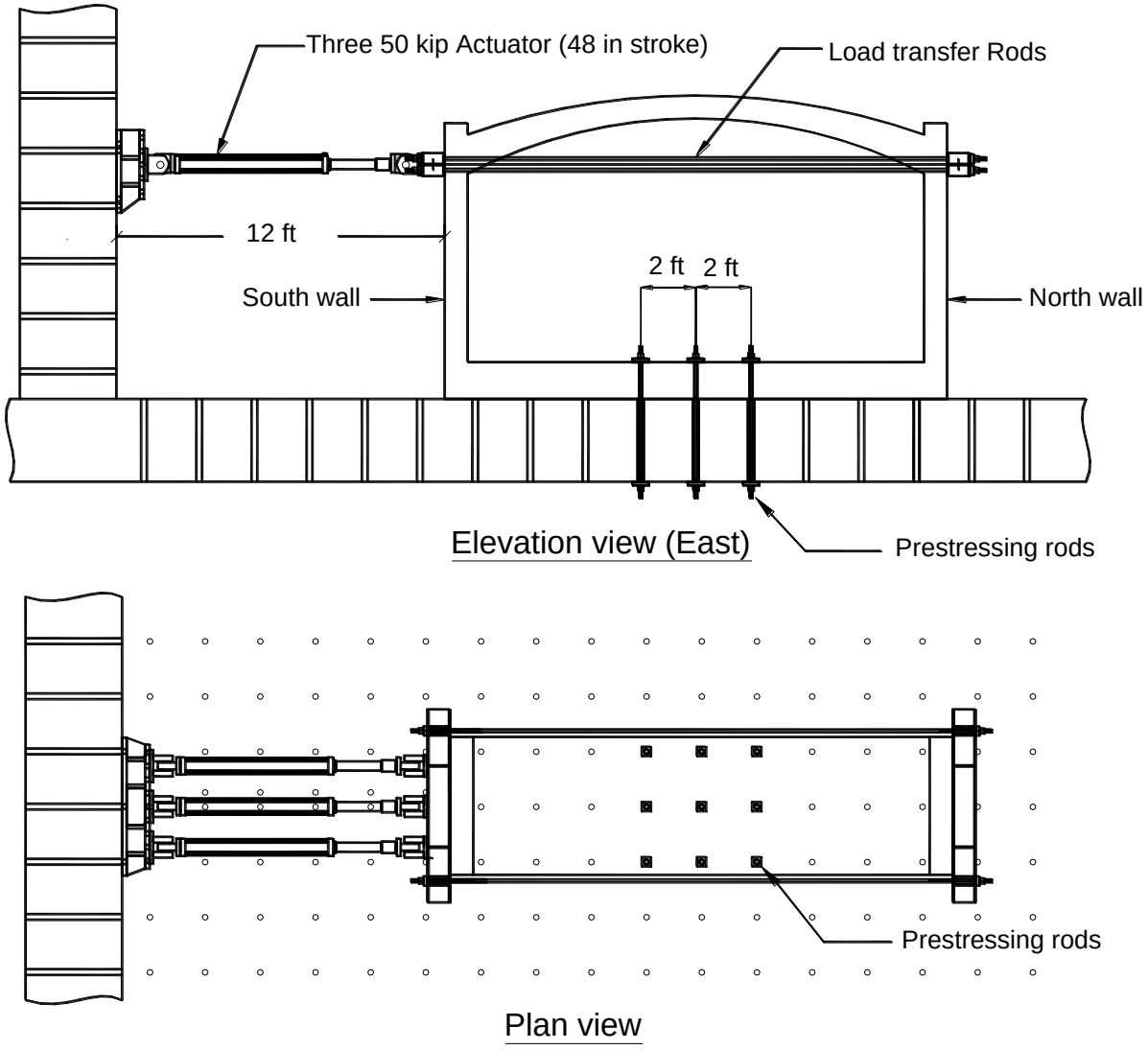

Figure G–3: Elevation and plan view of test setup in the UCSD South Powell Lab

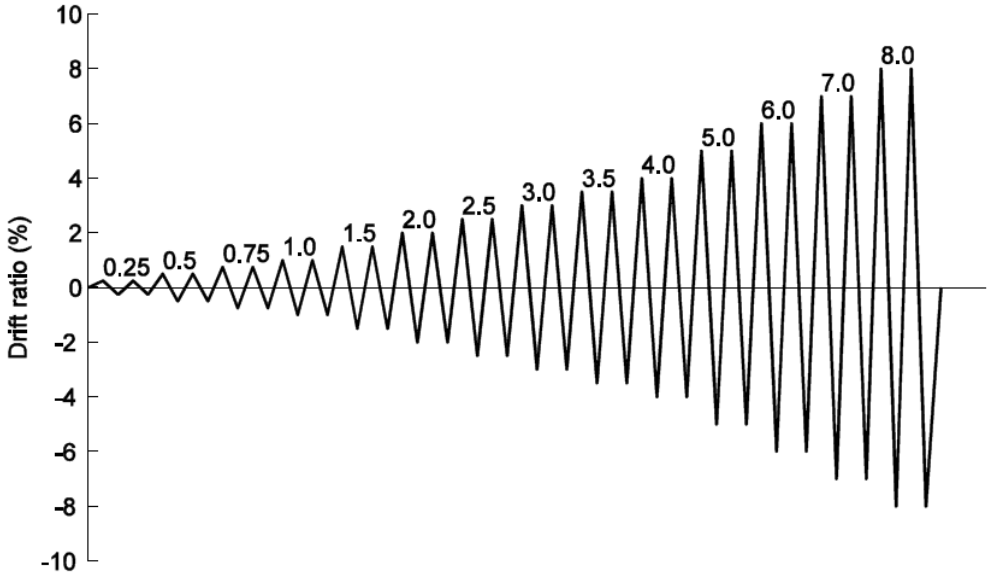

Figure G–4: Graphical representation of loading protocol

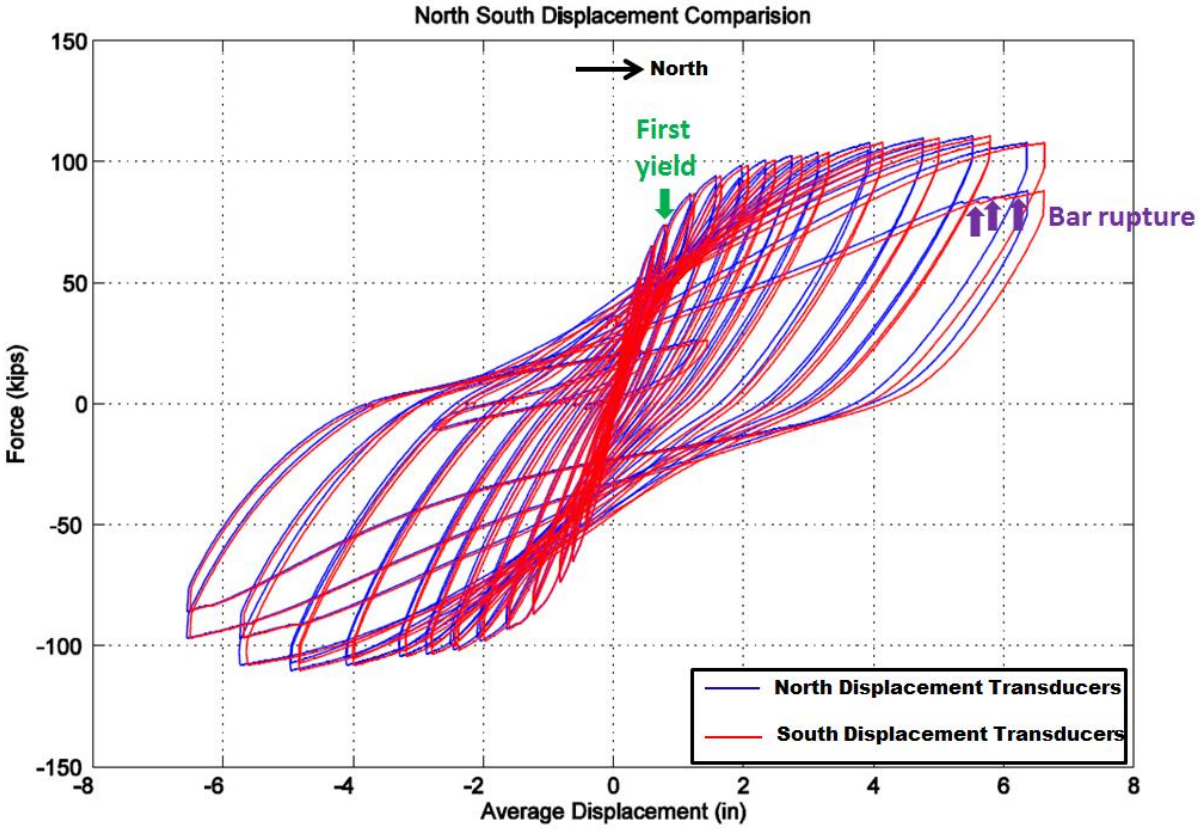

Figure G–5: Relationship of laterl force and displacement in model scale

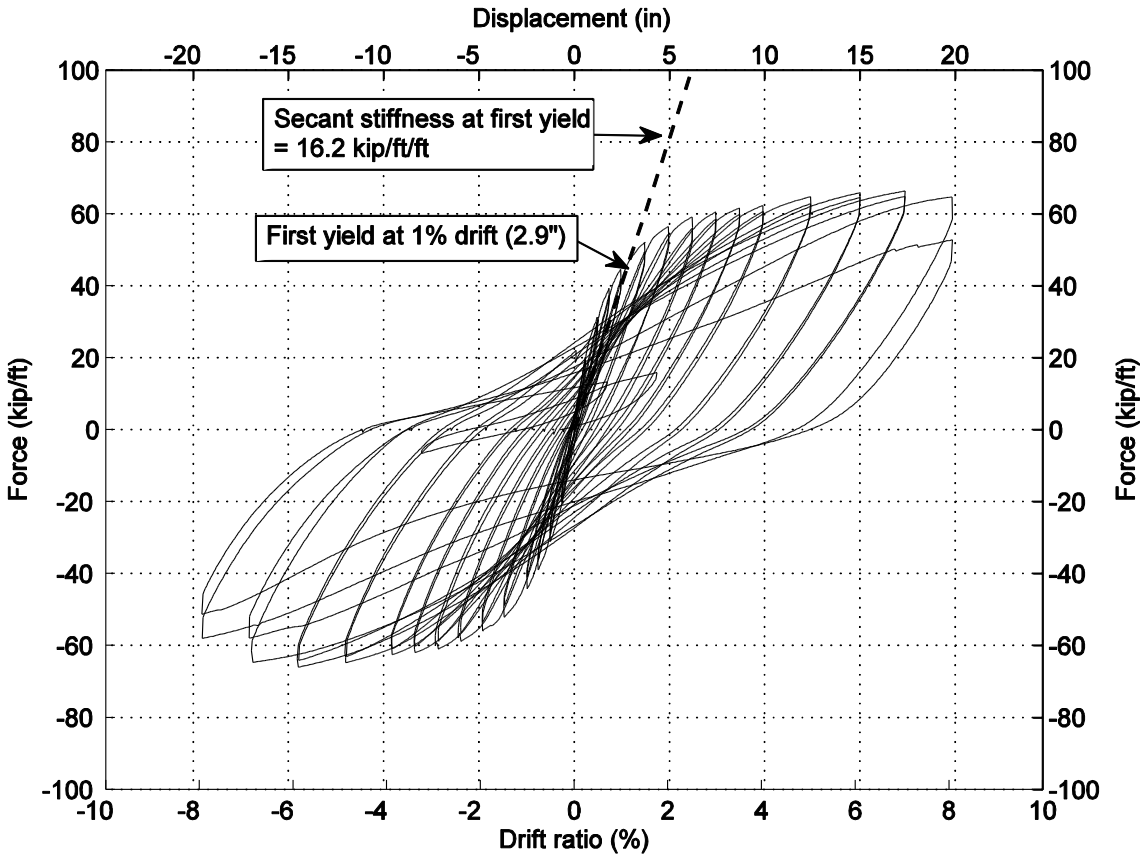

Figure G–6: Relationship of laterl force and displacement in model scale along with secant stiffness at the first yield in prototype scale

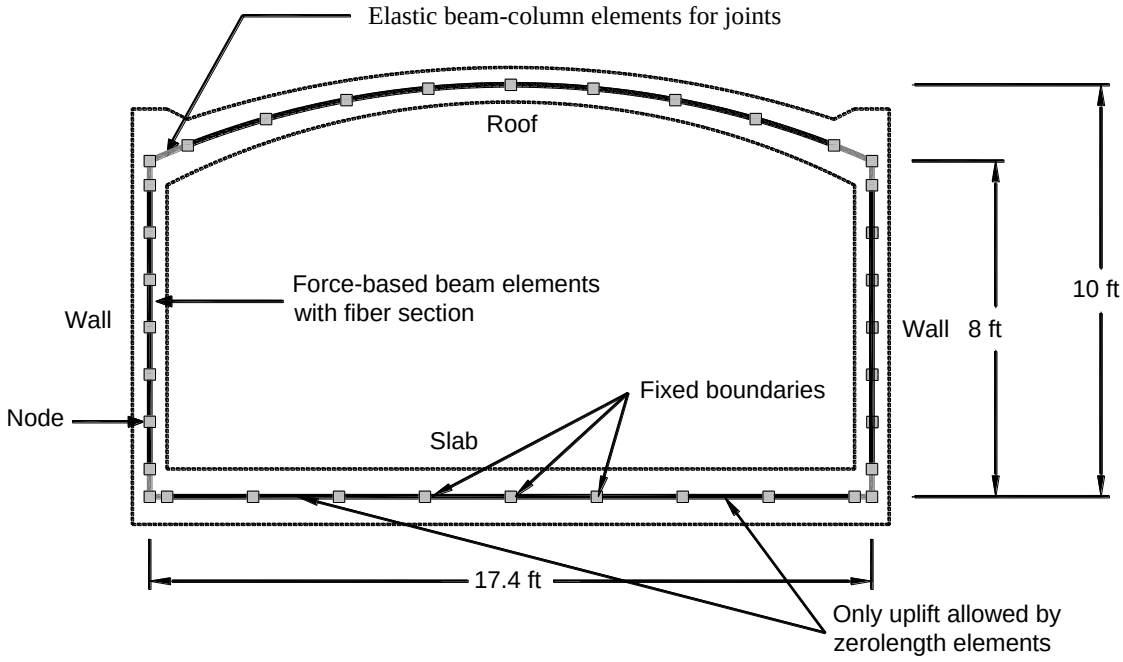

Figure G–7: FE mesh for the 1/3 scale tunnel specimen in the OpenSees platform

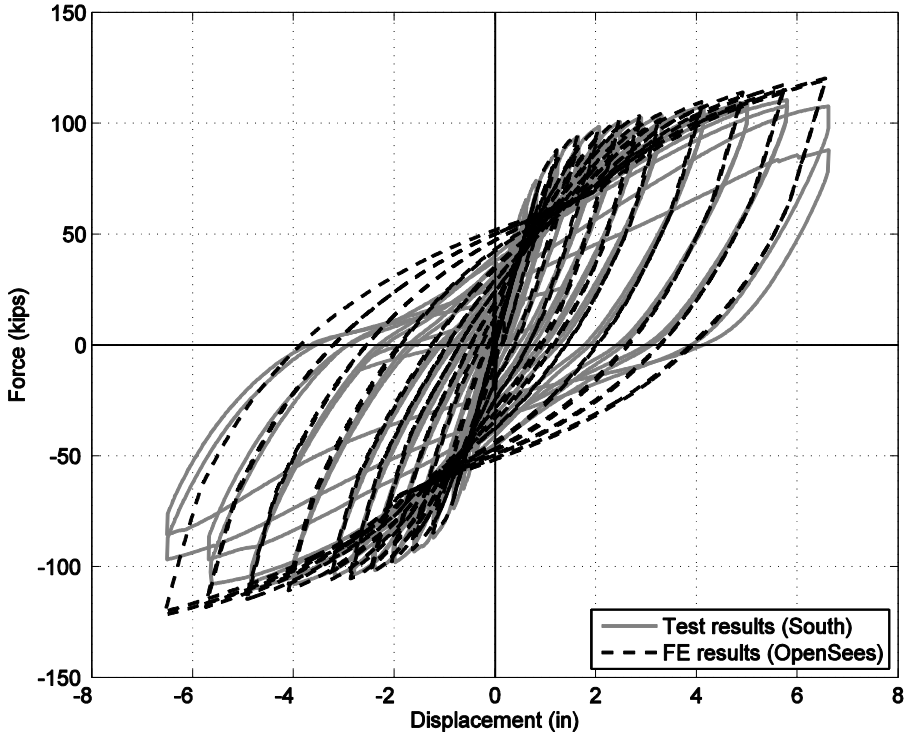

Figure G–8: Comparison of lateral load vs. displacement from the test and the OpenSees FE analysis in model scale

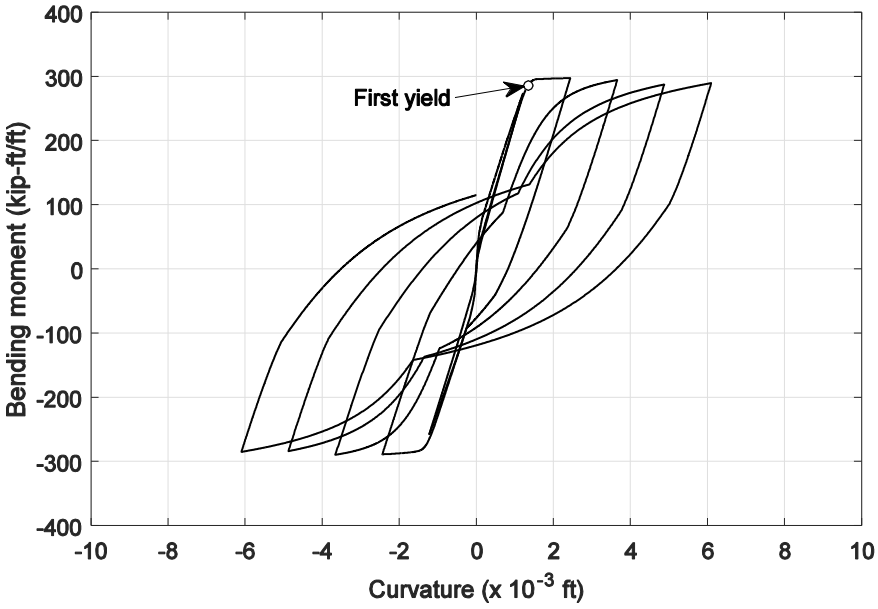

Figure G–9: OpenSees FE model moment-curvature response of wall cross section per unit wall length of 1 ft in prototype scale